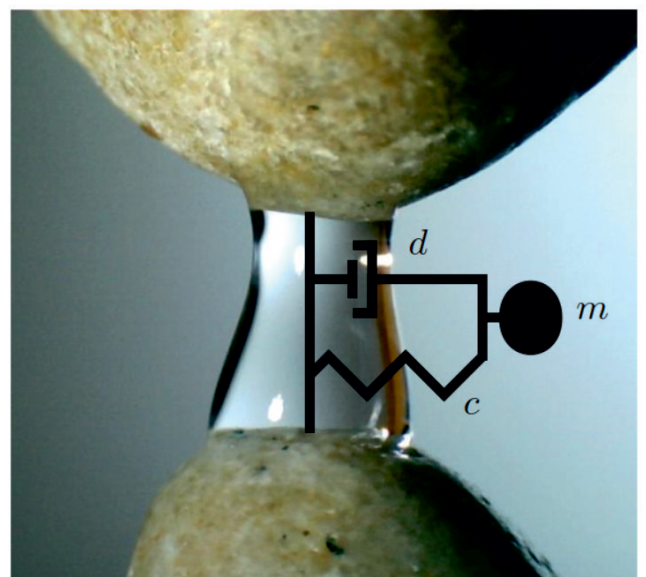
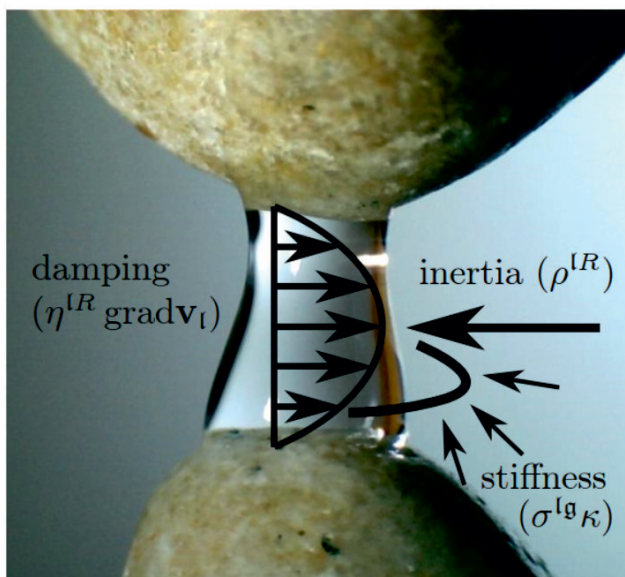


Waves in partially saturated porous media: an investigation on multiple scales

Patrick Sebastian Kurzeja



**Waves in partially saturated porous media:
An investigation on multiple scales**

Dissertation
zur
Erlangung des Grades
Doktor-Ingenieur

der
Fakultät für Maschinenbau
der Ruhr-Universität Bochum

von

Patrick Sebastian Kurzeja

aus Gleiwitz, Polen

Bochum 2013

Dissertation eingereicht am: 27.09.2013

Tag der mündlichen Prüfung: 03.12.2013

Erster Referent: Prof. Holger Steeb

Zweiter Referent: Prof. S. Majid Hassanizadeh

Dritter Referent: Prof. David M. J. Smeulders

Preface

The presented research was carried out during my time as a PhD student at the Chair of Continuum Mechanics at Ruhr-University Bochum from 2010 to 2013. I would like to thank all the people who supported me during this time inside and outside the university. In particular, but not exclusively:

Prof. Dr.-Ing. Holger Steeb, for professional and personal advice, the endless motivation starting with my diploma thesis in autumn 2009, the discussions and ideas, the support, the scientific freedom, and for the ignition of the spark.

Prof. Dr. Dr. h.c. S. Majid Hassanzadeh, Prof. Dr. ir. David M. J. Smeulders, and Prof. Dr.-Ing. Franz Peters as members of the examination board as well as Prof. Dr. Jörg Renner and Prof. Dr.-Ing. Tom Schanz for the discussions, their interest in my work, and extending my view to other fields.

The chair of continuum mechanics for the support in any form and the always convenient atmosphere; the experienced colleagues for showing me the importance and enjoyment of teaching and the other students for the discussions and the fun we had.

The German National Academic Foundation (Studienstiftung des deutschen Volkes), the REACH program between Ruhr-University Bochum and Princeton University, and the RUB Research School for ideological and material support.

Finally, I want to thank all my friends and my family, particularly Sarah, who became my wife in this exciting and challenging time, for their patience and encouragement not only during this time but also on the way and beyond.

Bochum, December 2013

Patrick S. Kurzeja

Abstract

Mechanical wave propagation in partially saturated porous media is of great interest in science and applications because it involves the interaction of various physical phenomena and can be used for non-destructive testing. Moreover, it plays a vital role in modern technologies such as geophysical exploration in water- and air-filled rocks, sound-absorbing materials, and support of ganglia mobilization. In all cases, understanding and predicting wave properties are essential preconditions.

This work models linear, mechanical wave propagation in partially saturated porous media. Balance laws and constitutive relations are combined to describe waves in a solid matrix and two continuous fluid phases. Three longitudinal waves and one shear wave are predicted and studied by means of their dispersion relations. Investigation of smaller-scale, oscillatory flow yields a generalized, characteristic frequency and further modes of solid deformation.

A study of the special case of residual saturation completes the theoretical approach. The corresponding heterogeneous structure of disconnected fluid clusters, such as water bridges, is considered via an oscillator-like rheology. Resonance oscillations produce an additional damping mechanism. An appropriate classification of oscillating fluid clusters follows, with a theoretical, numerical, and experimental investigation. The proposed conceptual approach allows a flexible implementation and investigation of individual phenomena, including damping mechanisms or grain compressibility. Using this approach, the developed models can be applied to the study of material properties, stimulation of enclosed fluids, and of frequency-dependent attenuation bands. In addition, the two-scale view extends understanding of the related processes and yields a generalization of characteristic wave properties.

Zusammenfassung

Mechanische Wellenausbreitung in teilgesättigten, porösen Medien ist von großem Interesse für die wissenschaftliche Forschung, z. B. durch die Kopplung verschiedener physikalischer Phänomene sowie den Einsatz in zerstörungsfreien Prüfmethoden. Zudem ist sie ein wesentlicher Bestandteil in modernen, technischen Anwendungen wie geophysikalischen Erkundungen in wasser- und luftgefülltem Gestein, schallabsorbierenden Materialien und der Mobilisierung von Fluidansammlungen. Zwei grundlegende Voraussetzungen sind dabei das physikalische Verständnis sowie die darauf aufbauenden Vorhersagen der Welleneigenschaften.

Mit diesem Ziel modelliert und untersucht die vorliegende Arbeit lineare, mechanische Wellen in teilgesättigten, porösen Medien. Zur Beschreibung eines Festkörpers, welcher mit zwei kontinuierlichen Fluiden gefüllt ist, werden Bilanzgleichungen und konstitutive Beziehungen genutzt. Dabei werden drei longitudinale und eine Scherwelle anhand ihrer Dispersionsrelationen untersucht. Ein zusätzlicher Fokus liegt auf den kleinskaligen, oszillierenden Flüssen und führt zu einer verallgemeinerten Definition der charakteristischen Frequenz sowie weiteren Freiheitsgrade der Festkörperdeformation.

Der Fall residualer Sättigung vervollständigt den theoretischen Ansatz für Situationen mit einer heterogenen Struktur verschiedener, diskontinuierlicher Fluidansammlungen wie z. B. Wasserbrücken. Diese wird durch eine Oszillatorrheologie charakterisiert und bindet einen zusätzlichen Dämpfungsmechanismus mittels Resonanzschwingungen ein. Anschließend erfolgt eine Klassifizierung der Resonanzeffekte von oszillierenden Liquidclustern durch eine theoretische, numerische und experimentelle Studie.

Das vorgestellte Konzept erlaubt eine flexible Umsetzung und individuelle Untersuchung einzelner Phänomene wie Dämpfungsmechanismen oder Kornkompressibilität. Damit können die entwickelten Modelle auf die Untersuchung von Materialeigenschaften, die Stimulation von unerwünschten Fluideinschlüssen sowie frequenzspezifische Dämpfungsbänder angewendet werden. Zusätzlich erweitert die zweiskalige Betrachtungsweise das Verständnis der beteiligten, physikalischen Prozesse und verallgemeinert die bestehende Charakterisierung von Welleneigenschaften.

Contents

List of Figures	V
List of Tables	IX
Notations and conventions	XI
Introduction and physical principles	1
1 Introduction	3
1.1 Motivation	3
1.2 Scope and outline	6
2 Basic principles of porous media theories	9
2.1 Some history	9
2.2 Multiphase	11
2.3 Multiscale	12
2.4 Upscaling and scale separation	13
3 Basic principles of oscillations and waves	15
3.1 Some history	15
3.2 Harmonic oscillator	17
3.3 Uni-dimensional waves	21
I Waves in partially saturated porous media	25
4 Introduction	27
4.1 Motivation and literature survey	27
4.2 Aims and structure	29
5 Leading equations	31
5.1 The physical system	31
5.2 Balance equations	34
5.3 Constitutive equations	36
5.4 Final equations	48

6	Model properties and selected examples	53
6.1	Preliminary comments and the common initial system	53
6.2	General example and basic model properties	53
6.3	Saturation range	58
6.4	Grain compressibility	60
6.5	Interfacial fluid-fluid areas	61
6.6	Dynamic fluid pressure difference	63
6.7	Viscoelastic solid matrix	64
6.8	Scattering	65
6.9	Remarks on definitions	67
7	Mesosopic extensions	71
7.1	Introduction	71
7.2	Types of mesoscopic losses: squirt-flow, leak-off, and interlayer flow . .	72
7.3	Local flow and its characteristic frequency	73
7.4	Implementation in the current model	75
7.5	Double pore space	78
7.6	Further mesoscopic losses	80
8	Review	81
8.1	Summary and main findings	81
8.2	Conclusions and outlook	82
II	Microscopic pore channel oscillations	85
9	Introduction	87
9.1	Motivation	87
9.2	Aims and structure	87
10	Oscillatory flow in a rigid tube	89
10.1	Dimensional analysis	89
10.2	Biot's solution of a microscopic, oscillatory flow in a rigid tube	92
10.3	Frequency-dependent momentum interaction	93
11	About the use of a characteristic frequency	95
11.1	Characteristic and transition frequency	95
11.2	Phenomenological motivation	96
11.3	General approach	97
11.4	Examples	101
11.5	Conclusion	103
12	Oscillatory flow in elastic tubes	105
12.1	Introduction	105
12.2	Bernabé's model	106
12.3	Conclusion and open questions	111
13	Review	113
13.1	Summary and main findings	113
13.2	Conclusions and outlook	113

III	Waves in residually saturated porous media	115
14	Introduction	117
14.1	Motivation and literature	117
14.2	Aims and structure	118
15	Model	119
15.1	The physical system	119
15.2	Idea	120
15.3	Leading equations	120
16	Examples	125
16.1	Preliminary comments and the common initial system	125
16.2	Basic example	125
16.3	Residually saturated Berea sandstone	127
16.4	Continuous distributions	128
17	Review	133
17.1	Summary and main findings	133
17.2	Conclusions and outlook	134
IV	Microscopic, oscillating fluid clusters	135
18	Introduction	137
18.1	Motivation and literature	137
18.2	Aims and structure	138
19	Theory and variational formulation	141
19.1	The physical system	141
19.2	Geometric properties and relationships	142
19.3	Structure of the set of equations	144
19.4	Mass balance	144
19.5	Relationships between stress and deformation	145
19.6	Variational approach & volume momentum balance	148
19.7	Momentum balance at surfaces	151
19.8	Momentum balance at curves	152
19.9	Final equations	158
19.10	Oscillator modeling	161
20	Numerical investigation	165
20.1	Methodology	165
20.2	Results and discussion	168
21	Experimental study of a liquid bridge	181
21.1	Introduction	181
21.2	Methodology	181
21.3	Results and discussion	183
21.4	Conclusion	186

22 Review	187
22.1 Summary and main findings	187
22.2 Conclusions and outlook	188
Treatise conclusion	189
Appendix	195
A Material properties	197
B Wave equations for partial saturation	201
B.1 Exchange of linearization and compositions	201
B.2 Simplification of linearized products	202
B.3 Algebra of the wave decomposition	202
B.4 Coefficients of the stiffness matrices	203
C Characteristic frequencies	205
D Upscaling of discontinuous fluid clusters	207
E Investigation of oscillating fluid clusters	211
E.1 Numerical data	211
E.2 Experimental data	217
F Objectivity and initial configuration	219
F.1 Introduction	219
F.2 Recapitulation	220
F.3 Source of misunderstanding	221
F.4 Explanation	222
Bibliography	225
Curriculum Vitae	243

List of Figures

1.1	Examples of porous media.	4
1.2	Examples of waves.	4
1.3	Overview of the outline.	8
2.1	Example of a partially saturated porous medium: sandstone, air & ink.	10
2.2	Historical devices of Karl v. Terzaghi.	11
2.3	Schematic sketch of a multiphase system.	12
2.4	Micro- and macroscale of sand.	12
2.5	Schematic visualization of the upscaling process.	13
2.6	The concept of scale separation.	14
3.1	Harmonic oscillator.	17
3.2	Oscillator displacement for different damping ratios.	18
3.3	Examples of free and driven oscillator motion.	20
3.4	Oscillating, elastic rope element.	21
3.5	Propagating, damped wave signal.	22
5.1	Schematic visualization of the modeling concept for a macroscopic, partially saturated system.	32
5.2	Fluid shearing in different structures.	37
5.3	Equilibrium capillary pressure and relative permeabilities.	45
6.1	Dispersion relations for Nivelsteiner sandstone with 40 % water and 60 % air: phase velocity and inverse quality factor.	56
6.2	Dispersion relations for Nivelsteiner sandstone with 40 % water and 60 % air: normalized displacements and relative phase shifts.	57
6.3	P1 phase velocities with air at ambient conditions/reservoir depth. . .	58
6.4	Comparison of dispersion relations with experimental data.	59
6.5	Seismic P1-wave in loose subsurface soil with varying water saturation.	60
6.6	P1 phase velocities for variations of the grain bulk modulus.	61
6.7	P1- and P3-wave phase velocities for different p_{eq}^c - s^I paths.	62
6.8	Dispersion relations accounting for a dynamic fluid pressure difference.	63
6.9	SLS-model.	64
6.10	Dispersion relations for different variations of an SLS-model.	65
6.11	Wavelengths of different wave modes for Nivelsteiner sandstone with 40 % water and 60 % air.	66
6.12	Recorded signal in air-filled glass beads with different diameters. . . .	66
6.13	Hydraulic tortuosity for low and high Reynolds numbers.	68

7.1	Mesoscopic structures in the form of layers and a second characteristic pore space.	72
7.2	Basic concepts of mesoscopic losses.	73
7.3	Difference between global (Darcy-like) flow and local flow.	73
7.4	Stiff and compliant pores.	74
7.5	Dispersion relations for mesoscopic loss due to local flow.	77
7.6	Dispersion relations of a double porosity medium.	79
9.1	Microstructure of natural and artificial materials.	88
9.2	Pores of different porous materials compared to a cm-scale.	88
10.1	Parabolic velocity profile of Hagen-Poiseuille flow in a rigid tube.	89
10.2	Oscillating velocity profile in a rigid tube according to Biot.	92
11.1	Velocity profiles for an idealized Gedankenexperiment.	96
11.2	Ratio of Biot's characteristic frequency and transition frequency.	102
11.3	Dispersion relations for aluminum foam and water.	103
12.1	Dispersion relations according to Bernabé.	108
12.2	Axial, absolute velocity profile of the slow wave according to Bernabé.	109
12.3	Comparison of Bernabé's theory and experimental results.	109
12.4	Measured phase velocities of an air-filled silicone tube	110
14.1	Partial vs. residual saturation.	117
15.1	Schematic visualization of the modeling concept for a macroscopic, partially saturated system.	120
16.1	Basic example of one fluid oscillator.	126
16.2	Dispersion relations of residually saturated Berea sandstone filled with three types of water clusters.	128
16.3	Probability density function as a beta distribution.	129
16.4	Dispersion relations for different eigenfrequency distributions.	130
16.5	Dispersion relations for different damping ratio distributions.	130
19.1	The physical system of a fluid cluster and corresponding definitions.	142
19.2	Idealized sketch of surface tension as molecular attraction.	146
19.3	Contact curve with three enclosed angles and balance of surface tensions.	153
19.4	Influence of solid imperfections.	155
19.5	Movement for typical contact curve conditions.	157
19.6	Physical behavior of an oscillating fluid cluster as a harmonic oscillator.	161
19.7	Typical forms of cluster oscillations for different conditions.	162
20.1	Numerical work flow for the study of cluster oscillations.	167
20.2	Investigated types of fluid clusters.	168
20.3	Fitted curves for variations of V of model I, transversal oscillation.	171
20.4	Eigenfrequency and damping for model I and its variations with oscillation direction transversal to the symmetry axis.	172
20.5	Eigenfrequency and damping for model I and its variations with oscillation direction parallel to the symmetry axis.	173

20.6	Eigenfrequency and damping for model II and its variations with oscillation direction parallel to the symmetry axis.	174
20.7	Eigenfrequency and damping ratio over interfacial areas.	176
20.8	Stiffness and damping for different N values and cluster types.	177
20.9	Influence of N on the velocity profile.	177
21.1	Experimental setup of the oscillating liquid bridge.	183
21.2	Experimental results of the oscillating liquid bridge.	185
F.1	One point for two observers.	220
F.2	A vector between two points for two observers.	221

List of Tables

10.1	Characteristic properties of oscillatory tube flow.	90
16.1	Oscillator types used for the example calculation.	127
19.1	Final variations of mass and momentum balance for different conditions.	160
A.1	Material properties of bulk solid materials.	197
A.2	Material properties of porous solid materials.	198
A.3	Material properties of fluids.	199
A.4	Properties of material combinations.	199
E.1	Fitting of ω_0	215
E.2	Fitting of D	216
E.3	Experimental results of a stimulated, oscillating liquid bridge.	217

Notations and conventions

General comments on notations and conventions

All symbols are introduced throughout the text and a comprehensive overview of the symbols used is given below. For convenient access, however, main aspects of the used notation should be mentioned beforehand. Scalars denote scalar properties while lower case (upper case), boldface characters refer to first (second or higher) order tensors. Lower or upper indices basically express a connection to the respective bulk phase, interface, or curve. Following a convention within theories of porous media, lower phase indices are used for kinematic quantities and upper phase indices for the remaining ones. Despite phase indices, general indices may illustrate special conditions or physical origins.

Note that indices are used to distinguish between phases, which is the most important distinction in the present treatise. They do not indicate covariance or contravariance of tensors. For convenience, (index-free) tensor notation is mostly used. Furthermore, a distinction between micro- and macroscale is avoided because it is obvious within the self-consistent parts. This compromise - against multiple kinds of indices to distinguish phases, tensorial bases, and scale affiliation - was made to aid readability. Few exceptions (use of index notation, mixture of micro- and macroscale properties) occur very rarely and are explicitly mentioned.

Also note that some parts of this work have been previously published and are indicated appropriately. However, such publications may differ with respect to the used notation or formulations, due to deviating requirements or context, respectively.

The most important symbols and abbreviations are summarized in the following. For the sake of brevity and clarity, all individual combinations of indices are not listed. Special characters appearing only in a limited context (especially in the appendix) are neglected in the following lists.

Two chapters of Part II and the entire Part IV are based on microscopic properties. Although the corresponding notations are similar to those of the other parts, it is convenient to introduce the microscopic properties in their own context. This avoids confusion with other definitions that are relevant for macroscopic theories. For accurate handling, they are also listed separately. Some properties appear for micro- and macroscale theories.

Miscellaneous

$\frac{\partial}{\partial_*}(\bullet)$	partial derivative with respect to general variable *
$\frac{\partial}{\partial t}(\bullet), \partial_t(\bullet), (\dot{\bullet})$	partial time derivative
$\frac{D^{\zeta}(\bullet)}{Dt}$	material time derivative with respect to phase ζ
$\frac{\partial}{\partial x}(\bullet)$	partial, local derivative with respect to x -direction; note the difference between position vectors \mathbf{x} and \mathbf{X} (or \mathbf{X}_{ζ}) of the current and reference configuration, cf. grad vs. Grad $_{(\zeta)}$
\cdot	scalar/inner product
\times	cross product between vectors (used in equations) emphasizes (scalar) product between scalars in the normal text, units, or labels
\otimes	dyadic/tensor product
(\sim)	characteristic property (length, time, modulus, etc.)
(\bullet)	dimensionless property
$\Re(\bullet), (\bullet)_{\Re}$	real part
$\Im(\bullet), (\bullet)_{\Im}$	imaginary part
$(\bullet) _{a=b}$	• evaluated at $a = b$
$(\bullet)_0$	0 refers to reference state/configuration; often equilibrium
$(\bullet)_{\text{eq}}$	equilibrium part
$(\bullet)_{\text{neq}}$	non-equilibrium part
$(\bullet)_{\text{lin}}$	linearized
\parallel	index for waves parallel to propagation direction (longitudinal waves, later replaced by P)
\perp	indicates orthogonality and index for waves perpendicular to propagation direction (shear waves, later replaced by S)
$[\bullet]$	unit (types) of • (classical definition; used in running text, e.g., [T ⁻¹])
$\bullet[*]$	[*] is used as a suffix with * indicating the units of • with specific measurement units (no defined convention but widely used custom in relevant dis- ciplines; used in labels for the sake of brevity, e.g., [s ⁻¹])
[...]	squared brackets in formulas do not refer to units but are used for structuring purposes

Parts I - III and introductory chapters

Latin characters

$a_{0,1,2,\dots}$	used to represent unspecified constants in equations
$a^{\alpha\beta}$	interfacial areas $\alpha\beta$
$a_{00,01,\dots}$	constants of the quadratic relationship between interfacial areas, saturation, and equilibrium capillary pressure
a_{sf}	geometric parameter for mesoscopic loss mechanisms
\mathcal{A}, A	area
A	index indicating a stiff solid skeleton (in Chapter 11)
$A_{0,1,2,3}$	constant of oscillator solution (in Chapter 3)

A	matrix accounting for inertia terms
AT	averaging technique
asw	adjacent solid walls
$b_{0,\mathfrak{f}}$	proportionality factor of viscous (Biot-like) interaction
b_{osc}	proportionality factor of momentum interaction of an oscillating fluid cluster
B	index indicating a weak solid skeleton (in Chapter 11)
$B(\bullet, \bullet, \bullet, \bullet)$	beta distribution
$B_{0,1,2,3}$	constant of oscillator solution (in Chapter 3)
B	matrix accounting for viscous terms
c	stiffness of oscillator-like rheology
$c_{\text{SLS},1}, c_{\text{SLS},2}$	the two spring stiffnesses of an SLS-model
c_{phase}	phase velocity (in Chapter 3)
c_{χ}	phase velocity of wave mode χ
$c_{\text{phase,C}}$	complex-valued phase velocity approach (in Chapter 3)
c_{group}	group velocity
$c^{\alpha\beta\gamma}$	curve fractions of curve $\alpha\beta\gamma$
c_{JKD}	frequency-dependent correction function of momentum exchange
c_{sf}	frequency-dependent correction function of mesoscopic loss
c_{cl}	frequency-dependent function accounting for momentum interaction of fluid clusters
$c_{p_{\text{eq}}}^c$	constant relating saturation rate and production of interfacial areas of type \mathfrak{lg}
c	index for continuous fluid
C	matrix accounting for elasticity terms
d	damping coefficient of oscillator-like rheology
d_{SLS}	damping coefficient of an SLS-model
d_{pore}	characteristic pore diameter
\mathfrak{d}	index for discontinuous fluid
D	damping ratio of an oscillator-like rheology
D_l	damping ratio of oscillating clusters with index l
DP	index for properties of a double pore space extension
E	Young's modulus, indicates extensional waves when used as an index
$E^{\mathfrak{lg}}$	production term of interfacial areas of type \mathfrak{lg}
f	frequency
$f_{c,\text{Biot}}$	Biot's characteristic frequency for a mixture with one pore fluid
$f'_{c,\text{Biot}}$	Biot's microscopic characteristic frequency for a mixture with one pore fluid
f_{\bullet}	(probability) density with respect to distribution \bullet
\mathfrak{f}	index for fluid phases, usually $\mathfrak{f} \in \{\mathfrak{l}, \mathfrak{g}\}$
\mathbf{f}	volumetric/body forces, usually due to gravity
F	deformation gradient
F	external force on an oscillator (in Chapter 3)
\hat{F}	amplitude of F
FE	Finite Element
g	gravitational acceleration constant
\mathbf{g}	gravitational acceleration vector
\mathfrak{g}	index for the gas phase

grad	gradient with respect to current configuration
Grad	gradient with respect to reference configuration
Grad_ζ	gradient with respect to reference configuration of phase ζ
GW	Gassmann-Wood (limit)
i	$\sqrt{-1}$
I, II, III	indicating the linearization point of the frequency correction for $\omega \ll \omega_{c,\text{Biot}}$, $\omega \approx \omega_{c,\text{Biot}}$, $\omega \gg \omega_{c,\text{Biot}}$
I	three-dimensional unit tensor
I^A	three-dimensional surface unit tensor
j	used as index for different microscopic clusters in Part III
J	Jacobian determinant (of F)
k	scalar (complex-valued) wave number used as index for different clusters in Part III
k^s	intrinsic permeability
k_{rel}^f	relative permeability factor for fluid f
k	(complex-valued) wave vector
K^α	bulk modulus of bulk phase α
K^{grains}	bulk modulus of the bulk material composing the solid skeleton
K^{lg}	Reuss-average of fluid bulk moduli
l	index for liquid phase
l	generally used as length used as index for different clusters in Part III
l_{compl}	length of compliant pores
l_{stiff}	length of stiff pores
m	mass
m_{sf}	exponent for the characteristic frequency of mesoscopic loss
mic	indicates microscopic properties in Part III
M^s	P-wave modulus
MT	mixture theory
n^α	volume fraction of bulk phase α
n^{kl}	volume fraction of clusters with index kl
n^{sf}	volume fraction portion of mesoscopic loss mechanisms
n	normal vector
n^k	normal vector of wave propagation direction
p^ζ	partial pressure of phase ζ
$p^{\zeta R}$	real pressure of phase ζ
p^c	capillary pressure
$p^{\Delta \text{gl}l}$	fluid pressure difference between g and l
p^b	air-entry/bubbling pressure
$\hat{\mathbf{p}}^{\bullet *}$	momentum exchange from \bullet to $*$
$\hat{\mathbf{p}}^\bullet$	total momentum exchange from \bullet
$\hat{\mathbf{p}}_{\text{neq,id}}^f$	momentum exchange of fluid f due to inertial drag
$\hat{\mathbf{p}}_{\text{neq,vd}}^f$	momentum exchange of fluid f due to viscous drag
P	index for longitudinal waves
P1, P2, P3	index for first/second/third longitudinal wave
P_{BW}	Biot-Willis parameter
q	displacement of oscillator or wave (in Chapter 3)
q_{hom}	homogeneous solution of q
q_{part}	particular solution of q
\hat{q}	amplitude of q
Q , Q-factor	quality factor with Q^{-1} as the inverse quality factor

r_{Berryman}	geometric factor for tortuosity approximation
rs	index to indicate residual saturation
REV	representative elementary volume
R	radius
R_{BW}	Biot-Willis parameter
s^f	saturation of fluid f
s_{res}^f	residual saturation of fluid f
s^{LR}	effective liquid saturation
s	index for solid phase
S	index for shear wave
S_{BW}	Biot-Willis parameter
SLS	standard linear solid (model)
t	time
t_0	reference time
[T]	fundamental time unit
T	oscillation period
\mathbf{T}^ζ	partial stress tensor of phase ζ
$\mathbf{T}^{\zeta R}$	real stress tensor of phase ζ
TPM	theory of porous media
u	displacement value (scalar, without direction)
\hat{u}	displacement amplitude
\mathbf{u}	displacement vector
$\hat{\mathbf{u}}$	displacement vector amplitude
\mathbf{v}	velocity
V_{amp}	amplification function
$V_{\text{amp,max}}$	maximum of amplification function
\mathbf{w}_f	seepage velocity, i.e. relative velocity between fluid f and solid
x, x_i	used as uni-dimensional spatial coordinate
\mathbf{x}	position vector
\mathbf{X}	position vector at reference time
y	used as uni-dimensional spatial coordinate

Greek characters

α	replacement character for arbitrary bulk phase index
$\alpha\beta$	replacement character for arbitrary interface index
$\alpha\beta\gamma$	replacement character for arbitrary contact curve index
α_{Biot}	Biot's coefficient
α_{id}	inertial drag parameter
α_{hyd}	hydraulic tortuosity
α^{kl}	volume ratio of cluster with index kl
α^{pdf}	continuous volume ratio distribution of clusters
Γ	gamma function
δ	phase lag
δ_x	delta-distribution around x
Δ	indicates a difference (e.g. of pressure), not a diff. operator
ε	(linearized) strain tensor
ε_s	linearized solid strain
ϵ	volumetric deformation

ζ	universal replacement character for arbitrary bulk phase/interface/contact curve index
η^fR	dynamic viscosity of fluid f
θ	temperature
ϑ	logarithmic damping decrement
Θ	contact angle
Θ_{Young}	Young's/equilibrium contact angle
κ	total curvature
λ	wavelength
λ^s	Lamé parameter of the solid skeleton
λ^{sR}	Lamé parameter of the solid skeleton with respect to real stress
λ_{BC}	Brooks & Corey parameter
λ_{distr}	relative-width scaling of the used beta distribution
Λ^{grains}	coupling term of skeleton and grain deformation
μ^s	Lamé parameter of the solid skeleton
μ^{sR}	Lamé parameter of the solid skeleton with respect to real stress
μ_{distr}	mean value of the used beta distribution
ν	constant of harmonic approach (in Chapter 3)
ρ^ζ	partial density
$\rho^{\zeta R}$	real density
$\hat{\rho}^{\bullet *}$	mass exchange from \bullet to $*$
$\hat{\rho}^\bullet$	total mass exchange from \bullet
σ	surface tension
τ	coefficient for dynamic capillary pressure/fluid pressure diff.
ϕ	porosity
ϕ_0^R	effective initial porosity
φ^ζ	phase ζ
φ^{DP}	logistic sigmoid function for modeling of a double pore space
χ	replacement character for wave modes P1, P2, P3, or S
ψ	replacement character for P or S
ω	angular oscillation frequency
ω_0	undamped, angular oscillation frequency/eigenfrequency
$\omega_{0,k}$	undamped, angular oscillation frequency/eigenfrequency; particularly used for clusters with index k
$\omega_{c,\text{Biot}}$	Biot's characteristic (angular) frequency
$\omega'_{c,\text{Biot}}$	Biot's microscopic characteristic (angular) frequency
ω^*	alternative characteristic (angular) frequency
$\omega_{c,f}$	characteristic (angular) frequency of fluid f in a mixture with multiple pore fluids; based on $\omega_{c,\text{Biot}}$
$\omega_{c,\text{VE},f}$	characteristic (angular) frequency for mesoscopic, local flow of fluid f
$\omega_{\text{trans},\text{P1/P2/S}}$	characteristic (angular) transition frequency of the P1/P2/S-wave
$\omega_{\text{trans},\text{osc}}$	characteristic (angular) transition frequency of an oscillating fluid cluster
ω_\bullet	with \bullet containing the name of a wave mode and index A, B, I, II, and/or III: analytical solution of the respective transition frequency
Ω	driving angular frequency of external stimulation
Ω_{res}	angular resonance frequency

Special microscopic properties in Part II

$c_{0,f}$	fluid speed of sound
c_{Bernab}	frequency-dependent phase velocity after Bernabé
Eu	Euler number
J_0, J_1	Bessel functions of first kind
Fr	Froude number
Sr	Strouhal number
R	tube radius
Re	Reynolds number
$v_{f,i}$	fluid velocity component in i -direction
v_{ax}	axial velocity of oscillatory flow in a tube
V_S	bulk solid shear velocity
Wo	Womersley number
x_i	spatial coordinate in i -direction
X_{ex}	external tube flow stimulation due to pressure gradient or gravity
y	radial coordinate
δ_{vs}	viscous skin depth

Part IV

Latin characters

$a^{\alpha\beta}$	interfacial areas $\alpha\beta$
\mathcal{A}	area
b	index for the boundary
c	stiffness of a harmonic oscillator
\mathcal{C}	curve
Ca	capillary number
d	damping of a harmonic oscillator
D	damping ratio of a harmonic oscillator
div	divergence operator
$\text{div}^{\mathcal{A}}$	surface divergence operator
$\text{div}^{\mathcal{C}}$	curve divergence operator
$f^{\text{lg}s}$	contact line resistance
f	replacement character for fluid phase indices
\mathbf{f}	volume force
f_0	excitation amplitude
g	index for the gas bulk phase
gs	index for the gas-solid interface
lgs	index for the liquid-gas-solid contact curve
\mathbf{g}	gravitational acceleration vector
grad	gradient operator
$\text{grad}^{\mathcal{A}}$	surface gradient operator
$\text{grad}^{\mathcal{C}}$	curve gradient operator
h	characteristic length for frequency dependence
\mathbf{I}	three-dimensional unit tensor

\mathbf{I}^A	three-dimensional surface unit tensor
\mathbf{I}^C	three-dimensional curve unit tensor
K^f	fluid bulk modulus
K^{grains}	bulk modulus of the solid (bulk) phase
\tilde{l}	typical length
l	index for the liquid bulk phase
ls	index for the liquid-solid interface
lg	index for the liquid-gas interface
m	mass
N	dimensionless number for frequency dependence
\mathbf{n}	normal vector
$p^{\zeta R}$	(real) pressure of ζ
q_0	amplitude of oscillation
R	Radius
s	index for the solid bulk phase
\mathbf{t}^{ext}	external load vector at the boundary
$\mathbf{T}^{\zeta R}$	(real Cauchy) stress tensor of ζ
$\mathbf{T}_{\text{extra}R}$	extra stress tensor
\mathbf{v}	velocity
\mathcal{V}	volume
V	liquid cluster volume \mathcal{V}_l
\mathbf{x}	position vector

Greek characters

α	replacement character for arbitrary bulk phase index
$\alpha\beta$	replacement character for arbitrary interface index
$\alpha\beta\gamma$	replacement character for arbitrary contact curve index
γ	line tension/energy
$\boldsymbol{\varepsilon}_s$	linearized solid strain
ζ	replacement character for universal index of bulk phases/interfaces/contact curves
η^{fR}	dynamic viscosity of fluid f
θ	temperature
Θ	contact angle
Θ_{Young}	Young's/equilibrium contact angle
κ	total curvature
κ_c	curve/line curvature
κ_g	geodesic curvature
κ_n	normal curvature
λ^{grains}	Lamé parameter of the solid (bulk) phase
Λ	slenderness
μ^{grains}	Lamé parameter of the solid (bulk) phase
$\rho^{\zeta R}$	(real) density of ζ
σ	surface tension/energy
ω	angular oscillation frequency
ω_0	undamped, angular oscillation frequency/eigenfrequency
Ω_{res}	angular resonance frequency

Introduction and physical principles



Chapter 1

Introduction

1.1 Motivation

Fluid-filled porous media and waves have always been part of our environment. Consciously or unconsciously, porous media belong to our everyday experience, for example, footprints in wet sand or shaping of snowballs. Moreover, our environment is significantly influenced by fluids in porous media. For instance, the porosity of soil is an essential precondition for water storage and it made settlement near the fertile Nile Delta possible.

Today, porous materials are even more important than ever. On the one hand, properties such as storage capacity are utilized for fuel cells, aquifers, diapers, or geothermal reservoirs. On the other hand, fluid-filled porous media can be hazardous, for example, landslides caused by liquefaction. Thus, control, adjustment, and characterization of such materials are major goals for science and industry. For instance, geoen지니어ing aims at forming inorganic material or to restrict deformation in tunnel bores. Furthermore, characterization of organic, porous materials such as bones is important for medical applications.

In all cases, the fluid content plays a vital role for the physical behavior. For example, the speed of an earthquake wave strongly depends on whether the earth is fully saturated with water or only partially.

Whereas fluid-filled, porous media are the object of investigation, wave propagation is the physical phenomenon that will be studied in this work. Waves are often encountered more directly: waves in the ocean, the sound of thunder, or vibrations of an earthquake. Moreover, they appear in a variety of forms (body waves, surface waves, planar waves, rotational waves, ...) and in various media (mechanical waves in solids or electromagnetic waves without a carrier medium). Applications involving waves are varied and range from radio waves in signal transmission over seismic waves in geophysical exploration to ultrasonic waves for prenatal care. Waves from natural sources also play an important role in fields such as risk management or energy supply. Yet, we are also not able to follow Jules Verne's [213] journey to the center of the earth. But seismic waves provide information directly from what holds the world together in its innermost folds.



Figure 1.1: Examples of porous media (from left to right, top to bottom): rock, aluminum foam, synthetic foam, sand, soil, foam for household use, bread, and sintered glass beads.



Figure 1.2: Examples of waves (from left to right): Water waves at the surface of the ocean (coast of Australia), air waves made visible by oscillations of grass (Ireland), and monitoring of earthquake waves at Ruhr-Universität Bochum (Germany).

Consequently, the scientific investigation of wave propagation involves almost all natural sciences and technical disciplines. Major applications include signal transmission and stimulation in industry as well as destruction-free testing in scientific research. In the process, interpretation and prediction of wave propagation strongly depend on understanding the relevant physical processes and appropriate mathematical modeling.

Combining both - the system of partially saturated porous media with the phenomenon of wave propagation - yields a multifaceted research area with interesting applications. This combination constitutes the central focus of investigation in this treatise.

Characterizing partially or fully saturated porous media via waves is highly important. For example, it complements other methods that may disturb fragile mixtures, cf. [81, 196, 198]. Furthermore, exploration techniques [119], sound-absorbing materials [231, 235], and ganglia stimulation [38, 174] rely on understanding of this research area. The intricate structure of porous media is a major challenge for two reasons: Detailed information is often missing and - if available - difficult to process. For instance, determining of a rock's permeability by characterizing the properties of each single pore misses the target. Instead and almost intuitively, expressions such as porosity or saturation are used. Figuratively, the term porosity unifies the individual pores by means of a superordinate description. Similarly, current scientific studies make use of superordinate concepts.

As such, fundamental contributions to understanding waves in fully saturated porous media were made during the last century, for instance, [24, 25, 74, 76, 160, 226]. Additional aspects include phenomena such as layered structures or squirt-flow, cf. [54, 56, 140, 223]. Basic elements are an elastic, solid skeleton that is composed of elastic grains and coupled to one pore fluid. The more general case of partial saturation adds at least one more fluid phase. Relevant wave propagation theories developed significantly during the last quarter century, for example, [3, 22, 121, 128, 132, 181, 198, 211, 220].

In recent years, improvements in imaging techniques, computational capabilities, and conceptual frameworks have made more sophisticated studies possible and more precise information has become available. Nevertheless, this topic is young and many areas remain to be explored, including, amongst many others: origins of attenuation, interaction between length scales, stimulation of wave types, or dynamics of residually saturated porous media. This understanding is not only of immanent scientific interest but also contributes to safe, responsible design in engineering and accurate detection of environmental processes.

Welcome to a topic that unifies fundamental physical phenomena, via scale-bridging and conceptual strategies, with modern applications!

1.2 Scope and outline

The present thesis focuses on propagation of linear, mechanical waves in partially and residually saturated porous media. It aims to

- **understand** the relevant physical processes
(what are the origins of attenuation, how do the constituents move, ...?)
- **predict** the wave behavior
(which waves can be stimulated, how fast do they travel, ...?)
- **compare** assumptions with possible observations
(do grains deform less than fluids, which processes can be neglected on the basis of the available data, ...?)
- **interpret** phenomena on different length scales
(are tube surface waves observable in a network, which information has to be transferred, ...?)

The structure of this treatise follows the related research process and its resulting publications. The two major topics of wave propagation in partially and residually saturated porous media constitute the classical thread (Part I & III). Additionally, they are extended by two parts of microscale investigations as they occurred during the research process (Part II & IV). These extensions are implemented in a logical order and with respect to the physical processes involved, cf. Fig. 1.3.

Thus, the entire work is divided into seven parts. In addition to the introduction, treatise conclusion, and appendix, four main parts (I, II, III, and IV) constitute the central treatise. They build on each other but are self-contained. With regard to their foci, each part contains its specific motivation, literature survey, and discussion.

- Two chapters follow this introductory part, presenting the fundamentals of porous media theory and wave propagation. They provide historical overviews and establish basic terms and definitions.
- **Part I** develops a basic framework for describing wave propagation in porous media that are filled with two continuous fluid phases. In a first step, leading equations of the physical principles are presented and combined into a final mathematical model. This model is the fundamental basis for the following investigations identifying the principles of wave propagation in porous media. Additionally, it will be applied to specific examples with an excursion into mesoscopic losses.
- **Part II** turns to microscopic processes of wave propagation described in Part I. Thereby, it specifically addresses questions raised by current research. Three chapters focus on: oscillatory flow in a rigid pipe, characteristic frequencies, and the influence of microscopic tube elasticity. These smaller scale phenomena are studied with respect to their influence on macroscopic models.
- While Part I presents a modeling technique for a porous medium with two continuous fluids, **Part III** completes the theory by extending it to a fluid in the state of residual saturation. This fluid fills the pore space as distinct conglomerations/clusters, each with a separate dynamic behavior. Such clusters

are modeled as oscillators and combined with the findings of Part I via a two-scale approach. Various examples of cluster distributions are studied and include resonance effects as an additional damping mechanism.

- **Part IV** constitutes the microscale study of residually saturated porous media. Fluid clusters are described theoretically and classified with respect to their dynamic properties. Thereafter, a systematic, numerical study provides an overview of eigenfrequencies and damping. It accounts for different material and geometric parameters and is supported by an elementary experiment. This part completes the microscopic study of oscillatory pore channel flow described in Part II by considering fluid-fluid interface effects.
- Finally, the previous parts are summarized within a general treatise review and conclude with a preview of further amendments and future research.
- The appendix provides material data, more detailed explanations, and a comprehensive overview of numerical results that supports the main parts with further details.

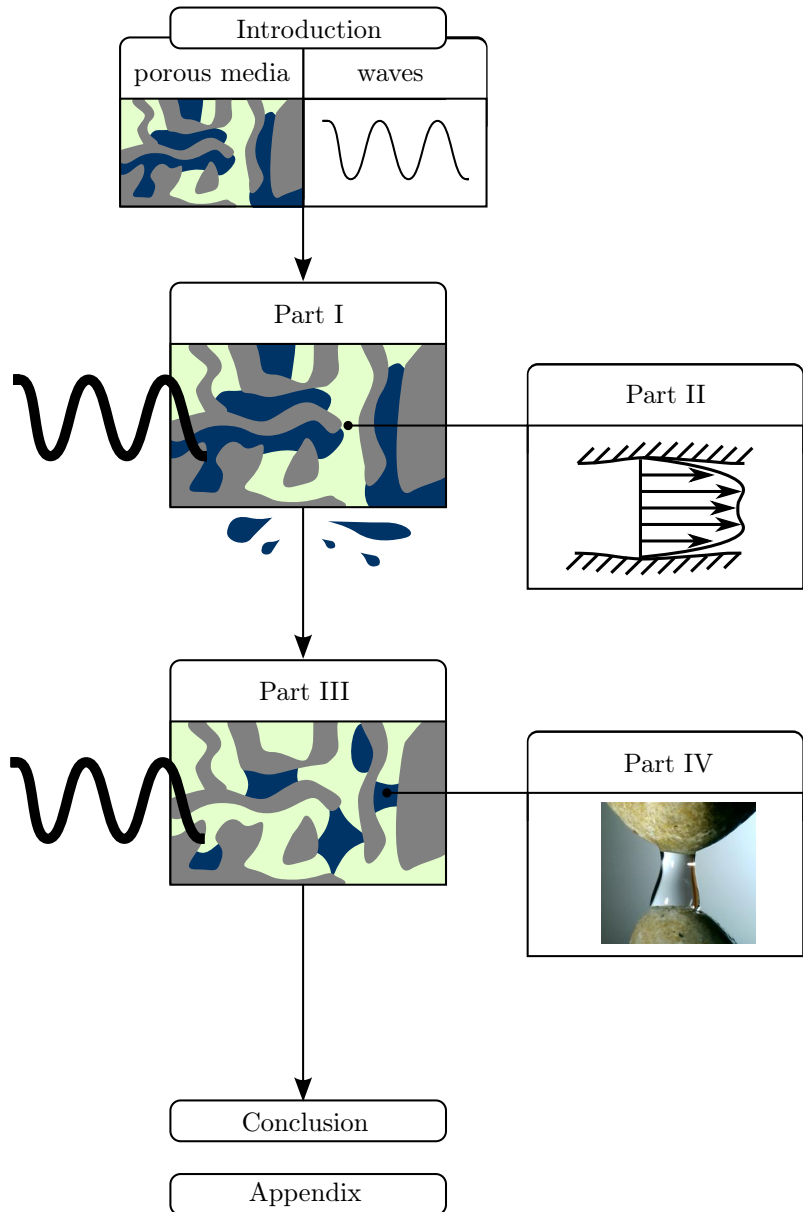


Figure 1.3: Overview of the outline.

Chapter 2

Basic principles of porous media theories

This chapter introduces basic terms and well-established concepts describing fluid-filled porous media. It starts with a historical overview and classifies modern research approaches. Finally, an explanation of the terms multiphase, multiscale, upscaling, and scale separation is given. The expressions and definitions used will appear throughout the entire treatise.

2.1 Some history

In a general sense, porous media and mixtures have been studied for centuries. For example, a concept of weighting factors was introduced by the use of mole fractions in Dalton's law, which was motivated by the work of J. Dalton in the early 19th century. Some decades later, Darcy was probably the first scientist to initiate the development of the distinct research field of porous media in 1856 [43]. He postulated, empirically, a linearity between fluid flow rate through a porous medium and pressure gradient. During the following decades, consolidation and storage in a confined aquifer were the driving topics, cf. Wang's work [217], which also serves as a basis for the following survey and provides further details. Three disciplines can be considered as starting points for modern theories of porous media: geomechanics, petroleum engineering, and hydrogeology [217].

In 1892, King [46] examined the rise of the water level in a well that depended on the load of bypassing trains. Observations at that time were restricted to natural, porous media because man-made materials such as synthetic foam were not available. In 1909 and in addition to the empirical observations of that early century, the Cosserat brothers [40] laid the foundation for the theory of extended continua of higher kinematic order. This approach was later extended by investigators like Mindlin and Eringen [61, 146]. Meinzer [141] related the flow process in an aquifer to its compressibility in the beginning 20th century. In the same period, the investigations of large scale coupling between fluid and porous solid by Pratt & Johnson [162] and Muskat [152] were motivated by petroleum engineering.

The analogy of transient flow in porous media and heat conduction as diffusion equations is based on the work of Terzaghi, Theis & Lubin, and Jacob, cf. [99, 206].



Figure 2.1: Example of a partially saturated porous medium: sandstone, air, and ink.

Terzaghi contributed to the theory of porous media in many ways [204, 205]. Uni-dimensional consolidation in soils is known as the Terzaghi problem. It reveals that a load is first carried by the pore fluid and transferred to the solid skeleton with delay because fluid outflow is hindered by viscous effects. He was also instrumental (perhaps next to other scientists like Fillunger [68] who, unfortunately, was involved in an intractable debate with Terzaghi) in developing the effective stress principle, which is important for deformation of the solid skeleton or soil liquefaction; also cf. Terzaghi's experimental devices in Fig. 2.2. Another important landmark is Biot's [23] contribution to the theory of poroelasticity in the middle of the last century.

Today, current theories can be divided into three categories following the overview of Hassanizadeh & Gray [86]. First, there are various initial attempts that rely on descriptive models. They often contain single constitutive laws and/or empirical findings. Their precise description contrasts with their limitation to special applications, for example, Darcy's law [43] and its specialized extensions such as anisotropy.

Second, there is the (continuum) theory of mixtures, or mixture theory (MT), cf. the contributions of Truesdell [209, 210] or Eringen & Ingram [63] and Atkin & Craine [7]. It basically describes the different constituents as overlapping continua, which are also called phases. These phases coexist everywhere and each of them is related to continuous field quantities such as displacement, density, or pressure. Balance laws and constitutive laws yield a framework that is similar to classical, single-phase continuum mechanics but with multiple overlapping and interacting phases. Bowen [29, 30] extended the theory of mixtures by volume fractions to the theory of porous media (TPM). Further fundamental contributions to TPM were made by Coussy [41] and, amongst others, by de Boer [47] and Ehlers & Bluhm [59].

The third group is related to local volume averaging and includes works such as Hassanizadeh & Gray [86–88], Slattery [190], and Whitaker [222]. They should be abbreviated as AT (averaging techniques). In contrast to the previous category, the physical description is not developed *ab initio*. It starts on a smaller scale that is usually better understood. For example, flow through a single rock pore can often be analyzed with greater accuracy than through an entire rock. A new theory is developed from the smaller scale by averaging over a representative elementary volume (REV). This process is also called *upscaling*. The averaged quantities and laws build a new self-consistent theory on the larger scale.

In addition to the three groups of so-called macroscopic theories, two alternative approaches have to be mentioned. Their development was especially supported by the capabilities of modern computational calculations and imaging procedures. On the one hand, a straightforward possibility for studying porous media is to model the so-called microscopic physics; i.e. to calculate the behavior of each single pore and flow through it. On the other hand, so-called two-scale approaches combine a macroscopic



Figure 2.2: Historical devices in the laboratory founded by Karl v. Terzaghi at Vienna University of Technology in 1929: Worldwide, the first triaxial apparatus for pore water pressure measurement. Pictures taken at the Institute for Geotechnics and published with permission of Em. O. Univ.-Prof. Dipl.-Ing. Dr. techn. Dr. h.c. mult. Heinz Brandl, TU Vienna, Austria.

continuum theory with the study of the smaller, discontinuous scale. The corresponding numerical implementation is also known as FE², cf. [67, 100, 143]. The physical system is usually described as a homogeneous continuum whose constitutive behavior (for example, strain due to stress) is determined by a smaller-scale calculation of the heterogeneous structure. In particular, regular structures or physical phenomena with an interaction between multiple length scales can benefit from this strategy.

In addition to further research and application, many textbooks were produced for comprehensible access. These include [13, 41, 59, 217] as well as [80] with a focus on averaging and [5, 35, 139] with exclusive discussions of wave propagation. The scientists and works mentioned above are only a small selection from various research fields that deal with mixtures and porous media. AT are often more general, theoretical approaches. TPM and MT also provide a basic framework but are mostly (and historically) motivated by direct observations and findings at larger scales. Specialized and initial concepts are usually helpful but limited to certain questions and applications.

The present work will follow the framework of AT, especially the work of Hassanizadeh & Gray [86–89], because of its benefits with respect to generality, consistency, and physical interpretation. For this reason, basic terms of averaging/homogenization theory are summarized in the following sections.

2.2 Multiphase

The term multiphase system or multiphase media is generally used to describe a system with distinguishable constituents. Examples range from steel, which is composed of different crystalline structures, up to Russian chocolate cheesecake or fried potato chips [218], whose consistency is precisely adjusted in industrial production. Separation of involved constituents can be visible or invisible to the human eye.

In the present study, the multiphase system of interest consists of a porous solid matrix and two immiscible fluids. This can be a rock filled with water and air or a synthetic foam filled with liquid and gaseous fuel. Each constituent has its own properties such as density, pressure, or velocity. According to the theory of porous media, the constituents are also called phases. This name should not be confused with the description of an aggregate state as it is used in other fields.

A multiphase system can contain interfaces, contact curves (sometimes also called contact lines), and contact points between the bulk phases. Each of them can, again, possess their own energy, density, stress, etc.

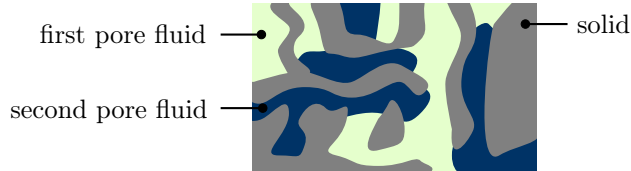


Figure 2.3: Schematic sketch of a multiphase system.

2.3 Multiscale

The term multiscale is generally used to distinguish between characteristic sizes of a measurable unit. For example, processes can sometimes be distinguished with respect to their length scale or time scale (gravitational interaction vs. quantum tunneling or evolutionary radiation vs. cell division). To account for different spatial lengths or temporal durations, a prefix will be used in combination with the respective SI unit, for example, km or μs .

In addition, the terms *microscale* and *macroscale* have to be introduced. Their origins are the ancient Greek words $\mu\kappa\rho\sigma$ (mikros) and $\mu\alpha\kappa\rho\sigma$ (makros), indicating small and long. Here, they account for two characteristic lengths, which are not specified by a certain length scale but by a different concept of physical modeling. The microscale is defined as the scale at which the heterogeneity of the structure is of major importance. For example, flow in arteries and deformation of bulk cargo beads can each be related to a microstructure. The diameters of an artery and of bulk cargo pieces constitute the respective microscopic length scales but they differ.



Figure 2.4: Micro- and macroscale of sand.

From the point of view of current research, there is no definite smallest or largest length scale and transitions are sometimes continuous. Thus, the present study cannot account for physical processes on all possible length scales and therefore focuses on systems within limited sizes. It is assumed that classical continuum mechanics describes microscale processes such as Navier-Stokes equations for fluids and Hookean elasticity for solids. Length scales smaller than approximately $1\ \mu\text{m}$, for example, molecular dynamics, are not

taken into account. The macroscopic investigations will focus on length scales from mm to km and exclude, for example, a variation of the gravitational constant. The link between micro- and macroscale can be created in many ways of which homogenization or averaging is a fundamental one.

2.4 Upscaling and scale separation

During decades of intensive studies on porous media, analytical tools have continuously improved. Amongst others, upscaling has proved to be a comprehensive approach for combining well-known microscopic relationships, such as Navier-Stokes equations and linear elasticity, with macroscopic principles like Darcy's law. The term upscaling is sometimes replaced by homogenization or averaging, although these terms may be used differently in other scientific disciplines.

The present work will be based on the work and understanding of Hassanizadeh & Gray, especially [79, 86–89]. Their work provides a consistent, theoretical basis for the macroscale physics that is derived from microscopic balance laws. The basic concept is to average over one representative elementary volume (REV), cf. Fig. 2.5.

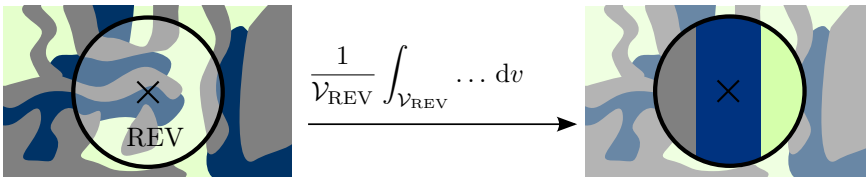


Figure 2.5: Schematic visualization of the upscaling process. A macroscopic material point contains all three phases and their properties as averaged, continuous fields.

Averaging conservation of mass, momentum, angular momentum, and energy yields macroscopic counterparts of density, velocity, etc., for each phase. The resulting framework is comparable to the framework of classical continuum mechanics, but for multiple phases. It also allows the use of a concept of objectivity¹ and evaluation of an entropy inequality by development of a macroscopic temperature. Special relationships, like Darcy's law, can be derived straightforwardly from the general concept. Furthermore, the averaging is based on a very general concept, which adds interfacial areas, contact lines, and contact points to volume fractions within the set of macroscopic geometric properties. The two most fundamental benefits are its self-consistency and comparison with microscopic physics. Thus, it serves as a strong basis for a general theory of wave propagation in porous media.

Nevertheless, the use of such macroscopic theory requires appropriate localization of its validity, namely fulfillment of *scale separation*² [84, 153]. To give an example, a theory describing bridge-deformation cannot be extended unconditionally to molecular motion and vice versa. On the larger scale, a material point may be defined and measured to be at rest, whereas this statement becomes invalid on the atomistic

¹The interested reader is referred to a comment about the concept of objectivity in engineering science and a misunderstanding with respect to initial configuration in Appendix F.

²The scale separation condition is also known as the so-called MMM-principle, cf. Hashin [84], Nemat-Nasser & Hori [153]. The (M)icroscale is homogenized over a larger (M)esoscopic REV that is used to describe the much larger (M)acroscale system. The respective characteristic lengths increase and necessarily differ, so that the related physical processes can be separated.

scale. Obviously, different scales can be related to different definitions and processes. In conclusion, use of the macroscopic theory requires two things in the sense of scale separation: well-defined and interpretable physical quantities and consideration of all relevant physical processes.

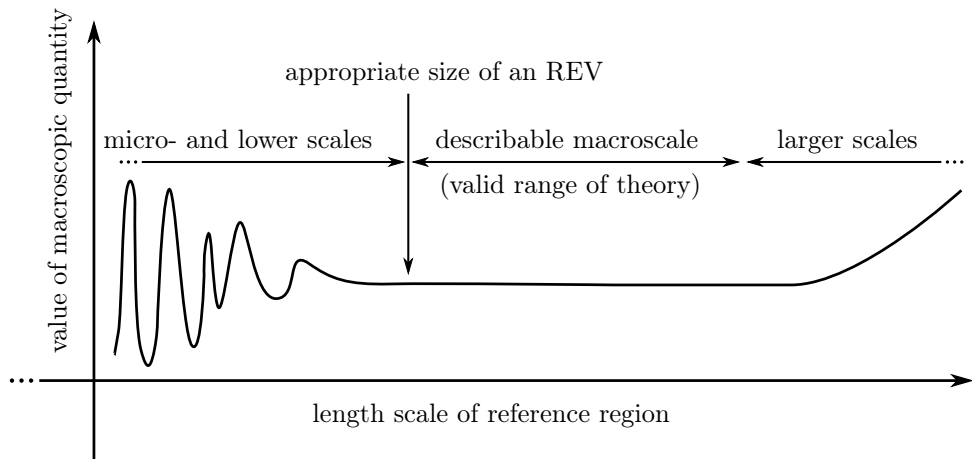


Figure 2.6: The concept of scale separation for an averaged macroscopic quantity such as density measured over an REV, e.g., according to [86] (modified).

Chapter 3

Basic principles of oscillations and waves

The following chapter introduces the fundamentals of wave theory. Following a historical survey, free and driven harmonic oscillations are characterized. Subsequently, uni-dimensional, linear waves are described and studied.

This chapter is technical in nature, to achieve a focus on the physical processes in the later study. It shows mathematical tools and relates physical characteristics of propagating waves to their mathematical formulation. Derived properties, especially phase velocity and quality factor, will appear frequently in all parts of this work.

3.1 Some history

This chapter should be introduced by quotation from a collaboratively edited internet encyclopaedia:

“In physics a wave is a disturbance or oscillation that travels through space and matter, accompanied by a transfer of energy.”³

It reflects a current, intuitive understanding of waves and was developed against the educational background of a versatile community. With respect to this treatise, it introduces the physical starting point: oscillations traveling in space. After a historical survey, fundamentals of oscillation theory are presented first and followed by those of wave theory.

Generally, waves belong to the basic physical phenomena in the environment and have always been observed: they are seen in the water of the ocean and heard and sensed in the ground after a tremor. Their scientific investigation also has a long history that is not easy to trace. Similar to many other topics, it is likely that the theory of wave propagation was developed stepwise in different regions and at different times. Thus, the following description represents an exemplary extract that can be reconstructed from available records. It is predominantly based on information from [45, 131] and contains a list of famous scientists from various fields.

³Wave. (2013, August 17). In *Wikipedia, The Free Encyclopedia*. Retrieved 12:57, August 19, 2013, from <http://en.wikipedia.org/w/index.php?title=Wave&oldid=568924650>

Davis [45] provides a short introduction to the history of wave theory and also recapitulates the historical work of Love [131]. Both mention Galileo's motivation and Hooke's theoretical foundation from 1660 when considering the relationship between strain and stress. Corresponding experimental investigations were carried out by Hooke and Mariotte. Further important progress was made by scientists in the late 18th/beginning of the 19th century. Young added the modulus of elasticity while Coulomb was one of the first to consider shear strain. The foundations were extended by L. Euler and Bernoulli to differential equations of vibrating bars and investigated experimentally by Chladni. A further systematic investigation was carried out by Navier, based on Newton's concepts. [45, 131]

In addition to mechanical waves, Young and Fresnel contributed to the wave theory of light. Cauchy has to be mentioned because of his mathematical treatment of the physical phenomenon of wave propagation. Poisson was probably one of the first to distinguish types of longitudinal and transversal waves within the theory of elasticity. His solutions were extended by the theories of Clebsch and Stokes. The mathematically interesting calculus of variations was applied by Green and Hamilton. Riemann not only provided an important mathematical basis but also contributed directly to the study of shock waves. Around the transition from the 19th to the 20th century, Christoffel related wave propagation to a propagating discontinuity surface and Lord Rayleigh (formerly Strutt) was probably one of the first scientists who explicitly investigated surface waves. Applications were expedited by several famous scientists including von Neumann, Kistiakowsky, Friedrichs, and von Kármán in the 20th century. [45, 131]

During the 20th century, mathematical treatment of wave propagation was developed into a consistent framework and physical studies became more structured. In addition, computational calculations allowed examination of difficult solutions. Modern research with different kinds of waves (mechanical waves, electromagnetic waves, etc.), with different propagation directions (plane waves, spherical waves, etc.), and in different systems (longitudinal or transversal body waves, surface waves like Love-, Stoneley-, or Rayleigh-waves, etc.).

The well-known uni-dimensional wave equation may be considered as the basic intersection of all previous findings and as a first step into the theory of waves:

$$\left(\frac{\partial^2}{\partial t^2} - c^2 \frac{\partial^2}{\partial x^2} \right) q(x, t) = 0.$$

The wave is described by the spatial and temporal behavior of q , which can be a transversal displacement of a beam or an electric field. Factor c^2 represents wave velocity squared and can be interpreted as the ratio of stiffness (connected to the second spatial derivative $\partial^2/\partial x^2$) to inertia (connected to the second time derivative $\partial^2/\partial t^2$). The basic wave equation and its modifications will be considered and studied in the following technical introduction.

3.2 Harmonic oscillator

A classical harmonic oscillator consists of a mass m , a spring with stiffness c , and a damper with damping coefficient d . Its uni-dimensional displacement in time is $q(t)$ with velocity \dot{q} and acceleration \ddot{q}

$$\dot{q}(t) = \frac{\partial q(t)}{\partial t}, \quad (3.1a)$$

$$\ddot{q}(t) = \frac{\partial^2 q(t)}{\partial t^2}. \quad (3.1b)$$

For example, $q(t)$ can a displacement for a mechanical oscillator but can generally describe arbitrary oscillations such as electric fields or population growth. In addition, the mechanical harmonic oscillator can be stimulated by an external force $F(t)$. The balance of forces is written as

$$m\ddot{q} + d\dot{q} + cq = F(t). \quad (3.2)$$

Parameters c , d , and m are assumed to be constant material parameters for a linear theory, i.e. independent of q and its derivatives. Furthermore, they can be assumed to be positive due to physical restrictions, which is not necessary, in general. With reference to later results, two further parameters are introduced; i.e. the angular, undamped eigenfrequency ω_0

$$\omega_0 = \sqrt{\frac{c}{m}} \quad (3.3)$$

and the dimensionless damping ratio D

$$D = \frac{d}{2m\omega_0}. \quad (3.4)$$

With ω_0 and D , the balance of forces can be reformulated as

$$\ddot{q} + 2D\omega_0\dot{q} + \omega_0^2q = \frac{F(t)}{m}. \quad (3.5)$$

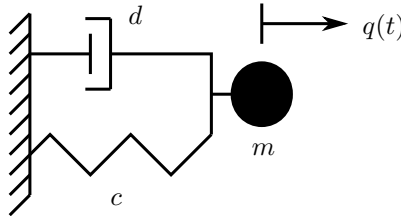


Figure 3.1: Harmonic oscillator.

3.2.1 Free oscillations: homogeneous solution

For free oscillations, i.e. $F(t) = 0$, a solution approach can be achieved by, [69],

$$q(t) = q_0 e^{i\omega t} \quad \text{with} \quad i := \sqrt{-1}.$$

Inserting this approach into Eq. (3.5) leads to $\nu_{1,2} = iD\omega_0 \pm \omega$ with angular oscillation frequency

$$\omega = \omega_0 \sqrt{1 - D^2}. \quad (3.6)$$

Angular oscillation frequency ω of a free oscillator is sometimes also called (damped) eigenfrequency, in contrast to the undamped eigenfrequency ω_0 . For physical interpretations, note that the real part of this approach, its imaginary part, as well as their superpositions, solve the differential equation. Knowing Euler's formula, $e^{i\omega} = \cos \omega + i \sin \omega$, $\forall \omega \in \mathbb{R}$, the solution consists of sin- and cos-oscillations with angular frequency ω . If the sin-part and the cos-part are combined separately with different prefactors, both prefactors then account for the initial conditions $q_0 = q(t_0)$ and $\dot{q}_0 = \dot{q}(t_0)$. Furthermore, the sin-part and the cos-part can be unified to one sin- or cos-term with a phase lag via the addition theorem. The corresponding solution is called the homogeneous solution and three cases can be distinguished, cf. [69]:

$$\begin{aligned} \bullet D < 1: \quad q_{\text{hom}}(t) &= e^{-D\omega_0 t} (A_0 \sin(\omega t) + B_0 \cos(\omega t)) \\ &= e^{-D\omega_0 t} A_1 \cos(\omega t + B_1) \end{aligned} \quad (3.7a)$$

$$\bullet D = 1: \quad q_{\text{hom}}(t) = (A_2 + B_2 t) e^{-D\omega_0 t} \quad (3.7b)$$

$$\bullet D > 1: \quad q_{\text{hom}}(t) = A_3 e^{-(D+\sqrt{D^2-1})\omega_0 t} + B_3 e^{-(D-\sqrt{D^2-1})\omega_0 t} \quad (3.7c)$$

The coefficients A_i and B_i , $i \in \{0, 1, 2, 3\}$, depend on the initial conditions q_0 and \dot{q}_0 . The underdamped oscillator, $D < 1$, shows a damped oscillation in time, cf. Fig. 3.2. The critically damped oscillator, $D = 1$, shows the fastest convergence to the position of rest, compared to the exponential decay of the overdamped oscillator, $D > 1$.

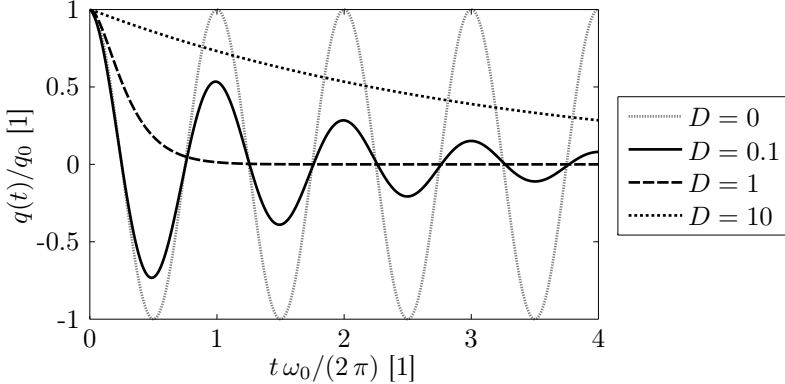


Figure 3.2: Oscillator displacement $q(t)$ for different damping ratios D . Initial displacement is $q_0 = 1$ and initial velocity is $\dot{q}_0 = 0$.

Moreover, angular frequency ω is related to the (classical) frequency f as

$$\omega = 2\pi f \quad (3.8)$$

and to the period T of the oscillation as

$$T = \frac{1}{f} = \frac{2\pi}{\omega}. \quad (3.9)$$

The frequency f represents cycles per seconds and is sometimes related to the unit Hz, while ω is sometimes related to the unit rad s^{-1} . Nevertheless, the correct unit

of (angular) frequency corresponds to inverse time $[f] = [\omega] = [\text{T}^{-1}]$ with SI unit s^{-1} . The factor 2π in ω simplifies its use in trigonometric functions. Hence, angular frequency ω will be preferred to f .

The oscillator properties can be back-calculated from a given signal. Three points are required to determine the central point of oscillation, ω , and D . From these, all other parameters can be calculated. For the underdamped oscillator, the amplitudes of three consecutive extrema q_1 , q_2 , and q_3 (for example, maximum, minimum, maximum) at times t_1 , t_2 , and t_3 can be used. It follows that

$$\omega = \frac{2\pi}{t_3 - t_1}, \quad (3.10a)$$

$$D = \frac{-\ln\left(\frac{q_3 - q_0}{q_1 - q_0}\right)}{\sqrt{4\pi^2 + \left(\ln\left(\frac{q_3 - q_0}{q_1 - q_0}\right)\right)^2}}, \quad (3.10b)$$

$$q_0 = \frac{q_2^2 - q_1 q_3}{2q_2 - q_1 - q_3}. \quad (3.10c)$$

A further important property of a harmonic oscillator is the logarithmic damping decrement

$$\vartheta = D\omega_0 T = 2\pi \frac{D}{\sqrt{1 - D^2}}. \quad (3.11)$$

It can be used to describe the ratio of displacement or velocity before and after one period for underdamped oscillations as

$$\frac{q(t)}{q(t+T)} = \frac{\dot{q}(t)}{\dot{q}(t+T)} = e^{-\vartheta}. \quad (3.12)$$

Defining the oscillator energy as

$$\Phi(t) = \frac{1}{2}c q(t)^2 + \frac{1}{2}m \dot{q}(t)^2, \quad (3.13)$$

the relative decrease of energy Φ during one period becomes, cf. [33],

$$\frac{\Phi(t) - \Phi(t+T)}{\Phi(t)} = 1 - e^{-2\vartheta}. \quad (3.14)$$

The quality factor Q is closely related to the logarithmic damping decrement and is defined here as

$$Q = \frac{\pi}{\vartheta} = \frac{\pi}{D\omega_0 T}. \quad (3.15)$$

A possible interpretation of Q is that the energy decreases after one cycle by the factor of

$$\frac{\Phi(t+T)}{\Phi(t)} = e^{-2\pi/Q}. \quad (3.16)$$

Using the series expansion of the exponential function, and if the oscillator is weakly damped, the quality factor approximates

$$\begin{aligned} Q &\stackrel{D \ll 1}{\approx} 2\pi \frac{1}{1 - e^{-2\pi/Q}} = 2\pi \frac{\Phi(t)}{\Phi(t) - \Phi(t+T)} \\ &= 2\pi \frac{\text{energy at the beginning of a cycle}}{\text{energy dissipated during the cycle}}. \end{aligned} \quad (3.17)$$

This is a widely used explanation of the quality factor but coincides with the definition above only for $D \ll 1$. It also yields $Q \approx 1/(2D)$. There are other interpretations of the quality factor especially in the field of wave propagation, for example, the ratio of maximum elastic energy stored to energy dissipated during one cycle according to [108, 156]. This is described in more detail below in the wave theory introduction.

3.2.2 Driven oscillations: particular solution

If the oscillator is driven by an external force $F(t)$, the solution consists of two parts: the homogeneous solution and the particular solution

$$q(t) = q_{\text{hom}}(t) + q_{\text{part}}(t).$$

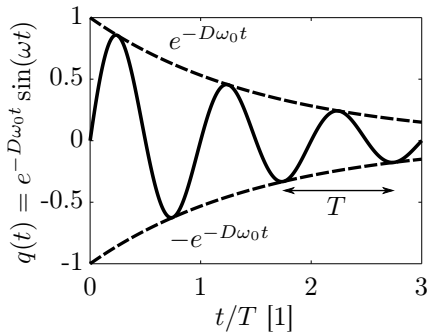
Assuming a damped system, the homogeneous solution becomes negligible after a certain time and only the particular solution remains. For a harmonic excitation with $F(t) = \hat{F} \cos(\Omega t)$, the particular solution becomes, cf. [33],

$$q_{\text{part}}(t) = \hat{q} \cos(\Omega t + \delta) \quad (3.18)$$

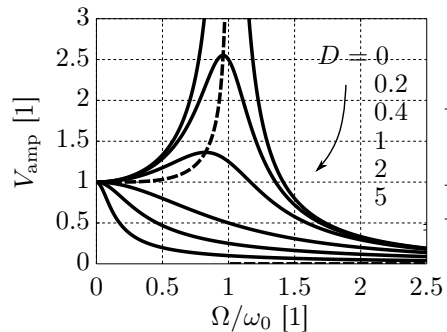
with amplitude \hat{q} and phase lag δ

$$\hat{q} = \frac{\hat{F}}{c} \frac{1}{\sqrt{(1 - (\Omega/\omega_0)^2)^2 + (2D\Omega/\omega_0)^2}} =: \frac{\hat{F}}{c} V_{\text{amp}}(\Omega),$$

$$\delta = -\arctan\left(\frac{2D\Omega/\omega_0}{1 - (\Omega/\omega_0)^2}\right).$$



a) Underdamped oscillator with $\omega = 2\pi$ and $D = 0.1$.



b) Amplification function of a stimulated harmonic oscillator for different D . The dashed line indicates the maxima locations.

Figure 3.3: Examples of free and driven oscillator motion.

One important property is the amplification function $V_{\text{amp}}(\Omega)$, which is the ratio of oscillation amplitude \hat{q} to the amplitude of harmonic excitation \hat{F}/c . It reaches its maximum, cf. [33],

$$V_{\text{amp,max}} = \frac{1}{2D\sqrt{1-D^2}} \quad (3.19)$$

at the angular resonance frequency

$$\Omega_{\text{res}} = \omega_0 \sqrt{1-2D^2}. \quad (3.20)$$

Note the difference between the resonance frequency of a harmonically driven oscillator Ω_{res} and the eigenfrequency of a free oscillator ω , cf. Eq. (3.20) and Eq. (3.6).

3.3 Uni-dimensional waves

As stated in the introductory quotation of this chapter, a wave can be understood as an oscillation that propagates in space. With the propagation in space, a further space dimension comes into play. For this reason, and as a first example, imagine an elastic rope element. It should have thickness Δx , cross-sectional area A , density ρ , and elastic modulus E . Its longitudinal displacement should be $q(x, t)$.

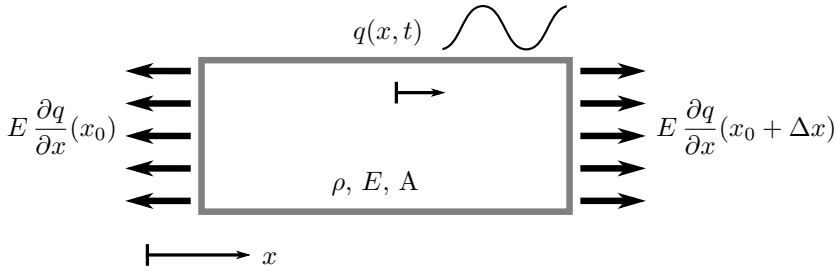


Figure 3.4: Oscillating, elastic rope element.

Its stress, i.e. force per area, is proportional to elasticity and strain, $E \partial q / \partial x$. Balance of forces divided by Δx then reads

$$\frac{\left(E \frac{\partial q}{\partial x} A\right)(x_0 + \Delta x) - \left(E \frac{\partial q}{\partial x} A\right)(x_0)}{\Delta x} = \frac{m \ddot{q}}{\Delta x}.$$

Linearization around x_0 and taking the limit $\Delta x \rightarrow 0$ with $m/\Delta x \approx \rho A$ yields

$$E \frac{\partial^2 q}{\partial x^2} = \rho \ddot{q}.$$

This is a typical wave equation with wave velocity $\sqrt{E/\rho}$. Adding a viscous damping factor d_{rope} that is proportional to velocity \dot{q} results in

$$\rho \ddot{q} + d_{\text{rope}} \dot{q} - E \frac{\partial^2 q}{\partial x^2} = 0. \quad (3.21)$$

This equation is similar to a volumetric version of the free harmonic oscillator, Eq. (3.2), except for an elastic response that depends on the second spatial derivative of q instead of on q itself.

3.3.1 Solution and properties

A possible solution of a wave equation like Eq. (3.21) is the approach

$$q(x, t) = q_0 e^{i(kx - \omega t)} = q_0 e^{-k_{\Im} x} e^{i(k_{\Re} x - \omega t)}. \quad (3.22)$$

The wave number k is complex

$$k = \Re(k) + \Im(k) i =: k_{\Re} + k_{\Im} i \in \mathbb{C} \quad (3.23)$$

and usually depends on ω . For example, applying Eq. (3.22) to the differential equation Eq. (3.21) results in a quadratic function

$$\begin{aligned} (-\rho\omega^2 - i d_{\text{rope}} \omega + k^2 E) q_0 &= 0, \\ \xrightarrow{q_0 \neq 0} k &= \pm \sqrt{\rho\omega^2 + i d_{\text{rope}} \omega}. \end{aligned}$$

The given solution Eq. (3.22) describes a uni-dimensional wave that starts at $x_0 = 0$ and propagates in the positive x -direction. Changing the sign between kx and ωt or choosing a solution for k with opposite sign results in the opposite direction of travel. The first factor of the solution, $e^{-k_{\Im} x}$, accounts for the amplitude decrease, while the second factor, $e^{i(k_{\Re} x - \omega t)}$, accounts for the pure oscillation traveling in space. As for an oscillator, a superposition of real and imaginary parts of the solution approach solves the differential equation with weighting factors that depend on the initial conditions of displacement and velocity.

The period of oscillation is the same as for the oscillator, Eq. (3.9). In addition, the wave length λ behaves towards the real part of the wave number in space in the same way as the period behaves towards the angular frequency in time

$$\lambda = \frac{2\pi}{k_{\Re}}. \quad (3.24)$$

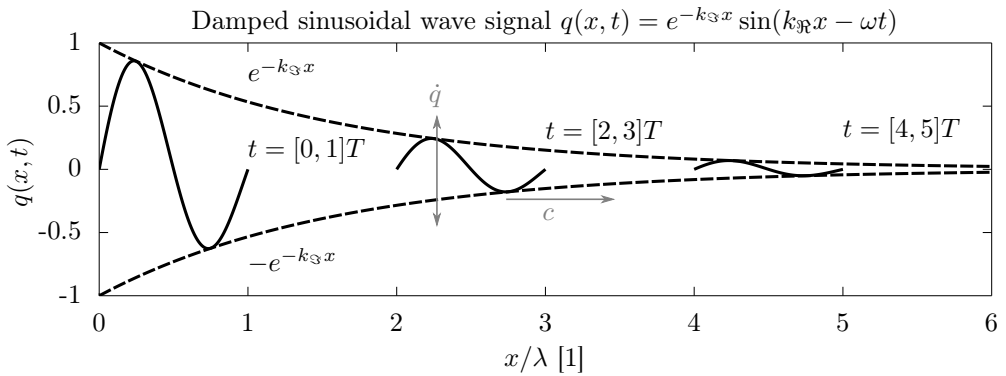


Figure 3.5: Propagating, damped wave signal of one period length at different time spans for $\omega = 20\pi \text{ s}^{-1}$ and $k = (1 + 0.1i) \text{ m}^{-1}$. Note the similarity to the damped oscillator in the time domain Fig. 3.3 a).

For a given angular frequency ω , the so-called phase velocity of the wave, is defined as

$$c_{\text{phase}}(\omega) = \frac{\omega}{k_{\Re}} = \lambda f. \quad (3.25)$$

This should not be confused with the local oscillation rate $\dot{q} = \partial q(x, t) / \partial t$. In fact, q can be a displacement perpendicular to the wave direction x or even an electric field with units $[\dot{q}] = \text{kgm s}^{-4} \text{ A}^{-1}$. On the contrary, phase velocity $c_{\text{phase}}(\omega)$ is the velocity of the traveling wave, cf. Fig. 3.5. For example, the phase velocity can be understood as the traveling velocity of a peak in q for a monochromatic signal. Following a peak or any other point of the wave signal means following the constant value $e^{i(k_{\Re} x - \omega t)} = \text{const}$. This implies that $(k_{\Re} x - \omega t) = \text{const}$. or $\partial x / \partial t = \omega / k_{\Re} = c_{\text{phase}}(\omega)$ for the fixed point of the wave signal.

If k is directly proportional to ω , the phase velocity is constant. This is the case if no damping occurs. Otherwise, the phase velocity generally depends on frequency, which is called dispersion.

The quality factor of a wave can be expressed analogously to the quality factor of an oscillator. Traveling with a monochromatic wave of frequency ω , i.e. $x(t) = c_{\text{phase}}(\omega)t$, the displacement becomes $\propto e^{-k_{\Im}\omega/k_{\Re}t}$, cf. Eq. (3.22). Comparing this amplitude decay of the wave signal with the decay of an underdamped oscillator, cf. $e^{-D\omega_0 t}$ in Eq. (3.7a), yields

$$\frac{k_{\Im}}{k_{\Re}} = \frac{D}{\sqrt{1-D^2}}.$$

With this relationship, the quality factor of a wave with frequency ω is, cf. Eq. (3.11) and Eq. (3.15),

$$Q(\omega) = \frac{1}{2} \frac{k_{\Re}}{k_{\Im}}(\omega). \quad (3.26)$$

Knopoff & MacDonald [108] introduced the same definition to achieve a dimensionless damping measurement (Eq. (2.7) *ibid.*). Their definition is based on the ratio of stored energy at maximum strain to temperature times generated irreversible entropy. Additionally, Knopoff & MacDonald also stated that there was no general agreement about such a measurement for stress waves and called k_{\Im} the attenuation coefficient. O'Connell & Budiansky [156] described this quality factor approach as the maximum value of stored elastic energy of one cycle divided by the energy dissipated during one cycle.

Due to the results that will be presented later on, the inverse quality factor Q^{-1} will be studied rather than Q itself because the former value is limited for vanishing attenuation. Q^{-1} is constantly zero and independent of ω if no damping occurs. With damping, Q^{-1} can become dispersive, i.e. frequency dependent, like the phase velocity. The special case of $Q^{-1} = 2$ corresponds to $D = 1/\sqrt{2}$ and $\omega = D\omega_0$, which is an oscillator with vanishing resonance frequency. This means it is just not excited by external stimulation, cf. Eq. (3.20), as the corresponding maximal amplification is one. Oscillator displacement equals stimulation amplitude.

3.3.2 Further approaches and properties

Waves can be characterized by further properties. Those that may be important for comparison with further literature, will be briefly mentioned. A different approach using a complex-valued velocity $c_{\text{phase},\mathbb{C}} \in \mathbb{C}$ can be written as $\propto e^{i\omega(x/c_{\text{phase},\mathbb{C}}-t)}$. It yields the same results but the physical interpretation is different. For example, the physical phase velocity is then equal to $\Re(c_{\text{phase},\mathbb{C}}) + \Im^2(c_{\text{phase},\mathbb{C}})/\Re(c_{\text{phase},\mathbb{C}})$.

The so-called group velocity becomes important for transport of energy or information. The phase velocity, introduced above in Eq. (3.25), is the wave velocity for a certain, fixed frequency ω . But if a signal contains more than one frequency and dispersion (i.e. frequency dependence) occurs, its parts travel with different velocities. As a result, the signal shape may change during propagation. Whereas the phase velocity was introduced as ω/k_{\Re} , the group velocity of an oscillating wave can be introduced as

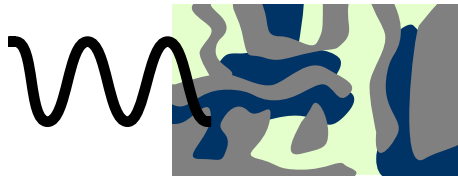
$$c_{\text{group}} = \frac{\partial \omega}{\partial k_{\Re}}.$$

If ω and k_{\Re} are directly proportional, phase and group velocity coincide. This is the case for a purely elastic wave without attenuation. If the relationship contains a

constant shift, $\omega = a_0 + a_1 k_{\mathfrak{R}}$ with $a_0 \neq 0$, the shape/envelope of the wave package remains undeformed while traveling with constant group velocity a_1 . Its monochromatic parts move with their individual phase velocity within the envelope they compose. Furthermore, special wave forms have not been investigated here. Spherical waves in higher spatial dimensions or superposition of reflected waves can be achieved by modification of the mathematical approach. The interested reader is referred to further literature. Textbooks about mathematical physics provide deep insights into the character of wave solutions, for instance, [45, 69], while specialized works often premise basic knowledge and focus on certain phenomena. Introductions of wave theory in the context of porous media - with different approaches - can be found, for example, in [5, 15, 35, 139].

Part I

Waves in partially saturated porous media



Chapter 4

Introduction

4.1 Motivation and literature survey

The previous introductory part presented the fundamentals of porous media and wave propagation separately. It focused on historical and basic findings. Now, both topics are combined and the view turns to modern applications and current research. Wave propagation processes in fluid-filled porous media are of major scientific interest and cover many application areas. For example, the possibility of non-destructive testing is an important advantage for characterization of organic materials [196]. Wave reflections of irregularities or inclusions support exploration techniques in engineering and geophysics [119]. Furthermore, modern applications include ganglia mobilization for ground water remediation [38] and noise reduction via gas bubbles at offshore structures [231]. In the process, wave properties strongly depend on the pore fluids, for example, the ratio of water to air in the mixture. Hence, accurate predictions rely on understanding and knowledge of the physical interaction of all constituents.

Scientific investigation of wave propagation in multiphase media is presumably almost as old as the study of wave propagation itself. The works of Frenkel, Zwikker & Kosten, Gassmann, and Biot undoubtedly rank amongst the fundamental works that initiated the development of a general theory for wave propagation in porous media. One of the very first investigators, Frenkel [74], derived equations for plane, mechanical, longitudinal and transversal waves. He also predicted seismoelectric coupling in a biphasic medium. In the same century, Zwikker & Kosten [235] demonstrated the absorption of sound in fluid-filled porous media. Gassmann [76] described mechanical wave propagation incorporating assumptions about the low-frequency regime, due to viscous coupling by a so-called Gedankenexperiment. Later, Biot provided a detailed and fundamental study on wave propagation, in 1956, focusing on the dispersion relations, i.e. the frequency-dependent wave behavior [24]. He implemented two materials: an elastic solid matrix with inertia, compressibility, shear resistance, and composed of compressible grains, as well as a compressible, viscous fluid with its own inertia. Coupling between both phases is due to viscosity and tortuous pore geometry. Biot's theory predicts two longitudinal waves, a fast one and the so-called slow Biot-wave, as well as one shear wave. In a second investigation, [25], Biot introduced a frequency-dependent correction function for the application of Darcy's law to wave propagation in porous media, as had also been predicted by Womersley for arterial flow in [226, 227]. Furthermore, surface waves in fluid-saturated porous media have been studied [51, 104].

In the second half of the 20th century, emergent frameworks such as MT, TPM, and AT played a major role in the extension of Biot's theory to a porous medium that included a mixture of pore fluids. Saturation became a basic new property expressing the volume fraction relationship of the fluids. The next two important steps were hydraulic conductivity models and soil-water characteristic curves, which were motivated by research on static systems, for instance, by Brooks & Corey [32] and van Genuchten [77]. Hydraulic conductivity models made it possible to determine the apparent permeability for each fluid, depending on saturation. Soil-water characteristic curves relate capillary pressure to saturation. With those two findings, the first frameworks could be derived, although experiments were and still are rare. Brutsaert & Luthin [34] demonstrated experimentally a relationship between the speed of sound of different wave modes and soil moisture content. Another example is provided by the experiments conducted by Murphy [151] in Massilon sandstone and porous glass. Nevertheless, the experimental investigation of partially saturated porous media is often challenging. An example of the difficulty may be found in the experimental evidence of Biot's slow wave in fully saturated porous media, cf. Plona's work [160] and the review of Smeulders [191].

The late 1980s and the early 1990s marked the start of a productive period with a couple of general, theoretical approaches, for example, [75] that highlights the importance of viscous coupling, [211] as one of the first comprehensive formulations in terms of displacements, or the textbook of Bourbié et al. [28]. Many theories are seen as extensions of Biot's theory such as [22]. Based on [180], Santos et al. [98, 181] simulated propagating waves in a rock with two immiscible fluids in time and space for special conditions. Lo et al. [128–130] concentrated on the dependence on saturation in more specialized cases (low frequency conditions or neglected capillary pressure). More general modeling approaches were derived by others, cf. Lu et al. [132, 133], who evaluated the influence of different model parameters in the lower frequency range, in particular. Albers [3] studied different wave types in terms of initial saturation and frequency. Muraleetharan & Wei constituted the basis for their wave propagation models [219–221] in [149]. These investigations are based on or comparable to frameworks such as the theory of mixtures or the fundamental work of Hassanizadeh & Gray [86] and belong to the list of very general approaches accounting for basic principles such as the evaluation of entropy inequality.

Research on wave propagation in partially saturated porous media is still incomplete. For instance, mesoscopic loss mechanisms such as squirt-flow in fully and partially saturated systems remain to be entirely elucidated. Biot's theory is often assumed to predict velocities well but underestimates attenuation in natural geophysical materials [56, 140]. Additionally, double permeability [20, 166], interlayer flow [54, 170, 223], and anisotropic conditions [4, 123] are part of modern research activities. The exact determination of static and dynamic capillary pressure in oscillating systems also represents a current challenge [93, 134]. Li et al. [121] provided a comprehensive survey with detailed insights into the pore scale physics, while the handbook of Mavko et al. [139] provides explanations and comparisons of different approaches against the background of rock physics. Other newer extensions are micropolar media [62, 189] and higher-order continua such as gradient elasticity models [142] that yield further wave modes. They are mathematically interesting but yet difficult to observe experimentally. A few studies provide a comprehensive theory for the special case of residual saturation [72, 92, 198], which is only one of many unanswered questions.

Many of the existing theories can be divided into three categories. One group is motivated by special observations and focuses only on special wave phenomena. The second group derives the final set of equations in the form of stress-strain relationships such as Biot [24] and Berryman et al. [22]. The third group uses a final formulation in terms of displacements and their derivatives [132, 211, 219]. This category usually contains the most general theories and, like others, still struggles with a lack of material data. Thus, some authors add notes on how to derive the necessary material parameters from experiments in the most convenient way [133, 219].

Common to almost all modern theories is their basis of an elastic solid matrix filled with two viscous fluids. All constituents have their own inertia and compressibility while the solid contributes to shear resistance. Wave velocities and attenuation are the main foci of observation. Three longitudinal body waves and one shear body wave are generally predicted.

The models differ mainly with respect to their assumptions. It is important to note that no model should be regarded as right or wrong but rather as suitable or unsuitable for modeling of certain physical systems. For example, Wilmański [224] and Steeb [196] showed that the assumption of a constant porosity is usually too strong if the solid is deformable. Porosity is not a classical material parameter but depends on the solid's deformation, because the pores may open or close. Often, a compromise between general capability and applicability requires specializations and assumptions. Limiting factors can be resolvability and missing information about material parameters or boundary conditions.

Building on these earlier findings, the following work aims at extending the understanding of and the interest in wave propagation in partially saturated porous media - a topic that unifies fundamental physical processes and fascinating applications.

Parts of this study have been submitted previously for publication and will probably be available shortly after completion of this treatise in [199].

4.2 Aims and structure

This first part aims at developing a mathematical model describing linear, mechanical waves in a porous medium that is saturated with two continuous fluid phases. It is a basis for the prediction of wave dynamics and characterization of materials via wave signals. With it, three points will be illustrated: (i) capabilities and basic properties of the model; (ii) physical interpretation of the mathematical structure divided into inertia, damping, and elasticity; and (iii) relevance of individual phenomena by means of specific examples.

In addition to this introduction, Part I is structured into four further chapters.

- First, a relatively extensive chapter summarizes the important physical relationships, including balance laws and constitutive relations. Terms and definitions are introduced as well as presentation of their physical origins. Finally, a harmonic approach is applied to the final set of differential equations and yields the governing equations for the determination of wave properties.
- Subsequently, specific examples provide insights into the model's properties and capabilities. Different types of waves are classified with respect to their physical behavior. Individual phenomena are then investigated with respect to their influence on wave propagation.

- Motivated by observations of waves in natural geological materials, the concept of mesoscopic losses is discussed in the following chapter. A condensed review explains possible effects phenomenologically, to highlight their importance within the present framework.
- Finally, a review concludes Part I including a summary and outlook.

Chapter 5

Leading equations

This chapter summarizes all relevant physical relationships starting with a survey of the initial physical situation. It presents kinematics and segmentation into three bulk phases (one solid and two pore fluids), interfaces, and contact curves. Subsequently, balance laws, above all mass and momentum balance, are introduced. Conservation of momentum determines the final shape of the equation system.

Constitutive equations are presented and explained with respect to their physical meaning. The first group relates stress to deformation or velocity for all constituents. This is followed by a relatively detailed section dealing with equilibrium and non-equilibrium momentum exchange. Momentum exchange is of particular importance for the wave behavior and special attention is paid to this point. A relationship for the pressure difference between both fluids, often identified as capillary pressure, closes the set of equations.

The discussion of the multiplicity of equations is extensive but substantial for a wave theory that is developed from basic physical principles. It is beneficial for the physical interpretation and a focused review relates the final results to the origins. Moreover, the so-called hybrid model approach [196] reduces the complexity of the mathematical structure and is valid for a wide range of applications. Finally, a harmonic approach and decomposition into longitudinal and shear waves yield the governing equations of the mathematical model describing wave propagation in partially saturated porous media.

5.1 The physical system

5.1.1 Set-up and definitions

The physical system includes one solid matrix and two immiscible fluids denoted by \mathfrak{s} , \mathfrak{l} , and \mathfrak{g} ⁴. Properties that belong to the bulk phases are generally denoted with index $\alpha \in \{\mathfrak{s}, \mathfrak{l}, \mathfrak{g}\}$; lower index for kinematic quantities, upper index otherwise⁵. Index

⁴Both fluids' symbols are motivated by the typical combination of a liquid (\mathfrak{l}) and a gas (\mathfrak{g}), but note that the following framework is valid for systems with two arbitrary fluids. Another typical distinction in the literature is that of wetting and non-wetting. However, a distinction via wetting properties is of less importance for the following general investigations.

⁵This notation was established in several TPM research groups and should not be confused with the summation rule of lower and upper indices in tensor calculus.

$f \in \{l, g\}$ is used for relationships that are generally related to one of the fluids. The bulk phases themselves are also commonly abbreviated by φ^α in TPM. One interface with index $\alpha\beta \in \{sl, sg, lg\}$ exists between each pair of the bulk phases. Three different bulk phases, as well as the three different interfaces, meet in one contact curve marked by index $\alpha\beta\gamma \in \{slg\}$. Interfaces and contact curves also constitute their own phases $\varphi^{\alpha\beta}$ and $\varphi^{\alpha\beta\gamma}$ that are distinct from the bulk phases. On the atomistic scale, interfaces and contact curves usually possess a dilatation in all three spatial dimensions. Nevertheless, they are characterized by a very small dilatation in certain directions. Following [79, 144, 148], they are modeled as reduced geometric entities. Consequently, an interface has a two-dimensional dilatation and a contact curve has a one-dimensional dilatation. Accordingly, properties such as density refer to a unit surface or unit length, respectively. These quantities can be understood as averages over the neglected dilatation and are sometimes considered as excess properties of the bulk phases.

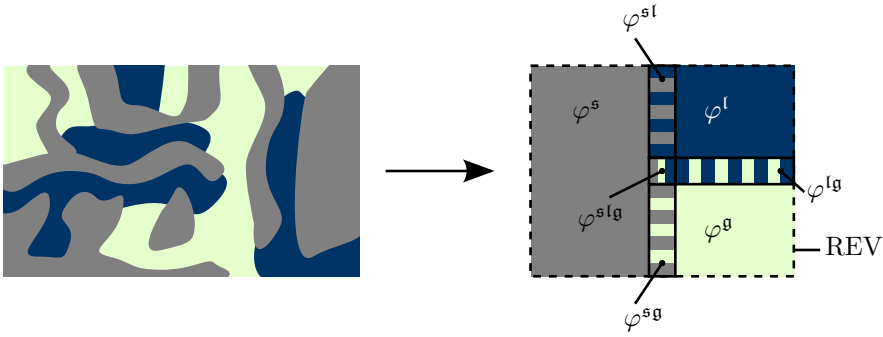


Figure 5.1: Schematic visualization of the modeling concept for a macroscopic, partially saturated system.

The symbol $\zeta \in \{\alpha, \alpha\beta, \alpha\beta\gamma\}$ is used as a universal index for all bulk phases, interfaces, and contact curves. Volumes, faces (including interfaces and boundary surfaces), and curves (including contact curves and boundary lines) are generally denoted by \mathcal{V} , \mathcal{A} , and \mathcal{C} , respectively. The volume of one phase α in an REV is defined by \mathcal{V}_α as are the areas $\mathcal{A}_{\alpha\beta}$ and lengths $\mathcal{C}_{\alpha\beta\gamma}$. From that, volume fractions n^α , interfacial areas $a^{\alpha\beta}$, and curve fractions $c^{\alpha\beta\gamma}$ are introduced as

$$n^\alpha := \mathcal{V}_\alpha / \mathcal{V}_{\text{REV}}, \quad (5.1a)$$

$$a^{\alpha\beta} := \mathcal{A}_{\alpha\beta} / \mathcal{V}_{\text{REV}}, \quad (5.1b)$$

$$c^{\alpha\beta\gamma} := \mathcal{C}_{\alpha\beta\gamma} / \mathcal{V}_{\text{REV}}. \quad (5.1c)$$

All three bulk phases constitute the volume of one REV by definition

$$\sum_{\alpha} n^\alpha = 1. \quad (5.2)$$

A widely used and fundamental property of a porous solid is its porosity ϕ representing the volume fraction of the pore space

$$\phi := 1 - n^s = n^l + n^g. \quad (5.3)$$

The pore space is distributed between both fluids via their saturation

$$s^f := \frac{n^f}{\phi} \quad (5.4)$$

with

$$\sum_{f \in \{\mathfrak{l}, \mathfrak{g}\}} s^f = 1. \quad (5.5)$$

The movement of each material point of a bulk phase, interface, or curve ζ can be described as $\mathbf{x}(\mathbf{X}_\zeta, t)$, where \mathbf{X}_ζ is the position at reference time t_0 . The corresponding displacement and velocity are $\mathbf{u}_\zeta = \mathbf{x} - \mathbf{X}_\zeta$ and \mathbf{v}_ζ , respectively. Furthermore, spatial derivatives are defined by $\text{grad}(\bullet) := \partial(\bullet)/\partial\mathbf{x}$ with respect to the current configuration and by $\text{Grad}_\zeta(\bullet) := \partial(\bullet)/\partial\mathbf{X}_\zeta$ with respect to the reference configuration (that can be different for different phases ζ). Partial time derivatives are defined by $\partial(\bullet)/\partial t = \dot{(\bullet)}$, while material time derivatives are introduced as $D^\zeta(\bullet)/Dt := \partial(\bullet)/\partial t + \text{grad}(\bullet) \cdot \mathbf{v}_\zeta$. Therein, the convective part is related to the velocity of phase ζ . Based on these definitions, the deformation gradient \mathbf{F}_α , its Jacobian determinant J_α , the linearized strain tensor $\boldsymbol{\varepsilon}_\alpha$, and the volumetric deformation ϵ_α of a bulk phase α are introduced as

$$\mathbf{F}_\alpha := \text{Grad}_\alpha \mathbf{x}_\alpha, \quad (5.6a)$$

$$J_\alpha := \det \mathbf{F}_\alpha, \quad (5.6b)$$

$$\boldsymbol{\varepsilon}_\alpha := \frac{1}{2}(\text{grad} \mathbf{u}_\alpha + \text{grad}^T \mathbf{u}_\alpha), \quad (5.6c)$$

$$\epsilon_\alpha := \text{div} \mathbf{u}_\alpha. \quad (5.6d)$$

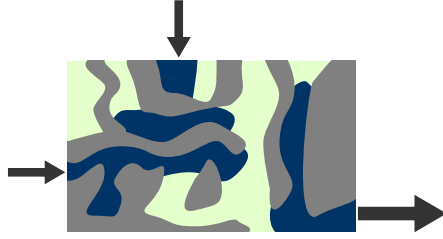
5.1.2 Preliminary assumptions

A few assumptions are made in advance to achieve a good compromise between complexity and validity in a wide range of scientific and practical applications. They hold exactly or are in good approximation for many cases and are

- wavelength \gg characteristic length of micro-structure (scale separation condition)
- temperature changes are negligible
- massless interfaces and contact curves
- non-polar phases
- symmetric (partial) Cauchy stresses
- homogeneous and isotropic initial state
- no chemical potentials except for the surface tension of liquid-liquid interfaces, which is responsible for capillary pressure

Justifications and limitations of these assumptions are discussed in detail where appropriate in the following sections.

5.2 Balance equations



5.2.1 Mass balance

Balance of mass is written for each bulk phase, interface or contact curve ζ as

$$\frac{D^\zeta}{Dt} \rho^\zeta + \rho^\zeta \operatorname{div} \mathbf{v}_\zeta = \hat{\rho}^\zeta. \quad (5.7)$$

Herein, the so-called real density is $\rho^{\zeta R} = m^\zeta / \mathcal{V}_\zeta$ and equals mass of ζ over volume of ζ in an REV, as is usual in classical mechanics. Partial densities include weighting via geometric fractions and are defined as

$$\begin{aligned} \rho^\alpha &:= \rho^{\zeta R} n^\alpha, \\ \rho^{\alpha\beta} &:= \rho^{\alpha\beta R} a^{\alpha\beta}, \\ \rho^{\alpha\beta\gamma} &:= \rho^{\alpha\beta\gamma R} c^{\alpha\beta\gamma}. \end{aligned} \quad (5.8)$$

For a bulk phase, mass production $\hat{\rho}^\alpha$ can appear due to inner mass production and exchange with the adjacent interfaces $\hat{\rho}^{\alpha|\alpha\beta}$. Inner mass production may be due to nuclear reactions, for example. Mass exchange formally appears between adjacent regions such as bulk phases and adjacent interfaces. In the following, influential mass production and mass exchange effects are neglected because they appear at much larger time scales than wave propagation in virtually all known systems. Linearization around equilibrium then yields

$$\frac{\partial}{\partial t} \rho^\zeta + \rho_0^\zeta \operatorname{div} \mathbf{v}_\zeta = 0 \quad (5.9)$$

and after integration in time for bulk phases α

$$\rho^\alpha = \rho_0^\alpha (1 - \epsilon_\alpha), \quad (5.10)$$

where $\rho_0^\alpha := \rho^\alpha(t_0)$ is the initial partial density and $\epsilon_\alpha = \operatorname{div} \mathbf{u}_\alpha$ is the volumetric change. In the special case of an incompressible material, for instance, for rigid grains that compose the solid matrix, real density is constant and cancels out. Thus, mass balance becomes balance of volume, reading

$$n^\alpha = n_0^\alpha (1 - \epsilon_\alpha), \quad \text{if } \rho^{\alpha R} = \text{const.}$$

In particular, incompressibility of the solid material yields a relationship for porosity

$$\phi = \phi_0 + (1 - \phi_0) \epsilon_s, \quad \text{if } \rho^{sR} = \text{const.} \quad (5.11)$$

Conservation of mass also holds for interfaces and contact curves, but exceeds the scope of this work. They are assumed to be massless, which still captures the relevant physical effects for the majority of applications including capillary pressure⁶.

⁶Cf. Section 19.7.1 for a detailed explanation.

5.2.2 Momentum balance

Balance of momentum is written for each bulk phase as

$$\rho^\alpha \frac{D^\alpha}{Dt} \mathbf{v}_\alpha - \operatorname{div}(n^\alpha \mathbf{T}^{\alpha R}) - \rho^\alpha \mathbf{f}^\alpha = \hat{\mathbf{p}}^\alpha. \quad (5.12)$$

It includes the real⁷ stress tensor $\mathbf{T}^{\alpha R}$, near-field forces \mathbf{f}^α (also known as volumetric or body forces), and momentum exchange $\hat{\mathbf{p}}^\alpha$. Stress tensor and momentum exchange will be discussed in Section 5.3 in more detail. Assuming negligible near field forces, i.e. gravity and electric fields have a minor influence, linearization around equilibrium yields

$$\rho_0^\alpha \frac{\partial^2}{\partial t^2} \mathbf{x}_\alpha - \mathbf{T}_0^{\alpha R} \cdot \operatorname{grad} n^\alpha - n_0^\alpha \operatorname{div}(\mathbf{T}^{\alpha R}) = \hat{\mathbf{p}}^\alpha \quad (5.13)$$

for all three bulk phases. These momentum balances will constitute the frame of the final set of equations. Moreover, balance of momentum for interfaces and contact curves is

$$\rho^{\alpha\beta} \frac{D^{\alpha\beta}}{Dt} \mathbf{v}_{\alpha\beta} - \operatorname{div}(a^{\alpha\beta} \mathbf{T}^{\alpha\beta R}) - \rho^{\alpha\beta} \mathbf{f}^{\alpha\beta} = \hat{\mathbf{p}}^{\alpha\beta} \quad (5.14a)$$

$$\rho^{\alpha\beta\gamma} \frac{D^{\alpha\beta\gamma}}{Dt} \mathbf{v}_{\alpha\beta\gamma} - \operatorname{div}(c^{\alpha\beta\gamma} \mathbf{T}^{\alpha\beta\gamma R}) - \rho^{\alpha\beta\gamma} \mathbf{f}^{\alpha\beta\gamma} = \hat{\mathbf{p}}^{\alpha\beta\gamma}. \quad (5.14b)$$

Momentum balance of interfaces between both fluids, \mathfrak{lg} , will merge into the relationship of capillary pressure, cf. Section 5.3.4. On the other hand, momentum balances of solid-fluid interfaces, \mathfrak{sf} , and of contact curves, \mathfrak{slg} , are assumed to be negligible. They become trivial, $\mathbf{0} = \mathbf{0}$, based on the assumption of vanishing density, stresses and interaction. This is valid for most applications because of two conditions on the microscale: firstly, the surface energy of the solid-fluid interfaces is negligible compared to the deformation energy of the solid, cf. Section 19.6.2 and Section 19.7.1 for details; secondly, wetting phenomena, due to contact curve resistance and movement, are not explicitly taken into account but are implicitly included later on via hysteresis of the capillary pressure-saturation relationship. In conclusion, momentum balances of solid-fluid interfaces do not contribute to the bulk phase momenta and transfer momentum directly between solid and fluids. Likewise, the contact curve directly transfers momentum between the interfaces.

5.2.3 Balance of angular momentum, balance of energy, and entropy inequality

Balance equations are generally completed by conservation of angular momentum, conservation of energy, and entropy inequality. A detailed discussion of their role in the theory of multiphase continua can be found in the work of Hassanizadeh and Gray [86–89]. Symmetry of the stress tensors follows from the balance of angular momentum if the phases are postulated to be non-polar [87] and if (direct) angular momentum production vanishes, which is assumed. Although the investigated systems are dissipative by nature, temperature effects, due to occurring dissipation, are assumed to be negligible. Thus, a constant and equal initial temperature θ_0 is

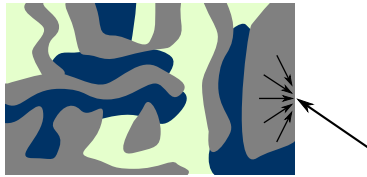
⁷With respect to the nomenclature of densities, the term effective stress suggests itself as well. Nevertheless, it is avoided because the so-called effective stress (principle) is historically related to another concept.

assumed for all phases. Consequently, balance of energy is not necessary to solve for temperature as an unknown and information about temperature dependency of material parameters is also not required.

Entropy inequality can be evaluated to develop and specify constitutive equations for remaining unknowns, for example, via the Coleman-Noll or Liu-Müller method. This process is not evaluated here but results are implicitly included in the following, cf. [79, 89, 219] for a detailed discussion.

5.3 Constitutive equations

5.3.1 Stress tensors



Momentum balances include the so-called real stress tensors $\mathbf{T}^{\alpha R}$ for each bulk phase. Like densities, they have to be distinguished from the so-called partial stresses, \mathbf{T}^α , which include weighting with the volume fractions

$$\mathbf{T}^\alpha = n^\alpha \mathbf{T}^{\alpha R}. \quad (5.15)$$

Multiplication by volume fractions changes the reference volume of the stress average from the phase volume in one REV (real stress) to the total volume in one REV (partial stress).

Fluids

Stresses of the fluids are composed of an isotropic real pressure p^{fR} as

$$\mathbf{T}^{fR} = -p^{fR} \mathbf{I}. \quad (5.16)$$

According to a convention in theoretical mechanics, where tensile stresses are indicated by positive signs, the pressure has a negative sign. In the same way that thermodynamic pressure is related to atomistic fluctuations, the macroscale pressure contains smaller scale fluctuations. These include classical pressure as well as microscopic velocity fluctuations. In contrast to classical fluid mechanics, viscous fluid shear stresses are not included on the macroscale, cf. the dimensional analysis in [85]. Another interpretation for negligible, macroscopic fluid shearing is that the microscopic shear stresses approximately cancel each other out after averaging. To clarify this assumption, imagine a flow through a pore channel, for example, as in Fig. 5.2a). Integration of the shear stresses in the fluid volume becomes very small because each microscopical fluid particle has an opposite counterpart with respect to the channel axis, which has a reversed velocity gradient. Thus, the averaged material fluid point does not undergo shearing on the macroscale. This assumption is valid for fluid flow through typical, non-oriented structures.

The assumption of negligible macroscopic fluid shear stress fails in the very special case of flow profiles that are systematically oriented in one shearing direction, Fig. 5.2b). However, such a situation requires an anisotropic solid structure and special flow boundary conditions, which occur periodically and in accordance with an oriented pore structure. This special case is possible [168], but, due to its special character, it is neglected in the further investigations. In contrast, shear stress at the solid walls does not vanish after averaging over the interfaces and will play an important role in momentum interaction later on.

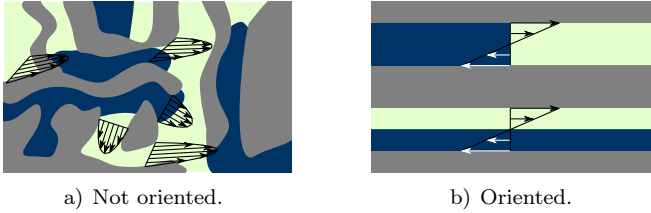


Figure 5.2: Fluid shearing in different structures.

Solid

Stresses of the solid phase consist of two parts:

$$\mathbf{T}^{sR} = \mathbf{T}_{\text{extra}}^{sR} - p^{sR} \mathbf{I}. \quad (5.17)$$

On the one hand, solid pressure p^{sR} is due to the fluid pressures acting on the solid walls. Their combined influence is weighted by the respective saturation, cf. equilibrium solid pressure in [89] or the fundamental Dalton's law for mixtures of gases

$$p^{sR} = s^l p^{lR} + s^g p^{gR}. \quad (5.18)$$

On the other hand, the so-called extra stresses result from deformation of the solid skeleton (excluding the influence of the fluid pressures). A relationship for real extra stresses, $\mathbf{T}_{\text{extra}}^{sR}$, or for partial extra stresses, $\mathbf{T}_{\text{extra}}^s = n^s \mathbf{T}_{\text{extra}}^{sR}$, can be used.

Classical experiments can often be related to the partial extra stresses, which refer to the total REV. Imagine a porous media compressed between two parallel plates. Pressure induced on the plates, i.e. force per total plate area, is often easier to control or measure than pressure over the contact area of the plate and the solid frame. Therefore, preference will be given to the use of the partial extra stresses. Similar to classical mechanics, an elastic solid matrix can be described as a Hookean material with

$$\mathbf{T}_{\text{extra}}^s = 2 \mu^s \boldsymbol{\varepsilon}_s + \lambda^s \epsilon_s \mathbf{I}. \quad (5.19)$$

Here, μ^s and λ^s are the Lamé parameters of the dry solid skeleton. Its bulk modulus is

$$K^s = \lambda^s + \frac{2}{3} \mu^s. \quad (5.20)$$

Note that the extra stresses may also make a volumetric contribution in addition to the fluid pressure contribution. For example, a porous foam with an open and connected pore space in vacuum can undergo a compression with volumetric stresses and volumetric deformation.

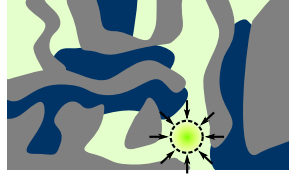
For the sake of completeness, the relationship for real extra stresses is

$$\mathbf{T}_{\text{extra}}^{sR} = 2 \mu^{sR} \boldsymbol{\varepsilon}_s + \lambda^{sR} \epsilon_s \mathbf{I} := 2 \frac{\mu^s}{n^s} \boldsymbol{\varepsilon}_s + \frac{\lambda^s}{n^s} \epsilon_s \mathbf{I}. \quad (5.21)$$

The elastic parameters for real extra stresses are divided by the volume ratios (initial volume ratios if linearized around equilibrium). This needs to be considered for comparison with theories that use real extra stresses.

5.3.2 Constitutive relationship for pressure and density

Fluids



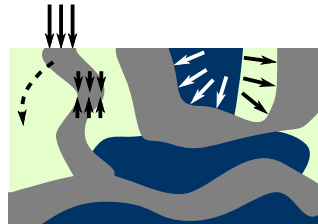
Neglecting the influence of temperature, real pressure and density of barotropic fluids can be related via the fluids' bulk modulus K^f in a linear form as

$$p^{fR} = p_0^{fR} + K^f \left(\frac{\rho^{fR}}{\rho_0^{fR}} - 1 \right) \quad (5.22)$$

or, equivalently,

$$\rho^{fR} = \rho_0^{fR} + \frac{\rho_0^{fR}}{K^f} (p^{fR} - p_0^{fR}). \quad (5.23)$$

Solid



The real density of the solid is related to the solid pressure via the bulk modulus of the solid material, composing the solid matrix, K^{grains} . Motivated by the research community in geophysics, which was and is traditionally connected to corresponding questions, the solid material is often referred to via the name *grains*.

Remembering that the skeleton's deformation can also contribute to volumetric stress, the solid's density also changes, due to the pressure induced by volumetric skeleton deformation. In contrast to classical continuum mechanics, part of the volumetric skeleton deformation is absorbed via alteration of the shape of the skeleton and does not fully contribute to density changes. For example, ideally incompressible beams of a synthetic foam may bend under compression with a change of sample volume, but without significant change of volume or density of the individual beams themselves. Deformation energy is stored via shape change of the microstructure but not via grain compression, cf. the discussion in [224] about closing possibilities of pores.

In order to describe this situation, one further scalar relationship is required to close the set of equations. For the final mathematical implementation, a preferable form

determines the solid's density (after possible reformulation) as a function of the volumetric deformations, i.e. $\rho^{sR}(\epsilon_s, \epsilon_l, \epsilon_g)$. For example, it can be achieved via a ratio of volume changes of the skeleton and grains or as an empirical relationship between porosity and deformation. There are various approaches and for a detailed discussion about this issue and the effective stress principle see, for instance, [26, 52, 155].

One approach, directly applicable to the wave theory, can be found in [219]. Therein, Wei & Muraleetharan introduced a parameter that accounts for the solid's density changes resulting from volumetric skeleton deformation. This parameter is named Λ^{grains} in the present treatise. It is a coupling parameter between stiffness of the solid grains (influenced by elasticity of the solid bulk material) and stiffness of the solid skeleton (influenced by elasticity of the solid bulk material and skeleton geometry). Moreover, it should not be confused with the Lamé parameter of the solid grain material. The density-pressure relationship of the solid becomes

$$\rho^{sR} = \rho^{sR}(\epsilon_s, \epsilon_l, \epsilon_g) = \rho_0^{sR} + \frac{\rho_0^{sR}}{K^{\text{grains}}} \left(\underbrace{p^{sR} - p_0^{sR}}_{\substack{\text{fluid pressure} \\ \text{contribution}}} - \Lambda^{\text{grains}} \epsilon_s \right). \quad (5.24)$$

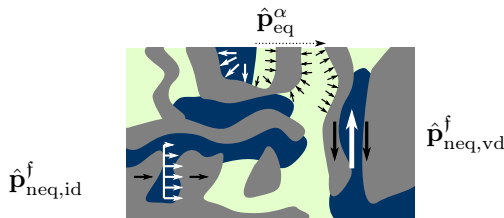
The term $\Lambda^{\text{grains}} \epsilon_s$ can be understood as pressure inside the solid grains or material composing the skeleton, which is due to volumetric skeleton deformation but not absorbed via alteration of the shape of the skeleton. Furthermore, the ratio $\Lambda^{\text{grains}}/K^{\text{grains}}$ accounts for the part of volumetric skeleton deformation that is absorbed by the grains: if $\Lambda^{\text{grains}}/K^{\text{grains}} = 0$, the entire deformation is absorbed by the skeleton. This is the case for the assumption of rigid grains, $K^{\text{grains}} \rightarrow \infty$, whereby information about Λ^{grains} is not required.

Wei & Muraleetharan [219] compared Λ^{grains} with Biot's coefficient α_{Biot} for the fully saturated case, which leads to, neglecting capillary effects for full saturation,

$$1 - \frac{K^s}{K^{\text{grains}}} =: \alpha_{\text{Biot}} = 1 - \frac{(1 - \phi_0) \Lambda^{\text{grains}}}{K^{\text{grains}}}.$$

For partially saturated systems, Λ^{grains} is generally also influenced by the dependence of capillary pressure on volume fraction changes [219].

5.3.3 Momentum exchange



Equilibrium momentum exchange

Momentum exchange can be initially divided into an equilibrium and a non-equilibrium part.

$$\hat{\mathbf{p}}^\alpha = \hat{\mathbf{p}}_{\text{eq}}^\alpha + \hat{\mathbf{p}}_{\text{neq}}^\alpha. \quad (5.25)$$

In equilibrium, a fluid phase exchanges momentum in the form of

$$\hat{\mathbf{p}}_{\text{eq}}^f = p^{fR} \text{grad } n^f. \quad (5.26)$$

From the viewpoint of a macroscopic interpretation, total pressure in one REV is the sum of all partial pressures. These include weighting by the respective volume fractions. Hence, the pressure contribution of phase φ^α changes if volume content n^α changes. As a result, momentum in equilibrium is macroscopically exchanged between the phases if their volume fractions change. Note that other theories express equilibrium momentum interaction by a more general driving potential, for instance, [89].

Non-Equilibrium momentum exchange: inertial drag

Non-equilibrium momentum exchange has various physical origins and is of vital importance for the behavior of a dynamic, multiphase system. One reason is inertial drag. Some part of the fluids is trapped in pore ends or other geometric inclusions and cannot move independently. Therefore, this part is accelerated with the solid and receives momentum from it. The corresponding parameter is denoted by α_{id} and acts on both fluids as

$$\hat{\mathbf{p}}_{\text{neq,id}}^f = (\alpha_{\text{id}} - 1)\rho^f \left(\frac{\partial^2}{\partial t^2} \mathbf{u}_s - \frac{\partial^2}{\partial t^2} \mathbf{u}_f \right). \quad (5.27)$$

The non-equilibrium exchange $\hat{\mathbf{p}}_{\text{neq,id}}^f$ is due to form-locking between the solid matrix and the portion of trapped fluid. For instance, the latter can also be considered individually, as in [195]. Further note that a general constitutive approach, directly including acceleration for momentum interaction, may contradict the principle of objectivity; cf. the discussion of Wilmański [224] and his remark on the special case of a linear theory.

The coefficient α_{id} depends on tortuosity of the pore channels. It is ≥ 1 by physical definition but usually $\alpha_{\text{id}} > 1$ for all cases of porous media that deviate from straight, non-intersecting tubes. Because of various tortuosity definitions, the single term tortuosity is avoided and it is named the inertial drag parameter or tortuosity parameter α_{id} . Note the discussion about the definition of tortuosity in Section 6.9.2.

Moreover, this influence may generally depend on frequency, due to varying, frequency-dependent flow profiles. Nevertheless, it becomes significant in the high-frequency limit as soon as the constituents are decoupled. For convenience, α_{id} is assumed to be constant. An approximation by porosity is provided in [21] and [139], which refer to Berryman's work [19], as

$$\alpha_{\text{id}} = 1 + r_{\text{Berryman}} \left(\frac{1}{\phi_0} - 1 \right). \quad (5.28)$$

The geometric factor r_{Berryman} is 0.5 for a matrix consisting of spheres and used from now on for approximation, cf. also [19, 20] for specific application to dynamic systems, including wave propagation.

Non-Equilibrium momentum exchange: viscous drag

Another well-known origin of momentum exchange in porous media is due to the relative velocity of fluid and solid, also called viscous drag. A first starting point is

that of a Darcy-like flow, [43], where momentum exchange between fluid and solid is proportional to their relative velocity, also known as seepage velocity $\mathbf{w}_f = \mathbf{v}_f - \mathbf{v}_s$,

$$\hat{\mathbf{P}}_{\text{neq,vd}}^f = b_{0,f} (\mathbf{v}_s - \mathbf{v}_f) \quad (5.29)$$

with

$$b_{0,f} = \frac{(n^f)^2 \eta^{fR}}{k^s k_{\text{rel}}^f}. \quad (5.30)$$

The proportionality factor $b_{0,f}$ contains dynamic fluid viscosity η^{fR} , intrinsic permeability of the solid matrix k^s , and the relative permeability factor k_{rel}^f . Eq. (5.29) indicates that momentum is transferred to the fluid by the factor $b_{0,f}$ if the solid moves relatively faster and vice versa. The intrinsic permeability definition k^s introduced here is a property of the solid phase only and is independent of the fluid.

The relative permeability factor k_{rel}^f accounts for the fact that the apparent permeability for a specific fluid phase is determined by the respectively occupied pore space. Hydraulic conductivity models such as that of Brooks and Corey [32] relate relative permeability to capillary pressure or saturation as

$$k_{\text{rel}}^l = s^{lR \frac{2+3\lambda_{\text{BC}}}{\lambda_{\text{BC}}}} \quad (5.31)$$

$$k_{\text{rel}}^g = (1 - s^{lR})^2 \left(1 - s^{lR \frac{2+\lambda_{\text{BC}}}{\lambda_{\text{BC}}}} \right). \quad (5.32)$$

Here, λ_{BC} is a parameter that depends on the investigated materials. Effective saturation s^{lR} is a scaling between the residual saturations s_{res}^l and s_{res}^g ,

$$s^{lR} := \frac{s^l - s_{\text{res}}^l}{1 - s_{\text{res}}^l - s_{\text{res}}^g}. \quad (5.33)$$

Note that the Brooks & Corey model is limited by the residual saturation endpoints, cf. Fig. 5.3. The values of these endpoints depend strongly on the solid material [125, 151]. For the following investigations, continuous fluid phases and a situation far from residual saturation are assumed. Hence, the given equations for k_{rel}^f can be used.

Joekar-Niasar et al. [102] provide a further expression for relative permeabilities that depend on saturation and interfacial areas a^{lg} . This captures hysteresis effects. For the current investigation of wave propagation, relative permeability is assumed to be a constant parameter after linearization. Only its initial value has to be known. Therefore, hysteresis effects need to be considered by knowing their influence on the initial values of k_{rel}^f . This point will be discussed in more detail during the introduction of capillary pressure.

The Darcy-like approach in Eq. (5.29) is motivated by the fundamental, empirical findings of Darcy [43] for laminar, steady flow through porous media. Nevertheless, the equally fundamental work of Biot [25] showed that this approach requires an extension for application to wave propagation at higher frequencies.

The interaction of solid and fluid is due to viscosity and the microscopical velocity gradient at the solid walls. Darcy's law describes steady, laminar flow in the pore channels. It thus assumes a viscosity-dominated Hagen-Poiseuille flow with fixed velocity gradient. For oscillating flows, however, inertia terms become dominant for

higher frequencies [112, 114]. Hence, Biot introduced a correction factor for momentum exchange that depends on the ratio of angular frequency to Biot's characteristic frequency in [25], for a fluid f as

$$\omega_{c,\text{Biot}} = 2\pi f_{c,\text{Biot}} = \frac{\eta^{fR}\phi}{k^s \alpha_{\text{id}} \rho^{fR}}. \quad (5.34)$$

Note, that Biot originally investigated a system with only one fluid. Adoption to the current system with two fluid yields the modified characteristic frequencies

$$\omega_{c,l} = \frac{\eta^{lR} n^l}{k^s k_{\text{rel}}^l \alpha_{\text{id}} \rho^{lR}}, \quad \omega_{c,g} = \frac{\eta^{gR} n^g}{k^s k_{\text{rel}}^g \alpha_{\text{id}} \rho^{gR}}. \quad (5.35)$$

The ratio $\omega/\omega_{c,f}$ (and $\omega/\omega_{c,\text{Biot}}$) accounts for the ratio of inertia forces to viscous forces and has also been developed by Womersley [226, 227]. Therefore, it is also known as the squared Womersley number and, furthermore, as the ratio of pore radius to viscous skin depth.⁸

Biot's correction function also depends on a structural parameter, which is a function of the pore geometry (for example, circular or slit-like pores) and sinuosity of the channels. A corresponding and subsequently used approximation of Biot's correction function is based on the work of Johnson et al. [103], denoted as JKD-correction c_{JKD} . It modifies the velocity-dependent fluid momentum exchange to

$$\begin{aligned} \hat{\mathbf{p}}_{\text{neq,vd}}^f &= c_{\text{JKD}} \left(\frac{\omega}{\omega_{c,f}} \right) b_{0,f} (\mathbf{v}_s - \mathbf{v}_f) \\ &:= \sqrt{1 + \frac{1}{2} i \frac{\omega}{\omega_{c,f}}} b_{0,f} (\mathbf{v}_s - \mathbf{v}_f). \end{aligned} \quad (5.36)$$

Total momentum exchange

Finally, momentum exchange between the fluids, the so-called Yuster-effect [8, 186, 187], is assumed to be of higher than first order and vanishes after linearization. The fluids only transfer momentum to the solid

$$\begin{aligned} \hat{\mathbf{p}}^l &= \hat{\mathbf{p}}^{l|s} + \hat{\mathbf{p}}^{l|g} \approx \hat{\mathbf{p}}^{l|s} \\ \hat{\mathbf{p}}^g &= \hat{\mathbf{p}}^{g|s} + \hat{\mathbf{p}}^{g|l} \approx \hat{\mathbf{p}}^{g|s} \end{aligned}$$

Therefore, momentum exchange terms can be subsumed for the fluids as

$$\begin{aligned} \hat{\mathbf{p}}^f &= \hat{\mathbf{p}}_{\text{eq}}^f + \hat{\mathbf{p}}_{\text{neq}}^f = p^{fR} \text{grad } n^f \\ &+ (\alpha_{\text{id}} - 1) \rho^f \left(\frac{\partial^2}{\partial t^2} \mathbf{u}_s - \frac{\partial^2}{\partial t^2} \mathbf{u}_f \right) + c_{\text{JKD}} \left(\frac{\omega}{\omega_{c,f}} \right) b_{0,f} (\mathbf{v}_s - \mathbf{v}_f) \end{aligned} \quad (5.37)$$

and for the solid as

$$\hat{\mathbf{p}}^s = \sum_{f \in \{l,g\}} \hat{\mathbf{p}}^{s|f} = - \sum_{f \in \{l,g\}} \hat{\mathbf{p}}^{f|s} = - \sum_{f \in \{l,g\}} \hat{\mathbf{p}}^f. \quad (5.38)$$

⁸This issue of frequency-dependent flow profile correction is discussed in more detail in Chapter 11 and includes the investigation of limitations and extensions.

Remark: Note that, for comparison with biphasic media, equilibrium momentum exchange of the solid is not necessarily equal to $\text{grad}(n^s) p^{sR} = -\text{grad}(\phi) p^{sR}$. This is only the case if the pressures of both liquids are equal, i.e. if capillary effects are negligible. If both fluid pressures do not coincide and saturation changes, pressure on the solid changes because one fluid exhibits a pressure that differs from the other. Hence, solid momentum may change in equilibrium even if $\text{grad} n^s = \mathbf{0}$ because of $\text{grad} s^l \neq \mathbf{0}$.

5.3.4 Fluid pressure difference and capillary pressure



Equilibrium capillary pressure at micro- and macroscale

Microscopic, equilibrium fluid pressure difference or equilibrium capillary pressure (sometimes also called Laplace pressure [48]) was already a focus of research two centuries ago [233]. The famous Young-Laplace equation relates the equilibrium pressure difference between two fluids to surface curvature κ and surface tension σ as⁹

$$\Delta p = \kappa \sigma.$$

Because of the differences in the molecular energetic potentials of both fluids, the interface possesses its own energy and momentum and thus influences the pressure distribution. It can be further expressed as a divergence of a microscopical surface tension tensor $\sigma \mathbf{I}^A$ with surface unit tensor $\mathbf{I}^A = \mathbf{I} - \mathbf{n} \otimes \mathbf{n}$ and normal vector \mathbf{n} as⁹

$$\Delta p = \text{div}(\sigma \mathbf{I}^A).$$

On the macroscale, this relationship merges into the equilibrium momentum balance of the fluid-fluid interface, Eq. (5.14a). Neglecting density and gravity forces yields

$$-\text{div}(a^{lg} \mathbf{T}^{lg}) = \hat{\mathbf{p}}_{\text{eq}}^{lg} = -\hat{\mathbf{p}}_{\text{eq}}^{l|lg} - \hat{\mathbf{p}}_{\text{eq}}^{g|lg} + \hat{\mathbf{p}}_{\text{eq}}^{lg|s|lg}.$$

The interface exchanges momentum with the adjacent bulk fluids and the contact curve, whereas an explicit momentum exchange with the contact curve $\hat{\mathbf{p}}^{lg|s|lg}$ can be neglected for implementation of capillary pressure⁹, cf. [89]. Furthermore, momentum exchange with the bulk phases is determined via the average of the bulk stresses at the interfaces [79]. Assuming that the interface average of the fluid stresses approximately equals the volume averages and knowing that the normal vectors of both fluids point in opposite direction at the interface, the right-hand side of the above equation becomes the equilibrium pressure difference of both fluids, i.e.

$$-\text{div}(a^{lg} \mathbf{T}^{lg}) = \hat{\mathbf{p}}_{\text{eq}}^{lg} = (p^{lR} - p^{gR}) \mathbf{I}.$$

⁹A detailed physical discussion of the microscale phenomena will be found in Chapter 19.

This is the macroscopic equivalent of the microscopic equation. Both emerge from the interface momentum balance. Similar to the microscale physics, Hassanizadeh [89] derived the macroscopical interface tension thermodynamically from a Helmholtz energy potential of the interfaces H^{lg} as

$$\mathbf{T}^{\text{lg}} = -a^{\text{lg}} \rho^{\text{lg}} \frac{\partial H^{\text{lg}}}{\partial a^{\text{lg}}}.$$

Equilibrium fluid pressure difference and capillary pressure

Being aware of unequal fluid pressures makes the need for an additional equation clear. First, however, an important issue needs to be considered: the definition of capillary pressure p^c . Capillary pressure and fluid pressure difference are used as synonyms in equilibrium

$$p_{\text{eq}}^c \stackrel{(\text{eq})}{=} p^{\text{gR}} - p^{\text{lR}} \quad (5.39)$$

at the microscale and the macroscale. In a more general sense, the total capillary pressure can be split additively into its equilibrium and non-equilibrium part

$$p_{\text{total}}^c = p_{\text{eq}}^c + p_{\text{neq}}^c = p^{\text{gR}} - p^{\text{lR}} + p_{\text{neq}}^c.$$

Nevertheless, a more general definition of capillary pressure, including non-equilibrium effects, is not consistent in the multiphase physics literature, cf. [30, 89]. The terms p_{neq}^c and p_{total}^c may be approached and interpreted differently. For example, Hassanizadeh [89] introduced p_{total}^c as an inversely temperature-weighted derivation of the system's energy with respect to saturation, in current notation with Helmholtz energies H^ζ , temperatures θ^ζ , wetting phase l , and non-wetting phase g

$$\frac{\phi p_{\text{total}}^c}{\theta^{\text{lg}}} = - \sum_{\alpha} \frac{\rho^{\alpha}}{\theta^{\alpha}} \frac{\partial H^{\alpha}}{\partial s^{\text{l}}} - \sum_{\alpha\beta} \frac{\rho^{\alpha\beta}}{\theta^{\alpha\beta}} \frac{\partial H^{\alpha\beta}}{\partial s^{\text{l}}}.$$

This definition was developed within the thermodynamic framework by means of a general resistance against penetration by the wetting phase. To avoid misunderstanding of the term capillary pressure, the pure pressure difference between both fluids is used in formulations when non-equilibrium effects are considered. For convenience, it is abbreviated by

$$p^{\Delta\text{gl}} := p^{\text{gR}} - p^{\text{lR}} \quad (5.40)$$

and equals the commonly used capillary pressure definitions only in equilibrium. For equilibrium effects, the term capillary pressure will still be used additionally, because of convention and the wide impact of this term.

The remaining goal is to achieve a closing equation for $p^{\Delta\text{gl}}$. This is first determined for the equilibrium state. In geomechanical and geotechnical applications, the empirical relationships between equilibrium (or static) capillary pressure and saturation by Brooks & Corey [32] and van Genuchten [77] are generally popular. These so-called soil-water characteristic curves are fitting curves of quasi-static wetting and de-wetting experiments. Following Brooks & Corey [32], as in the case of relative permeabilities and introducing air-entry (also named bubbling) pressure p_{b} , yields

$$p_{\text{eq}}^c(s^{\text{l}}) = p_{\text{eq}}^{\Delta\text{gl}}(s^{\text{l}}) = p^{\text{b}}(s^{\text{lR}})^{-\frac{1}{\lambda_{\text{BC}}}}. \quad (5.41)$$

As in the case of relative permeabilities, validity vanishes near the state of residual saturation, cf. Fig. 5.3. Due to technical restrictions in experiments, the suction pressure, used to extract a fluid from a porous medium, increases drastically when a residual endpoint is reached. This is in agreement with the microscopic Young-Laplace equation, because capillary pressure increases (theoretically) infinitely for small radii, i.e. for increasing curvature. However, residual saturation is not within the scope of this part and validity of Eq. (5.41) can be assumed.

Finally, Eq. (5.41) is a fundamental basis for determination of the fluid pressure difference. Extensions of this first approach are presented in the following.

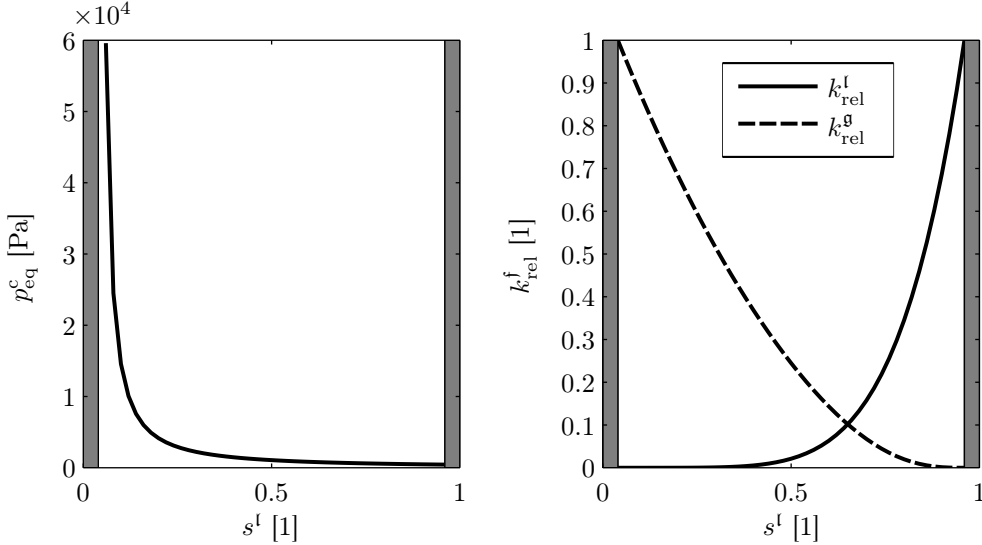


Figure 5.3: Equilibrium capillary pressure and relative permeabilities as Brooks & Corey functions [32] for $\lambda_{\text{BC}} = 0.78$, $p_b = 440$ Pa, and $s_{\text{res}}^l = s_{\text{res}}^g = 0.04$. Gray regions indicate residual saturation.

Hysteresis effects of classical soil-water characteristic curves

Hysteresis effects of classical soil-water characteristic curves are known to occur in unsaturated, porous media [102, 107, 138, 154]. This accounts for rate-independent cycles of quasi-static wetting and dewetting. Different capillary pressures can be found for the same saturation, depending on the (quasi-stationary) state during an imbibition or drainage process. This can be explained microscopically by different geometric configurations, which adjust variably if a fluid is pressed through a porous medium (entering the largest pores first), sucked (remaining in the smallest pores), or if a fluid enters a pre-wetted porous medium (as water seeps into pre-wetted ground more easily).

A physically founded and consistent approach to account for such hysteresis is the additional use of interfacial areas a^{lg} . It was theoretically explained by Niessner & Hassanizadeh [154] and evaluated for a pore network by Joekar-Niasar et al. [102]. The interfacial areas involved act as a second geometric parameter, describing the geometric situation of the capillars more accurately and uniquely.

The initial approach from above becomes

$$p_{\text{eq}}^c(s^l) \rightarrow p_{\text{eq}}^c(s^l, a^{\text{lg}}) \quad \text{or} \quad p_{\text{eq}}^{\Delta \text{gl}}(s^l) \rightarrow p_{\text{eq}}^{\Delta \text{gl}}(s^l, a^{\text{lg}}) \quad \text{respectively.}$$

The contributors mentioned, [102, 154], provide a quadratic relationship between interfacial areas, saturation, and capillary pressure in the form of

$$a^{\text{lg}}(s^l, p_{\text{eq}}^c) = a_{00} + a_{10}s^l + a_{01}p_{\text{eq}}^c + a_{20}(s^l)^2 + a_{11}s^l p_{\text{eq}}^c + a_{02}(p_{\text{eq}}^c)^2, \quad (5.42)$$

which can be reformulated to $p_{\text{eq}}^c(s^l, a^{\text{lg}})$. Compared to the previous $p_{\text{eq}}^c(s^l)$ -relationship, the new relationship contains one more, unknown value. To close this equation for the new unknown, the interface mass balance is used. In the present case of massless interfaces it reduces to the balance of interfacial areas as

$$\frac{\partial a^{\text{lg}}}{\partial t} + \text{div}(a^{\text{lg}} \mathbf{v}_{\text{lg}}) = E^{\text{lg}}.$$

The production term E^{lg} was approximated in [154] with the saturation rate

$$E^{\text{lg}} = c_{p_{\text{eq}}^c} \frac{\partial s^l}{\partial t},$$

$$c_{p_{\text{eq}}^c}(s^l, p_{\text{eq}}^c) := \left(\frac{\partial a^{\text{lg}}}{\partial p_{\text{eq}}^c} \frac{d p_{\text{eq}}^c}{d s^l} \Big|_{\text{line}} + \frac{\partial a^{\text{lg}}}{\partial s^l} \right). \quad (5.43)$$

Here, $\frac{d p_{\text{eq}}^c}{d s^l} \Big|_{\text{line}}$ is the total derivative at the current $a^{\text{lg}}-s^l-p_{\text{eq}}^c$ path and usually unknown. Niessner and Hassanizadeh [154] use the two known main drainage curves and calculate the path for $c_{p_{\text{eq}}^c} = 0$ to interpolate $c_{p_{\text{eq}}^c}(s^l, p_{\text{eq}}^c)$ between these three known cases, where $c_{p_{\text{eq}}^c}$ represents the total derivative $\frac{d a^{\text{lg}}}{d s^l}$ within the $a^{\text{lg}}-s^l-p_{\text{eq}}^c$ field. The last two equations become, linearizing around equilibrium and neglecting volume forces as well as the flux term of interfacial areas with interfacial velocity [154],

$$\frac{\partial a^{\text{lg}}}{\partial t} = c_{p_{\text{eq}}^c, 0} \frac{\partial s^l}{\partial t}$$

and, after integration in time,

$$a^{\text{lg}}(s^l) = a_0^{\text{lg}} + c_{p_{\text{eq}}^c, 0}(s^l - s_0^l). \quad (5.44)$$

The proportionality constant $c_{p_{\text{eq}}^c, 0}$ represents the actual position on the $a^{\text{lg}}-s^l-p_{\text{eq}}^c$ path and therefore explicitly accounts for the hysteresis effects. It can be interpreted as a parameter of the specific, physical situation relating the rates of a^{lg} and s^l . Finally, combination of Eq. (5.42) - Eq. (5.44) yields a relationship between equilibrium capillary pressure and saturation as classical soil-water characteristic curves in the form of

$$p_{\text{eq}}^c(s^l, a^{\text{lg}}(s^l)) \quad \text{or} \quad p_{\text{eq}}^{\Delta \text{gl}}(s^l, a^{\text{lg}}(s^l)) \quad \text{respectively.} \quad (5.45)$$

Hysteresis and interfacial areas of the current physical system are expressed by the parameter $c_{p_{\text{eq}}^c, 0}$.

Dynamic capillary pressure or dynamic fluid pressure difference

Dynamic capillary pressure or dynamic fluid pressure difference is a focus of modern studies [93, 134] and extends the equilibrium part by dependence on the saturation rate,

$$p^{\Delta g|l} = p_{\text{eq}}^{\Delta g|l} + p_{\text{neq}}^{\Delta g|l} = \underbrace{p_{\text{eq}}^{\Delta g|l}(s^l)}_{=p_{\text{eq}}^c(s^l)} + \tau \frac{\partial}{\partial t} s^l. \quad (5.46)$$

If saturation changes in time for dynamic processes, velocity profiles appear and can change the fluid-fluid interfaces. As a result, capillary forces alter depending on interface curvature. Hence, dynamic effects cannot be neglected for capillary pressure. With respect to wave propagation, changes in saturation are periodic with angular frequency ω , i.e. $\partial s^l / \partial t = \partial(s^l - s_0^l) / \partial t = -i\omega(s^l - s_0^l)$. In this case, the fluid pressure difference can be written again as a function of saturation as

$$p^{\Delta g|l} = p_{\text{eq}}^{\Delta g|l}(s^l) + \tau(-i\omega)(s^l - s_0^l). \quad (5.47)$$

Values for the proportionality coefficient τ are still difficult to achieve and experimental data is rare. For example, Manthey et al. [134] provide values for sand in the range of -1×10^5 Pa s to -1×10^7 Pa s. Moreover, they provide a dimensional analysis and refer to an empirical relationship of Stauffer [194] as (in the current notation)

$$\tau_{\text{S}} = -\frac{0.1 \eta^{wR} \phi}{k^s \lambda_{\text{BC}}} \left(\frac{p_{\text{b}}}{\rho^{wR} g} \right)^2. \quad (5.48)$$

Viscosity η^{wR} and density ρ^{wR} belong to the wetting phase, which is usually the liquid l if combined with a gas. The gravity constant is denoted by g . However, this formula does not coincide with experimental data in every case and may diverge by one or two magnitudes [134]. It should be regarded as an empirical formula that cannot be used for arbitrary combinations without adaptation. However, its form helps to understand possible influences on the dynamic capillary pressure.

In particular, it motivates one further correction of dynamic capillary pressure for application to wave propagation. Typical experiments investigating dynamic capillary pressure induce a flow process to create a rate of saturation. Typically, such experiments do not involve oscillating flows. A modified τ -coefficient for wave propagation consequently follows by referring back to the correction of Darcy-like viscous drag, Eq. (5.36), and comparing it with Eq. (5.48) as

$$\tau = -c_{\text{JKD}} \left(\frac{\omega}{\omega_{c,l}} \right) \frac{0.1 \eta^{wR} \phi}{k^s \lambda_{\text{BC}}} \left(\frac{p_{\text{b}}}{\rho^{wR} g} \right)^2. \quad (5.49)$$

This correction is equivalent to the use of a frequency-dependent permeability. The linearized, dynamic $p^{\Delta g|l}(s^l)$ equation is finally written as

$$p_{\text{lin}}^{\Delta g|l}(s^l) = p_{\text{eq},0}^{\Delta g|l} + \left(\frac{\partial p_{\text{eq}}^{\Delta g|l}}{\partial s^l} \Big|_0 - i\omega\tau \right) (s^l - s_0^l), \quad (5.50)$$

for example, with equilibrium terms as proposed by Brooks & Corey [32] and given by Eq. (5.41) (or further including interfacial areas such as Eq. (5.45)) and the non-equilibrium determined by Eq. (5.49).

5.4 Final equations

5.4.1 Linearization

Balance and constitutive equations in the presented form are a set of equations that needs to be rearranged for practical use. Because of the focus on linear wave propagation, the equations can be linearized to achieve a more convenient handling. Note especially that linearization can be executed before the equations are combined and that linearization simplifies products significantly if the initial value(s) of one or both factors vanish (see Appendix B.1 and Section B.2). In particular, intricate constitutive equations can be reduced and the set of material parameters becomes smaller. Utilizing this, the equations can be combined in the following manner.

$$\begin{array}{l}
 \text{general} \\
 n^{\mathfrak{s}} + \phi = 1, s^{\mathfrak{l}} + s^{\mathfrak{g}} = 1 \\
 n^{\mathfrak{f}} = s^{\mathfrak{f}}/\phi \\
 \alpha \in \{\mathfrak{s}, \mathfrak{l}, \mathfrak{g}\}, \mathfrak{f} \in \{\mathfrak{l}, \mathfrak{g}\} \\
 \\
 \left. \begin{array}{l}
 \text{mass balance fluids} \\
 \rho^{\mathfrak{l}R}(s^{\mathfrak{l}}, \phi, \epsilon_{\mathfrak{l}}) \\
 \rho^{\mathfrak{g}R}(s^{\mathfrak{l}}, \phi, \epsilon_{\mathfrak{g}}) \\
 \text{barotropic fluids} \\
 p^{\mathfrak{l}R}(\rho^{\mathfrak{l}R}), p^{\mathfrak{g}R}(\rho^{\mathfrak{g}R}) \\
 \text{capillary pressure} \\
 (p^{\mathfrak{g}R} - p^{\mathfrak{l}R})(s^{\mathfrak{l}})
 \end{array} \right\} \left. \begin{array}{l}
 p^{\mathfrak{l}R}(s^{\mathfrak{l}}, \phi, \epsilon_{\mathfrak{l}}) \\
 p^{\mathfrak{g}R}(s^{\mathfrak{l}}, \phi, \epsilon_{\mathfrak{g}}) \\
 s^{\mathfrak{l}}(\phi, \epsilon_{\mathfrak{l}}, \epsilon_{\mathfrak{g}})
 \end{array} \right\} \left. \begin{array}{l}
 \rho^{\mathfrak{s}R}(\phi, \epsilon_{\alpha}) \\
 \phi(\epsilon_{\alpha})
 \end{array} \right\} \\
 \\
 \left. \begin{array}{l}
 \text{as above} \\
 p^{\mathfrak{l}R}(s^{\mathfrak{l}}, \phi, \epsilon_{\mathfrak{l}}) \\
 p^{\mathfrak{g}R}(s^{\mathfrak{l}}, \phi, \epsilon_{\mathfrak{g}}) \\
 \text{solid pressure} \\
 p^{\mathfrak{s}R}(s^{\mathfrak{l}}, p^{\mathfrak{l}R}, p^{\mathfrak{g}R}) \\
 \text{solid compressibility} \\
 \rho^{\mathfrak{s}R}(p^{\mathfrak{s}R}, \epsilon_{\mathfrak{s}})
 \end{array} \right\} \left. \begin{array}{l}
 \rho^{\mathfrak{s}R}(s^{\mathfrak{l}}, \phi, \epsilon_{\alpha}) \\
 \rho^{\mathfrak{s}R}(s^{\mathfrak{l}}, p^{\mathfrak{l}R}, p^{\mathfrak{g}R}, \epsilon_{\mathfrak{s}})
 \end{array} \right\} \\
 \\
 \text{mass balance solid} \\
 \rho^{\mathfrak{s}R}(\phi, \epsilon_{\mathfrak{s}})
 \end{array}$$

Note that, in the case of the rigid-grain assumption, mass balance of the solid directly produces a $\phi(\epsilon_{\mathfrak{s}})$ relationship. As a result, density $\rho^{\mathfrak{s}R}$ becomes constant and is not a variable. The entire lower part of the calculations vanishes. This case is known as the hybrid model, introduced by Steeb [196], for which the solid grains are incompressible but not the fluids or the solid skeleton.

Inserting back the results consecutively yields three balances of momentum for the bulk phases. They depend only on the three remaining, unknown bulk deformations.

The structure of the linearized momentum balances of the solid and the fluids becomes¹⁰

$$\begin{aligned} & (\rho_0^s + (\alpha_{\text{id}} - 1)(\rho_0^l + \rho_0^g)) \frac{\partial^2}{\partial t^2} \mathbf{u}_s - \sum_{\mathfrak{f}} (\alpha_{\text{id}} - 1) \rho_0^{\mathfrak{f}} \frac{\partial^2}{\partial t^2} \mathbf{u}_{\mathfrak{f}} \\ & + \sum_{\mathfrak{f}} c_{\text{JKD}} \left(\frac{\omega}{\omega_{c,\mathfrak{f}}} \right) \frac{n_0^{\mathfrak{f}2} \eta^{\mathfrak{f}R}}{k^s k_{\text{rel}}^{\mathfrak{f}}} \left(\frac{\partial}{\partial t} \mathbf{u}_s - \frac{\partial}{\partial t} \mathbf{u}_{\mathfrak{f}} \right) \end{aligned} \quad (5.51a)$$

$$\begin{aligned} & - n_0^s \text{div}(2\mu^s \boldsymbol{\varepsilon}_s + \lambda^s \boldsymbol{\varepsilon}_s \mathbf{I}) \\ & + \text{grad} p^{sR}(\boldsymbol{\varepsilon}_s, \boldsymbol{\varepsilon}_l, \boldsymbol{\varepsilon}_g) - \sum_{\mathfrak{f}} n_0^{\mathfrak{f}} \text{grad} p^{\mathfrak{f}R}(\boldsymbol{\varepsilon}_s, \boldsymbol{\varepsilon}_l, \boldsymbol{\varepsilon}_g) = \mathbf{0}, \end{aligned}$$

$$\begin{aligned} & \alpha_{\text{id}} \rho_0^{\mathfrak{f}} \frac{\partial^2}{\partial t^2} \mathbf{u}_{\mathfrak{f}} - (\alpha_{\text{id}} - 1) \rho_0^{\mathfrak{f}} \frac{\partial^2}{\partial t^2} \mathbf{u}_s \\ & + c_{\text{JKD}} \left(\frac{\omega}{\omega_{c,\mathfrak{f}}} \right) \frac{n_0^{\mathfrak{f}2} \eta^{\mathfrak{f}R}}{k^s k_{\text{rel}}^{\mathfrak{f}}} \left(\frac{\partial}{\partial t} \mathbf{u}_{\mathfrak{f}} - \frac{\partial}{\partial t} \mathbf{u}_s \right) \end{aligned} \quad (5.51b)$$

$$+ n_0^{\mathfrak{f}} \text{grad} p^{\mathfrak{f}R}(\boldsymbol{\varepsilon}_s, \boldsymbol{\varepsilon}_l, \boldsymbol{\varepsilon}_g) = \mathbf{0}.$$

The momentum balances, Eq. (5.51a) (one equation for \mathfrak{s}) and Eq. (5.51b) (two equations for $\mathfrak{f} \in \{\mathfrak{l}, \mathfrak{g}\}$), now only depend on the displacements and their derivatives in time and space. Although the foregoing algebra is extensive, it reduces the complexity of final calculations and results in three crucial benefits, compared to less detailed approaches. These benefits are: explicit consideration of all physical processes individually, flexibility of their implementation, and accurate connections between the physical origins and the final model.

5.4.2 Harmonic approach and decomposition

In order to obtain a wave solution for the linearized momentum balances, a harmonic approach is used to describe the displacements; thus, cf. Chapter 3,

$$\mathbf{u}_{\alpha} = \hat{\mathbf{u}}_{\alpha} e^{i(\mathbf{k} \cdot \mathbf{x} - \omega t)}. \quad (5.52)$$

Accordingly, each bulk phase α oscillates with amplitude $\hat{\mathbf{u}}_{\alpha}$, due to a wave of angular frequency ω and of wave vector \mathbf{k} . The wave vector can be further split into its normalized direction vector $\mathbf{n}^{\mathbf{k}}$ and the corresponding length k as

$$\mathbf{k} =: k \mathbf{n}^{\mathbf{k}} \quad (5.53)$$

with $\|\mathbf{n}^{\mathbf{k}}\| = 1$ and $k \in \mathbb{C}$. Further investigation focuses on a plane wave of constant direction, i.e. $\mathbf{n}^{\mathbf{k}} = \text{const.}$. This choice supports a precise physical interpretation that focuses on the fundamental wave propagation phenomena. Other wave forms can also be applied without imposing a restriction on the previously developed framework.

¹⁰It has been used for the solid's balance of momentum that, with $n^s = 1 - \phi$,

$$\text{div}(n^s p^{sR} \mathbf{I}) + \sum_{\mathfrak{f}} p^{\mathfrak{f}R} \text{grad}(n^{\mathfrak{f}}) = \text{grad} p^{sR} - \sum_{\mathfrak{f}} n^{\mathfrak{f}} \text{grad}(p^{\mathfrak{f}R}).$$

The displacements can be decomposed into a part parallel to the wave vector and a part perpendicular to it¹¹

$$\begin{aligned}\mathbf{u}_\alpha &= \mathbf{u}_\alpha^\parallel + \mathbf{u}_\alpha^\perp, \\ \mathbf{u}_\alpha^\parallel &:= \mathbf{u}_\alpha \cdot \mathbf{n}^k \quad \text{with} \quad \mathbf{u}_\alpha^\parallel \times \mathbf{n}^k = \mathbf{0}, \\ \mathbf{u}_\alpha^\perp &:= \mathbf{u}_\alpha - \mathbf{u}_\alpha^\parallel \quad \text{with} \quad \mathbf{u}_\alpha^\perp \cdot \mathbf{n}^k = 0.\end{aligned}$$

This decomposition acts directly on the amplitudes. Assuming an equation of the form

$$a_0 \partial_{tt} \mathbf{u}_\alpha + a_1 \partial_t \mathbf{u}_\alpha + a_2 \text{grad div } \mathbf{u}_\alpha + a_3 \text{div grad } \mathbf{u}_\alpha + a_4 \text{rot rot } \mathbf{u}_\alpha = \mathbf{0} \quad (5.54)$$

yields, using some algebra as explained in Section B.3,

$$\begin{aligned}(a_0 \omega^2 + i a_1 \omega + (a_2 + a_3) k^2) \hat{\mathbf{u}}_\alpha^\parallel &= \mathbf{0}, \\ (a_0 \omega^2 + i a_1 \omega + (a_3 - a_4) k^2) \hat{\mathbf{u}}_\alpha^\perp &= \mathbf{0}.\end{aligned}$$

Note that these two solutions are independent, because $\hat{\mathbf{u}}_\alpha^\parallel \cdot \hat{\mathbf{u}}_\alpha^\perp = 0$. Because of isotropy in the present case, they can be further transformed to a scalar problem by dividing $\hat{\mathbf{u}}_\alpha^\parallel$ and $\hat{\mathbf{u}}_\alpha^\perp$ by their normalized, constant direction. The remaining scalars represent the amplitude of the displacements for each individual phase.

$$(a_0 \omega^2 + i a_1 \omega + (a_2 + a_3) k^2) \hat{u}_\alpha^\parallel = 0, \quad (5.55a)$$

$$(a_0 \omega^2 + i a_1 \omega + (a_3 - a_4) k^2) \hat{u}_\alpha^\perp = 0. \quad (5.55b)$$

The two waves are parallel and perpendicular to the wave vector and conventionally named the longitudinal or P-wave and the transversal or S-wave. These terms will also be used from now on to distinguish between these two kinds of waves, i.e. $\parallel \rightarrow \text{P}$ and $\perp \rightarrow \text{S}$.

5.4.3 Dispersion relations

A propagating wave in multiphase media is finally described by applying the harmonic approach and decomposition, Eq. (5.54), Eq. (5.55a), and Eq. (5.55b), to the linearized momentum balances, Eq. (5.51a) and Eq. (5.51b). It results in the eigenvalue formulation

$$\boxed{\left(\omega^2 \mathbf{A} + i \omega \mathbf{B} + (k^\psi)^2 \mathbf{C}^\psi \right) \begin{pmatrix} \hat{u}_s^\psi \\ \hat{u}_l^\psi \\ \hat{u}_g^\psi \end{pmatrix} = \mathbf{0}, \quad \psi \in \{\text{P}, \text{S}\}. \quad (5.56)$$

Matrix \mathbf{A} contains the following inertia terms

$$\mathbf{A} = \begin{pmatrix} \tilde{\rho}_{11} & \tilde{\rho}_{12} & \tilde{\rho}_{13} \\ \tilde{\rho}_{21} & \tilde{\rho}_{22} & \tilde{\rho}_{23} \\ \tilde{\rho}_{31} & \tilde{\rho}_{32} & \tilde{\rho}_{33} \end{pmatrix} := \begin{pmatrix} \rho_0^s + (\alpha_{\text{id}} - 1)(\rho_0^l + \rho_0^g) & -(\alpha_{\text{id}} - 1)\rho_0^l & -(\alpha_{\text{id}} - 1)\rho_0^g \\ -(\alpha_{\text{id}} - 1)\rho_0^l & \alpha_{\text{id}}\rho_0^l & 0 \\ -(\alpha_{\text{id}} - 1)\rho_0^g & 0 & \alpha_{\text{id}}\rho_0^g \end{pmatrix}, \quad (5.57)$$

¹¹Another common variant of this approach with similar outcome is the use of a (Helmholtz) decomposition with potentials that lead to a curl-free and a divergence-free component.

and Matrix \mathbf{B} accounts for the viscous momentum interaction, including the frequency correction function

$$\mathbf{B} = \begin{pmatrix} \sum_{\mathfrak{f}} c_{\text{JKD}} \left(\frac{\omega}{\omega_{c,\mathfrak{f}}} \right) \frac{n_0^{\mathfrak{f}2} \eta^{\mathfrak{f}R}}{k^{\mathfrak{f}} k_{\text{rel},0}^{\mathfrak{f}R}} & -c_{\text{JKD}} \left(\frac{\omega}{\omega_{c,\mathfrak{l}}} \right) \frac{n_0^{\mathfrak{l}2} \eta^{\mathfrak{l}R}}{k^{\mathfrak{s}} k_{\text{rel},0}^{\mathfrak{l}R}} & -c_{\text{JKD}} \left(\frac{\omega}{\omega_{c,\mathfrak{g}}} \right) \frac{n_0^{\mathfrak{g}2} \eta^{\mathfrak{g}R}}{k^{\mathfrak{s}} k_{\text{rel},0}^{\mathfrak{g}R}} \\ -c_{\text{JKD}} \left(\frac{\omega}{\omega_{c,\mathfrak{l}}} \right) \frac{n_0^{\mathfrak{l}2} \eta^{\mathfrak{l}R}}{k^{\mathfrak{s}} k_{\text{rel},0}^{\mathfrak{l}R}} & c_{\text{JKD}} \left(\frac{\omega}{\omega_{c,\mathfrak{l}}} \right) \frac{n_0^{\mathfrak{l}2} \eta^{\mathfrak{l}R}}{k^{\mathfrak{s}} k_{\text{rel},0}^{\mathfrak{l}R}} & 0 \\ -c_{\text{JKD}} \left(\frac{\omega}{\omega_{c,\mathfrak{g}}} \right) \frac{n_0^{\mathfrak{g}2} \eta^{\mathfrak{g}R}}{k^{\mathfrak{s}} k_{\text{rel},0}^{\mathfrak{g}R}} & 0 & c_{\text{JKD}} \left(\frac{\omega}{\omega_{c,\mathfrak{g}}} \right) \frac{n_0^{\mathfrak{g}2} \eta^{\mathfrak{g}R}}{k^{\mathfrak{s}} k_{\text{rel},0}^{\mathfrak{g}R}} \end{pmatrix}. \quad (5.58)$$

Matrices \mathbf{C}^ψ represent stiffness of the system and are connected to the second spatial derivatives of displacements. The components can be found in Section B.4, where \mathbf{C}^{P} depends on the set $\{\lambda^{\mathfrak{s}}, \mu^{\mathfrak{s}}, K^{\text{grains}}, \Lambda^{\text{grains}}, K^{\mathfrak{l}}, K^{\mathfrak{g}}, \phi_0, s_0^{\mathfrak{l}}, p_0^{\Delta\mathfrak{g}|\mathfrak{l}}, \partial p^{\Delta\mathfrak{g}|\mathfrak{l}}/\partial s^{\mathfrak{l}}|_0\}$ while \mathbf{C}^{S} depends on $\{\mu^{\mathfrak{s}}\}$.

For given materials and angular wave frequency ω , the eigenvalue formulation Eq. (5.56) can be solved for eigenvalues (i.e. squared wave vectors k^{ψ^2}) and eigenvectors (i.e. amplitudes $(\hat{u}_{\mathfrak{s}}^\psi, \hat{u}_{\mathfrak{l}}^\psi, \hat{u}_{\mathfrak{g}}^\psi)^\text{T}$). Three solutions appear for the P-wave, denoted by the indices P1, P2, and P3. One solution appears for the S-wave, denoted by the index S. Only the solid resists shearing; therefore, \mathbf{C}^{S} contains only one entry.

Given the solution of the eigenvalues, the frequency-dependent phase velocity c_χ , and inverse quality factor Q_χ^{-1} are

$$c_\chi(\omega) = \frac{\omega}{\Re k^\chi}, \quad (5.59)$$

$$Q_\chi^{-1}(\omega) = 2 \frac{\Im k^\chi}{\Re k^\chi} \quad (5.60)$$

for each wave mode

$$\chi \in \{\text{P1}, \text{P2}, \text{P3}, \text{S}\}.$$

Finally, these two quantities, together with the displacement amplitudes, will form the basis of investigating and understanding the physical phenomena.

Closing remark The previously introduced characteristic frequencies, Eq. (5.35), emerge by dividing the (not frequency-corrected) second and third diagonal elements of \mathbf{B} by those of \mathbf{A} , and represent the ratio of viscous drag to inertial forces. Moreover, consistency of the initial values has to be assured. For example, capillary effects result in different initial fluid pressures while changes in bulk moduli or densities from ambient conditions are often negligible, cf. Section 19.7.1.

Chapter 6

Model properties and selected examples

The following examples start with an exemplary, initial system of Nivelsteiner sandstone that is saturated with 40 % water and 60 % air. More elaborate physics is added stepwise. This procedure allows a precise investigation of separate physical processes. It reveals the potential of the developed theory in particular and wave propagation effects in general.

Specific extensions include reservoir conditions, grain compressibility, interfacial fluid-fluid areas, dynamic fluid pressure difference, and viscoelastic solids. The chapter finishes with scattering effects and remarks on potentially ambiguous definitions in literature.

6.1 Preliminary comments and the common initial system

The subject of the first basic investigations is Nivelsteiner sandstone filled with 40 % water and 60 % air at ambient conditions. Rigid grains are assumed, $K^{\text{grains}} \rightarrow \infty$, and the dynamic fluid pressure difference is neglected, $\tau \rightarrow 0$, i.e. the hybrid-model approach according to Steeb [196] is used. If not stated otherwise, all further examples refer to the same system and extensions are mentioned explicitly.

Material properties can be found in Appendix A.

6.2 General example and basic model properties

6.2.1 Low-frequency range

This section studies the initial system as introduced above. Solutions of the dispersion relations can be subdivided into the four wave modes: three longitudinal waves (P1, P2, and P3) and one shear wave (S). At low frequencies, $\omega \rightarrow 0$, only the P1- and the S-wave appear. In this low-frequency range, the fluids are coupled to the solid because of viscosity. All three constituents move in phase without a lag angle.

Moreover, all amplitudes are equal for the P1-wave, whereas the second and third longitudinal waves vanish, Fig. 6.1. Relative movements of the slower longitudinal wave modes cannot develop. The inverse quality factor of the P2- and P3-wave equals two. These two waves are just not stimulated because their total energy is transferred to the P1-wave motion, cf. Eq. (3.26) and corresponding explanation.

The low-frequency limit of wave propagation in a binary mixture was described decades ago by Gassmann [76]. The corresponding velocity is also known as the Gassmann-Wood limit (GW-limit). Averaging both fluids to one single fluid-mixture with the inversely averaged bulk modulus K^{lg} yields the low-frequency limits for the rigid-grain assumption as

$$\lim_{\omega \rightarrow 0} c_{\text{P1}}(\omega) =: c_{\text{GW,P1}} = \sqrt{\frac{K^{\text{s}} + \frac{4}{3}\mu^{\text{s}} + K^{\text{lg}}/\phi_0}{\rho_0^{\text{s}} + \rho_0^{\text{l}} + \rho_0^{\text{g}}}}, \quad (6.1)$$

$$\lim_{\omega \rightarrow 0} c_{\text{S}}(\omega) =: c_{\text{GW,S}} = \sqrt{\frac{\mu^{\text{s}}}{\rho_0^{\text{s}} + \rho_0^{\text{l}} + \rho_0^{\text{g}}}}, \quad (6.2)$$

$$K^{\text{lg}} = \frac{1}{\frac{s_0^{\text{l}}}{K^{\text{l}}} + \frac{s_0^{\text{g}}}{K^{\text{g}}}}. \quad (6.3)$$

The introduced average of the fluid bulk moduli is also known as the Reuss average and its connection to the volume fraction-weighted density average is called Wood's formula, cf. [139].

6.2.2 Transition range

With increasing frequency, inertia effects become more dominant. They overcome viscous coupling and the fluids start to decouple, cf. the decreasing P1-wave amplitudes of the fluids in Fig. 6.2. In the present case, air decouples first and water decouples then at higher frequencies. Due to this decoupling process, one longitudinal wave propagates separately in each fluid, composing the P2- and the P3-wave. Because macroscopic Newtonian fluids are assumed to have no resistance against shearing, further shear wave modes do not develop¹². Furthermore, the decoupling process is indicated by the critical frequencies, cf. Fig. 6.1 and Eq. (5.35). They represent the ratio of viscous forces to inertia forces of the fluids and are generalized in Chapter 11. The decoupling process also induces a (viscous) relative movement of solid and fluids, which results in a loss of momentum for the P1-wave. It is observable by the peaks of Q_{P1}^{-1} and Q_{S}^{-1} . This damping mechanism, which is caused by viscous drag, is often called Biot-like damping, because it is the only damping mechanism of the famous Biot model for wave propagation [24, 25]. Only one visible peak occurs because of the relatively low density and energy contribution of air.

6.2.3 High-frequency range

At very high frequencies, $\omega \gg \omega_{\text{c,f}}$, inertia dominates over viscous forces. The only coupling between the fluids and the solid is due to the form-locking/tortuosity parameter α_{id} . If this coupling process also vanishes, $\alpha_{\text{id}} \rightarrow 1$, the fluids decouple completely. The fluids do not contribute to the P1- and S-wave and show lag angle of

¹²Note that special situations may appear, in which a slow fluid shear wave may be observed, cf. [168] and Fig. 5.2b).

90°. In this special case, the denominator in Eq. (6.2) can be replaced by the densities of the coupled phases to obtain the mid- and high-frequency limits of the S-wave. Note that for $\omega \rightarrow \infty$, the wavelength approaches the characteristic length of the micro-structure. As a result, the long wavelength approximation becomes invalid and scattering appears, cf. Section 6.8.

6.2.4 Stimulation of wave modes

On the one hand, the appearance of specific wave modes depends on the boundary conditions. An oscillating solid boundary will predominantly stimulate those wave modes that are connected to the solid movement. Mathematically, the given boundary condition splits into a linear combination of the displacements \mathbf{u}_s , \mathbf{u}_l , and \mathbf{u}_g . Moreover, a transformation of wave modes occurs due to interactions such as viscous coupling. Practical observation of single wave modes can become even more difficult, due to the required differentiation into time or frequency domain, low sensitivity, or high attenuation, cf. the work of Kelder & Smeulders [106].

For example, the slow, longitudinal (P2-)wave was predicted by Biot for a biphasic mixture [24]. Nevertheless, experimental observations required a long time, cf. [106, 160]. Two longitudinal wave modes can also be observed in bones [36, 123]. Bones, however, have an oriented structure, due to adaptation to mechanical loading, and are therefore highly anisotropic. For this reason, the slow wave only occurs in directions where fluid flow is possible along the bone channels [123].

In the event, the presented example already predicts the existence of four different wave modes and distinguishes between three different frequency ranges: the low-frequency range, where all constituents are coupled; the transition zone, where decoupling processes begin and further wave modes develop; and the high frequency range, where the decoupling process is completed.

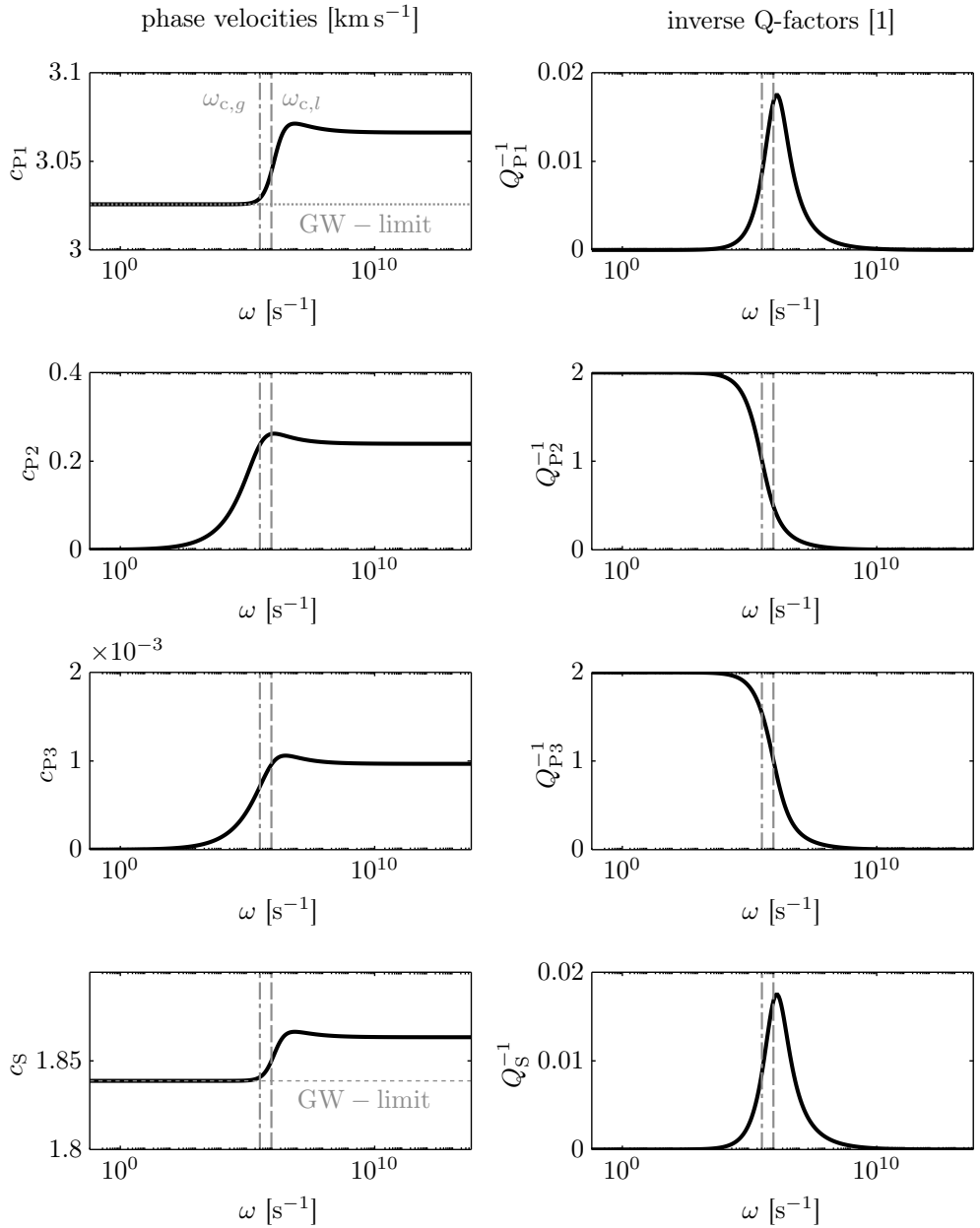


Figure 6.1: Dispersion relations for Nivelsteiner sandstone with 40% water and 60% air: phase velocity and inverse quality factor. The Gassmann-Wood limit for low frequencies is drawn as a horizontal line for the P1- and the S-wave. Characteristic frequencies after Biot for liquid and gas are plotted as vertical lines (g left and l right).

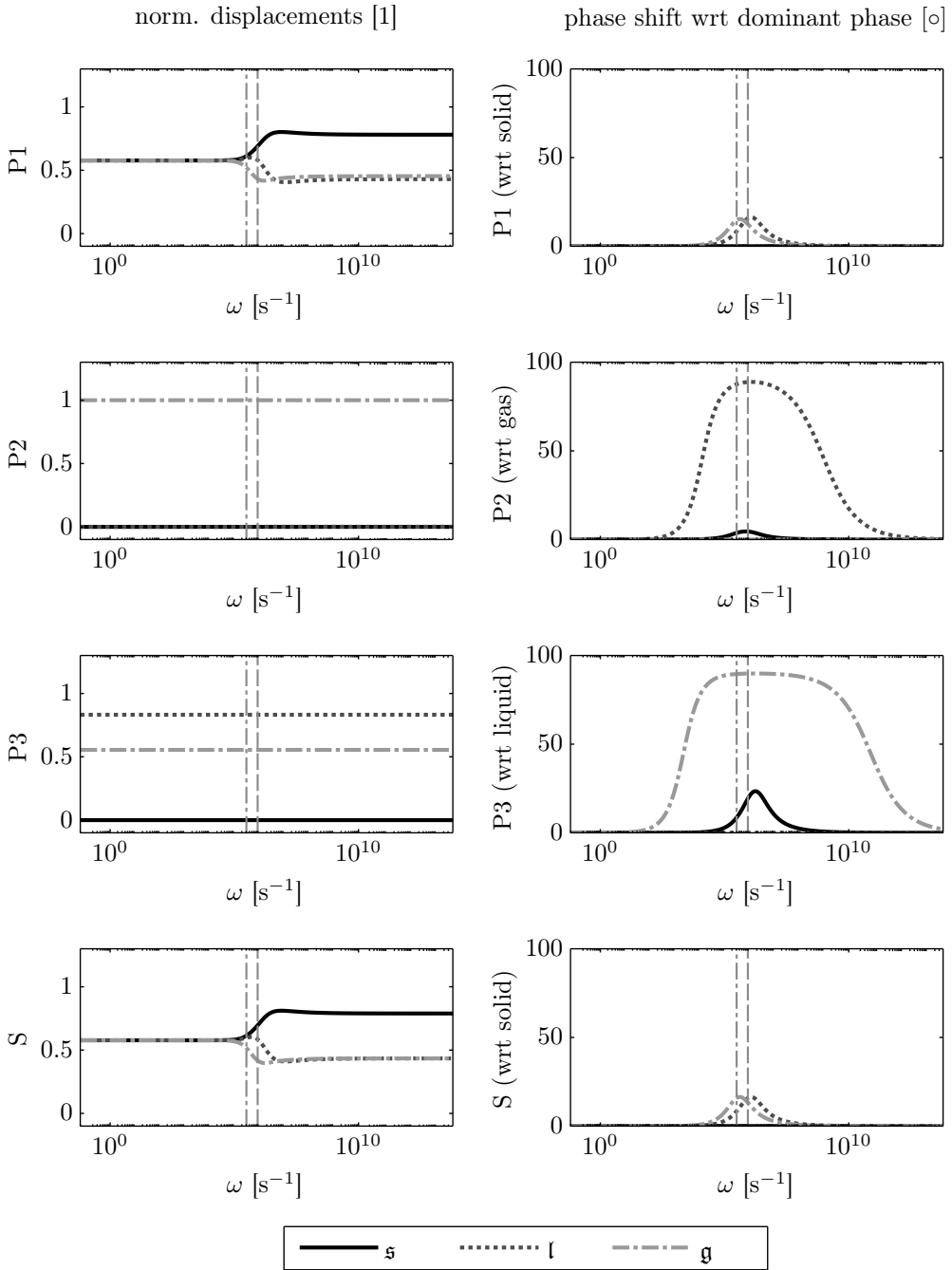


Figure 6.2: Dispersion relations for Nivelsteiner sandstone with 40% water and 60% air: normalized displacements and relative phase shifts between the single phases. Characteristic frequencies after Biot for liquid and gas are plotted as vertical lines (g left and l right).

6.3 Saturation range

In addition to frequency dependence, a further interesting aspect for research and applications is the view on saturation. Varying saturation conditions appear at different depths in the ground or in different regions on earth. For example, tunnel drilling machines are used in areas with varying moisture content. In such cases, exploration via mechanical waves depends on the saturation conditions.

6.3.1 Ambient and reservoir conditions

P1 phase velocity was determined for air at ambient conditions and at reservoir depth. For varying frequency, a distinct transition fault can be observed in both cases. It results from the decoupling process of the water phase. Decoupling of air is visible as a second transition step only for the case of reservoir conditions for low water saturation s^l , cf. the arrow in Fig. 6.3. For the case of ambient pressure, density, viscosity, and stiffness of air are small, so that the decoupling process is not even visible in the left graph. Due to their relatively low impact, gases at ambient conditions are often neglected when present in experimental tests of solid porous media. In particular, the current model serves as a tool for prediction of uncertainties caused by such assumptions.

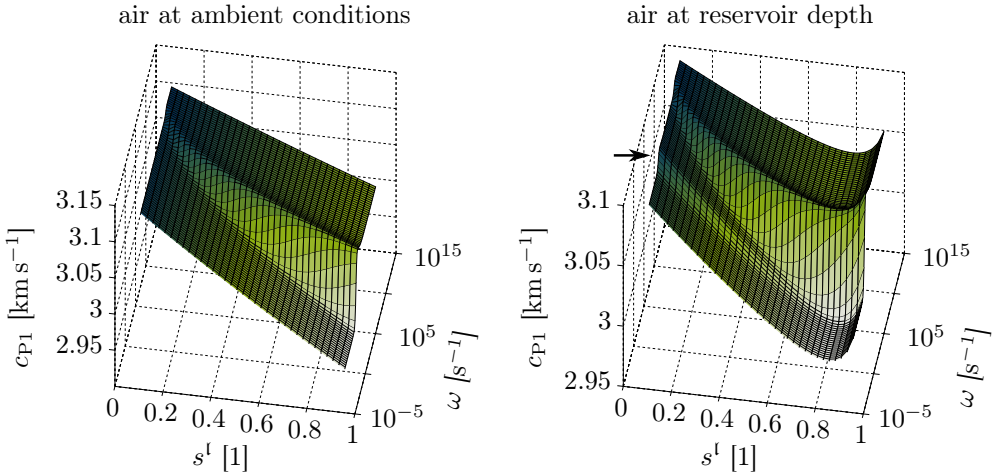


Figure 6.3: P1 phase velocities for Nivelsteiner sandstone with 40 % water and 60 % air at ambient conditions and at reservoir depth for different frequencies and saturations. The plotted saturation range for s^l is between 7.5 % and 92.5 %. The arrow indicates the decoupling process of air.

Considering saturation dependence at a fixed frequency, typical $c_{P1}-s^l$ curves bow between both saturation limits. This can be seen clearly in Fig. 6.3, right¹³. The mixed elasticity is lower than for a pure fluid phase. This behavior is supported by experimental observations as shown in the next subsection.

¹³Note, however, that for ambient conditions the increasing branch of P1-velocity in the high saturation regime is outside the plotting range. This is due to the high compressibility of the air phase, which weakens the system's stiffness, even for very high water saturations.

6.3.2 Application and comparison with experimental data

Comparison with experimental data of Murphy [151] is given for Massilon sandstone at different saturations of water and air. The agreement is excellent, including the steep increase at high water saturations, even though the hybrid model, i.e. the assumption of incompressible grains, is used throughout. The material data used is based on the respective fitting in [120, 219]. For $s^l \rightarrow 1$, a small deviation becomes apparent. Nevertheless, a model for residual saturation is more appropriate in this special case, as will be shown in Part III.

It should be noted that capillary effects or decoupling processes exert a minor influence at these comparably low frequencies. Only one type of longitudinal wave appears (P1). Transformation from longitudinal and shear wave velocities to extensional waves (index E) was executed analogously to transformation of the corresponding moduli as

$$c_E = \sqrt{\frac{c_S^2(3c_{P1}^2 - 4c_S^2)}{c_{P1}^2 - c_S^2}}.$$

The E-wave is related to the Young's modulus at uniaxial stress (for example, through thin wires with free boundaries) in the same way as the P-wave is related to the P-wave modulus at uniaxial strain, cf. Appendix B.4, (for example, for an infinitely broad, plane propagation front).

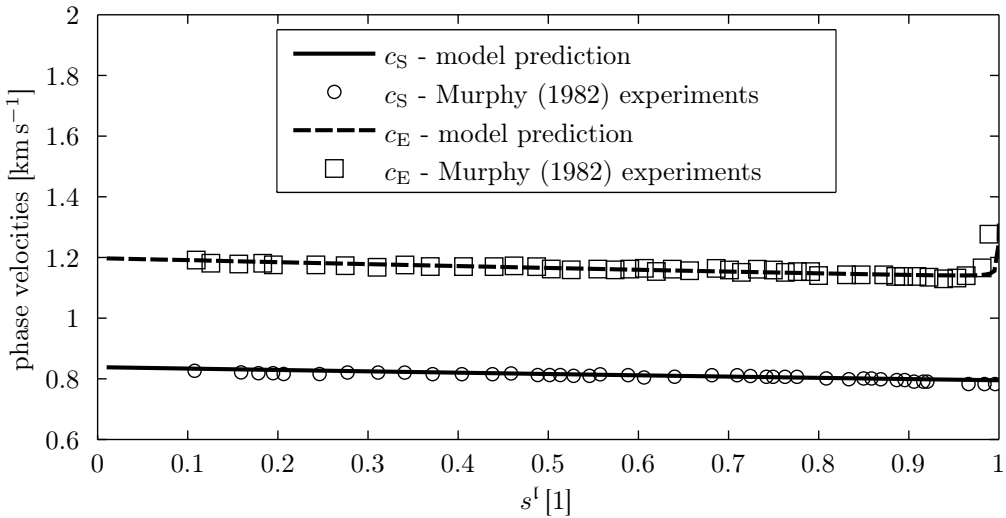


Figure 6.4: Comparison of dispersion relations with experimental data of Murphy [151]. Dispersion relations were calculated for $\omega = 2\pi \times 600 \text{ s}^{-1}$.

Additionally, saturation dependence of velocity at ambient conditions is illustrated in Fig. 6.5 by spatial propagation of a seismic subsurface P1-wave. A distortion of the traveling wave front develops with increasing time. This emphasizes the importance of knowledge about the wave velocity in field tests and exploration.

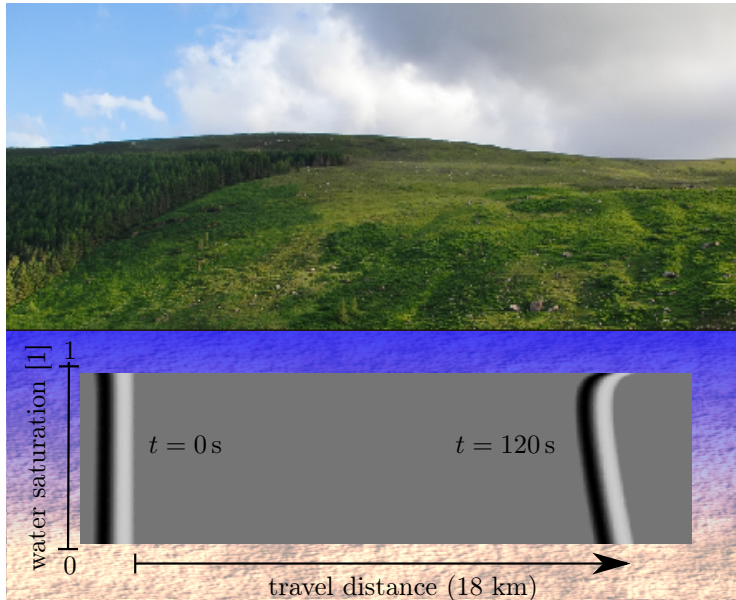


Figure 6.5: Seismic P1-wave (low-frequency range) in loose subsurface soil with different degrees of water saturation, for instance, moisturized by rain from top to bottom. Residual saturation ranges are left out. Material data is given in Appendix A.

6.4 Grain compressibility

A porous medium is composed of the matrix of a bulk solid. It can be a connected wire frame, as in the case of synthetic sponges, or a packing of grains, as for sands. Therefore, two compressibilities exist, one for the bulk material and one for the matrix. The latter is affected by its geometric structure. The Newtonian fluid phases possess only one compressibility, which is that of the bulk material. They do not exhibit elastic resistance against shape change.

Although the presented theory includes grain compressibility, its complexity reduces in the case of the rigid-grain assumption. Porosity can be directly determined from the solid mass balance with $\rho^{sR} = \text{const.}$ Furthermore, two material parameters, K^{grains} and Λ^{grains} , need not to be determined. This hybrid model approach was introduced by Steeb [196] for biphasic media.

Grain compressibility is negligible if it is low, compared to the compressibility of the fluids [196, 199]. Deviation of the low-frequency P1 phase velocities between compressible grains and the rigid-grain assumption practically vanishes if $K^{\text{lg}}/K^{\text{grains}} \ll 1$. For a binary mixture, K^{lg} has to be replaced by the bulk modulus of the single pore fluid.

The present calculations support these findings and extend them to the full frequency range for all four wave modes. Variations of the grain bulk modulus, K^{grains} , by factors of 0.5, 2, and 10 practically do not change the behavior of P1-wave for air at ambient conditions, cf. Fig. 6.6. Changes of the other wave modes are less pronounced. This is because alteration of the grain bulk modulus, K^{grains} , influences mostly the P1-wave, for the investigated material combination. The S-wave does not

depend on the grain bulk modulus, cf. definition of the stiffness matrix in Section B.4. The P2- and P3-waves are largely connected to the fluid movements, cf. amplitudes in Fig. 6.1.

Deviations, due to the rigid-grain assumption, are noticeable but remain below 1 % for the investigated case of air at reservoir depth conditions. It can be concluded that grain compressibility generally affects the longitudinal, i.e. compressional, wave of the solid. Nevertheless, the rigid-grain assumption emerged as a good approximation for the investigated samples. The corresponding hybrid model is generally applicable if $K^{lg}/K^{\text{grains}} \ll 1$ and covers many materials, in particular, when gases are present.

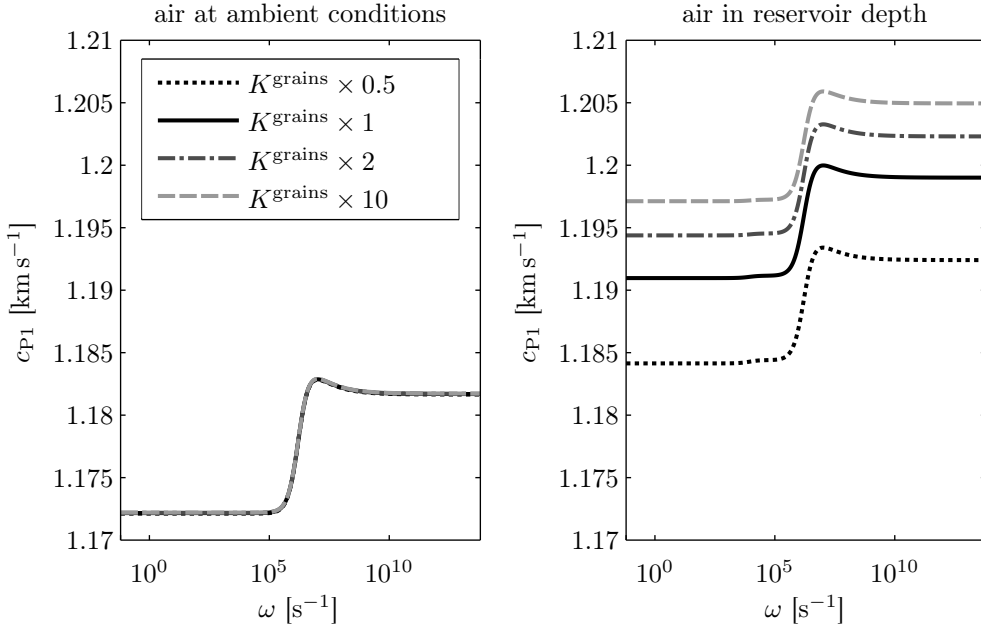


Figure 6.6: P1 phase velocities for a Massillon sandstone with 40 % water and 60 % air at ambient conditions/reservoir depth for variations of the grain bulk modulus.

6.5 Interfacial fluid-fluid areas

Interfacial fluid-fluid areas, a^{lg} , have been used by Niessner & Hassanizadeh [154] and Joekar-Niasar et al. [102] to explain hysteresis effects of the $p_{\text{eq}}^c-s^l$ -relationship. Different values of interfacial areas represent a different $p_{\text{eq}}^c-s^l$ path. To investigate the influence of interfacial areas on wave propagation, different $p_{\text{eq}}^c-s^l$ paths are studied for the same saturation. This is achieved by performing three variations of the initial Brooks & Corey parameters: $[\lambda_{\text{BC}} \times 1, p^b \times 2]$, $[\lambda_{\text{BC}} \times 2, p^b \times 1]$, and $[\lambda_{\text{BC}} \times 2, p^b \times 2]$. Measurements of a^{lg} are still rare and not available for the present material combination. Nevertheless, applying the values of saturation and equilibrium capillary pressure to the pore network models in [102] can serve as a first indicator. The mentioned changes of the $p_{\text{eq}}^c-s^l$ paths correspond to a variation of fluid-fluid interfacial areas of -16.62% , $+8.75\%$, and -1.76% respectively.

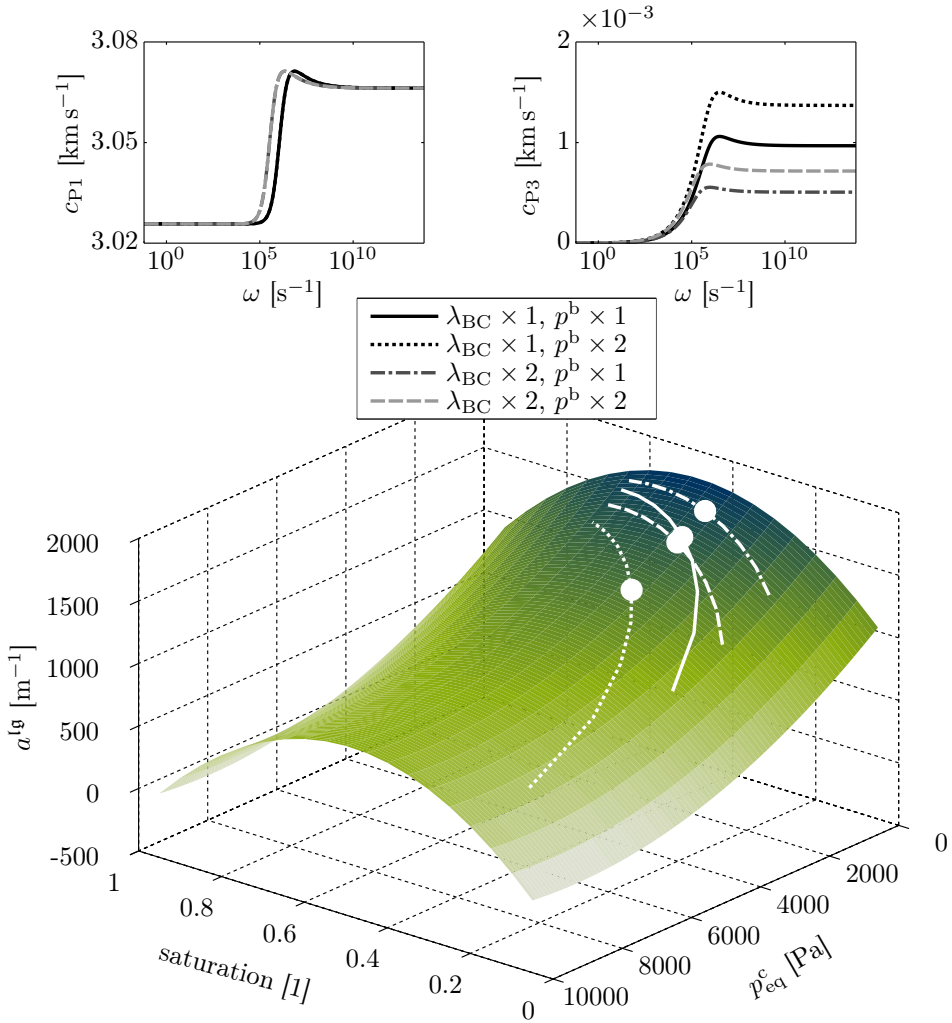


Figure 6.7: P1- and P3-wave phase velocities for different p_{eq}^c - s^l paths realized by different Brooks & Corey parameters (top). The paths are indicated at the a^{lg} - p_{eq}^c - s^l surface of the pore network model in [102] (bottom).

As a first result, relative permeabilities and capillary pressure change with varying λ_{BC} . This causes a shift of the decoupling processes, cf. the c_{P1} -shifts in Fig. 6.7. Additionally, the P3-wave is significantly influenced, whereas the P2 velocities remain virtually unaffected. Physically, capillary effects influence the interaction of both fluids, which became observable via the weak air-phase. The c_{P3} high-frequency limits grow stiffer by increasing initial capillary pressure for the investigated cases.

In conclusion, interfacial fluid-fluid areas became noticeable as changing relative permeabilities for all wave modes and especially through the changes in P3-wave behavior. This wave, however, is highly dissipative. Hence, it is usually difficult to observe and characterize experimentally, cf. difficulties observing the second wave in [160, 191].

6.6 Dynamic fluid pressure difference and dynamic capillary pressure

The effect of a dynamic fluid pressure difference (or dynamic capillary pressure) has not been completely explored, to date. Hence, it is of fundamental scientific interest to investigate its influence on wave propagation and vice versa. Dynamic fluid pressure difference is simulated by use of Eq. (5.49) and Eq. (5.50). Because the empirical origin of τ serves only as a rough approximation and may vary by one order of magnitude or more [134] it has been varied by the factors 1×10^3 and 1×10^{-3} .

The results are noteworthy compared to the equilibrium relationship, i.e. $\tau = 0$ Pa s. The τ -parameter causes an additional damping mechanism, superimposing and dominating the classical Biot-like damping of the P1-wave, Fig. 6.8. Varying τ results in a shift of the damping process as it does for varying viscosity in the case of viscous damping. Moreover, the P1-wave velocities increase noticeably in the high-frequency case and the P3-wave becomes a fluid-wave of much higher velocities than before. The dynamic parameter τ generally stiffens the system, particularly, at high frequencies like a classical damper. The P3-wave velocities become even higher than those of the P2-wave, whereas the latter and the S-wave remain unaffected.

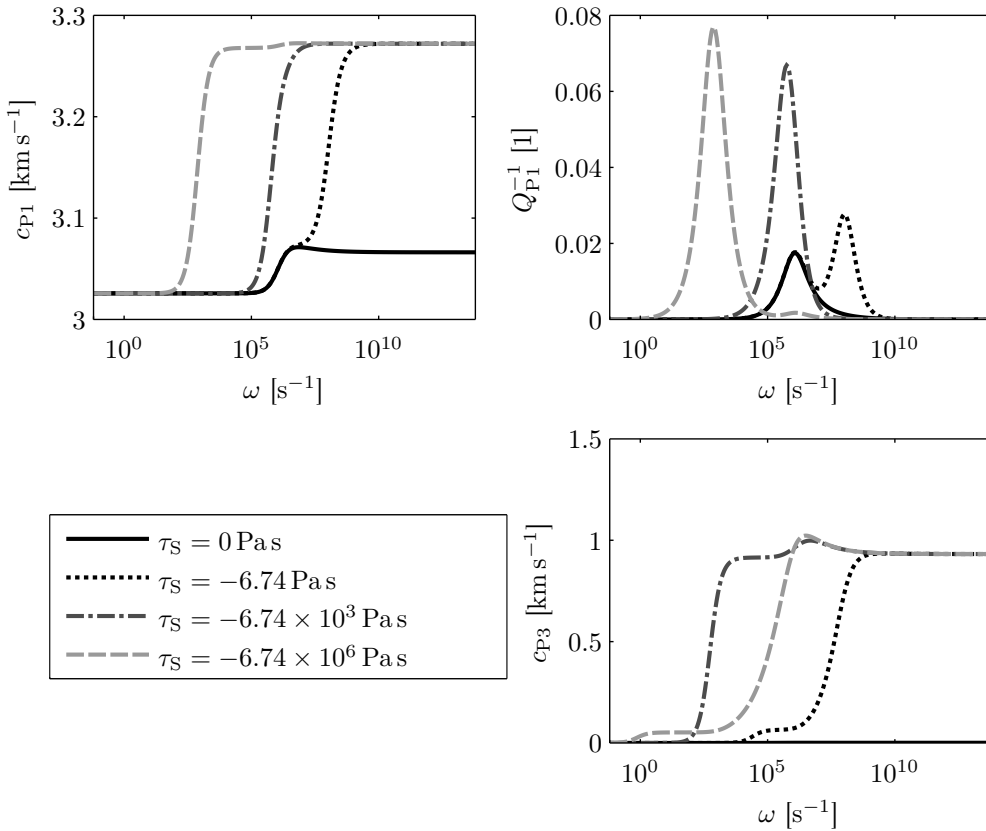


Figure 6.8: Dispersion relations accounting for a dynamic fluid pressure difference.

In the event, the theoretical implementation of dynamic fluid pressure difference shows a remarkable effect on wave propagation in the present example. Furthermore, it coincides qualitatively with the approach of Wei & Muraleetharan [220] that is based on the rate of volume fraction (\dot{n}^1) instead of saturation. However, the role of dynamic fluid pressure difference is not fully understood yet. Changes of traveling fluid-fluid interfaces may be stronger for long-range flow in sinusoidal pore channels than for the case of wave oscillations with small amplitudes. Thus, the impact of τ_S , assumed on the basis of steady flow, may deviate for propagating waves. The presented results show possible influences and, therefore, will help to sharpen the focus of experimental studies that are required for final conclusions.

Another microscopic view on this topic will be given in Part IV for the case of residual saturation. A limited frequency dependence will be demonstrated for the shape of flow profiles and the capillary pressure.

6.7 Viscoelastic solid matrix

A porous matrix can consist of various bulk materials. In particular, artificially created foams can be produced from synthetic material. Usually, materials such as plastics are not only elastic but show a viscoelastic behavior. As a first approach, the implementation of a standard linear solid (SLS) model is investigated, which consists of two springs of stiffness $c_{\text{SLS},1}$ and $c_{\text{SLS},2}$ and one damper of damping coefficient d_{SLS} attached to the second spring, cf. Fig. 6.9.

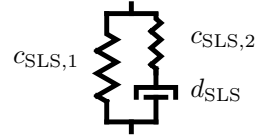


Figure 6.9: SLS-model.

The dynamic modulus describing the stress to strain ratio for vibrational excitation with ω becomes

$$c_{\text{SLS},1} + \frac{c_{\text{SLS},2} d_{\text{SLS}}^2 \omega^2 + i \omega c_{\text{SLS},2}^2 d_{\text{SLS}}}{d_{\text{SLS}}^2 \omega^2 + c_{\text{SLS},2}^2}. \quad (6.4)$$

The viscosity of the solid adds another damping mechanism as it can be seen by the inverse quality factors in Fig. 6.10. In the current example, damping of the viscous solid is much larger than due to viscous flow. Different relaxation times, determined by d_{SLS} , result in a shift of the Q^{-1} peaks. Additionally, stiffness is weak at low frequencies, at which the damper shows no resistance, and grows at higher frequencies, at which the damping element stiffens. The low- and high-frequency limits can therefore be used to determine the values of the two springs in the SLS-model. More interestingly, stiffening of the damper is analogous to the explanation of the high-frequency phase velocities of the P1- and P3-wave for dynamic fluid pressure difference, Fig. 6.8.

In addition to the used SLS-model, more sophisticated rheological models can be implemented, for instance, as used in [232] for asphalt. For realistic application, their respective properties can be fitted to experimental data.

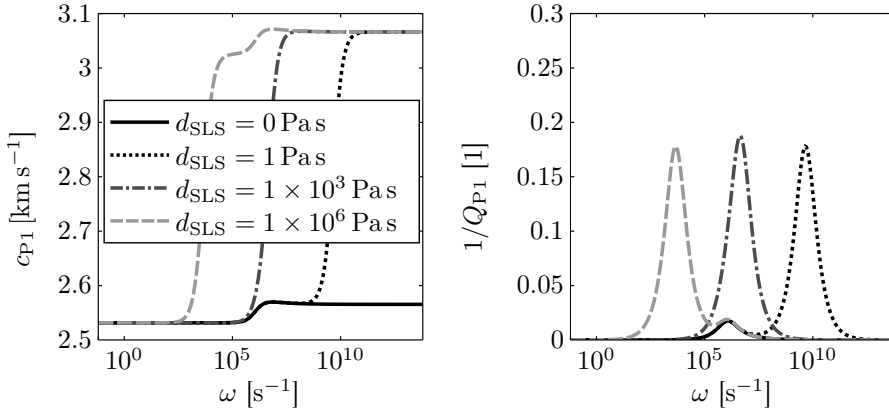


Figure 6.10: Dispersion relations of the P1-wave for different variations of an SLS-model with $c_{\text{SLS},1} = 0.7(\lambda^s + 2\mu^s)$, $c_{\text{SLS},2} = 0.3(\lambda^s + 2\mu^s)$, and damping variations of d_{SLS} . Note that the second rising of the left phase velocity curve and the higher middle peak of the inverse quality factor are caused by superposition with the Biot-like interaction.

6.8 Scattering

The presented macroscopic model for wave propagation is based on the assumption of scale separation, i.e., the wave length is much larger than the characteristic length of the microstructure. In this case, the gradient of the wave displacement is small at the microscale and single adjacent grains and pores move almost uniformly. The wave does not interact with the microstructure. In the opposite case, the wave amplitude changes at a scale that is similar to or smaller than the pore size. The wave displacement changes substantially between two pores. As a result, reflections occur at microscopic discontinuities such as the solid-fluid interfaces and the wave signal scatters.

For many experiments and theoretical investigations, it is convenient to replace the wave length condition for scale separation by a frequency condition via $\lambda_\chi = 2\pi c_\chi/\omega$. A general estimation for the valid frequency range cannot be given, because it depends on the specific materials. For rocks, a first approximation for the wavelength of the P1- and the S-wave is $\lambda_{\text{P1/S}}(\omega) \approx 2 \text{ km s}^{-1}/\omega$. Assuming at least $\lambda_{\text{P1/S}} \geq 1 \text{ mm}$, the frequency must be $f \leq 2 \times 10^6 \text{ s}^{-1}$ or $\omega \leq 1/3 \times 10^5 \text{ s}^{-1}$.

Wave lengths of the specific example of Nivelsteiner sandstone with water and air from Section 6.2 are plotted in Fig. 6.11. Similar to the P1- and S-waves, the P2- and P3-waves fulfill the requirements of a long wave length at low frequencies although they are highly dispersive. Due to their lower velocities, their wavelengths are smaller than for the P1- and S-wave. Additionally, the slope of the double-logarithmic $\lambda_\chi(\omega)$ relationship becomes similar for all waves in the high frequency range after the decoupling process.

Although the presented theory does not account for scattering effects, an investigation of the full frequency range remains useful, because the predicted physical phenomena are understood entirely and can be important for other material combinations.

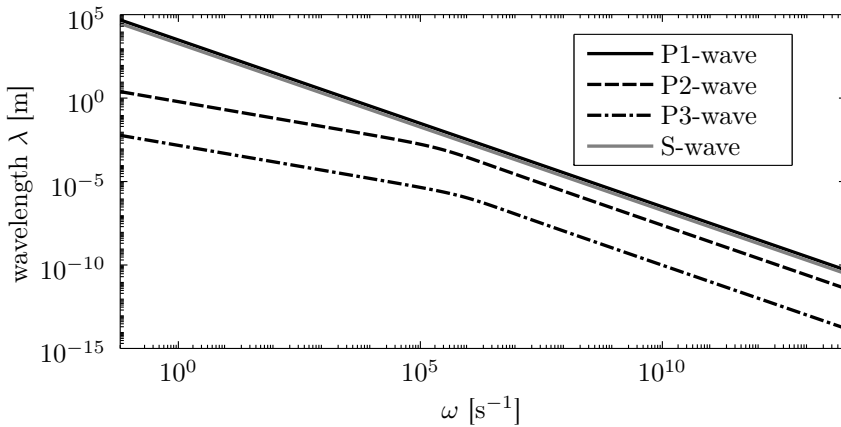


Figure 6.11: Wavelengths of different wave modes for Nivelsteiner sandstone with 40% water and 60% air as defined in Section 6.2.

Moreover, scattering effects can provide further information about the physical system. For example, Güven [82] sent a polychromatic wave through a cylindrical, air-filled sample of sintered glass beads and recorded the arriving signal. An extract of the experimental results is shown in Fig. 6.12.

For glass beads of 0.5 mm diameter, one part of the transmitted signal contains wavelengths larger than 0.5 mm and it fulfills the condition of scale separation. This part travels as a macroscopic, elastic wave and can be recorded distinctly, cf. Fig. 6.12 (left). The other part of smaller wavelengths is filtered, because of scattering effects. For glass beads of 8 mm diameter, no transmitted wavelength is large enough and the entire signal is scattered, cf. Fig. 6.12 (right).

In addition to theories of elastic wave propagation, scattering signals can also be used to characterize the physical system, for example, via a diffusion model [101].

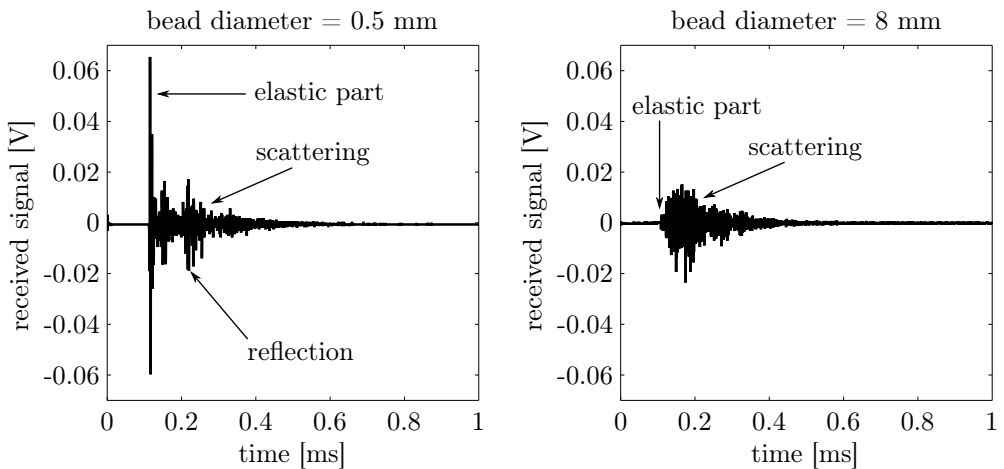


Figure 6.12: Recorded signal in air-filled glass beads with different diameters from experiments of Güven [82] and private communication with I. Güven.

6.9 Remarks on definitions and possible misunderstandings

6.9.1 Permeability

The used definition of permeability is that of an intrinsic (hydraulic) permeability k^s . It relates the pressure gradient to a laminar, steady-state fluid flow and is solely a property of the solid matrix. Note that there are other definitions of permeability. They can include further properties such as the fluid viscosity and can be motivated by specialized experiments, for example, water flow due to gravity g . Amongst others, one famous example is the so-called Darcy-permeability or hydraulic conductivity

$$k_{\text{Darcy}}^f = k^s \frac{\rho^{fR} g}{\eta^{fR}},$$

with units m s^{-1} and named after Darcy [43]. The unit Darcy (denoted as D and often used as $\text{mD} = 10^{-3} \text{ D}$) is closely related to this origin with $1 \text{ D} = 9.869 \times 10^{-13} \text{ m}^2$. In addition to the alternative definition above, some theories of wave propagation combine intrinsic permeability and its modifications such as frequency dependence to one complex-valued permeability, cf. [105]. Such alternatives can be useful for experiments when the proportionality factor between fluid flow and pressure gradient is considered directly. The present work, in contrast, separates the individual physical influences and, therefore, distinguishes between the intrinsic permeability and effects that exceed its original use for pressure-driven, steady-state flow.

Due to the frequency correction in Eq. (5.36), an additional imaginary part of the viscous drag forces appears. By this, it directly contributes to the inertia terms (as its origins are microscopic inertial forces). As a result, the imaginary part may be isolated from the real part and recognized as a permeability impact on inertia. Nevertheless, all such interpretations are just different reflections of the same physical phenomenon.

6.9.2 Tortuosity

Definitions of tortuosity are various and this circumstance cannot be clarified in full detail in the present work. What is more, use and interpretation of the same tortuosity approach diverge, even if they are inherently consistent [42]. The problem is perhaps best described by loosely following L. Wittgenstein: the meaning of a word is defined by its use in language¹⁴. A first attempt for a clear view on this subject also follows L. Wittgenstein: the meaning of a name is sometimes best explained by pointing on the object to which it refers¹⁴.

One well-known microscopic definition of a hydraulic (or sometimes called geometric) tortuosity should be mentioned. It describes the ratio of a flow path length with respect to the shortest connection between two points

$$\alpha_{\text{hyd}} = \frac{\overline{\text{flowpath}(A,B)}}{\overline{AB}}.$$

This property has, at least, two physical impacts. On the one hand, fluid flow is deflected, which yields a resistance against flow through the solid. Effectively, this becomes noticeable in the macroscopic permeability. For example, sinuous pore channels are tortuous and increase the resistance for fluid flow. Thus, terms of tortuosity

¹⁴Translated from [159], also cf. [225].

and permeability (or viscous drag) are related in some theories depending on their definitions.

On the other hand, hydraulic tortuosity affects from locking or trapping of fluid in the solid pores. Hence, inertial drag is also influenced by it. This was expressed by the macroscopic parameter α_{id} in the current framework and is not necessarily equal to α_{hyd} . For example, the latter does not account for dead ends of pores or inclusions, which are separated from the main flow.

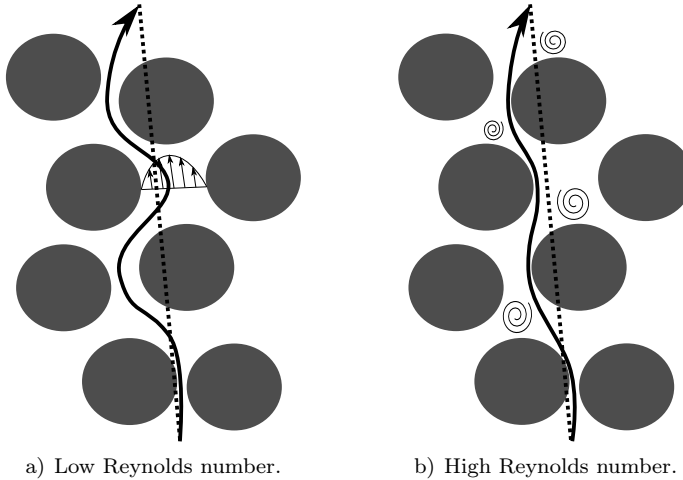


Figure 6.13: Deterministic lengths of the hydraulic tortuosity for low and high Reynolds numbers. The solid line indicates the stream line of a particle and the dotted line indicates the shortest connection in space. The value determined for low Reynolds numbers is often called geometric tortuosity.

Additionally, note that the above definition of the hydraulic tortuosity can depend on the flow properties. For steady flow with low Reynolds numbers, the streamline of a particle can be different from the case of high Reynolds numbers, Fig. 6.13¹⁵. Accordingly, a dependence on the oscillation frequency may occur as well. Moreover, it should be emphasized that the macroscopic tortuosity is an averaged parameter of the microscopic definition as given above.

The present work cannot solve the problematic circumstance of different tortuosity definitions. Instead, it distinguishes between the physical (macroscopic) effects of inertial drag and viscous drag. These effective physical phenomena are of major importance in the present investigation. The knowledge about their physical role and implementation in the current framework allows a comparison with literature and the respective definitions with appropriate care. Even more, the corresponding material parameters, α_{id} and κ^5 (or $b_{0,f}$), can be interpreted as coefficients of the respective processes of non-equilibrium momentum exchange.

6.9.3 Solid and fluid waves

The former investigations demonstrated the appearance of different wave modes, which were called P1-, P2-, P3-, and S-wave. The classification of the longitudinal

¹⁵Motivated by private communication with R. Sivanapillai.

(P-)waves was done with respect to the wave velocities and their dispersive behavior. In literature, they are sometimes connected to the single phases or boundary conditions, for instance, the so-called airborne wave [5]. Note that such definitions are common in specific research areas but are not appropriate for a general theoretical description. As could be seen, the wave modes are often connected to more than one phase, cf. Fig. 6.1. Moreover, the constituent that is connected to the slow P2-wave is not always the fluid, but can change to the solid as it will be shown later, cf. Section 11.4.2. Hence, a denotation connecting the wave modes to specific materials is only suitable in the case of unambiguousness.

6.9.4 Further terms and definitions

Various terms and definitions were established to describe dynamic processes in porous media during the last decades. They depend on the research area, research group, place, and time. Many terms have been mentioned in the previous discussion, whereas others cannot be considered due to the large spectrum of existing research. Therefore, it should be noted for comparison with literature that some terms may appear with other naming or alternative (re)formulations. This circumstance is often caused by differences in theoretical approaches or accessibility of experimental data.

One example is the representation of the response to cycling loading via dynamic moduli. They are often used for interpretation of experiments and further divided into storage modulus and loss modulus. The storage capacity of aquifers is often used/measured during field pumping tests. In the current framework, this is implicitly included in the stiffness matrices of the compressional P-waves as they include resistance of pressure with respect to volumetric deformation. Considering basic definitions, volume fractions and saturation are sometimes replaced by a so-called pore number or moisture content. With respect to alternative definitions and names, the interested reader is referred to textbooks such as [5, 13, 139], which also contain a deeper theoretical introduction.

Chapter 7

Mesosopic extensions

A classical distinction between two scales was used in the previous chapters. Nevertheless, natural materials, including rocks, wood, or arterial networks, can show a bandwidth of active length scales. This results in so-called mesoscopic effects, which are motivated and presented in this chapter. The implementation of two types of mesoscopic processes, namely squirt-flow and double pores space effects, is executed phenomenologically and illustrates its significant impact on attenuation.

7.1 Introduction

The presented theory accounts for a material with an inherent microstructure and describes it as a continuum on a macroscale. This approach works well for a multiplicity of materials, especially for artificially created porous materials used in the field of mechanical engineering. In contrast, natural structures - organic and nonorganic - do not possess just one single microstructure. Additionally, a heterogeneity may also appear on another length scale, the mesoscale (from the Greek word $\mu\acute{\epsilon}\sigma\omicron\varsigma$ indicating *middle*).

For example, rocks often have a grain structure on the μm -scale. A rock mass on the km-scale, however, does not consist of the grain structure throughout. It can also contain gaps, folds, and other irregularities on a dm- or m-scale. These irregularities are not only exceptional disturbances but are also distributed over the entire rock mass. Furthermore, saturation of two fluids or properties such as porosity can change on a scale that is larger than the typical pore diameter. In all mentioned cases, a further length scale becomes important for the physical behavior of the material: a mesoscale. Although a comprehensive study of mesoscopic losses exceeds the scope of this work, basic approaches are presented to improve understanding of the mesoscale impact on wave propagation and to create a link to further research.



Figure 7.1: Mesoscopic structures in the form of layers in sandstone (Valley of Fire, Nevada, USA) and in the form of a second characteristic pore space, created by additional cracks in the soil (Death Valley National Park, California, USA).

7.2 Types of mesoscopic losses: squirt-flow, leak-off, and interlayer flow

In natural media, theoretically predicted attenuation and quality factors often diverge from experimental data [56]. For example, the measured inverse quality factor (or attenuation respectively) of sandstone is significantly higher and appears at lower frequencies than predicted by Biot's theory [25]. Various approaches to modeling exist. Typical concepts for its explanation are presented in Fig. 7.2, based on several literature resources.

One well-known explanation is squirt-flow, which typically appears if pores and/or cracks of extreme aspect ratios are connected. One attempt to combine Biot's predictions and squirt-flow is the so-called Biot-squirt-flow-model (BISQ) that was introduced by Dvorkin & Nur [56] and revised in [58]. The key concept is the introduction of a radial squirt-flow, which occurs perpendicular to the propagating wave over a certain squirt-flow length. Macroscale equations are used for the mathematical description and yield a correction function for the relationship between pressure and derivatives of the displacements. Biot's theory [25] is thereby extended by a correction factor that depends on the new characteristic squirt-flow length.

Damping mechanisms in intersected and separated crack networks were investigated numerically in [78]. The cracks were much larger than the microscale pores and showed a high energy intake at low frequencies. A similar approach but with intersection of different geometries is based on contributions such as [2, 140, 157]. Furthermore, leak-off into the micropores can add to the list of mesoscopic loss mechanisms.

Layers with different properties can also cause mesoscopic loss. Considering a further fluid phase, White et al. [223], Dutta & Odé [54, 55], and Quintal et al. [171] investigated heterogeneities that can occur in the form of alternating layers of different saturations. The mesoscopic length scale is determined by the layer thickness. Even with neglected inertia, i.e. with a focus on the low-frequency regime, the layered structure can increase attenuation significantly [171, 223]. Furthermore, Cit et al. [39] describe a loss mechanism in alternating fluid-solid layers.

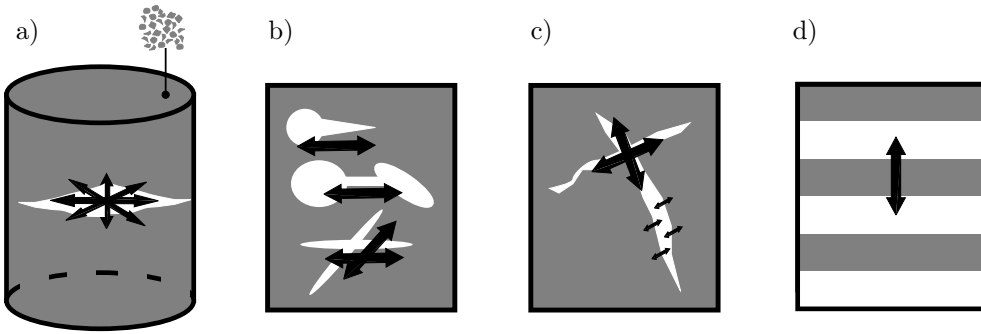


Figure 7.2: Basic concepts of mesoscopic losses. a) squirt-flow [56] b) squirt-flow in cracks/areas of high aspect ratios [2, 157] c) pressure diffusion in cracks and leak-off [78] d) layered media [39, 223]. Gray color represents the micro structure.

7.3 Local flow and its characteristic frequency

Until today, there is no universally accepted theory and various mechanisms may contribute to mesoscopic loss with different weighting for specific situations. Common to all previously mentioned concepts is a new characteristic length. Its origin can be an extra crack or layer but is not restricted to it. The following investigation will focus on mechanisms that are traditionally subsumed with the terms squirt-flow, pressure diffusion, and/or wave-induced fluid flow.

Indeed, porous media such as sandstones can contain such a mesoscopic length that is not included in classical Biot-like theories. Biot assumed a flow through a porous medium that is influenced by permeability of the solid matrix. Nevertheless, dead end pores can exist at various length scales, in which flow is not restricted by permeability but by the closed wall. For steady (Darcy-like) flow, the closed pore space acts similarly to dead water zones. At most, they include secondary flows but the key issue is: the pores do not deform during the flow process of steady flow, Fig. 7.3. As a result, influence of the dead end pores' elasticity on solid-fluid interaction is not accounted for neither in Darcy's nor in Biot's theory. However, these pores can deform for oscillatory flow as it appears for wave propagation.

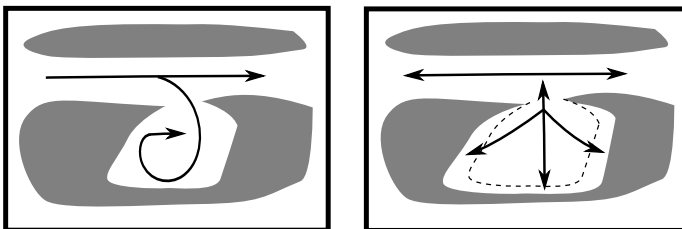


Figure 7.3: Difference between global (Darcy-like) flow (left) and local flow (right).

Thus, two different flow processes can occur in the pore space. On the one hand, there is classical Biot-flow that is constrained by the inverse permeability. In application, for example, this is known from consolidation, which is related to a boundary with

open pores. The characteristic length is based on the pore diameter. On the other hand, fluid inclusions exist, which are constrained by the closed, solid walls. Their dynamic response depends on viscous fluid flow between the elastic walls.

A differentiation between these two phenomena can also be represented by respective pore spaces. For example, compliant pores (adapting to deformation by outflow through the pore channels) and stiff pores (stiffer due to the solid boundary, which captures the deformation) are distinguished in [39, 57, 137, 188], cf. Fig. 7.4. Considering cracks of high aspect ratios and different orientations, some behave stiff with respect to load in lateral direction but others are loaded transversally and behave more compliant. Another differentiation is that between global and local or wave-induced fluid flow. This is because Biot's description is connected to the macroscopic (global) flow. On the contrary, the mesoscopic flow process is limited locally by the solid boundary.

In conclusion, two characteristic lengths can be distinguished: common to cracks or spaces bounded by connected grains is a large length l_{stiff} accounting for their elasticity and storage (local flow), whereas viscous flow through them is governed by the smaller characteristic pore distance l_{compl} (global flow).

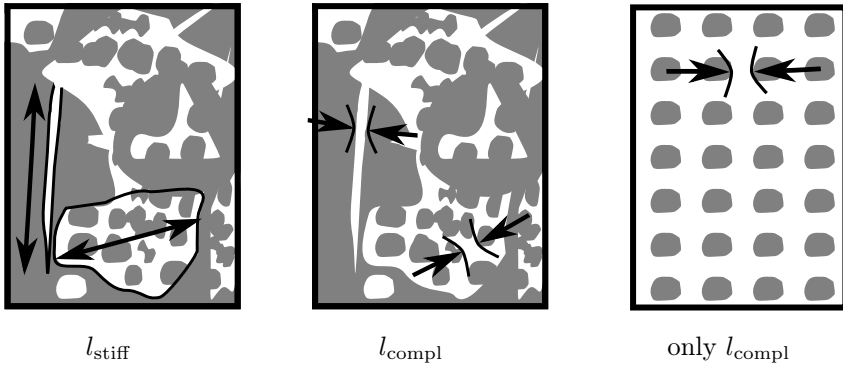


Figure 7.4: Idealized comparison between characteristic stiff and compliant pore lengths. No mesoscopic length scale appears in completely regular structures.

In the same way classical Biot-like damping is related to a characteristic frequency, mesoscopic attenuation is related to another characteristic frequency. Ciz et al. [39] expect the characteristic frequency of so-called local flow to be determined by the solid stiffness, fluid viscosity, and a characteristic length ratio of compliant pores to stiff pores $l_{\text{compl}}/l_{\text{stiff}}$ as

$$\omega_{\text{c,VE,f}} = \frac{\tilde{K}^{\text{s}}}{\eta^{\text{f}}R} \left(\frac{l_{\text{compl}}}{l_{\text{stiff}}} \right)^{m_{\text{sf}}} . \quad (7.1)$$

\tilde{K}^{s} represents the solid elasticity and is typically related to Young's or the shear modulus. The exponent m_{sf} can be approximated by values between 2 and 3 for the characteristic frequency but also other values are used [37, 39, 140, 165].

7.4 Implementation in the current model

7.4.1 Equations

Based on the previous thoughts and Eq. (7.1), the new local-flow mechanism is assigned to viscous damping of the solid matrix. From the macroscopic point of view, it is an intrinsic mechanism because the corresponding local, mesoscopic flow is undirected. Hence, it does not appear as a macroscopic movement as against the fluid flow of Biot-type. The damping of fluid inclusions depends on fluid viscosity η^{fR} . With it, the new viscous damping of the solid matrix is approached as, cf. Eq. (5.19),

$$\begin{aligned} \mathbf{T}_{\text{extra}}^{\text{s}} &= (2\mu^{\text{s}} \boldsymbol{\varepsilon}_{\text{s}} + \lambda^{\text{s}} \epsilon_{\text{s}} \mathbf{I}) (1 - n^{\text{sf}}) \\ &\quad + n^{\text{sf}} s^{\text{l}} (2\mu^{\text{s}} \boldsymbol{\varepsilon}_{\text{s}} + \lambda^{\text{s}} \epsilon_{\text{s}} \mathbf{I} + a_{\text{sf}} c_{\text{sf},\text{l}}(\omega) \eta^{\text{lR}} \dot{\epsilon}_{\text{s}} \mathbf{I}) \\ &\quad + n^{\text{sf}} s^{\text{g}} (2\mu^{\text{s}} \boldsymbol{\varepsilon}_{\text{s}} + \lambda^{\text{s}} \epsilon_{\text{s}} \mathbf{I} + a_{\text{sf}} c_{\text{sf},\text{g}}(\omega) \eta^{\text{gR}} \dot{\epsilon}_{\text{s}} \mathbf{I}) \\ &= \underbrace{2\mu^{\text{s}} \boldsymbol{\varepsilon}_{\text{s}} + \lambda^{\text{s}} \epsilon_{\text{s}} \mathbf{I}}_{\text{Biot-like approach}} + n^{\text{sf}} \sum_{\text{f} \in \{\text{l}, \text{f}\}} s^{\text{f}} a_{\text{sf}} c_{\text{sf},\text{f}}(\omega) \eta^{\text{fR}} \dot{\epsilon}_{\text{s}} \mathbf{I}. \end{aligned} \quad (7.2)$$

Physically, the viscous fluid inclusions (η^{fR}) resist the rate of volumetric change of the pores ($\dot{\epsilon}_{\text{s}}$) and induce viscous stress. The part of the solid that is assumed to be viscous is weighted by n^{sf} and further distributed to both fluid phases via their saturation in this first approach. The geometry of the fluid inclusions is represented by parameter a_{sf} . Following Eq. (7.1) motivates the approach

$$a_{\text{sf}} \approx \left(\frac{l_{\text{compl}}}{l_{\text{stiff}}} \right)^{-m_{\text{sf}}}. \quad (7.3)$$

The characteristic, mesoscopic length l_{stiff} is usually much larger than l_{compl} [39], which is the characteristic pore diameter in the present case, $l_{\text{compl}} \approx d_{\text{pore}}$.

Moreover, a frequency dependence is introduced by $c_{\text{sf}}(\omega)$ for two reasons. First, the distribution of stiff pores is usually irregular. For example, cracks of different orientations can occur with different characteristic damping frequencies. Thus, their dynamic response can depend on the angle of incidence and frequency.

Second and of fundamental influence, the wave length becomes smaller than l_{stiff} for $\omega \gg \omega_{\text{c,VE},\text{f}}$. In this case, the flow is not restricted by the dead-end pore walls any more. Due to the small wave length, the fluid can oscillate freely within the wall distance l_{stiff} . As a central result, resistance is more and more determined by permeability. The former stiff pores behave like compliant pores and the total pore space can be described by Biot-like flow for $\omega \gg \omega_{\text{c,VE}}$. This has to be accounted for by $c_{\text{sf}}(\omega)$ with

$$c_{\text{sf}}(\omega) \approx 0, \quad \text{for } \omega \gg \omega_{\text{c,VE},\text{f}}, \quad (7.4)$$

which distinguishes the physical process and the presented approach from a classical viscous damping mechanism.

Using the foregoing findings and applying linearization and the harmonic approach for plane waves replaces the elastic stiffness of the solid in Section B.4 by

$$\lambda^{\text{s}} + 2\mu^{\text{s}} \rightarrow (\lambda^{\text{s}} + 2\mu^{\text{s}}) \left[1 - i n^{\text{sf}} \left(s_0^{\text{l}} \frac{\omega}{\omega_{\text{c,VE},\text{l}}} c_{\text{sf},\text{l}}(\omega) + s_0^{\text{g}} \frac{\omega}{\omega_{\text{c,VE},\text{g}}} c_{\text{sf},\text{g}}(\omega) \right) \right], \quad (7.5)$$

$$\omega_{\text{c,VE},\text{l}} = \frac{\lambda^{\text{s}} + 2\mu^{\text{s}}}{\eta^{\text{lR}}} \frac{1}{a_{\text{sf}}}, \quad \omega_{\text{c,VE},\text{g}} = \frac{\lambda^{\text{s}} + 2\mu^{\text{s}}}{\eta^{\text{gR}}} \frac{1}{a_{\text{sf}}} \quad (7.6)$$

for P-wave stiffness (in the first diagonal element of \mathbf{C}^P) and

$$\mu^s \rightarrow \mu^s \left[1 - i n^{\text{sf}} \left(s_0^{\text{l}} \frac{\omega}{\omega_{\text{c,VE,l}}} c_{\text{sf,l}}(\omega) + s_0^{\text{g}} \frac{\omega}{\omega_{\text{c,VE,g}}} c_{\text{sf,g}}(\omega) \right) \right], \quad (7.7)$$

$$\omega_{\text{c,VE,l}} = \frac{\mu^s}{\eta^{\text{lR}}} \frac{1}{a_{\text{sf}}}, \quad \omega_{\text{c,VE,g}} = \frac{\mu^s}{\eta^{\text{gR}}} \frac{1}{a_{\text{sf}}} \quad (7.8)$$

for S-wave stiffness (in the first diagonal element of \mathbf{C}^S). This result is in accordance with Eq. (7.1) from [39].

The important, new physical parameter is the characteristic frequency $\omega_{\text{c,VE,f}}$. It develops directly from the ratio of solid elasticity to fluid viscosity. Therein, the geometric parameter a_{sf} contains both characteristic lengths, cf. Eq. (7.3). The first one, $l_{\text{stiff}}^{m_{\text{sf}}}$, represents the geometric influence on the stiff pore elasticity (the larger l_{stiff} the weaker the pore). The second one, $l_{\text{compl}}^{m_{\text{sf}}}$, represents classical permeability and is comparable to the squared radius for a straight tube. In conclusion, the dimensionless expression $\omega/\omega_{\text{c,VE,f}}$ represents the ratio of viscous drag forces of compliant pores with respect to elastic forces of the stiff pores.

Another interpretation can be done with respect to characteristic time scales. If $\omega/\omega_{\text{c,VE,f}} \ll 1$, stiffness of the mesoscopic pore, $\tilde{K}^s/l_{\text{stiff}}^{m_{\text{sf}}}$, is high enough to follow the deformation immediately. As soon as $\omega \rightarrow \omega_{\text{c,VE,f}}$, the relaxation time of the mesoscopic pore increases, due to the delaying effect of viscous damping inside of them. This results in a viscoelastic behavior of the system.

Also note the fundamental difference to Biot's damping mechanism, where fluid viscosity is of reciprocal influence on the characteristic frequency, cf. Eq. (5.34) vs. Eq. (7.1).

7.4.2 Example

A simple example of residually saturated sandstone was calculated with mesoscopic inclusions. The following approximations have been implemented for both fluids $\text{f} \in \{\text{l}, \text{g}\}$:

$$n^{\text{sf}} = 0.7, \quad (7.9)$$

$$a_{\text{sf}} = 10^{-10}, \quad (7.10)$$

$$c_{\text{sf,f}}(\omega) = \frac{1}{1 + \left(5 \frac{\omega}{\omega_{\text{c,VE,f}}} \right)^{3/2}}. \quad (7.11)$$

A sigmoid function has been used for $c_{\text{sf,f}}(\omega)$, because it induces a shift between two states with low complexity and can be adapted with little effort. In applications, the specific form of $c_{\text{sf,f}}(\omega)$ depends on the respective material and geometrical conditions as well as the origin of attenuation (squirt-flow, interlayer flow, leak-off, etc.).

The additional damping mechanism can be clearly seen in the plot of the inverse quality factor, cf. Fig. 7.5. It occurs at $\omega_{\text{c,VE,f}}$ for both fluid separately and shifts with it. Furthermore, local flow attenuation is many times higher than Biot-type damping, cf. Fig. 6.1 and Fig. 7.5.

Additionally, the phase velocity slightly increases due to the stiffening effect of the viscous inclusions. This deviation of Biot's prediction is not a conspicuous observation of experiments and may be less considerable in application, for example, because

the wave front is only partially influenced or because of the rough approximation of $c_{sf}(\omega)$. It should be further noted that the S-wave behaves similar to the P1-wave, whereas the slow P2- and P3-waves were practically not influenced in the investigated sample.

Finally, this simple example shows the basic influence and physical origin of mesoscopic loss. An accurate description requires more precise definitions of n^{sf} , a_{sf} , and $c_{sf,f}(\omega)$. Their forms depend on the respective physical system and origin of mesoscopic losses (squirt-flow, leak-off, patchy saturation, layered media, ...). In particular, the relationship between Q^{-1} and ω shows special characteristics for mesoscopic damping. Quintal et al. [171] obtained an increase of $Q^{-1} \propto \omega$ and a decrease of $Q^{-1} \propto 1/\sqrt{\omega}$ by numerical simulations of mesoscopic, patchy saturation, cf. the good agreement of the example provided in Fig. 7.5.

Exact modeling and prediction of mesoscopic processes remain an important topic of modern research. Comparison of experimental, numerical, and theoretical results will improve its prediction. A deeper understanding may even lead to a straight link between mesoscopic physics and macroscopic modeling of the fluid phase as it is the case for Biot-like interaction [25].

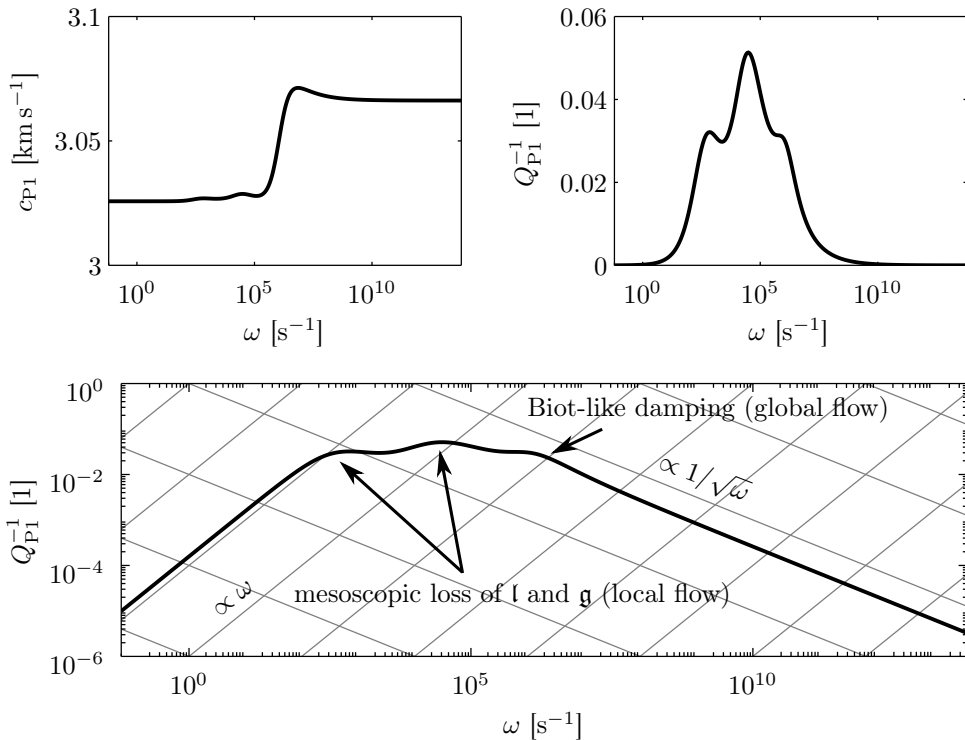


Figure 7.5: Dispersion relations of the P1-wave for mesoscopic loss in a partially saturated Nivelsteiner sandstone with local flow as described by Eq. (7.9) - Eq. (7.11). The upper right graph is a semi-logarithmic plot of the inverse quality factor, whereas the lower one is a double-logarithmic plot to illustrate the proportionality factor of $Q_{P1}^{-1}(\omega)$. Further note that the peak due to viscous, Biot-like damping is raised because of its superposition with the mesoscopic-loss contribution.

7.5 Double pore space

7.5.1 Introduction

The previously presented mechanisms were related to intrinsic or local flow. Their importance is based on a new mesoscopic process. Nevertheless, global (Biot-like) flow can also occur on more than one scale. A model with two pore spaces is used, for example, in [9, 20, 166, 167]. Each accounts for a separate length scale: the basic microscopic pore space and an additional mesoscopic pore space, cf. Fig. 7.1 (right). Following this idea, a porous medium can contain more than one characteristic (compliant) pore diameter. These diameters are not distinguished by their behavior (stiff/compliant) but only by their characteristic sizes.

7.5.2 Implementation

For a physical description, a double pore space material can, consequently, be modeled by two additional fluid phases. In this case, one distinguishes between a liquid and a gas phase in the microscopic pores and also in the mesoscopic pores. In addition to the increasing algebraic effort, difficulties arise in the description of the exchange of mass and momentum and determining/measuring the corresponding material parameters.

Nevertheless, the previous studies provide a detailed description of the behavior of the fluid phases for a single characteristic pore space as shown in Fig. 6.1 and Fig. 6.2: at low frequencies, the fluids are coupled to the solid by viscosity and a decoupling process starts at a characteristic frequency. If $\alpha_{id} \approx 1$, the fluids decouple completely with a phase lag of 90° and vanishing amplitude for the P1-wave contribution. Moreover, the gas phase's contribution to dispersion effects is often negligible because of its low density, viscosity, and elasticity.

Using these findings, one can easily approximate the decoupling process of a second mesoscopic pore space. Assuming that the previously developed model is valid in the entire domain, except for some additional mesoscopic pores, the hitherto used equations remain valid and do not need to be modified. Furthermore, it is assumed that only the liquid phase has a recognizable effect on the dispersion relations. Technically, the second pore space is included as an additional (viscoelastic) mass that contributes to the equations by interaction with the solid. Note that the previous equations do not change, except for the additional interaction terms via the solid phase.

The second pore space has a volume fraction of n^{DP} with partial density

$$\rho^{\text{DP}} = n^{\text{DP}} \rho^{\text{IR}} \quad (7.12)$$

and permeability $k^{s,\text{DP}}$. The ratio $n^{\text{DP}}/n^{\text{I}}$ can be interpreted as the volume ratio of liquid in the mesoscopic pore space with respect to liquid in the microscopic pore space. Because the mesoscale pore space is larger than the microscale pore space, form locking effects on this scale are neglected. The characteristic frequency of the mesoscale pore space is consistently defined with respect to Eq. (5.35) as

$$\omega_{c,\text{DP}} = \frac{n_0^{\text{DP}} \eta^{\text{IR}}}{k^{s,\text{DP}} \rho_0^{\text{IR}}}. \quad (7.13)$$

The decoupling process between the second pore space liquid and the solid can now be approximated by a logistic sigmoid function $\varphi^{\text{DP}}(\omega)$ as

$$\begin{aligned} \mathbf{u}_{\text{DP}} &= (1 - \varphi^{\text{DP}}(\omega)) \mathbf{u}_s \exp(i\varphi^{\text{DP}}(\omega)), \\ \varphi^{\text{DP}}(\omega) &= \frac{1}{1 + \exp\left[-c_\omega \log_{10}\left(\frac{\omega}{\omega_{c,\text{DP}}}\right)\right]}. \end{aligned} \quad (7.14)$$

The logistic function $\varphi^{\text{DP}}(\omega)$ increases from 0 to 1 with a transition at $\omega_{c,\text{DP}}$ and scaling c_ω in the logarithmic frequency range. Technically, the first diagonal elements of the matrices \mathbf{A} and \mathbf{B} , cf. Eq. (5.56), change as

$$A_{11}^{\text{DP}} = A_{11} + \rho_0^{\text{DP}} (1 - \varphi^{\text{DP}}(\omega)) \exp(i\varphi^{\text{DP}}(\omega))$$

and

$$B_{11}^{\text{DP}} = B_{11} + c_{\text{JKD}} \left(\frac{\omega}{\omega_{c,\text{DP}}}\right) \frac{n^{\text{DP}2} \eta^{\text{IR}}}{k^{s,\text{DP}}} [1 - (1 - \varphi^{\text{DP}}(\omega)) \exp(i\varphi^{\text{DP}}(\omega))]$$

based on the relative velocity of the second pore space liquid and the solid phase.¹⁶

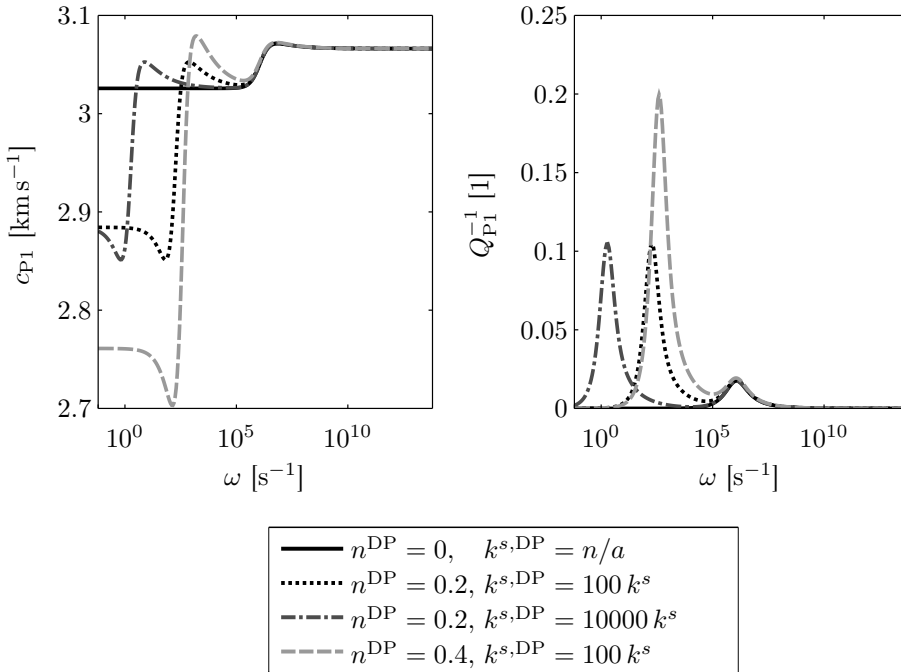


Figure 7.6: Dispersion relations of the P1-wave for different variations of volume content n^{DP} and permeability $k^{s,\text{DP}}$ of a double porosity medium with $c_\omega = 5$.

This approximation of a double porosity medium adds an additional transition zone in the frequency range with a Biot-like attenuation, Fig. 7.6. Its effects coincide with the behavior of the single porosity model. The higher permeability of larger pores

¹⁶The denominators of the low-frequency limits Eq. (6.1) and Eq. (6.2) increase by the term ρ^{DP} .

at the mesoscale cause a decoupling process at lower frequencies. Furthermore, the peak of the Q^{-1} -factor increases with growing mass of the decoupling liquid, i.e. with increasing ρ_0^{DP} or n_0^{DP} respectively. Because of the larger mesoscopic pore space, more liquid contributes to the mesoscopic losses and dominates over microscopic dispersion in the investigated sample.

The presented implementation is a first approach that illustrates the meaning of two characteristic pore spaces. With this approach, further complexity such as pore size distributions can be established by superposition of Eq. (7.13) and Eq. (7.14). Additionally, the so-called open porosity, i.e. the connected pore space, can be distinguished from the so-called closed (or ineffective) porosity, i.e. separate pores that are not connected to the main pore space and do not contribute to global flow.

7.6 Further mesoscopic losses

It should be first noted that the described physical processes are not only important for a macroscopic wave theory. They are also of great interest on their own length scale as distinct phenomena. For example, pumping tests [214] or shock-induced borehole waves [64] are closely related to attenuation mechanisms, which are commonly described by local/wave-induced fluid flow.

Finally, the pictured mesoscopic losses are a selected overview of possible mechanisms, which can occur in addition to the microscale processes. Generally, these mechanisms are not a specific research goal of partially saturated systems but common to wave propagation in all systems of fluid-filled porous media. This overview does not and cannot claim to be comprehensive, but provides first insights into the behavior of the presented model in combination with added mesoscopic phenomena. Based on the flexibility of the model, the examples demonstrated how mesoscopic effects can be linked to it, physically and mathematically. With the help of this model and considering the need for differentiation between specific mesoscopic losses, future research on mesoscopic studies can be applied to partially saturated media.

Chapter 8

Review

8.1 Summary and main findings

A mathematical model was derived to describe wave propagation in partially saturated porous media. First, physical relationships were presented and explained. In a second step, these were combined to achieve a set of equations related to displacements and their time and spatial derivatives. Application of a harmonic approach yielded an eigenvalue formulation, Eq. (5.56), which is the central result of the mathematical model. It determines the frequency-dependent wave number. Dispersion relations, especially phase velocities and quality factors, were then derived. Selected examples illustrated basic and more sophisticated results. The main findings for the investigated samples are:

- Four waves can be distinguished: three longitudinal (P-)waves and one shear (S-)wave. The second and third longitudinal wave are related to relative motion and are highly dispersive at low frequencies.
- Three frequency regimes can be distinguished: a viscosity-dominated low-frequency range, a transition range, and an inertia-dominated high-frequency range.
- The hybrid model, i.e. use of the rigid-grain assumption, reduces the complexity of the mathematical structure and the need for material parameters. This assumption is justified if at least one fluid is a gas at ambient conditions.
- Oscillatory motion requires two modifications, compared to steady flow:
 - frequency-dependent momentum exchange (caused by changes of the flow profile)
 - additional mesoscopic interaction for many natural materials (caused by oscillatory, elastic expansion of the mesoscopic pore space)
- Interfacial fluid-fluid areas influence the transition frequency of the P1-wave by their effects on the relative permeability and the P3-wave through their influence on capillary effects.

Scattering limits the validity of the model. Moreover, mesoscopic losses may appear for natural materials. Squirr-flow was added to the basic Biot-like approach on the basis of mesoscopic, stiff pore space. Furthermore, a double pore space was implemented phenomenologically with an additional Biot-like behavior.

8.2 Conclusions and outlook

The proposed concept allows a comprehensive study of wave propagation in partially saturated porous media. It shares a common basis with other Biot-like models such as [132, 219]. Compared to existing theories, the use of the hybrid model reduces the complexity and eliminates the need for an additional material parameter. This eases application to many systems that include air or another gas with low compressibility. Additionally, emphasis is placed on the straightforward implementation of available constitutive relationships. On the one hand, general theoretical frameworks have been available for decades and often prescribe forms of constitutive/closing equations on physical grounds [86]. Consequently, they form the theoretical basis of the current framework. On the other hand, experimental data or numerical results are often developed in alternative forms or described by a deviating set of parameters. Another advantage of this approach is its compatibility with such alternative forms. For example, constitutive equations can be implemented in arbitrary terms (saturation rate, gradient of velocity, ...) without modification. This enables direct testing of possible effects such as dynamic capillary pressure, interfacial areas, or viscoelastic solids. This flexibility is achieved by (and obtained at the cost of) the comprehensive linearization process, which eases substitution and backtracking of the physical origins. For example, the influence of capillary pressure or solid stiffness is clearly recognizable in the stiffness matrices. For this reason, special attention is paid to an intelligible derivation of the final equation.

The required compromise between generality and applicability resulted in certain assumptions. Thus, the model is limited to a homogeneous initial state, isotropic conditions, massless interfaces and contact curves, and to negligible temperature effects. Furthermore, macroscopic fluid shearing was neglected. By default, it also loses validity if wavelengths are close to the characteristic length of the microstructure.

Another challenge that is common to all theories for wave propagation in porous media is a lack of experimental data. Some effects appear at higher frequencies and could not yet be verified finally or estimated quantitatively. Hence, their observable impact on wave propagation remains to be quantified or in other words following G. Berkeley's work from 1710: "their esse is percipi" [70, 159].

As one result, the presented approach focuses on individual phenomena separately. The possibility of isolated implementation will allow a precise comparison with future data. Moreover, its predictions can sharpen the focus of corresponding studies.

Although various aspects of wave propagation in porous media could be investigated, various interesting extensions remain. In the short-term perspective, extensions of significant scientific value include:

- quantitative implementation of frequency-dependent inertial drag (or tortuosity parameter)
- material parameters for different confining pressure, cf. [44]
- anisotropy due to gravity and anisotropic materials [4, 36, 123]
- stiffening of granular media due to capillary effects
- other wave forms as well as transmission and reflection coefficients at partially saturated boundaries

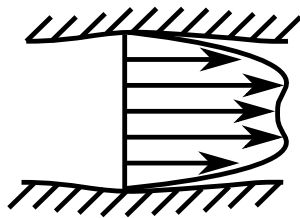
Other interesting aspects, which require more significant extensions are, in a long-term perspective:

- electromagnetic coupling [74, 163, 184]
- thermal influences
- non-linear effects [151]
- micropolar waves [62, 189]
- losses due to solid-solid interaction in loose, granular media such as grain-grain friction

In conclusion, fundamental properties could be explained physically and interesting extensions were presented. The developed model will hopefully complement existing research and motivate further efforts. The findings are promising and show how individual physical phenomena can be characterized by properties of mechanical waves. They emphasize the meaning of waves for non-destructive analysis and support their application to partially saturated porous media. Further interesting applications and information follow in the next parts.

Part II

Microscopic pore channel oscillations



Chapter 9

Introduction

9.1 Motivation

Macroscopic wave propagation was comprehensively studied in the preceding sections. The view will now turn to microscopic processes inside the pore channels.

Often, microscale processes are investigated first and understood in more detail. On these grounds, macroscale theories are developed and supported by smaller scale explanations (and vice versa). A historical example of such a two-scale research is the kinetic gas theory. It relates definitions of pressure or temperature to smaller scale particle motion and energy. This point of view supported the interpretation and sustainable understanding of the physical processes in a gas.

In a comparable way, two-scale approaches can be applied to porous media as explained for TPM and AT in Section 2.1. In computational modeling, for example, fluid-filled, porous media were successfully approximated by pore network models [102]. Because a pore channel represents the basic element of a porous medium, fluid flow in microscopic pore channels will be studied in the following chapters.

9.2 Aims and structure

The aim is to point out the significant effects of microscopic pore channel flow for wave propagation phenomena in porous media. This is done in terms of well-established methods and recent research findings. For convenience, the system of investigation is a biphasic medium composed of a porous solid material, cf. Fig. 9.1 and Fig. 9.2, and a single pore fluid. The findings remain valid for mixtures of two continuous fluids in a porous solid¹⁷.

The structure is threefold. Thus, each chapter is self-contained and deals with a separate aspect of oscillatory pore flow and its influence on the macroscale.

¹⁷The special case of pore channels with strong fluid-fluid interface effects is studied in Part IV.

- The following chapter introduces the frequency-dependent flow profile in a rigid tube on the basis of a dimensional analysis. Additionally, it reviews the results of Biot [25] and Womersley [226, 227].
- The chapter thereafter discusses the appropriate use of a characteristic frequency for macroscopic wave propagation, as introduced by Biot [25]. Its microscopic origin is explained and its macroscopic definition is enhanced by considering solid elasticity, solid inertia, and full-range upscaling.
- The last chapter of Part II deals with the elasticity of microscopic walls. The model of Bernabé [18] is presented and compared with experimental results [202].

Parts of the following chapters were previously presented in [114] (especially Chapter 11) and in [112] (especially Chapter 10 and Chapter 12).

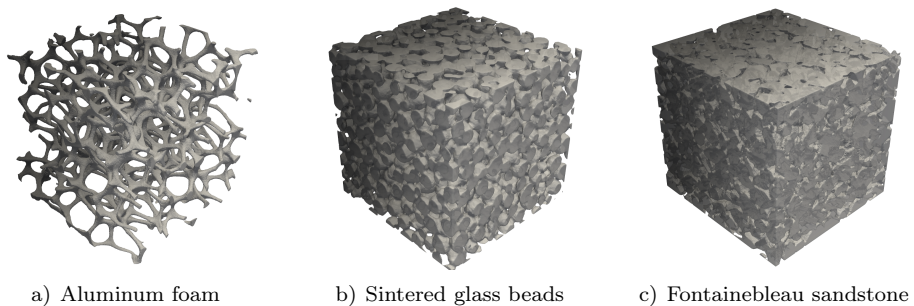


Figure 9.1: Microstructure of natural and artificial materials. The edge lengths are 18 mm (aluminum foam, glass beads) and 2.25 mm (Fontainebleau sandstone) respectively. A detailed investigation of waves in aluminum-foam can be found in [212].

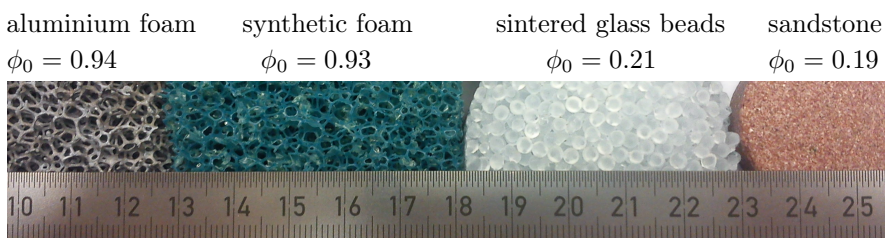


Figure 9.2: Pores of different porous materials compared to a cm-scale with indication of porosity.

Chapter 10

Oscillatory flow in a rigid tube

A rigid tube is one of the simplest representations of a pore channel in solid matrices. Furthermore, it provides insights into many important physical phenomena on the microscale. Therefore, the microscale study begins with the basis element of oscillatory flow in a rigid tube.

Based on a dimensional analysis, the results of Biot and Womersley are retraced [25, 226]. The fundamental impact on macroscopic momentum exchange, as founded by the seminal work of Biot [25], is recapitulated and leads to the following chapters.

10.1 Dimensional analysis

Based on the Navier-Stokes equations, momentum conservation of a Newtonian fluid \mathbf{f} reads, in terms of microscopic variables,

$$\rho^{\text{fR}} \frac{\partial v_{\text{f},i}}{\partial t} + \rho^{\text{fR}} v_{\text{f},j} \frac{\partial v_{\text{f},i}}{\partial x_j} + \frac{\partial p^{\text{fR}}}{\partial x_i} - \eta^{\text{fR}} \frac{\partial}{\partial x_j} \left(\frac{\partial v_{\text{f},i}}{\partial x_j} + \frac{\partial v_{\text{f},j}}{\partial x_i} - \frac{2}{3} \frac{\partial v_{\text{f},k}}{\partial x_k} \delta_{ij} \right) - \rho^{\text{fR}} f_i = 0. \quad (10.1)$$

For convenience and because this part is separated from the macroscopic theory, no special identification marks are used to distinguish these microscopic properties from the macroscopic counterparts. Furthermore, the index notation is preferred to symbolic notation in this section, because it allows a focused comparison between the physical and geometrical properties of individual terms and a clear dimensional analysis. The lower indices i, j , and $k \in \{1, 2, 3\}$ describe components with respect to a three-dimensional, orthonormal spatial basis and the (Einstein's) summation convention for index variables appearing twice is implied in this chapter.

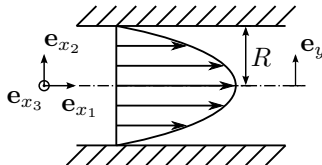


Figure 10.1: Parabolic velocity profile of Hagen-Poiseuille flow in a rigid tube. The x_i -coordinates belong to the initial orthonormal system, whereas the y -coordinate represents a general radial direction for later use of radial symmetry.

To achieve a dimensionless form of momentum conservation, the following characteristic properties are introduced:

characteristic time	\tilde{t}
characteristic velocity	\tilde{v}
characteristic length	\tilde{l}
characteristic fluid density	$\tilde{\rho}^{fR} = \rho_0^{fR}$
characteristic viscosity	$\tilde{\eta}^{fR} = \eta_0^{fR}$
characteristic volume force	$\tilde{f} = g$
characteristic pressure difference	$\Delta\tilde{p}$
reference pressure	p_0

Table 10.1: Characteristic properties of oscillatory tube flow.

Characteristic material properties are set to the initial values. Only one characteristic velocity and one characteristic length appear, because the flow is uni-axial and the geometry is fully determined by the constant tube radius R .

Dimensionless variables are defined as $\bullet := \bullet/\tilde{\bullet}$, while pressure is made dimensionless with respect to the reference pressure as $\Delta\bar{p} = (p - p_0)/\Delta\tilde{p}$. Dynamic viscosity η^f is often assumed to be constant if temperature and pressure changes are limited, so that $\tilde{\eta}^{fR} \approx 1$. A possible dimensionless variant of momentum conservation becomes

$$0 = \text{Sr} \tilde{\rho}^{fR} \frac{\partial \bar{v}_{f,i}}{\partial \bar{t}} + \tilde{\rho}^{fR} \bar{v}_{f,j} \frac{\partial \bar{v}_{f,i}}{\partial \bar{x}_j} + \text{Eu} \frac{\partial \Delta\bar{p}}{\partial \bar{x}_i} - \frac{1}{\text{Re}} \tilde{\eta}^{fR} \frac{\partial}{\partial \bar{x}_j} \left(\frac{\partial \bar{v}_{f,i}}{\partial \bar{x}_j} + \frac{\partial \bar{v}_{f,j}}{\partial \bar{x}_i} - \frac{2}{3} \frac{\partial \bar{v}_{f,k}}{\partial \bar{x}_k} \delta_{ij} \right) - \frac{1}{\text{Fr}^2} \tilde{\rho}^{fR} \bar{f}_i. \quad (10.2)$$

The dimensionless numbers are

$$\text{Strouhal number} \quad \text{Sr} = \frac{\tilde{l}}{\tilde{v} \tilde{t}}, \quad (10.3a)$$

$$\text{Euler number} \quad \text{Eu} = \frac{\Delta\tilde{p}}{\rho_0 \tilde{l}^2}, \quad (10.3b)$$

$$\text{Reynolds number} \quad \text{Re} = \frac{\rho_0 \tilde{v} \tilde{l}}{\eta_0}, \quad (10.3c)$$

$$\text{and Froude number} \quad \text{Fr} = \frac{\tilde{v}}{\sqrt{g \tilde{l}}}. \quad (10.3d)$$

For an uni-axial flow through a rigid tube, the flow direction ($x_i = x_1$ in Fig. 10.1) and the velocity gradient are perpendicular. Hence, the convective term of Eq. (10.2) vanishes as well as the second part of the viscous stresses¹⁸. For convenience, the last term of the viscous stresses is negligible if incompressibility is assumed or if the

¹⁸Note that this assumption of parallel streamlines fails when turbulence occurs. In this case, velocity perturbations occur on smaller scales, which are perpendicular to the main flow axis. This is usually the case for large Reynolds numbers ($\text{Re} \geq 2300$ is often used as an approximation for fully turbulent flows in tubes) and has to be accounted for by an additional term modeling turbulence. In the present study of linear oscillations, the appearing velocities are assumed to be arbitrarily small. However, turbulence effects may need to be considered in practical experiments.

axial dimension can be neglected (for example, if the flow does not change in axial direction, which is the case for axial tubes waves with sufficiently long wave lengths). The simplified, dimensionless momentum conservation becomes

$$\frac{1}{\text{Re}} \left[\text{Sr Re } \bar{\rho}^{\text{fR}} \frac{\partial \bar{v}_{\text{f},i}}{\partial \tilde{t}} - \bar{\eta}^{\text{fR}} \frac{\partial^2}{\partial \bar{x}_j^2} \bar{v}_{\text{f},i} \right] = \frac{1}{\text{Fr}^2} \bar{\rho}^{\text{fR}} \bar{g}_i - \text{Eu} \frac{\partial \Delta \bar{p}}{\partial \bar{x}_i}. \quad (10.4)$$

The right side of Eq. (10.4) includes the pressure gradient and volume forces. They act as an external stimulation inducing a fluid flow. The development of the velocity profile is determined by the left side of Eq. (10.4), namely the local inertia term and viscous stress. Weighting of the latter is represented by the dimensionless number

$$\text{Sr Re} = \frac{\tilde{l}^2 \rho_0^{\text{fR}}}{\tilde{t} \eta_0^{\text{fR}}}. \quad (10.5)$$

In case of steady flow (characteristic time of change $\tilde{t} \rightarrow \infty$), the flow profile is only determined by viscous stresses. This is the so-called Hagen-Poiseuille flow, cf. Fig. 10.1. On the other hand, if the flow pattern does change in time, the inertia term becomes influential. For oscillating flows with angular frequency ω , the characteristic time can be chosen to be proportional to the period of oscillation as $\tilde{t} = 1/\omega$ and the characteristic length is the radius $\tilde{l} = R$. For oscillatory flows in a rigid tube, the previously introduced dimensionless number Eq. (10.5) becomes

$$\text{Sr Re} = \frac{R^2 \omega \rho_0^{\text{fR}}}{\eta_0^{\text{fR}}} = \frac{\omega}{\omega'_{\text{c,Biot}}} = \frac{f}{f'_{\text{c,Biot}}} = \text{Wo}^2 = 2 \left(\frac{R}{\delta_{\text{vs}}} \right)^2, \quad (10.6)$$

with the microscopic characteristic frequency (sometimes also called critical frequency)

$$\omega'_{\text{c,Biot}} = 2 \pi f'_{\text{c,Biot}} = \frac{\eta_0^{\text{fR}}}{\rho_0^{\text{fR}} R^2}. \quad (10.7)$$

The number in Eq. (10.6) was already used decades ago within the solutions of oscillatory flow in tubes. Womersley introduced it in his work on viscous flow in arteries [226, 227]. Since then, the number is often named the Womersley number, Wo .

Another fundamental treatment dealing with oscillatory flows is the work of Biot [24, 25]. In [25], Biot introduced a characteristic frequency, $f'_{\text{c,Biot}} = \omega'_{\text{c,Biot}}/(2\pi)$, cf. Eq. (10.7). Like the Womersley number, the ratio $\omega/\omega'_{\text{c,Biot}}$ represents the ratio of viscous effects to inertia effects. Note that Biot states another characteristic, microscopic frequency in his first work [24], which is based on a halfspace solution and differs from the given one above by a constant prefactor. Moreover, he developed a macroscopic, critical frequency in [25] via upscaling, which is discussed in the following chapter.

Another interpretation of the dimensionless number in Eq. (10.6) is the ratio of radius R to viscous skin depth δ_{vs} , i.e. the depth of the viscosity-dominated part of the flow. Furthermore, the dimensionless number appears explicitly or implicitly in many other works dealing with oscillatory flows, for example, in [10, 18].

The central result of this section is the dependence of the Navier-Stokes solution and the velocity profile on the dimensionless number in Eq. (10.6) (and its variations). It is now followed by a specific solution.

10.2 Biot's solution of a microscopic, oscillatory flow in a rigid tube

Biot [25] derived a solution for oscillating flow between two parallel plates and in a rigid tube. The solution for the rigid tube case is (Eq. (3.8) *ibid.*)

$$v_{\text{ax}} = \left[1 - \frac{J_0 \left(i \sqrt{i \omega \rho_0^{\text{fR}} / \eta^{\text{fR}}} y \right)}{J_0 \left(i \sqrt{i \omega / \omega'_{\text{c,Biot}}} \right)} \right] \frac{X_{\text{ex}}}{i \omega}.$$

The relative axial velocity between fluid and solid is v_{ax} , $y \in [0 \text{ m}, R]$ is the radial coordinate, X_{ex} summarizes external excitations due to a pressure gradient or a volume force, and J_0 is the Bessel function of first kind.

Investigation of the solution clearly demonstrates the dependence of the velocity profile on the Womersley number, cf. Fig. 10.2. For small Wo , i.e. $\omega \ll \omega'_{\text{c,Biot}}$, viscous forces dominate and the velocity profile is that of a Hagen-Poiseuille flow. For increasing Wo and $\omega \gg \omega'_{\text{c,Biot}}$, inertia terms become more influential and a central flat profile emerges. This flat part also lags behind the viscous layer near the wall. The meaning of the viscous skin depth δ_{vs} figuratively describes the spatial extent of the boundary layer that remains dominated by viscous forces rather than inertia forces. In conclusion, the Womersley number Wo , or the ratio of ω to $\omega'_{\text{c,Biot}}$ respectively, determine the pattern of the velocity profile in a tube.

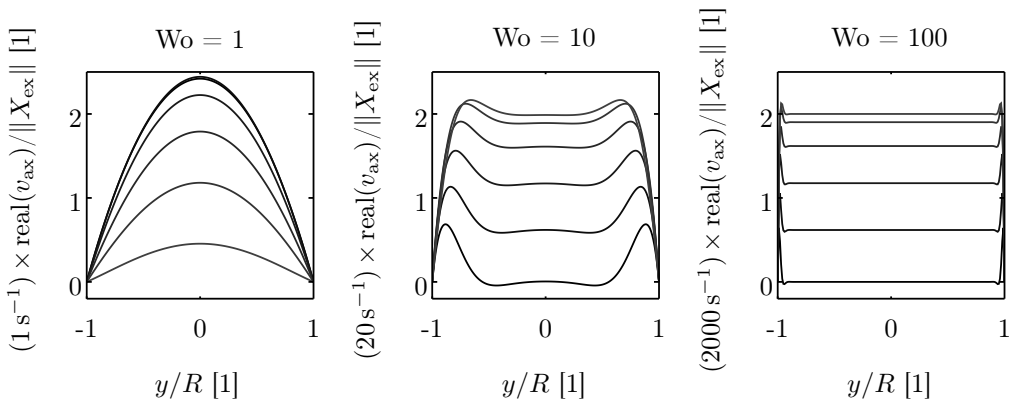


Figure 10.2: Oscillating velocity profile in a rigid tube according to Biot [25], Eq. (3.8) *ibid.*, for times $t = 2\pi/\omega \times \{0, 0.05, 0.10, 0.15, 0.20, 0.25\}$ (from top to bottom). X_{ex} is an external excitation due to a pressure gradient or volume force and v_{ax} is the axial relative velocity between fluid and solid according to [25]. The radial coordinate y is normalized with radius R . Also note the change in scale of the vertical axes.

10.3 Frequency dependence: from microscopic flow profiles to macroscopic momentum interaction

Influence on the macroscale

Because the flow profile depends on the ratio of frequency to characteristic frequency, this dependence appears likewise for the velocity gradient at the walls. The velocity gradient, in turn, determines the shear stress and momentum interaction between solid and fluid. In conclusion, momentum interaction is frequency dependent as well. This microscopic condition directly influences the macroscopic physics of momentum exchange. Namely, the classical Darcy-like approach of macroscopic momentum exchange between a porous solid and a fluid (cf. Eq. (5.29)) is based on a steady flow [43]. However, it does not account for frequency-dependent velocity profiles. Hence, a frequency correction of the Darcy-like approach is required to account for the case of oscillating flow.

... and Biot's solution

This circumstance has been investigated by Biot [25] in detail. As shown above, Biot determined the frequency-dependent velocity profile of a microscopic, oscillating flow. On this basis, he calculated the averaged momentum interaction induced by viscous wall stress over a unit wall surface. On the macroscale, he obtained a relationship between the averaged momentum interaction and the averaged, relative velocity. This was a first step to the required, new macroscopic equation. Nevertheless, it was still depending on the microscopic frequency ratio $\omega/\omega'_{c,\text{Biot}} = f/f'_{c,\text{Biot}}$ [25].

Furthermore, Biot introduced a macroscopic characteristic frequency via a dimensional analysis in his foregoing work [24], as defined in Eq. (5.34). This macroscopic characteristic frequency includes a porosity factor and replaces R^2 by the permeability, which are only macroscopic terms as desired. "The problem is, therefore, to compare $f'_{c,\text{Biot}}$ with f_c " [25]. Biot wanted to replace the microscopic characteristic frequency by the macroscopic one to formulate the momentum exchange entirely via macroscopic properties.

His idea was now to compare the known low-frequency case of microscopic and macroscopic momentum interaction. The former was known from Hagen-Poiseuille flow and the latter from Darcy's law. It resulted in a relationship between the microscopic and macroscopic characteristic frequency ($\omega'_{c,\text{Biot}}$ and $\omega_{c,\text{Biot}}$). Finally, he inserted that relationship to express the frequency-dependent momentum interaction in macroscopic terms only. Within Biot's work [25], the ratio $\omega/\omega_{c,\text{Biot}}$ became the key value for determination of the frequency-dependent momentum exchange between solid and fluid. For $\omega \ll \omega_{c,\text{Biot}}$, momentum exchange converges to the theory of Darcy.

Moreover, the correction of the classical Darcy law includes two geometry factors: sinuosity and pore shapes (slit-like, ducts, ...). They need to be considered for full precision in respective applications. A detailed discussion of the derivation process exceeds the scope of this work and the interested reader is referred to [25] and the next chapter. For the wave propagation model developed in Part I, an approximation based on [103] is used (cf. Eq. (5.36)). Its imaginary part represents the phase lag of the inertia-dominated center with respect to the viscous boundary layer.

The results of Biot's pioneering work were and still are of vital importance for wave propagation in porous media. Nevertheless, they come with assumptions and limitations, which are generalized in the following chapter.

Chapter 11

About the use of a characteristic frequency

One result of Biot's 1956 contributions is a characteristic frequency that is often used to distinguish the low-frequency from the high-frequency range [24, 25]. It represents the ratio of viscous forces to inertia forces of the fluid and is also directly applicable to multiple pore fluids. However, limiting assumptions were used during the derivation process. They rely on a focus on geomaterials and involve the transfer of microscale considerations to a macroscopic description.

Biot's microscopic derivation process is recapitulated and the assumptions made are indicated. With respect to the aim of a general approach in Part I, Biot's characteristic frequency is extended to general material combinations. The new characteristic frequency is consistently derived from a macroscopical approach and enhanced by three properties: solid inertia, solid elasticity, and frequency-dependent momentum exchange. These extensions become important for liquid-filled, highly porous media, as is highlighted by specific examples of aluminum foam and osteoporotic bone.

11.1 Characteristic and transition frequency

The previous section disclosed and explained the change of the fluid velocity profile in a pore channel for various frequencies. The characteristic microscopic frequency $\omega'_{c,\text{Biot}}$ indicates the regime between these two limits, i.e. the viscosity-dominated low-frequency limit ($\omega \ll \omega'_{c,\text{Biot}}$) and the inertia-dominated high-frequency limit ($\omega \gg \omega'_{c,\text{Biot}}$). Moreover, Biot introduced a macroscopic characteristic frequency

$$\omega_{c,\text{Biot}} = \frac{\eta^{\text{fR}} \phi^2}{\alpha_{\text{id}} \rho^{\text{f}} k^{\text{s}}} = \frac{\eta^{\text{fR}} \phi}{\alpha_{\text{id}} \rho^{\text{f}} k^{\text{s}}}. \quad (11.1)$$

It was also introduced in the macroscopic theory of Part I (Eq. (5.34)). The solutions of Part I further illustrate the transition between a low-frequency regime and a high-frequency regime, cf. Fig. 6.1. An angular frequency indicating this transition in the macroscopic wave model is henceforth defined as the transition frequency ω_{trans} .

It seems appropriate to use Biot's characteristic frequency as the transition frequency $\omega_{\text{trans}} \approx \omega_{c,\text{Biot}}$. This approximation is often used in geophysical investigations. In general, however, we will see that it is not advisable to equate or even mistake Biot's characteristic frequency $\omega_{c,\text{Biot}}$ (indicating the change of flow profile) and a transition frequency ω_{trans} (indicating the changing physical behavior of a macroscopic wave in a mixture). This is the key issue in this chapter.

11.2 Phenomenological motivation

Macroscopic transition with constant velocity profile

An initial fact that demonstrates that $\omega_{c,\text{Biot}}$ and ω_{trans} can be independent is the investigation of a wave propagation model in which the frequency dependence of the velocity profile is neglected. Let us assume a constant microscopic flow profile, for example, Hagen-Poiseuille flow, as in [24]. This corresponds to a frequency-independent momentum interaction term such as Eq. (5.29) for the model presented in Part I. In this case, i.e. even without use of $\omega_{c,\text{Biot}}$ in the macroscopic model, a transition occurs for the macroscopic model, including a low-frequency domain and a high-frequency domain comparable to Fig. 6.1. The low- and high-frequency limits are independent of $\omega_{c,\text{Biot}}$ [139]. Hence, the macroscopic transition ω_{trans} occurs independently of $\omega_{c,\text{Biot}}$.

Gedankenexperiment

Let us further expand the argumentation by a so-called Gedankenexperiment. First, assume a porous matrix that consists of parallel, fluid-filled, and almost rigid tubes. A wave travels in the axial direction, cf. Fig. 11.1a). At low frequencies, viscosity couples fluid and solid and both phases oscillate together. At high frequencies, the wave propagates much faster in the almost rigid, solid phase. Due to its inertia, the fluid phase decouples and oscillations within it propagate with the slower sound velocity of the fluid. This scenario is close to Biot's [25] microscopic investigations of oscillating flow and therefore $\omega_{c,\text{Biot}}$ is a good approximation for the transition frequency ω_{trans} .

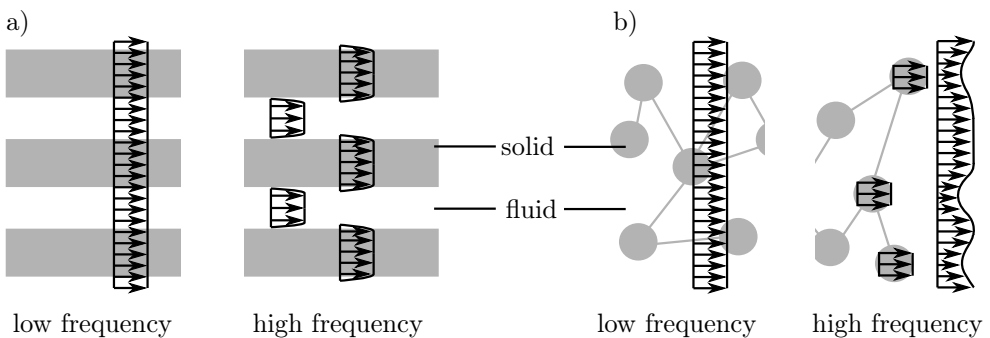


Figure 11.1: Velocity profiles for an idealized Gedankenexperiment: a) almost rigid solid matrix and b) weak solid matrix. Arrows indicate the displacement field.

Second, assume a porous matrix that consists of heavy, solid particles with high inertia and which are connected by thin, weak beams, cf. Fig. 11.1b). For oscillations at low frequencies, the pore fluid and the solid are coupled by viscosity, as in the example above. Now, however, the (macroscopic) solid's sound velocity is very low, due to the low elastic stiffness of the beam framework and the high inertia of the connected nodes. Thus, when both phases decouple at high frequencies, the fast wave travels through the fluid phase and a slower wave propagates in the solid matrix, cf. Fig. 11.1. Because the solid phase decouples from the fluid, the decoupling process is determined by the ratio of viscous forces to the solid's inertia forces. This is different from the above scenario, where the decoupling process is indicated by $\omega_{c,\text{Biot}}$, which relates viscous forces to fluid inertia, cf. numerator and denominator in Eq. (5.34). Thus, in this scenario, $\omega_{c,\text{Biot}}$ is not an appropriate indicator for the transition regime.

Limiting assumptions of Biot's characteristic frequency

Previous considerations have revealed two facts: First, the characteristic frequency of flow profile change, $\omega_{c,\text{Biot}}$, and the transition frequency of the macroscopic wave behavior, ω_{trans} , do not necessarily coincide. Second, $\omega_{c,\text{Biot}}$ is a good approximation for ω_{trans} if the implicit assumptions of Biot's investigations of microscopic oscillatory flow in [25] are valid; which are:

- rigid solid walls,
- an inert solid phase (or, equivalently, a focus on the relative fluid velocity),
- upscaling (comparison of microscopic and macroscopic characteristic frequency) for the low-frequency case.

Note that Biot's macroscopic theory includes inertia and elasticity of the solid phase. Only the microscopic investigation underlies the above assumptions, which hold well in many cases, including Biot's intentions for geophysical applications.

Two questions arise for the other situation, i.e. a solid matrix with significant compressibility and inertia such as synthetic foams or biological cells: (i) what is a good approximation for ω_{trans} ? (ii) how is the microscopic flow profile influenced, i.e. does $\omega_{c,\text{Biot}}$ remain a good indicator for the flow profile change for the case of elastic walls? The first question will be investigated in this chapter and the second question in the following one.

11.3 A general approach for the characteristic frequency

11.3.1 Recapitulation of Biot's framework

The following investigations are based on Biot's model for a biphasic mixture with solid \mathfrak{s} and fluid \mathfrak{f} . This allows an instructive comparison between the classical definition of Biot's characteristic frequency and the following extensions. Moreover, it is a special case of the model for three continuous phases in Part I. The results are therefore compatible and transferable to multiple pore fluids. In the current notation, Biot's model with the JKD-approximation, Eq. (5.36), reads in the form of an

eigenvalue formulation as [114, 196]:

$$\left(\omega^2 \mathbf{A}_{\text{Biot}} + i\omega \mathbf{B}_{\text{Biot}} + k^{\psi^2} \mathbf{C}_{\text{Biot}}^{\psi}\right) \begin{pmatrix} \hat{u}_s^{\psi} \\ \hat{u}_f^{\psi} \end{pmatrix} = \mathbf{0}, \quad \psi \in \{\text{P}, \text{S}\} \quad (11.2)$$

with

$$\mathbf{A}_{\text{Biot}} = \begin{pmatrix} \rho_0^s + (\alpha_{\text{id}} - 1)\rho_0^f & -(\alpha_{\text{id}} - 1)\rho_0^f \\ -(\alpha_{\text{id}} - 1)\rho_0^f & \alpha_{\text{id}}\rho_0^f \end{pmatrix}, \quad (11.3a)$$

$$\mathbf{B}_{\text{Biot}} = c_{\text{JKD}} \left(\frac{\omega}{\omega_{\text{c,Biot}}} \right) \frac{\phi_0^2 \eta^{\text{fR}}}{k^s} \begin{pmatrix} 1 & -1 \\ -1 & 1 \end{pmatrix}, \quad (11.3b)$$

$$\mathbf{C}_{\text{Biot}}^{\text{P}} = \begin{pmatrix} P_{\text{BW}} & S_{\text{BW}} \\ S_{\text{BW}} & R_{\text{BW}} \end{pmatrix}, \quad \mathbf{C}_{\text{Biot}}^{\text{S}} = \begin{pmatrix} \mu^s & 0 \\ 0 & 0 \end{pmatrix}. \quad (11.3c)$$

The mathematical structure of Eq. (11.2) is similar to the three-phase model, cf. Eq. (5.56). Because only one fluid fills the pores, two P-waves, P1 and P2, occur. This is in contrast to partial saturation, where a third P-wave is predicted due to compression of the second pore fluid. However, the P2- and the P3-wave are of similar characteristic behavior.

The elastic coefficients P_{BW} , S_{BW} , and R_{BW} are the so-called Biot-Willis parameters [114, 196]

$$\begin{aligned} P_{\text{BW}} &= K^s + \frac{4}{3}\mu^s + \frac{K^{\text{f}}}{\phi_0^{\text{R}}} \left(1 - \phi_0 + \frac{K^s}{K^{\text{grains}}} \right)^2, \\ S_{\text{BW}} &= \frac{K^{\text{f}}}{\phi_0^{\text{R}}} \left(1 - \phi_0 + \frac{K^s}{K^{\text{grains}}} \right), \\ R_{\text{BW}} &= \frac{K^{\text{f}}}{\phi_0^{\text{R}}} \phi_0^2, \end{aligned} \quad (11.4)$$

with effective porosity that equals porosity for rigid grains,

$$\phi_0^{\text{R}} = \phi_0 + \frac{K^s}{K^{\text{grains}}} \left(1 - \phi_0 - \frac{K^{\text{f}}}{K^s} \right). \quad (11.5)$$

11.3.2 Generalized, characteristic frequencies for the transition regime

The task, now, is to find an appropriate frequency that indicates the macroscopic transition zone between the viscous-dominated low-frequency regime and the inertia-dominated high-frequency regime. As yet, there is no unique definition of such a frequency. The smoothness of the transition makes a sharp definition even more difficult. As a result from the detailed investigation in Part I, it is known that the inverse quality factor Q^{-1} changes according to the physical phenomena of the low- and high-frequency regime, cf. Fig. 6.1. Moreover, the inverse quality factor is a measurable quantity, which is comparable with experiments and other theories. Hence, it will be used here to define a generalized, characteristic frequency indicating the transition regime.

In the case of the P1- and S-wave, the transition frequency is defined as the frequency where the inverse quality factor reaches its unique peak. Before this peak, all constituents move in phase so that viscous damping does not occur and $Q_{\text{P1,S}}^{-1}$ vanishes,

cf. Fig. 6.1. Behind the peak, inertia energy dominates over viscous damping so that the inverse quality factors of the P1- and S-wave vanish again. The P2-wave is a diffusive, damped mode at low frequencies and develops at higher ones. With increasing frequency, the corresponding inverse quality factor drops from its highest value to zero. Thus, the characteristic transition frequency of the P2-wave is defined as the unique frequency at which Q_{P2}^{-1} reaches its half value.

$$\omega_{\text{trans,P1}} = \{\omega \in \mathbb{R}_+ : Q_{P1}^{-1}(\omega) > Q_{P1}^{-1}(\hat{\omega}) \quad \forall \hat{\omega} \in \mathbb{R}_+\}, \quad (11.6a)$$

$$\omega_{\text{trans,S}} = \{\omega \in \mathbb{R}_+ : Q_S^{-1}(\omega) > Q_S^{-1}(\hat{\omega}) \quad \forall \hat{\omega} \in \mathbb{R}_+\}, \quad (11.6b)$$

$$\omega_{\text{trans,P2}} = \{\omega \in \mathbb{R}_+ : Q_{P2}^{-1}(\omega) = 0.5 Q_{P2}^{-1}(0)\}. \quad (11.6c)$$

These three frequencies shall now be described by macroscopic properties of the system. For this purpose, the inverse quality factor and its derivatives were analytically determined. For details please refer to Appendix C. However, the complexity of the mathematical structure increases due to the correction function of the velocity profile $c_{\text{JKD}}(\omega/\omega_{\text{c,Biot}})$. Therefore, three approximations of the frequency correction function are used and denoted by indices I, II, and III:

I low frequency limit: $c_{\text{JKD}}(\omega/\omega_{\text{c,Biot}}) \approx 1$,

II $c_{\text{JKD}}(\omega/\omega_{\text{c,Biot}})$ approximated by its linearization around $\omega_{\text{c,Biot}}$:

$$c_{\text{JKD}}(\omega/\omega_{\text{c,Biot}}) \approx \left[1.029 + 0.0543 \frac{\omega}{\omega_{\text{c,Biot}}} \right] + \left[0.243 + 0.230 \frac{\omega}{\omega_{\text{c,Biot}}} \right] i ,$$

III high frequency limit: $c_{\text{JKD}}(\omega/\omega_{\text{c,Biot}}) \approx \frac{1+i}{2} \sqrt{\omega/\omega_{\text{c,Biot}}}$.

For the same reason of high mathematical complexity, two typical material combinations A and B are distinguished in the analysis of P-waves:

A stiff solid skeleton, P_{BW} dominates stiffness matrix,

B weak solid skeleton, R_{BW} dominates stiffness matrix.

The elastic coefficient S_{BW} represents the coupling between both phases and is assumed to be small compared to P_{BW} and R_{BW} .

The following transition frequencies, now, are exact solutions or approximations of the analytically defined transition frequencies Eq. (11.6a) - Eq. (11.6c) for different cases I - III in combination with A and B.

S-wave

First, we focus on the exact, analytical solution of the S-wave neglecting the correction of the velocity profile. The corresponding transition frequency is

$$\omega_{\text{S,I}} = \omega_{\text{c,Biot}} \sqrt{\frac{1 + \frac{\rho_0^f}{\rho_0^s}}{1 + \frac{\rho_0^f}{\rho_0^s} \left(1 - \frac{1}{\alpha_{\text{id}}}\right)}}. \quad (11.7)$$

This solution underlines that there is a macroscopic transition also without a change of the pore channel flow profile. Furthermore, it clearly demonstrates that inertia of the solid influences the macroscopic transition. Only for a solid at rest, i.e. infinite

solid inertia $\rho_0^s \rightarrow \infty$, one exactly obtains Biot's characteristic frequency $\omega_{c,\text{Biot}}$.

Adding the physics of a frequency-dependent, microscopic velocity profile and knowing that the transition frequency is near $\omega_{c,\text{Biot}}$, yields a further, yet approximated, characteristic frequency

$$\omega_{\text{S,II}} = \omega_{\text{S,I}} \sqrt{\frac{1.118}{1 + 0.230 \frac{2\alpha_{\text{id}}(\rho_0^s + \rho_0^f) - \rho_0^f}{\rho_0^s + \rho_0^f} \left(\frac{\omega_{\text{S,I}}}{\omega_{c,\text{Biot}}}\right)^2}}. \quad (11.8)$$

Compared to Biot's initial approach [25], this further correction term becomes necessary considering the frequency-dependent momentum interaction. Biot's upscaling process was formulated for low frequencies and neglected frequency dependence.

P1-wave

For characteristic frequencies of the longitudinal waves, the mathematical complexity increases even more because, unlike for the case of S-waves, the fluid compressibility cannot be neglected. In the case of a solid skeleton that is much stiffer than the fluid phase, the P1-wave behaves similar to the S-wave. Hence, a corresponding characteristic frequency for the P1-wave is

$$\omega_{\text{P1,A,II}} \approx \omega_{\text{S,II}}. \quad (11.9)$$

This fact can be seen mathematically as the first diagonal entry of the P1-stiffness matrix, namely P_{BW} , dominates the total matrix giving it the same form as the S-stiffness matrix.

In the case of a solid skeleton that is weaker than the fluid phase, solid and fluid phase can change their roles. The sound velocity of the fluid is higher than that of the solid, which is then connected to the slow wave. Therefore, it is obvious to introduce a characteristic frequency which relates viscous forces to solid's inertia as

$$\omega^* = \frac{\eta^{\text{IR}} \phi_0^2}{(\rho_0^s + (\alpha_{\text{id}} - 1)\rho_0^f)k^s}. \quad (11.10)$$

Eq. (11.10) is the counterpart to Biot's characteristic frequency for a material combination with a weak solid matrix and can be derived consistently by a dimensional analysis from the diagonal entries of the damping and inertia matrices. Exchanging the influence of solid and fluid analogously to the solution of case A (stiff solid skeleton), yields two characteristic frequencies with and without frequency-dependent momentum interaction

$$\omega_{\text{P1,B,I}} = \omega^* \sqrt{\left(\frac{\rho_0^s}{\rho_0^f} + 1\right) \frac{\frac{\rho_0^s}{\rho_0^f} + \alpha_{\text{id}} - 1}{\alpha_{\text{id}} \frac{\rho_0^s}{\rho_0^f} + \alpha_{\text{id}} - 1}}, \quad (11.11)$$

$$\omega_{\text{P1,B,III}} = \omega_{\text{P1,B,I}} \frac{1}{\sqrt{2}} \frac{\omega_{\text{P1,B,I}}}{\omega_{c,\text{Biot}}} c_{\text{imp}} \left(1 + \frac{R_{\text{BW}}}{P_{\text{BW}}} \frac{\omega_{c,\text{Biot}}}{\omega^*}\right). \quad (11.12)$$

The correction factor c_{imp} accounts for the impedance contrast of both constituents. For example, a solid skeleton can be highly compressible and still have a high sound velocity, due to a low partial density. For the sake of simplicity, the correction factor c_{imp} is assumed to be 1 in the example calculations. A precise analytical solution exceeds the scope of this work but its appearance demonstrates the complexity of the system and the need for adapted characteristic frequencies for various material combinations.

P2-wave

The P2-wave (and P3-wave) is connected to the relative movement of solid and fluid, cf. Fig. 6.1. The approximated analytical solutions

$$\omega_{P2,A,II} = 0.441\omega_{c,Biot}, \quad \omega_{P2,B,II} = \frac{0.529}{1 + 0.190\frac{\omega^*}{\omega_{c,Biot}}}\omega^* \quad (11.13)$$

do not differ significantly from Biot's characteristic frequency and the latter usually remains a good approximation for the transition zone of the P2-wave. The reason for this close match is that the P2-wave is a relative movement as it was assumed for Biot's microscale study [25]. Moreover, it differs from the formulas for the P1- and S-waves and demonstrates that transition frequencies do not only differ for varying material combinations but may also be different for each wave mode.

In conclusion, it has been shown that Biot's characteristic frequency $\omega_{c,Biot}$ needs to be extended for a weakly compressible solid matrix. All three assumptions in [25], a rigid solid, an inert solid, and the low-frequency momentum interaction showed up in the difference between the analytical solutions and $\omega_{c,Biot}$. A second, easy to use characteristic frequency ω^* , Eq. (11.10), can be used as a basic approximation for the case of a weak solid and as a counterpart to Biot's characteristic frequency. For a more precise, practical estimation of the low- or high-frequency range, the analytical approximations provided or a (computationally very cheap) numerical determination of the dispersion relations are suggested. These results are validated in the examples below.

11.4 Examples

11.4.1 Biot's characteristic and transition frequency for different material combinations

The ratio of Biot's characteristic frequency $\omega_{c,Biot}$ to the transition frequencies, as defined in Eq. (11.6a) - Eq. (11.6c), was determined for a variety of different materials. The behavior of the S-wave demonstrates a significant influence of the solid's inertia on the transition frequency for highly porous materials with liquids, cf. Fig. 11.2. Materials such as aluminum foam and osteoporotic bone are predominantly affected. The difference between the P2 transition frequency and Biot's characteristic frequency is also more pronounced for the case of liquid-filled, highly porous media. Deviations for both wave modes, S- and P2-waves, reached 60% within the examples investigated. The impact of the correction function for frequency-dependent flow profile occurs systematically in all cases but is usually less influential compared to solid elasticity for the considered material combinations. Moreover, different wave modes of the same physical system demonstrably belong to different transition frequencies.

The most important effect occurs for the P1-wave, which depends strictly on the stiffness of the solid and the fluid, cf. the Δ -term in Appendix C. For the combinations of high porosity and a relatively weak solid skeleton, i.e. aluminum foam and water or osteoporotic bone and bovine marrow, $\omega_{c,Biot}$ and the transition frequency differ by more than one order of magnitude. Thus, $\omega_{c,Biot}$ is not an appropriate indicator for distinguishing between the low- and the high-frequency regime in these cases. The following investigation of aluminum foam and water shows that the newly introduced characteristic frequency ω^* is more suitable.

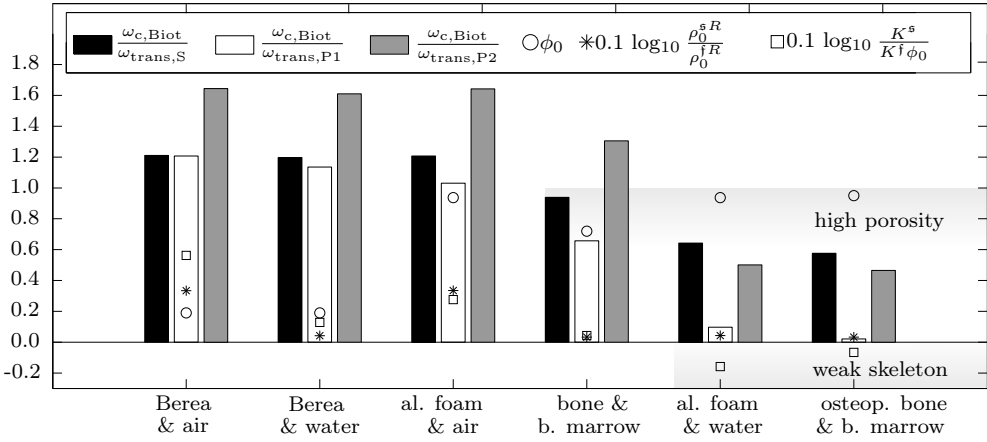


Figure 11.2: Biot's characteristic frequency over the transition frequencies as defined in Eq. (11.6a) - Eq. (11.6c) and according to [114]. The markers indicate porosity, solid-fluid density ratio, and solid-fluid stiffness ratio.

11.4.2 Aluminum foam and water

In contrast to rocks or sand in geophysical and geomechanical studies, highly porous materials, such as metal foams and bones, are more common in mechanical engineering or biomechanics. The combination of aluminum foam and water is an important example for a weak solid skeleton compared to the stiffness of the pore fluid.

Interestingly, aluminum foam and water have individual sound velocities of the same order. This similarity is reflected in the similar displacements of oscillations for the P1-wave, Fig. 11.3. No phase dominates over the other one considerably. Furthermore, the P2-wave shows that its relative movement is linked to the solid phase (of slightly lower sound velocity), which has the role of the slower, decoupling phase. These facts emphasise the special role of the chosen combination in contrast to classical rock-liquid or rock-gas combinations, where the sound velocity of the fluid is well under that of the solid matrix.

Biot's characteristic frequency $\omega_{c,Biot} = 3.35 \text{ rad s}^{-1}$ is far too low to indicate the transition regime sufficiently. The transition frequency, defined by the Q_{P1}^{-1} -peak, is $\omega_{trans,P1} = 34.51 \text{ rad s}^{-1}$ and much higher. The change of the P1-velocity just started to become visible at $\omega_{c,Biot}$ and solid and fluid did not decouple yet, cf. Fig. 11.3.

The alternatively given indicators for the transition frequency in Section 11.3.2, $\omega^* = 16.10 \text{ rad s}^{-1}$ and $\omega_{P1, B, III} = 62.82 \text{ rad s}^{-1}$, confine the transition regime much better. They do not provide an exact match because the impedance contrast is not very high as assumed for the case of an extremely weak solid, cf. c_{imp} in Eq. (11.12). The small impedance contrast can be related to the small difference of the individual sound velocities as discussed above. Nevertheless, the approximation of the order of magnitude, as it is often used to distinguish between the low- and high-frequency regimes, is superior to $\omega_{c,Biot}$ in the present case. From the qualitative physical viewpoint, ω^* and $\omega_{P1, B, III}$ indicate the transition regime well as can be seen in the logarithmic P1-wave plots, Fig. 11.3.

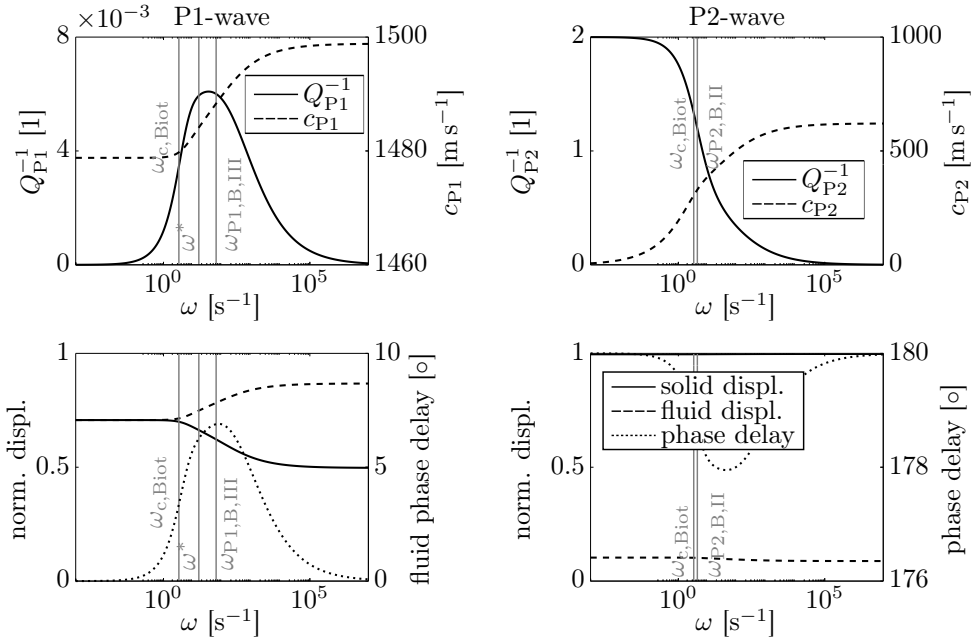


Figure 11.3: Dispersion relations for aluminum foam and water for the P1- and the P2-wave. The two characteristic frequencies $\omega_{c,Biot}$ and ω^* are indicated as well as an analytical approximation of the transition frequency as defined above. Material data is given in Appendix A.

11.5 Conclusion

The analytical investigation of Biot's model demonstrated that the transition frequency depends not only on Biot's characteristic frequency but also on the solid's inertia, compressibility, and frequency-dependent momentum exchange. As supported by numerical investigations, these influences can be neglected for typical systems with low porosity or with gases as pore fluids. However, they should be considered for systems of highly porous media with liquids. Even more, the characteristic transition frequency can differ between individual wave modes.

With respect to the variety of porous systems and because the transition zone cannot be reduced to one unique frequency, the aim of this work can only remain of qualitative nature. The analytical solutions can be used as indicators, whereas accurate solutions can be calculated numerically with little effort, for example, by the model of Part I. Currently, Biot's model is enhanced by more sophisticated attenuation mechanisms and other extension. Even so, the significant conclusions remain valid. These include the characteristic frequencies introduced in this work as well as the need for a consistent theory on all considered scales.

Chapter 12

Oscillatory flow in elastic tubes

The previous chapter illustrated the importance of solid elasticity for hydro-mechanical interaction in macroscopic wave propagation. Thus, the question about the impact of a solid's elasticity on microscopic pore channel oscillations arises. For this reason, this chapter studies Bernabé's theory [18]. It generalizes Biot's solution of oscillating, microscopic pore-channel flow by one additional degree of freedom of the elastic solid. Moreover, it is compared to experiments of Strutz and Renner [202] and reveals measurable effects for waves in (microscopic) elastic tubes. Finally, the impact on macroscopic wave propagation is discussed.

12.1 Introduction

The importance of microscopic pore channel flow for macroscopic wave propagation was shown in Chapter 10. Biot [25] derived two important results by upscaling from micro- to macroscale. The first result was a characteristic frequency and it was studied in the previous chapter. Its definition was generalized by the solid's inertia and compressibility because of the assumption of rigid walls at the microscopic origin. The second result of Biot's microscopic investigations was frequency-dependent momentum interaction, due to a microscopic change of the velocity profile. Here, Biot also assumed a rigid solid wall. Congruently, the questions of how elasticity and inertia of the solid influence the microscopic oscillations arises and, with it, frequency-dependent momentum interaction between fluid and solid.

Investigations of oscillatory flow in elastic tubes and other geometric structures are plentiful. Elastic pore channels are not only relevant as a part of comprehensive macroscopic systems, but also have their own importance. Applied research ranges from pulses in boreholes [64] over tremors [66] to waves in the arterial system [136, 228]. The following list can only provide a brief survey of all the contributions made and is not exhaustive.

In the previous study, the work of Womersley was mentioned. He focused on oscillations of arterial flow. A rigid-tube solution appears in one of his most-cited works in this area [226], cf. Eq. (9) *ibid.* with Eq. (3.8) in Biot's contribution [25]. Womersley refers to the real part of this solution as derived by Lambossy [118]. In [227], he provides a set of equations to determine the frequency-dependent wave velocity in elastic arteries. However, this work is limited to long wave lengths and lower fre-

quencies and one has to be aware of ambiguous denotations. Unfortunately, a second part was announced in [227] but, to the author's knowledge, it was never published by Womersley. This may be due to his wide-spread scientific interest and the low frequencies in arterial flows. Womersley continued to publish works on arterial flows - including added mass due to adjacent tissue [228], waves at junctions and inserts [229], and frequency-dependent viscosity [230] - but no longer with a focus on a general, frequency-dependent wave velocity profile.

Another early work dealing with waves in elastic tubes is that of Zwikker & Kosten [235], which refers back to Kirchhoff's theory in Rayleigh's work [172]. Lin & Morgan [124] provide several solutions of special cases based on mathematical approximations. Several oscillation modes are presented within a mathematically motivated framework. Tijdeman [207] presents a broad literature review and describes a general theoretical approach. Physical interpretation is supported by axial and radial velocity profiles, which are similar to that of Biot (and Womersley). Its key aspect is the so-called low-reduced-frequency solution, which is limited to low Womersley numbers and also by the fluid sound velocity. Interestingly, the Womersley number is named shear wave number or Stokes number in [207]. Bansevicius & Kargaudas [10, 11] also provide a very general mathematical framework including thermal effects. Nevertheless, the general approach makes a numerical solution of the frequency-dependent velocity difficult and the discussed solutions were simplified for special cases.

There are infinitely many solutions for the vibrational modes of an elastic beam or an elastic disc; similarly, there are infinitely many mathematical solutions for a propagating wave in a fluid-filled, elastic tube. The contributions mentioned above concentrate on selected solutions by incorporating physical assumptions that simplify the equations or the applied solution approach. Knowledge about these limitations is essential for the physical interpretation and difficult to extract in some works; especially if the assumptions are justified more mathematically, rather than on physical grounds. A very common assumption is the long wave length approximation, which means (in this particular case) that the wave length is large compared to the tube radius. This assumption avoids interaction on the tube radius scale. Furthermore, linearization leads to disregarding the convective term. Moreover, inertia terms are neglected for some low-frequency solutions [24, 227].

In addition to bulk waves in fluid-filled, elastic tubes, surface waves can propagate at the solid-fluid interfaces, for instance, Krauklis waves as described by Korneev [109, 110]. This highlights the situation of a variety of research groups from various areas with different aims but without a final integration, to date.

12.2 Bernabé's model

12.2.1 Bernabé's theory

The model of Bernabé [18] is chosen as an example for oscillatory flow in elastic tubes. In the limiting case of a rigid tube, its solution is easily comparable to that of Biot and Womersley for rigid tubes, compare Eq. (23) and (25) in [18] with Eq. (3.8) in [25]. Amongst other assumptions, Bernabé assumes wavelengths much larger than the tube radius, radial symmetry, a constant pressure profile in the radial direction, axial displacements dominating over radial displacements, and an infinitely thick tube (outer radius $\rightarrow \infty$).

Bernabé's dispersion relations, i.e. the frequency-dependent wave velocities $c_{\text{Bernabé}}(\omega)$, are given by Eq. (46) in [18]

$$\begin{aligned}
 0 &= c_{\text{Bernabé}}^4 + p_{\text{Bernabé}} c_{\text{Bernabé}}^2 + q_{\text{Bernabé}} & (12.1) \\
 p_{\text{Bernabé}} &= - \left(\frac{2 J_1(\kappa_{\text{Bernabé}} R)}{\kappa_{\text{Bernabé}} R J_0(\kappa_{\text{Bernabé}} R)} \frac{\rho_0^{\text{f}R}}{\rho_0^{\text{s}R}} c_{0,\text{f}}^2 + c_{0,\text{f}}^2 + 2 V_S^2 \right), \\
 q_{\text{Bernabé}} &= 2 V_S^2 c_{0,\text{f}}^2 \left(1 - \frac{2 J_1(\kappa_{\text{Bernabé}} R)}{\kappa_{\text{Bernabé}} R J_0(\kappa_{\text{Bernabé}} R)} \right), \\
 \kappa_{\text{Bernabé}} &= \sqrt{\frac{i\omega \rho_0^{\text{f}R}}{\eta^{\text{f}R}}}.
 \end{aligned}$$

J_0 and J_1 are Bessel functions of first kind, V_S is the shear wave velocity of the bulk solid material, and $c_{0,\text{f}}$ is the sound velocity of the bulk fluid. Note that the term $\kappa_{\text{Bernabé}} R$ contains the Womersley number and that the solid's influence is due to its bulk shear velocity. Two non-negative solutions are achieved describing a fast and a slow wave

$$c_{\text{Bernabé,fast/slow}} := -\frac{p_{\text{Bernabé}}}{2} \pm \sqrt{\left(\frac{p_{\text{Bernabé}}}{2}\right)^2 - q_{\text{Bernabé}}}. \quad (12.2)$$

The velocities are complex-valued in Bernabé's approach and can be related to the physical wave velocity as $c_{\text{Bernabé,physical}} = \Re(c_{\text{Bernabé}}) + \Im^2(c_{\text{Bernabé}})/\Re(c_{\text{Bernabé}})$. The low- and high-frequency limits are

$$c_{\text{Bernabé,fast}} = \begin{cases} \sqrt{\left(\frac{\rho_0^{\text{f}R}}{\rho_0^{\text{s}R}} + 1\right) c_{0,\text{f}}^2 + V_S^2} & , \text{ for } \omega \rightarrow 0 \\ c_{0,\text{f}} & , \text{ if } c_{0,\text{f}} > \sqrt{2} V_S \\ \sqrt{\frac{1}{2} c_{0,\text{f}}^2 + V_S^2} = c_{\text{slow}} & , \text{ if } c_{0,\text{f}} = \sqrt{2} V_S \\ \sqrt{2} V_S & , \text{ if } c_{0,\text{f}} < \sqrt{2} V_S \end{cases} \quad (12.3)$$

$$c_{\text{Bernabé,slow}} = \begin{cases} 0 & , \text{ for } \omega \rightarrow 0 \\ \sqrt{2} V_S & , \text{ if } c_{0,\text{f}} > \sqrt{2} V_S \\ \sqrt{\frac{1}{2} c_{0,\text{f}}^2 + V_S^2} = c_{\text{fast}} & , \text{ if } c_{0,\text{f}} = \sqrt{2} V_S \\ c_{0,\text{f}} & , \text{ if } c_{0,\text{f}} < \sqrt{2} V_S, \end{cases} \quad (12.4)$$

using

$$\lim_{\omega \rightarrow 0} \frac{2 J_1(\kappa_{\text{Bernabé}} R)}{\kappa_{\text{Bernabé}} R J_0(\kappa_{\text{Bernabé}} R)} = \frac{1}{2}, \quad \lim_{\omega \rightarrow \infty} \frac{2 J_1(\kappa_{\text{Bernabé}} R)}{\kappa_{\text{Bernabé}} R J_0(\kappa_{\text{Bernabé}} R)} = 0.$$

In contrast to Biot's microscopic investigations, Bernabé's model predicts two waves. If the tube material is rigid or has a high shear velocity compared to the fluid's sound velocity, the slow wave is dispersive and strongly connected to the fluid phase as in the case of Biot's theory. This becomes obvious from the high-frequency solution of the slow wave, Eq. (12.4), and the example calculations for a steel tube, Fig. 12.1a). The fast wave is based on the shear velocity of the solid and includes the density ratios for low frequencies, Eq. (12.3).

The slow wave, by contrast, does not depend on the densities representing inertia terms. This is in good agreement with the macroscopic theory, where the slow wave is a relative mode between the constituents. Pure relative motion already premises decoupling of the constituent with higher inertia and neglects further influence by inertia of the second phase. Biot's microscopic focus on a relative velocity is therefore well grounded for the slow wave.

In the opposite case, the solid's shear elasticity is weak compared to the fluid's stiffness and yields $V_S \ll c_{0,f}$. The slow wave of Bernabé's solution is then determined by the solid's bulk shear velocity and the fast wave is linked to the fluid's sound velocity, Eq. (12.3), Eq. (12.4), and Fig. 12.1b). This change of roles was observed as well on the macroscale for the compressional waves through a water-filled, weak aluminum foam, cf. Section 11.4.2. Thus, Bernabé [18] does not only predict a further wave mode but supports the presented macroscopic theory about the characteristic frequency (change of roles of solid and fluid) by his microscopic investigations.

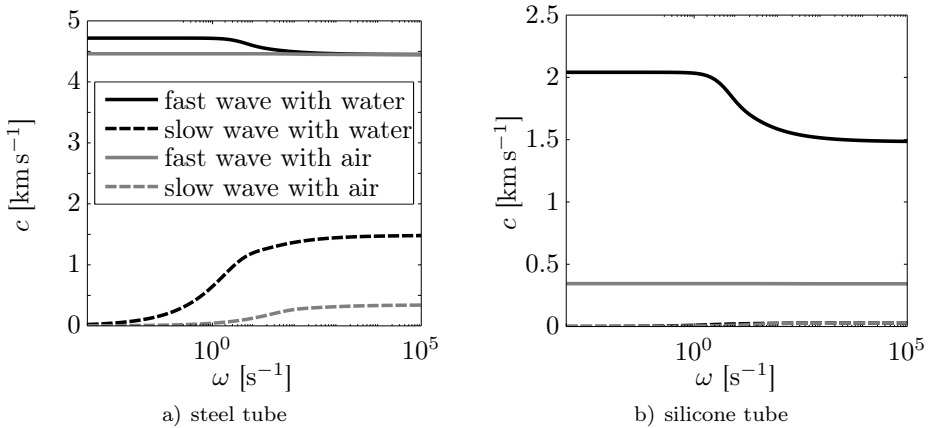


Figure 12.1: Dispersion relations according to Bernabé [18] for a steel and a silicone tube of 1 mm radius with water and air. The slow waves of the silicone tube are very close and overlap.

Considering the velocity profile, Bernabé's solution is a half-space solution. The displacement vanishes for increasing distance from the symmetry axis. In case of a rigid or very stiff tube, the slow wave is physically comparable to Biot's solution as it is consistent with Biot's assumptions. For the other case, namely silicone and water, Fig. 12.2 shows the velocity profile that belongs to the slow wave according to [18]. The slow wave is delayed by the slowly oscillating shear mode of the solid. Additionally, a considerably amount of fluid is coupled to the movement. Nevertheless, comparing the profile Fig. 12.2 with Biot's solution Fig. 10.2, both seem qualitatively similar for the relative (decoupled) mode.

12.2.2 Comparison with experimental data and limitations

Renner & Strutz performed experiments based on the so-called oscillation flow method, cf. [202]. For these experiments, a tube was connected to an up-stream and a down-stream reservoir. An oscillating pressure was applied to the upstream reservoir and the pressures of both reservoirs were measured in time. The experimental results in-

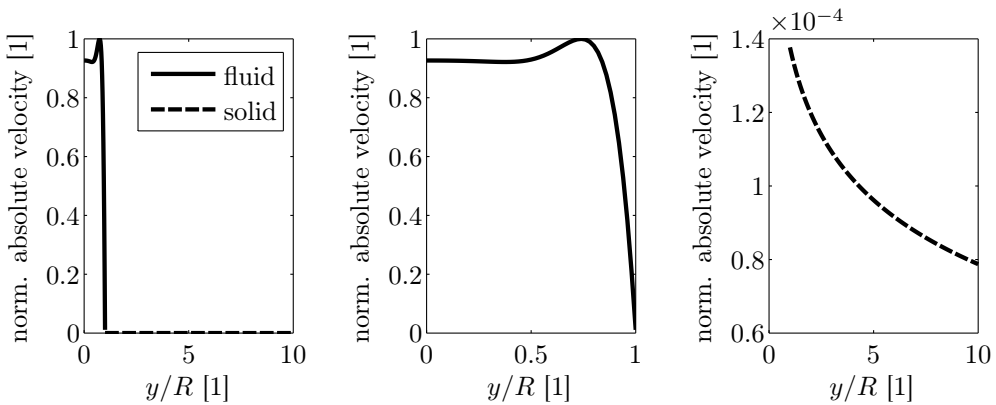


Figure 12.2: Axial, absolute velocity profile of the slow wave in a water-filled silicone tube of 1 mm radius at $\omega = 2\pi \times 1000 \text{ s}^{-1}$ according to Bernabé [18]. The velocity profile is normalized with respect to the highest appearing value.

clude the pressure ratio and phase lag for different frequencies, which can be related to the propagating wave in the elastic tube. A small excerpt of the data from [202] is now compared with Bernabé's theory.

In case of a steel tube, the results between the rigid-tube and the elastic-tube approach differ marginally and both match the experimental results well, Fig. 12.3. Still, the elastic approach performs better and an extended theory, including finite wall thickness, could even improve the match, due to the higher elasticity of a finite wall thickness. Thus, the theoretical influence of tube elasticity was confirmed experimentally.

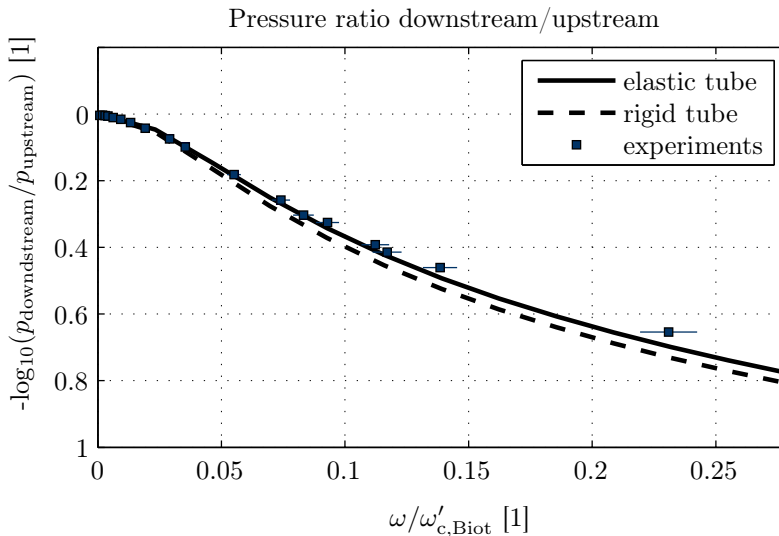


Figure 12.3: Comparison of Bernabé's theory and experimental results of oscillating flow in an air-filled silicone tube from [202]. The inner diameter was 0.5 mm, the outer diameter was 1.4 mm, and the length was 0.51 m.

Additionally, frequency-dependent wave velocities could be determined from comparison of experimental phase lag for different lengths of the same tube ([202] and private communication with J. Renner). Interestingly, the fluid-bound wave, recorded for silicone-air combinations, showed a highly dispersive behavior with vanishing velocity for low frequencies, Fig. 12.4. This result is in contrast to Bernabé's theory, which predicts a fast wave through air with non-vanishing low-frequency velocity, cf. Fig. 12.1b) (solid grey line).

Physically, it can be explained by a further wave mode that was neglected in Bernabé's theory. Taking into account an additional longitudinal wave in silicone, three wave modes occur in total: the very fast longitudinal silicone-bound wave ($\approx 1013 \text{ m s}^{-1}$), followed by the air-bound wave ($\approx 343 \text{ m s}^{-1}$), and, at last, the silicone-bound shear mode in the low two-digit m s^{-1} -regime. Because the fastest wave is the longitudinal wave in silicone, the former fast wave of Bernabé becomes one of the slower wave modes now.

As could be seen in the theories above, Part I and Chapter 11, slower wave modes are related to relative movements and highly dispersive¹⁹. They do not appear at low frequencies, because they are coupled to the fast wave mode by viscosity. This effect explains the experimental observation. The measured air-wave in the silicone-tube appears, but it is not the fastest mode and, therefore, dissipative at low frequencies. Furthermore, it shows that Bernabé's theory extends Biot's considerations but is also limited to a certain kind of wave modes: a fluid wave and a shear mode of the solid. The solid's microscopic, longitudinal wave is not considered.

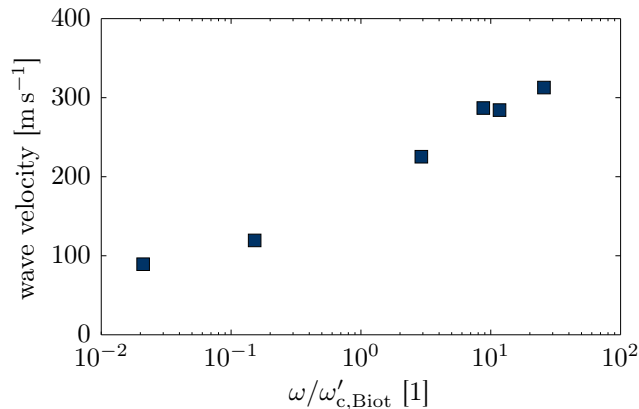


Figure 12.4: Measured phase velocities of an air-filled silicone tube (from [202] and private communication with J. Renner). The inner & outer diameters of the used tubes included combinations of 5 mm & 14 mm, 10 mm & 19 mm, and 10 mm & 30 mm. The lengths were between 0.2 m and 2 m.

¹⁹This is an illustrative example how results of macroscopic theories can help to understand smaller-scale physics.

12.3 Conclusion and open questions: about the impact of tube elasticity on wave modes, flow profiles, and momentum interaction

As mentioned in the introduction of this chapter, there is an infinite number of oscillation modes for flow in an elastic tube. Consequently, comparison of Bernabé's theory [18] with that of Biot [25] showed that elasticity of a tube can lead to further wave modes on the microscale. In general, such wave modes can be based on compression or shearing of the solid, but also on bending of thin-walled tubes or interface waves. The theoretical prediction of such wave modes depends on limiting assumptions for the leading equations, or the solution approach. Practically, the applied boundary conditions cause stimulation of certain wave modes, whereas damping and impedance contrasts further determine experimental observability.

Various works dealing with this topic show that a simple, general description cannot be given and that it depends on the respective application. Moreover, thermal or electrical boundary layer effects can cause/influence further waves. In addition, a change of cross section may influence the relative fluid motion at acoustic velocities, as it is known from a Laval nozzle.

With respect to macroscopic wave propagation, typical existing theories include only few wave modes, such as P-waves, S-waves, and rotational waves for micropolar media. Physically, a macroscopic wave belongs to a certain boundary condition on the microscale. In turn, very few microscopic waves represent an (experimentally) observable macroscopic wave. For example, oscillatory flow in a rigid tube represents Biot's slow wave for a very stiff solid skeleton. Many other microscopic waves, such as interface waves, may be highly damped on a macroscopic scale, due to microscopic attenuation or annihilation. Others are only stimulated in special cases. For example, Frehner [71] showed that Krauklis-waves are predominantly induced at crack-tips.

Nevertheless, understanding and investigating microscopic physics remains of vital importance, for instance, for comparison of tube network models or for the origins of attenuation. Moreover, many physical relationships are based on upscaled microscopic relationships such as the frequency-dependent momentum interaction proposed by Biot [25]. Whether or how the latter is influenced by the elasticity of the tube cannot be answered here conclusively. There are good reasons to expect that the microscopic-flow assumptions of Biot are valid for the relative wave modes of many situations including: velocity profiles calculated above (Fig. 12.2), velocity profiles illustrated in [207], as well as assumptions of negligible radial wall-displacement in microscopic theories [18, 110]. Neglect of a significant pore wall movement is usually based on the high aspect ratio of a solid's to a fluid's bulk modulus and/or a balanced load on both sides of a pore wall.

Note that, even for weak solid skeletons, the pores can often be assumed to be of constant microscopic diameter. Due to its porosity, the macroscopic solid represents a skeleton with much lower stiffness compared to the microscopic pore walls, i.e. $K^{\text{grains}} \gg K^{\text{s}}$. For example, even if a metal foam is more compressible than its pore fluid, the flow profile through the pore channels may be well described with the assumption of an incompressible pore because of the low compressibility of bulk metal. This implies that Biot's frequency correction for the flow profile can often be used for weak porous media - even though the macroscopic finding of a characteristic frequency has to be corrected. It may fail for very thin walls or an unbalanced load but remains as an interesting case for future research.

Chapter 13

Review

13.1 Summary and main findings

A dimensional analysis illustrated the origin of frequency-dependent flow profiles for microscopic, oscillatory flow in rigid pipes as proposed by Biot [25] and Womersley [226]. As a result, the macroscopic momentum exchange between fluid and solid is also frequency dependent. Subsequently, Biot's macroscopic characteristic frequency was generalized for systems with a weak solid frame. The extensions include

- the solid's elasticity
- the solid's inertia
- upscaling considering frequency-dependent momentum exchange

and are important for combinations of weak solid frames, such as aluminum foam or osteoporotic bone, with pore liquids.

Finally, Bernabé's theory [18] was presented to show the impact of elastic tubes on microscopic pore channel oscillations. A corresponding effect has been proven experimentally [202]. An influence on macroscopic momentum exchange could not be clarified conclusively but is expected to be less significant, because the grain elasticity is usually larger than the skeleton elasticity, $K^{\text{grains}} \gg K^{\text{s}}$.

13.2 Conclusions and outlook

The results showed that a consistent, physical treatment is important on all scales. Characteristic frequencies were derived for a variety of situations but they can only remain approximations for specific applications. Moreover, the frequency-dependent momentum exchange was only considered exemplarily, because it depends on the specific morphology. In conclusion, the analytical solutions should be used as a first estimation. For the case of new materials or other uncertainties, especially for high porosities, a numerical evaluation of the dispersion relations can be performed with little effort and is highly recommended.

The aspect of microscopic tube elasticity could only be investigated in a first, principle view. Further experimental evaluation will be undertaken in the near future and will include various combinations of weak/stiff fluids and solids. In any case, tube

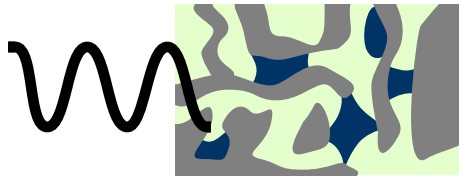
elasticity turned out to be influential. Admittedly, results obtained to date indicate that microscopic waves, which do not belong to a macroscopic deformation, are not likely to be stimulated by waves of long wavelengths in porous media. By contrast, the influence of microscopic tube elasticity can appear via intrinsic damping and needs to be taken into account in widely used pore network models.

The main conclusions are:

- Microscopic flow profiles are frequency dependent.
→ A description via macroscopic phases with one degree of freedom, therefore, requires frequency-dependent coefficients within the differential equations.
- A macroscopic characteristic frequency needs to consider all properties of the macroscopic system (fluid's and solid's).
- Different wave modes can belong to different characteristic/transition frequencies.
- For weak solid matrices, the alternative characteristic frequency ω^* should be (at least) considered additionally.
- Solid elasticity influences microscopic waves and causes further modes.

Part III

Waves in residually saturated porous media



Chapter 14

Introduction

14.1 Motivation and literature

A model for wave propagation in porous media with two continuous fluid phases was presented in Part I. It was assumed that the amount of both fluids is large enough to exceed residual saturation. In residually saturated porous media, by contrast, one fluid fills the pore space only fractionally. It does not form one continuous fluid phase but exists as disconnected clusters such as bridges and patches.

Each of these clusters can differ with respect to geometry and mass. As a result, each cluster's response to excitation by a mechanical wave is different. Thus, modeling by one single phase is not suitable to account for the differences in properties. This gap will be closed by the following model. It is based on the concepts of the group of Frehner, Steeb, Schmalholz, Podladchikov, and Kurzeja presented in [72, 73, 197, 198].

Motivating applications for wave propagation in residually saturated porous media include groundwater remediation [38, 173, 174] or enhanced oil recovery [17]. Initial investigations and experiments have been performed to promote the development of this young field of research. Ganglia mobilization was studied in a sand core [175] and in glass beads [38]. Stimulation by acoustic waves increased ganglia outflow significantly at certain frequencies during experiments of Chrysikopoulos & Vogler [38]. Mobilization of single clusters was studied in more detail in [16, 94–96], from seismic to ultrasound frequencies. Pride et al. [164] argued that seismic frequencies are usually too low for exact resonance stimulation in enhanced oil recovery but still registered a supportive effect by wave stimulation in simulations. Furthermore, sound absorption near habitats of sound-sensitive animals relies on the disconnected state of one fluid phase, cf. [72, 231].

Research on wave propagation in residually saturated porous media is relatively new and includes many unexplored areas. In all cases, a foresighted treatment of the stimulated region has to be assured with respect to possible damages of the solid framework. The following model may help to characterize and predict the behavior of mechanical waves at the state of residual saturation.

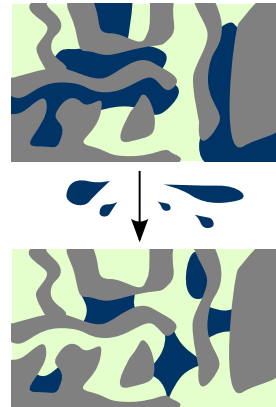


Figure 14.1: Partial vs. residual saturation.

Parts of the following investigation were presented previously in [198] (especially the concept and idea) and [115]. Further parts have been submitted previously and will probably be available shortly after completion of this treatise in [113].

14.2 Aims and structure

To complete the description of wave propagation in partially saturated porous media, the case of low, namely residual, saturation is described in this third part. The first goal is to predict wave properties such as velocity or attenuation, analogously to the model presented in Part I. An additional focus is on the characteristic properties of the disconnected fluid, because it is important for applications like sound absorption or ganglia stimulation.

Three further chapters constitute the following study.

- The modeling concept is presented in the first chapter and covers physical origins to governing equations. Therein, the disconnected phase is described as individual oscillators.
- Specific examples illustrate the influence of fluid cluster oscillations. An additional damping mechanism, due to resonance effects, occurs. Various kinds of cluster distributions are studied.
- The conclusion recapitulates the impact of fluid cluster properties on wave propagation and presents an outlook for future research and applications.

Chapter 15

Model

The development of a mathematical model for wave propagation in residually saturated porous media is presented. The physical system is illustrated and motivates modeling of the discontinuous fluid clusters in the form of harmonic oscillators, as proposed in [72, 73, 197]. The mathematical modeling approach is twofold and divided into continuous and discontinuous phases. On the one hand, the continuous solid and continuous liquid phase are described by a poroelastic model, for instance, as introduced by Biot [25] and described in Part I for two pore fluids.

On the other hand, the discontinuous fluid phase (of residual saturation) evolves from an averaging process over the residually distributed, microscopic fluid clusters. In contrast to classical continuum models, upscaling of the residual phase is not executed for the total fluid phase. Averaging is applied individually and distinctions are made between the clusters' dynamic properties: mass, stiffness, and damping.

Coupling between continuous and discontinuous phases is realized via momentum exchange. Finally, the mathematical description extends well-established poroelastic models by an additional, single term. This term includes the statistical distribution of the clusters' mass, stiffness, and damping. The two-scale approach presented here transfers relevant microstructure information to the macroscopic description of strong coupling between microstructure and macroscale dynamics.

15.1 The physical system

A residually saturated porous medium consists of a solid matrix that is saturated by two immiscible fluids. One fluid occupies most of the pore space and is continuously distributed throughout. The other fluid occurs at residual saturation. Thus, it is distributed in the form of single clusters (bridges, patches, and other kinds of fluid conglomerations), which are not connected.

The solid phase is referred to by index \mathfrak{s} as before. The continuous fluid is denoted by \mathfrak{c} , and the discontinuous fluid is denoted by \mathfrak{d} ²⁰. For convenience and near-surface applications, for example, in the vadose zone, it will be assumed that the discontinuous

²⁰Another distinction, common in the literature, is that between a wetting and a non-wetting fluid. The wetting fluid is often assumed to be the discontinuous fluid after a drainage process. This is, however, too restrictive for a general investigation, because it assumes a special relationship between both fluids.

fluid is a liquid and the continuous fluid is a gas. This assumption holds for many applications in the vadose zone, where air dominates the pore space and water clusters occupy the little remaining space in the pores. A generalization to arbitrary fluids is included in the capability of the basic approach and will be discussed later on.

15.2 Idea

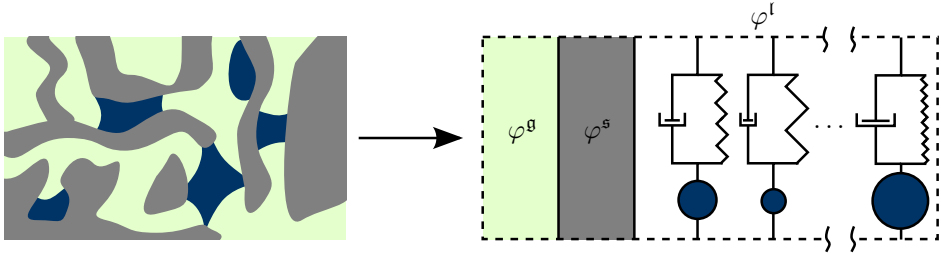


Figure 15.1: Schematic visualization of the modeling concept for a macroscopic, partially saturated system.

The following concept was presented in and is also based on the work of Steeb et al. [198]. The solid and the continuous fluid, \mathfrak{s} and \mathfrak{c} , coincide with the situation of the model described in Part I. Hence, a continuous approach can be used to describe these constituents. In the following, Biot’s theory (as recapitulated in Section 11.3.1) is used for the two continuous phases. Other approaches are also applicable, for example, a hybrid (rigid-grain) model can be used, as described by Steeb [196] and reformulated here via Eq. (B.1).

The discontinuous fluid occurs in the form of various fluid clusters. Each cluster can have its own geometric and material properties. Thus, the clusters cannot be generalized as one continuous fluid phase with one single capillary pressure or one common mass/inertia. Based on the ideas in [72, 73, 197], each cluster of the discontinuous fluid is modeled as an individual harmonic oscillator. From a conceptual point of view, B. de Spinoza’s words illustrate this idea best: “The order and connection of ideas is the same as the order and connection of things.” [159, 193]

With respect to the focus on linear wave propagation, only the important dynamic properties are included in the macroscopic description. These are mass, damping, and stiffness. The three additional parameters constitute a link between the microscopic behavior of the clusters and a macroscopic description. This link results in a two-scale model, which accounts for the relevant cluster properties for wave propagation.

15.3 Leading equations

15.3.1 Continuous phases

Inertia, damping, and stiffness matrices of the continuous phases for residual saturation are defined as \mathbf{A}_{RS} , \mathbf{B}_{RS} , and \mathbf{C}_{RS} . They can be derived straightforwardly from the continuous models in Part I and Section 11.3.1. The saturation of the continuous fluid is assumed to be near full saturation so that the momentum exchange between continuous fluid \mathfrak{c} and solid \mathfrak{s} does not differ significantly from the full saturation case.

The corresponding matrices write

$$\mathbf{A}_{\text{rs}} = \begin{pmatrix} \rho_0^s + (\alpha_{\text{fl}} - 1)\rho_0^c & -(\alpha_{\text{fl}} - 1)\rho_0^c \\ -(\alpha_{\text{fl}} - 1)\rho_0^c & \alpha_{\text{fl}}\rho_0^c \end{pmatrix}, \quad (15.1a)$$

$$\mathbf{B}_{\text{rs}} = c_{\text{JKD}} \left(\frac{\omega}{\omega_{c,c}} \right) \frac{(n_0^c)^2 \eta^{cR}}{k^s} \begin{pmatrix} 1 & -1 \\ -1 & 1 \end{pmatrix}, \quad (15.1b)$$

$$\mathbf{C}_{\text{rs}}^{\text{P}} = \begin{pmatrix} P_{\text{BW}} & S_{\text{BW}} \\ S_{\text{BW}} & R_{\text{BW}} \end{pmatrix}, \quad \mathbf{C}_{\text{rs}}^{\text{S}} = \begin{pmatrix} \mu^s & 0 \\ 0 & 0 \end{pmatrix}. \quad (15.1c)$$

The continuous fluid is characterized by its saturation s^c , volume fraction $n^c = \phi s^c$, partial density $\rho^c = \rho^{cR} n^c$, and dynamic viscosity η^{cR} . The stiffness matrices are similar to those of Biot's model, cf. Eq. (11.3c) and Eq. (11.4).

In addition, the discontinuous clusters contribute to momentum exchange. Assuming the continuous fluid phase to be a gas with low density, viscosity, and stiffness, interaction between the continuous gas phase and the liquid clusters is neglected. The clusters exchange momentum with the solid predominantly, almost unhindered by the surrounding gas. This assumption is supported by microscopic investigations, cf. Section 19.6.2. Thus, momentum exchange \hat{p}^{d} adds to the momentum balance and occurs only between solid phase and discontinuous fluid phase:

$$\left(\omega^2 \mathbf{A}_{\text{rs}} + i\omega \mathbf{B}_{\text{rs}} + k^{\psi 2} \mathbf{C}_{\text{rs}}^{\psi} \right) \begin{pmatrix} \hat{u}_s^{\psi} \\ \hat{u}_f^{\psi} \end{pmatrix} + \begin{pmatrix} -\hat{p}^{\text{d}} \\ 0 \end{pmatrix} = \mathbf{0}, \quad \psi \in \{\text{P}, \text{S}\}. \quad (15.2)$$

15.3.2 Discontinuous phase

The discontinuous phase consists of fluid clusters that can be different in their dynamic properties. First, a single microscopic cluster with index j is assumed to follow the classical momentum balance of a harmonic oscillator [72, 73, 197, 198]. The cluster's displacement $\mathbf{u}_{\text{mic},j}$ depends on its mass $m_{\text{mic},j}$, stiffness $c_{\text{mic},j}$, and damping $d_{\text{mic},j}$. Stiffness and damping can be replaced by eigenfrequency $\omega_{0,k}$ and damping ratio D_k . Note the introductory Section 3.2 that recapitulates the basic properties of a harmonic oscillator. The displacement of the adjacent solid walls is $\mathbf{u}_{\text{asw},k}$ and the momentum balance of the microscopic harmonic oscillator becomes

$$\begin{aligned} -m_{\text{mic},j} \ddot{\mathbf{u}}_{\text{mic},j} &= m_{\text{mic},j} \omega_{0,\text{mic},j}^2 (\mathbf{u}_{\text{mic},j} - \mathbf{u}_{\text{asw},j}) \\ &\quad + 2 m_{\text{mic},j} \omega_{0,\text{mic},j} D_{\text{mic},j} (\dot{\mathbf{u}}_{\text{mic},j} - \dot{\mathbf{u}}_{\text{asw},j}) \\ &= -\hat{\mathbf{P}}_{\text{mic}}^j. \end{aligned} \quad (15.3)$$

The inertia force is balanced by the contribution of stiffness and damper and transferred to the solid wall. This microscopic momentum balance is upscaled to combine it with the macroscopic theory of the continuous phases. The upscaling is executed as an averaging process, cf. Appendix D for details. With respect to the primary idea, the average is not applied to the total amount of discontinuous fluid clusters but with distinction of their eigenfrequency and damping ratio.

Let \mathcal{M}_{ω_0} and \mathcal{M}_D contain all countable indices of different occurring eigenfrequencies and damping ratios respectively. All macroscopic oscillators with eigenfrequency $\omega_{0,k}$ and damping ratio D_l are unified and indexed with $k \in \mathcal{M}_{\omega_0}$ and $l \in \mathcal{M}_D$.

The averaging process combines all microscopic oscillators with the same eigenfrequency and damping ratio to one macroscopic oscillator. The volume fraction of the macroscopic oscillators with eigenfrequency $\omega_{0,k}$ and damping ratio D_l is

$$n^{kl} = \frac{V_{kl}}{V_{\text{REV}}} = \frac{1}{V_{\text{REV}}} \bigcup_{\substack{\text{micr. cluster} \in \text{REV} \\ \omega_{0,\text{cluster}} = \omega_{0,k} \\ D_{\text{cluster}} = D_l}} V_{\text{cluster}}. \quad (15.4)$$

It is related to the volume fraction of the total discontinuous phase

$$n^{\text{d}} = \frac{V_{\text{d}}}{V_{\text{REV}}} = \frac{1}{V_{\text{REV}}} \bigcup_{[k,l] \in \mathcal{M}_{\omega_0} \times \mathcal{M}_D} V_{kl} = (1 - s^{\text{c}}) \phi \quad (15.5)$$

by

$$\alpha^{kl} = \frac{V_{kl}}{V_{\text{d}}} = \frac{n^{kl}}{n^{\text{d}}}. \quad (15.6)$$

The latter, α^{kl} , is the volume ratio of clusters with eigenfrequency $\omega_{0,k}$ and damping ratio D_l with respect to all clusters. For convenience, the initial density ρ_0^{d} is assumed to be constant, so that it does not need to be distinguished for each cluster type. Moreover, initial capillary pressure effects are neglected with respect to density changes (cf. Section 19.7.1 for a detailed justification). Using the introduced parameters, momentum interaction between a cluster and the solid phase becomes, cf. Appendix D,

$$\hat{\mathbf{p}}^{kl}(\omega) = -\alpha_0^{kl} \rho_0^{\text{d}} (\omega_{0,k}^2 - 2\omega_{0,k} \omega D_l i) \left(\frac{\omega_{0,k}^2 - 2\omega_{0,k} \omega D_l i}{(\omega_{0,k}^2 - \omega^2) - 2\omega_{0,k} \omega D_l i} - 1 \right) \mathbf{u}_s. \quad (15.7)$$

The influence of a macroscopic oscillator is fully determined by the set $\{\alpha^{kl}, \omega_{0,k}, D_l\}$. Alternatively, the macroscopic harmonic oscillator can be described by stiffness $c_{kl} = \alpha^{kl} n^{\text{d}} \rho^{\text{d}R} \omega_{0,k}^2$, damping coefficient $d_{kl} = 2D_l \omega_{0,k}$, and $\rho^{kl} = \alpha^{kl} n^{\text{d}} \rho^{\text{d}R}$, cf. Section 3.2.

15.3.3 Combination of continuous and discontinuous phases

The total amount of momentum that is exchanged between the clusters and the solid is

$$\hat{\mathbf{p}}^{\text{d}} = \sum_{[k,l] \in \mathcal{M}_{\omega_0} \times \mathcal{M}_D} \hat{\mathbf{p}}^{kl} = -\rho_0^{\text{d}} c_{\text{cl}}(\omega) \mathbf{u}_s \quad (15.8)$$

with

$$c_{\text{cl}}(\omega) = \sum_{[k,l] \in \mathcal{M}_{\omega_0} \times \mathcal{M}_D} \alpha_0^{kl} (\omega_{0,k}^2 - 2\omega_{0,k} \omega D_l i) \left(\frac{\omega_{0,k}^2 - 2\omega_{0,k} \omega D_l i}{(\omega_{0,k}^2 - \omega^2) - 2\omega_{0,k} \omega D_l i} - 1 \right). \quad (15.9)$$

A realistic, porous medium contains a finite set of clusters. For practical description, however, it may be convenient to approximate their eigenfrequencies and damping ratio distribution by a probability density function. Instead of a discrete distribution of volume ratios $\alpha^{kl}(\omega_{0,k}, D_l)$, a probability measure

$$\alpha^{\text{pdf}} : \mathbb{R}_{\sigma}^2 \rightarrow [0, 1] \quad (15.10)$$

can be used with units $[\alpha^{\text{pdf}}] = \text{s}$ and \mathbb{R}_σ^2 being the Borel σ -Algebra of \mathbb{R}^2 . Due to physical restrictions $\alpha^{\text{pdf}}(\hat{\omega}_0, \hat{D}) = 0 \text{ s}$, if $\hat{\omega}_0 \leq 0 \text{ s}^{-1}$ or $\hat{D} \leq 0$. In this case, Eq. (15.9) changes from a sum to an integral

$$c_{\text{cl}}(\omega) = \int_{\mathbb{R}_{\geq 0}^2} \alpha^{\text{pdf}}(\hat{\omega}_0, \hat{D}) \left(\hat{\omega}_0^2 - 2 \hat{\omega}_0 \omega \hat{D} i \right) \left(\frac{\hat{\omega}_0^2 - 2 \hat{\omega}_0 \omega \hat{D} i}{(\hat{\omega}_0^2 - \omega^2) - 2 \hat{\omega}_0 \omega \hat{D} i} - 1 \right) d\hat{\omega}_0 d\hat{D}. \quad (15.11)$$

The final set of equations is then determined by the continuous phases, Eq. (15.1a) - Eq. (15.1c), and discontinuous phase Eq. (15.9) or Eq. (15.11) respectively. For plane waves, the resulting eigenvalue formulation becomes, for $\psi \in \{\text{P}, \text{S}\}$,

$$\left(\mathbf{A}_{\text{cl}} + \omega^2 \mathbf{A}_{\text{rs}} + i\omega \mathbf{B}_{\text{rs}} + k^{\psi^2} \mathbf{C}_{\text{rs}}^{\psi} \right) \begin{pmatrix} \hat{u}_{\text{s}}^{\psi} \\ \hat{u}_{\text{f}}^{\psi} \end{pmatrix} = \mathbf{0}, \quad \mathbf{A}_{\text{cl}} = \begin{pmatrix} \rho_0^{\text{d}} c_{\text{cl}}(\omega) & 0 \\ 0 & 0 \end{pmatrix}. \quad (15.12)$$

The addition \mathbf{A}_{cl} can be interpreted as a frequency-dependent added-mass effect of the solid phase. This reflects figuratively the concept of harmonic oscillators, which are attached to the solid phase. The volume ratio α^{kl} or α^{pdf} respectively represents weighting of the added mass effect of each individual cluster type.

15.3.4 Variants

Arbitrary fluid combinations

For the general case of arbitrary fluids, momentum exchange between the clusters and the continuous fluid phase has to be considered. Such an extension exceeds the current aim but can be implemented straightforwardly. Mathematically, it is represented by the second diagonal term of matrix \mathbf{A}_{cl} . For instance, the cluster interaction can be distributed between the solid and the continuous fluid according to their respective stiffness. Such implementation can be executed without the need for additional material parameters. The present case is achieved if the compressibility of the continuous fluid is relatively low, which is in accordance with the physical situation of a gas.

Simplified approach: distinction via eigenfrequencies only

The presented approach distinguishes between eigenfrequencies and damping ratios. The model complexity reduces if the clusters are distinguished solely by their eigenfrequencies. In this case, a separate classification by D_l vanishes, together with the respective indices and integration. The damping ratio becomes an averaged damping ratio D_k for all clusters with the same eigenfrequency $\omega_{0,k}$, cf. Eq. (D.15). The corresponding model was described in [198].

Such an assumption holds well if all clusters differ in eigenfrequency and damping ratio, so that clusters of the same eigenfrequency also show approximately the same damping ratio. This can be the case, for example, if a few typical groups of clusters, which differ in stiffness and damping, are considered. The advantage of such an approach is that the cluster classification can be achieved with a single parameter. An appropriate use is discussed in the following chapter.

Chapter 16

Examples

The following examples illustrate the capabilities and characteristics of the previously presented model for wave propagation in residually saturated porous media. Emphasis is placed on eigenfrequency ω_0 , which centrally determines resonance effects, and damping ratio D , which determines whether resonance effects are covered by viscous damping. The corresponding mass distribution is a weighting factor for different kinds of clusters.

A basic example explains the relationships between the mathematical structure and its physical significance. It is followed by a specific example of three different cluster types. In the end, implementation of continuous, statistical distributions is presented with respect to its influence on wave propagation in residually saturated porous media.

16.1 Preliminary comments and the common initial system

The basis of the material parameters is Berea sandstone filled with 90 % air and 10 % water at ambient conditions, cf. Appendix A for material properties. The water phase is distributed in the form of single oscillators as described by specific distribution functions in the individual examples.

Dispersion relations are shown for the P1-wave and are comparable for the S-wave. The P2-wave is virtually unaffected due to negligible interaction between both fluids.

16.2 Basic example

The presented model can be generally characterized best by the introduction of a single oscillator. This single oscillator has an eigenfrequency $\omega_{0,1}$ and a damping ratio D_1 .

For an oscillator with low damping ($D_1 \ll 1$), a sharp peak of the inverse quality factor occurs at a frequency of $\omega_{0,1}$, cf. Fig. 16.1. This damping effect is a new physical phenomenon, compared to classical wave propagation models. It accounts for energy that is stored by oscillations of the fluid cluster. If a traveling wave passes the cluster and stimulates it with the appropriate frequency, the cluster responds with its own oscillations. While the wave propagates further through the system, the cluster

continuous to oscillate. This oscillation energy is lost from the point of the traveling wave. The wave is damped effectively on the macroscale, which can be predicted and observed as a peak of the inverse quality factor. As for the continuous model, cf. Section 6.3, damping due to the air phase is small and not recognizable in the plot. The fluid cluster also significantly influences the phase velocity. The results follow the physical implementation of an added mass with its own stiffness and damping. In contrast to the smooth transition of a continuous model, a cluster with low damping causes a velocity fluctuation, Fig. 16.1. The right-hand limit near the resonance effect shows an increase of phase velocity. The left-hand limit shows a decreasing phase velocity. This interesting behavior, which converges to a singularity for vanishing damping, is also known as a negative mass or negative elasticity effect, cf. [53, 65, 97, 145] and their very similar mathematical structure. An analogous example is a pendulum in an oscillating building, which can counteract the building's movement by opposite oscillation.

Singularities of the dispersion relations are weakened by increasing damping, $\nearrow D$, cf. Fig. 16.1. The dispersion relations approach those of continuous phases. This behavior is in accordance with physical expectations. For $D_1 \gg 1$, influence of the restoring capillary forces is dominated by viscous damping. The clusters are overdamped and do not exhibit resonance effects. This is the case, for example, if several clusters combine to form larger or longer ones, namely come close to a continuous phase.

In conclusion, this simple model demonstrates two interesting results. First, a new damping mechanism, the clusters' resonance oscillations, can be described physically. Second, the difference between discontinuous and continuous effects can be represented by the parameter D . This accounts for the ratio of viscous forces to capillary forces.

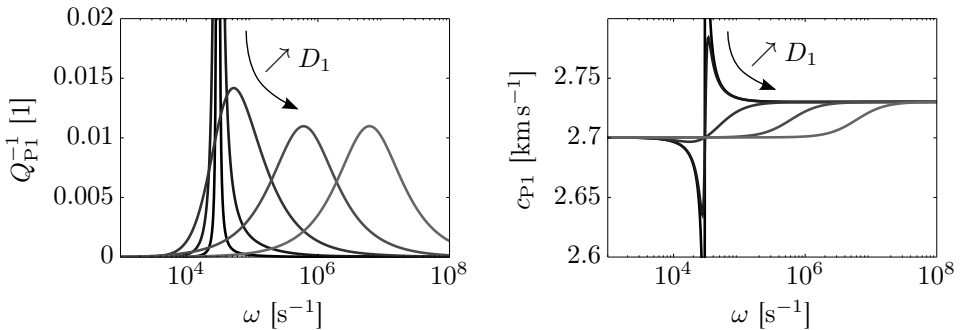


Figure 16.1: Basic example of one fluid oscillator with $\omega_{0,1} = 30 \times 10^3 \text{ s}^{-1}$ and different damping ratios $D_1 = 0.01/0.1/1/10/100$.

Remark on the transition frequency of the discontinuous fluid

A transition frequency, indicating the peak of the inverse quality factor and the transition from the low- to the high-frequency regime, can be determined as before for continuous phases (cf. Chapter 11). For a single oscillator and a continuous gas phase of high compressibility, the transition frequency of the P1-wave is

$$\omega_{\text{trans, osc}} = \frac{b_{\text{osc}}}{\rho^{\text{d}}} \sqrt{1 + \frac{\rho^{\text{d}}}{\rho^{\text{s}}}} \rightarrow \begin{cases} \omega_{0,1}, & \text{for } D_1 \ll 1 \\ 2 D_1 \omega_{0,1} \sqrt{1 + \frac{\rho^{\text{d}}}{\rho^{\text{s}}}}, & \text{for } D_1 \gg 1. \end{cases} \quad (16.1)$$

Parameter b_{osc} is the solution of a quartic equation

$$b_{\text{osc}} = \sqrt{-\frac{\chi_{\text{osc}}}{2} + \sqrt{\left(\frac{\chi_{\text{osc}}}{2}\right)^2 - \psi_{\text{osc}}}}, \quad \text{with} \quad (16.2)$$

$$\chi_{\text{osc}} = (\omega_{0,1}\rho^{\text{d}})^2 \left(1 + \frac{1}{1 + \frac{\rho^{\text{d}}}{\rho^{\text{s}}}}\right) - (2\rho^{\text{d}}D_1\omega_{0,1})^2, \quad \psi_{\text{osc}} = -3(\omega_{0,1}\rho^{\text{d}})^4 \frac{\rho^{\text{d}}}{\rho^{\text{s}}}$$

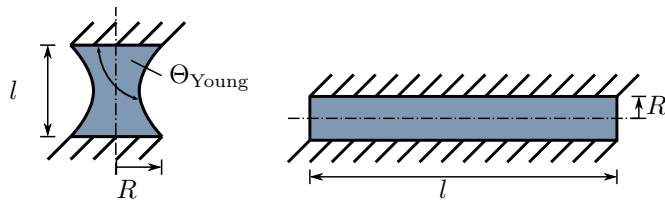
Its physical meaning is comparable to that of the viscous drag coefficient for continuous phases, cf. Eq. (5.29).

The undamped limit of Eq. (16.1), $D_1 \ll 1$, represents damping of the wave by the cluster's oscillations with $\omega_{0,1}$. Note that for higher damping, a simple harmonic oscillator shows a reduced oscillation frequency, Eq. (3.6). In contrast, the transition frequency of the current model does not reduce because it considers and superposes both energy losses: energy loss due to pure cluster oscillations and due to viscous drag. For increasing D , the solution converges to the behavior of a continuously distributed fluid, Eq. (16.1) ($D_1 \gg 1$). As for the case of continuous fluids, higher damping increases the transition frequency, cf. Fig. 16.1, and the role of viscosity in Eq. (11.1) and Eq. (11.10).

Hence, the transition frequency also illustrates the capability of the presented model to account for the physics of both: the classical continuous approach and the extension by a discontinuous fluid simultaneously.

16.3 Residually saturated Berea sandstone with water clusters of different size

An applied example is provided by the investigation of Berea sandstone that is residually saturated by three kinds of water clusters, cf. Tab. 16.3. The first two clusters represent small bridges, which can occur between two single grains with different contact angles. The third cluster represents a water patch in a long pore channel.



cluster no.	1	2	3
l [m]	1×10^{-5}	1×10^{-5}	2×10^{-2}
R [m]	0.5×10^{-5}	0.5×10^{-5}	1×10^{-4}
α_k [1]	1/3	1/3	1/3
$\omega_{0,k}$ [s ⁻¹]	30×10^3	25×10^3	2×10^3
D_k [1]	0.037	0.028	0.18
Θ_{Young} [°]	65	115	90

Table 16.1: Oscillator types used for the example calculation. Dynamic properties are estimated with respect to the results in Chapter 20 and based on oscillations parallel to the pore walls.

Their corresponding dispersion relations clearly reflect the different resonance effects. The inverse quality factor and phase velocity are distinctively influenced by each cluster individually, cf. Fig. 16.2. This offers the possibility of characterizing different kinds of fluid clusters in a porous medium on the basis of their frequency-dependent response.

Caution is advised for the characterization of oscillating fluid clusters by frequency-dependent phase velocity. In realistic experiments, rapid changes of the frequency-dependent phase velocity are expected to occur less intensively. Applications usually include a broader distribution of various cluster types and a broader frequency range of the signal. Additionally, further dissipative effects, between an experimental transmitter and receiver, can smear out the wave signal and they must be considered. Furthermore, a traveling wave will probably not be disturbed over the entire wave front by single clusters even if they are assumed to be distributed homogeneously. Nevertheless, the inverse quality factor may be a more satisfactory experimental tool to investigate and characterize residually saturated porous media. It relates energies of the wave, which can be averaged more easily over a restricted space and time domain. An energy loss is also observable if the wave passes a region with enclosed fluid clusters and then smears out. Thus, fluid clusters can be distinguished by their differing dynamic properties.

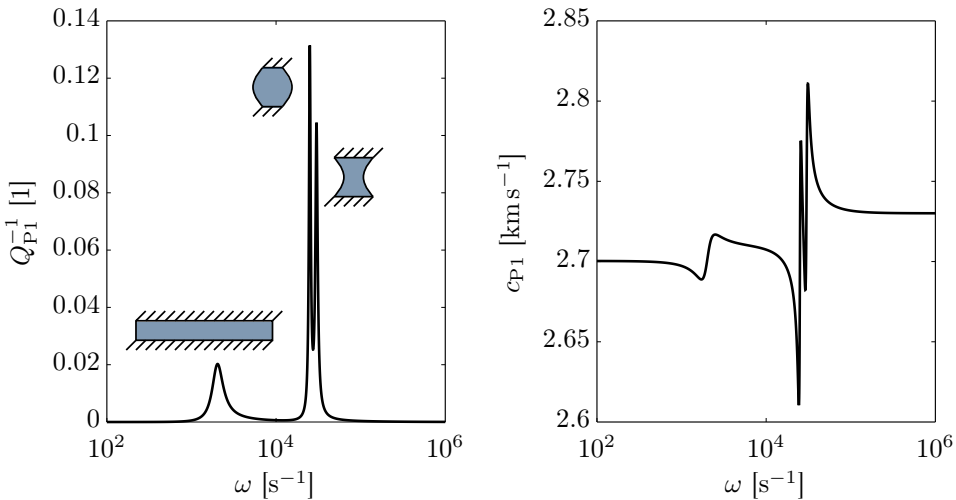


Figure 16.2: Dispersion relations of residually saturated Berea sandstone filled with three types of water clusters.

16.4 Continuous distributions

The previous example included single clusters. A continuous distribution of eigenfrequencies or damping ratios, $\alpha^{\text{pdf}}(\hat{\omega}_0, \hat{D})$, can account for more sophisticated systems in real application with sophisticated cluster distribution. Moreover, use of a probability density function allows an investigation of the difference between narrow and broad distributions. For this purpose, the distribution of clusters, α^{pdf} , will be varied separately for eigenfrequencies $\hat{\omega}_0$ and damping ratio \hat{D} . One parameter of $\hat{\omega}_0$ and \hat{D} will be fixed while the other one is studied for a narrow and a broad spreading around a mean value.

For this reason, two distributions are used. A single, fixed value is represented by the delta-distribution δ_x . It describes a discrete distribution at value x . The other distribution is a general beta distribution $B(a, b, p, q)$ with probability density

$$f_{B(a,b,p,q)}(x) = \frac{\Gamma(p+q)}{\Gamma(p)\Gamma(q)(b-a)^{p+q-1}}(x-a)^{p-1}(b-x)^{q-1}. \quad (16.3)$$

Γ is the gamma function and $p = q = 2$ is used for the present investigation, cf. Fig. 16.3. It has a mean value of μ_{distr} and spreads between $(1 - \lambda_{\text{distr}})\mu_{\text{distr}}$ and $(1 + \lambda_{\text{distr}})\mu_{\text{distr}}$. Higher values of λ_{distr} cause a broader spreading.

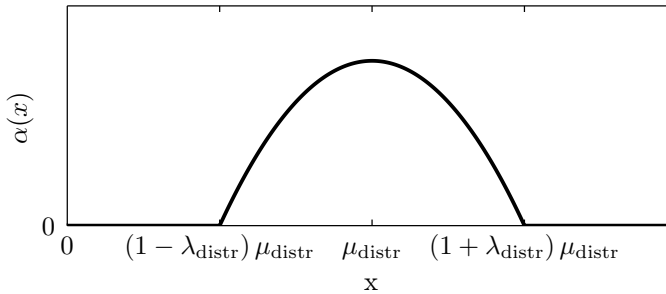


Figure 16.3: Probability density function as a beta distribution $\alpha \sim B((1 + \lambda_{\text{distr}})\mu_{\text{distr}}, (1 - \lambda_{\text{distr}})\mu_{\text{distr}}, 2, 2)$.

The clusters' final volume ratio distribution is multiplicatively split into its dependence on eigenfrequencies and on damping ratios as $\alpha^{\text{pdf}}(\hat{\omega}_0, \hat{D}) = \alpha_\omega(\hat{\omega}_0) \alpha_D(\hat{D})$. It further remains limited to non-negative values of $\hat{\omega}_0$ and \hat{D} , due to physical reasons.

16.4.1 Study of eigenfrequency distributions

To investigate the influence of different eigenfrequency distributions, a fixed damping ratio $\alpha_D \sim \delta_{D_1}$ is assumed first. The eigenfrequency distribution varies around a value of $\omega_1 = 1000 \text{ s}^{-1}$ with $\lambda_{\text{distr}} \in \{0.01, 1\}$ and $\alpha_\omega \sim B(\omega_1(1 - \lambda_{\text{distr}}), \omega_1(1 + \lambda_{\text{distr}}), 2, 2)$. For weakly damped clusters ($D_1 = 0.1$), a broader distribution of clusters ($\lambda_{\text{distr}} = 1$) differs significantly from a distribution around one cluster type ($\lambda_{\text{distr}} \rightarrow 0$), cf. Fig. 16.4 (left side). A broader distribution results in a smoother and broader transition regime, which is additionally shifted to higher frequencies. Furthermore, the dispersion relations show a bias towards higher frequencies although the used probability density function $\alpha^{\text{pdf}}(\hat{\omega}_0, \hat{D})$ is symmetric, cf. Eq. (16.3) and Fig. 16.3.

The tendency to higher frequency can be explained by the fact that the added-mass component of the leading equations is not linear in $\hat{\omega}_0$ and \hat{D} , cf. Eq. (15.11). Furthermore, the damping coefficient of a harmonic oscillator scales with the damping ratio and eigenfrequency $d_{kl} = 2 D_l \omega_{0,k}$. Due to these two mathematical properties, a broader, symmetric distribution of eigenfrequencies causes a higher weight of strongly damped clusters. As a result, the transition zone is not only smoothed out but also shifted to higher frequencies.

For a high damping ratio D_1 , the distribution of the eigenfrequencies is less influential, cf. Fig. 16.4 (right side). In this case, capillary effects are dominated by viscous effects. Because eigenfrequencies represent the stiffness of capillary effects, the impact of their distribution vanishes and is not observable for large values of D_1 .

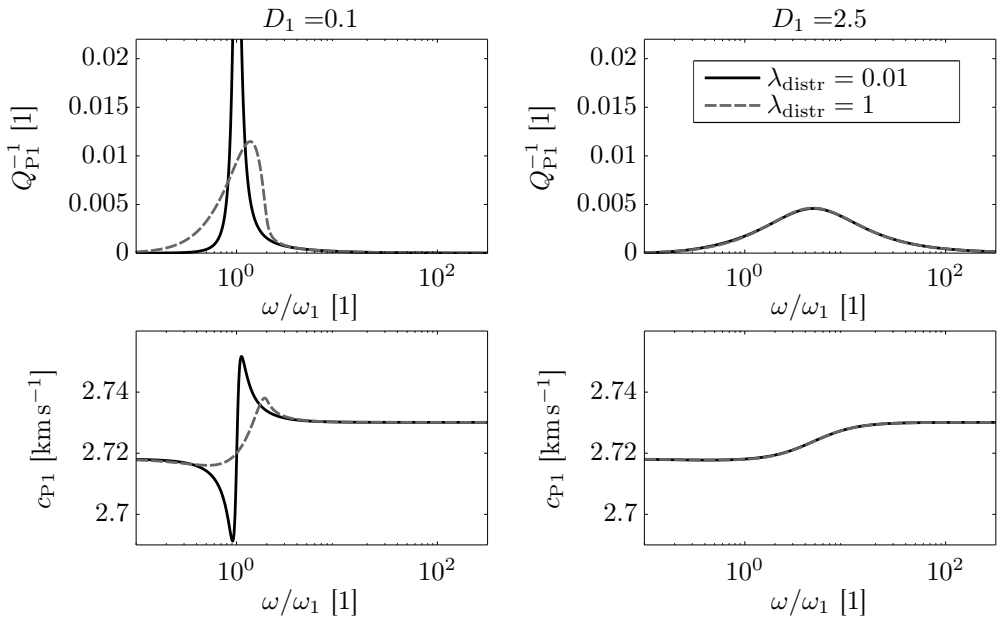


Figure 16.4: Dispersion relations for different continuous distributions of eigenfrequencies at constant single damping ratio D_1 represented by $\alpha_D \sim \delta_{D_1}$. The eigenfrequency distribution is $\alpha_\omega \sim B(\omega_1(1 - \lambda_{\text{distr}}), \omega_1(1 + \lambda_{\text{distr}}), 2, 2)$ with $\omega_1 = 1000 \text{ s}^{-1}$. The two curves overlap in both right figures.

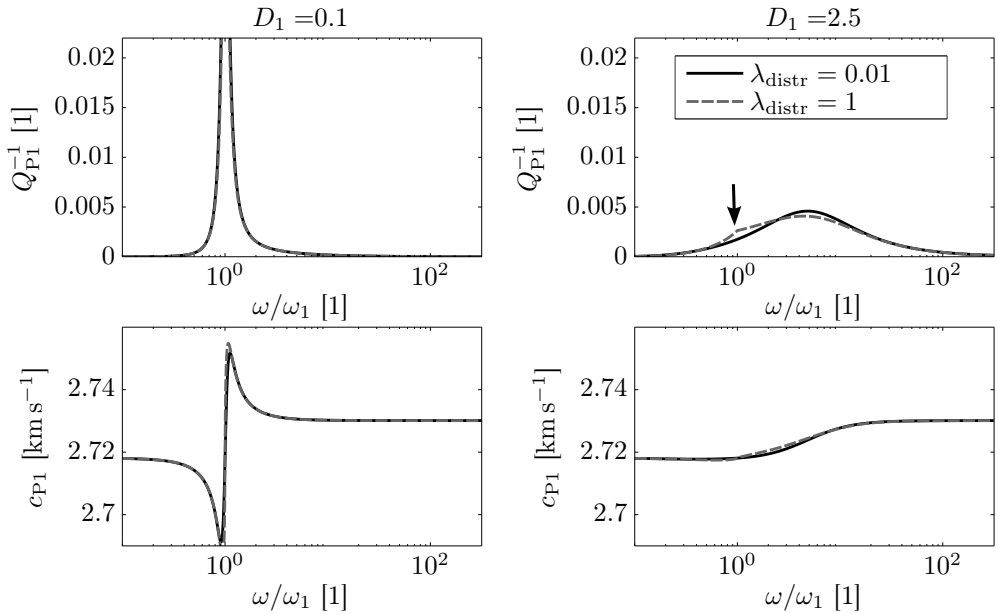


Figure 16.5: Dispersion relations for different continuous damping distributions at a constant single eigenfrequency $\omega_1 = 1000 \text{ s}^{-1}$ represented by $\alpha_\omega \sim \delta_{\omega_1}$. The damping ratio distribution is $\alpha_D \sim B(D_1(1 - \lambda_{\text{distr}}), D_1(1 + \lambda_{\text{distr}}), 2, 2)$. The arrow indicates a second peak in the inverse quality factor, due to clusters with low damping compared to the viscosity-dominated main peak.

16.4.2 Study of damping ratio distributions

The influence of a damping ratio distribution is investigated like the eigenfrequency distribution but with fixed eigenfrequency $\alpha_\omega \sim \delta_{\omega_1}$ and $\alpha_D \sim B(D_1(1-\lambda_{\text{distr}}), D_1(1+\lambda_{\text{distr}}), 2, 2)$. A varying damping ratio distribution is less influential for weakly damped clusters, Fig. 16.5 (left), because capillary effects dominate over viscous damping.

For a higher mean value of damping, the difference between a narrow and a wide distribution becomes noticeable. Still, it is not as distinctive as a change of the eigenfrequency distribution of the investigated case above.

Instead, another very interesting result appears. The inverse quality factor shows two peaks for a wide distribution around a cluster type with high mean damping ratio, cf. Fig. 16.5 (upper right graph). The major peak is due to viscous damping as it also appears for a narrow distribution. The second peak is caused by clusters that are weakly damped and show oscillations around the eigenfrequency ω_1 .

In conclusion, the characterization via eigenfrequencies is more important for the investigated case. In particular, clusters of various eigenfrequencies can be traced back from the dispersion relations for weak damping, which is of major importance in residually saturated porous media. The more the clusters differ by their eigenfrequency, the easier they are distinguishable.

In contrast, a broader damping ratio distribution was less influential and less distinctive in the present study. It only became important for higher damping ratios. For instance, it can play an important role in characterization of systems that include high- and low-damped clusters such as small blobs between crack tips and larger conglomerations in long pore networks.

Chapter 17

Review

17.1 Summary and main findings

A mathematical model was developed that described wave propagation in residually saturated porous media. The continuous solid and the continuous fluid phase were described by classical poroelasticity. The discontinuous fluid of residual saturation was modeled in the form of harmonic oscillators.

The heterogeneous structure of disconnected fluid clusters was accounted for by characterizing them according to their mass m , eigenfrequency ω_0 , and damping D . These dynamic properties were preserved during the upscaling process. Coupling was achieved via momentum exchange with the solid phase and resulted in one additional parameter within the established mathematical formulation of biphasic media. This extension is determined by the statistical distribution of clusters' mass, eigenfrequency, and damping.

Specific examples of sandstone with air and water in the residual state yield the following results.

- The state of residual saturation adds an additional, macroscopic damping mechanism due to the energy stored by resonance oscillations.
- The damping ratio D determines whether the new damping mechanism is dominant ($D \ll 1$) or whether classical viscous damping covers capillary effects ($D \geq 1$). The latter case coincides with larger conglomerations and therefore converges to the case of a continuous distribution.
- The cluster distributions have a distinct and characteristic influence on the dispersion relations.
- Clusters can be better differentiated by deviations of their eigenfrequency-distribution than by their damping-distribution.
- The clusters' influence is an intrinsic mechanism and not observable as an additional wave mode. The effects are clearly of a two-scale nature.

17.2 Conclusions and outlook

The results predict a strong relationship between cluster properties and wave behavior. Therefore, the dynamic properties could be clearly related to their effect on dispersion relations. In turn, conclusions about cluster geometry and distribution are possible on the basis of experimental wave measurements. Hence, the presented model can serve as a tool for inverse analysis. It allows a characterization of the physical situation and data interpretation with very little computational effort. Possible applications include systems for which material data is known but the state of residual saturation is of interest, for example, the vadose zone or laboratory samples. Moreover, understanding of the physical situation will be further supported in combination with modern imaging techniques [121]. An experimental comparison will doubtlessly be the most interesting and important next step for future research.

Referring to the theoretical approach, the model relies on momentum exchange between clusters and the solid. This is limited to a liquid-gas combination and examples were provided for a liquid in the residual state. The inverse situation was also studied, for example, by Minnaert [147], Smeulders & van Dongen [192], and Frehner et al. [73].

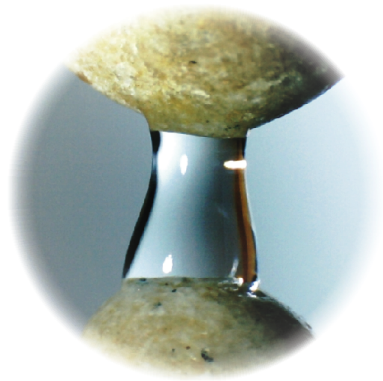
A generalized framework for two arbitrary pore fluids, especially two liquids, can be achieved consistently by an intermediate-term step. This is the determination of fluid-fluid momentum interaction, for example, based on microscopic studies, as used for liquid clusters in Part IV. Moreover, a second, straightforward extension can be constructed from frequency-dependent, dynamic properties such as stiffness or eigenfrequency, to account for multiple modes of resonance.

Ganglia mobilization in residually saturated porous media is a topic of ongoing discussions, cf. [38, 94, 96]. Two of its main motivations are enhanced oil recovery [17] and ground water remediation [38, 173, 174]. The presented results (together with oscillator data from Part IV) lead to the conclusion that seismic stimulation has to be considered skeptically, for two reasons. The first is that seismic waves act in a frequency range that is typically too low. This is in agreement with the conclusion of Pride et al. [164]. The second relates to the relatively high attenuation for distances beyond a few km. To date, and to the current knowledge of the author, linear seismic waves do not seem to be an appropriate technique for ganglia stimulation at great depths.

However, application of higher frequencies in smaller samples was successful in first experiments [38], encouraging future application under laboratory conditions or for ground water remediation in near-surface regions. In all cases, a foresighted treatment of the stimulated region has to be assured with respect to possible damage of the solid framework. Thus, models like the presented one are essential for understanding and applicable prediction.

Part IV

Microscopic, oscillating fluid clusters



Chapter 18

Introduction

18.1 Motivation and literature

The previous part described wave propagation in residually saturated porous media by the combination of two scales. On the one hand, modeling of the continuous phases is known from previous investigations. On the other hand, the fluid clusters were implemented exemplarily, and a general theory was not presented, due to the focus on macroscopic wave theory. For this reason, the following part provides a detailed study and classification of oscillating fluid clusters on the microscale.

Fluid clusters have been of interest for hundreds of years [48, 49, 233]. Their physical description is based on fluid dynamics and unifies research areas such as thermodynamics and surface chemistry. The physical processes are reflected in various applications such as dispersive solutions in modern apparatus manufacture and sound-absorbing air blobs at offshore drilling. Fluid clusters have also attracted considerable attention in modern research. Numerous investigations deal with their static and dynamic behavior theoretically, experimentally, and numerically.

An early but fundamental treatise on oscillations of cylindrical liquid bridges is that of Sanz & Diez [183]. They provide analytical solutions and results of zero-gravity experiments from a space lab mission [135]. The non-linearity of droplet oscillations was studied by Kowalewski & Bruhn [111]. A boundary layer analysis was used by Higuera & Nicolás [91] for unsymmetrical oscillations of nearly inviscid liquid bridges at the limit of large capillary Reynolds numbers. Perez et al. [158] focused on the influence of the droplet shape on resonance frequencies, comparing experimental and theoretical results. Symmetric oscillation modes of liquid bridges under gravity load were investigated by Demin [50]. Motivated by blob mobilization, the analytic treatment and Lattice-Boltzmann models of Hilpert et al. [94] and Hilpert [92] concentrated on entrapped fluid clusters in slender pore channels. This was extended by Hsu et al. [96] with experimentally proven resonance effects.

Recent developments in numerical tools have also enriched the investigation of dynamic fluid clusters by a variety of approaches. Resonance of a single liquid bridge was found numerically by Liang & Kawaji [122] within a discrete range of excitation frequencies. A Level Set Function tracked the fluid-fluid interface. Situations such as spreading and meniscus forming were modeled in the numerical studies of Walkley et al. [215, 216] using an adaptive, arbitrary Lagrangian-Eulerian Finite Element method to solve the Stokes equations. It was followed by the contributions of Sak-

sono & Perić [177, 178] on the basis of a fundamental FE-description for static and dynamic fluid clusters, including stretched liquid bridges and freely oscillating blobs.

Much study in the past and in recent years has helped to improve our understanding of fluid cluster dynamics. Various questions have been addressed, ranging from equations for basic phenomena to sophisticated solution techniques. Nevertheless, important and interesting questions remain. With respect to wave propagation in residually saturated porous media, oscillating fluid clusters constitute one part of a more comprehensive, dynamic system. In special applications, their oscillations are important for ground water remediation or characterization [38, 92, 198]. The preceding chapter demonstrated that traveling waves are influenced by the existence of clusters in characteristic frequency bands (cf. Section 16.3). Therefore, it is of great importance to combine the complicated, dynamic cluster physics with more comprehensive models and characteristic observations. Thus, a key question arises: how can dynamic clusters be classified qualitatively and quantitatively?

The following chapters define the physical system of an oscillating fluid cluster and develop a theoretical model for its description. Subsequently, a typical classification with respect to dynamic parameters is presented and discussed. Finally, a systematic, numerical investigation quantifies a wide range of pinned cluster types with respect to several variations.

Parts of this study have been submitted previously for publication and may be available shortly after completion of this treatise in [116, 117].

It should be further noted that all physical properties belong to one scale, which corresponds to the microscale of the previous sections. No macroscale properties appear by default. Hence, a special distinction of microscale and macroscale properties is not required and avoided. The symbols are similar to those of the previous chapters and definitions are not renewed if they can be transferred directly from the previous chapters. The main difference is the omission of partial properties such as partial densities or pressure. A separate list of symbols for this part is given in the section on notations and conventions.

18.2 Aims and structure

The original motivation is to implement the fluid cluster behavior into a comprehensive wave model. Thus the aims are: (i) description of the clusters' dynamic behavior; (ii) classification of the clusters' oscillations; and (iii) quantification of the dynamic properties of specific clusters. The structure of the chapters is as follows.

- A theoretical description of a fluid cluster inside a porous matrix is derived first. This leads to a variational formulation of the governing equations and is specialized for a Newtonian liquid cluster in a rigid solid matrix and surrounded by a gas. The cluster is then reduced to a harmonic oscillator model. Various types of oscillations are classified and assumptions and modifications are discussed.
- A systematic, numerical study follows. Eigenfrequency and damping ratio are determined for various geometries and material parameters. Moreover, the role of clusters as oscillators in macroscopic wave propagation is discussed quantitatively.

-
- An oscillating liquid bridge is investigated experimentally and compared to the results of the theoretical and numerical studies.
 - The conclusion summarizes the qualitative and quantitative findings and illustrates the resonance effects in terms of wave propagation in porous media.

Chapter 19

Theory and variational formulation

The motion of a fluid cluster in a solid matrix is described mathematically. First, the physical situation is introduced and specific, geometric relationships of (sub-)manifolds are provided. Subsequently, physical relationships are reviewed and assumptions are justified. Momentum balances at the fluid-fluid interface and at the contact curve are emphasized because they govern the motion of oscillating fluid clusters.

Different variants of motions are distinguished such as pinned or sliding clusters. A special focus is on incompressible, Newtonian liquid clusters surrounded by a gas and captured in a rigid matrix. Finally, a variational formulation of mass and momentum conservation is presented. These equations determine the cluster's motion via calculation of pressure and velocity.

19.1 The physical system

The physical system of interest is a fluid cluster embedded in a solid matrix and surrounded by another immiscible fluid. The word cluster should include bridges, patches, columns, and all other kinds of fluid conglomerations. The solid matrix can be a package of grains or a skeleton such as synthetic foam. Symbol \mathfrak{s} denotes the solid. The cluster fluid is denoted by \mathfrak{l} and the surrounding fluid is denoted by \mathfrak{g} . This naming is motivated by a later specialization on a liquid cluster and a surrounding gas. Nevertheless, the general approach and theoretical development accounts for arbitrary fluid-fluid combinations (including liquids or gases on either side) and \mathfrak{l} and \mathfrak{g} only serve as a first symbolic distinction. The symbol \mathfrak{f} indicates that the relationship or statement is valid for both fluids $\mathfrak{f} \in \{\mathfrak{l}, \mathfrak{g}\}$.

Geometrically, the system can be divided into volumes, surfaces, and curves (also called lines), cf. Fig. 19.1. The volumes of the three bulk phases $\alpha \in \{\mathfrak{l}, \mathfrak{g}, \mathfrak{s}\}$ read \mathcal{V}_α . Surfaces can be subdivided into two categories. Interfaces between two bulk phases $\alpha \neq \beta$ write $\mathcal{A}_{\alpha\beta}$ for all pairs $\alpha\beta \in \{\mathfrak{l}\mathfrak{g}, \mathfrak{l}\mathfrak{s}, \mathfrak{g}\mathfrak{s}\}$. Boundary surfaces, intersecting bulk phase α at the spatial boundary of the investigated system, are written as $\mathcal{A}_\alpha^{\mathfrak{b}}$. The total boundary surface is composed of the single boundary surfaces $\mathcal{A}^{\mathfrak{b}} = \mathcal{A}_\mathfrak{l}^{\mathfrak{b}} \cup \mathcal{A}_\mathfrak{g}^{\mathfrak{b}} \cup \mathcal{A}_\mathfrak{s}^{\mathfrak{b}}$. In a similar manner to the surfaces, two types of curves can be distinguished. Three

bulk phases, or three interfaces respectively, meet in the contact curves $\mathcal{C}_{lg\text{s}}$. The boundary curves $\mathcal{C}_{\alpha\beta}^b$ confine the interfaces $\mathcal{A}_{\alpha\beta}$ at the system's boundary. For general relationships, ζ represents any arbitrary bulk phase α , surface $\alpha\beta$, or curve $\alpha\beta\gamma$. Additionally, normal vectors $\mathbf{n}^{\mathcal{A}\alpha\beta}$ point from phase α to phase β . A single index is used, $\mathbf{n}^{\mathcal{A}\alpha}$, to denote an arbitrary normal vector at the boundary of bulk phase α pointing outwards. At the boundary surfaces, normal vectors are denoted by \mathbf{n}_α^b . Normal vectors $\mathbf{n}^{\mathcal{C}\alpha\beta}$ at the contact line $\mathcal{C}_{lg\text{s}}$ are oriented outwards of the interfaces and tangential to them. This is similar at the boundary curves, where the defined normal vectors $\mathbf{n}_{\alpha\beta}^b$ also point outwards and are tangential to the interfaces.

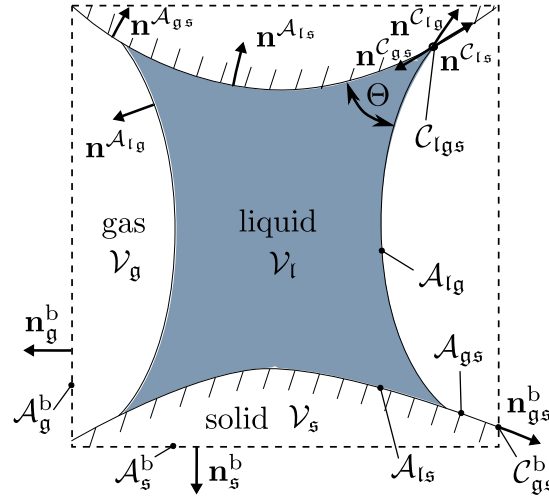


Figure 19.1: The physical system of a fluid cluster and corresponding definitions.

19.2 Geometric properties and relationships

Further definitions and relationships are provided for the geometry of an oscillating fluid cluster, because they are useful for formulation and interpretation of the physical laws. This section follows the work of Steinmann [200] in most parts, which provides a fundamental description of deformational continuum mechanics. Phase indices are avoided for better readability and because of general validity.

For each surface \mathcal{A} with normal vector \mathbf{n} , the surface unity tensor $\mathbf{I}^{\mathcal{A}}$ is defined as

$$\mathbf{I}^{\mathcal{A}} = \mathbf{I} - \mathbf{n} \otimes \mathbf{n}, \quad (19.1)$$

where $\mathbf{I} = \delta_{ij} \mathbf{e}_i \otimes \mathbf{e}_j$, $1 \leq i, j \leq 3$, is the 2nd order unity tensor. With it, surface gradient and surface divergence follow as

$$\text{grad}^{\mathcal{A}}(\bullet) = \text{grad}(\bullet) \cdot \mathbf{I}^{\mathcal{A}}, \quad (19.2)$$

$$\text{div}^{\mathcal{A}}(\bullet) = \text{grad}^{\mathcal{A}}(\bullet) : \mathbf{I} = \text{grad}^{\mathcal{A}}(\bullet) : \mathbf{I}^{\mathcal{A}}. \quad (19.3)$$

The total curvature κ (twice the mean curvature) is then defined as

$$\kappa := -\operatorname{div}^{\mathcal{A}}(\mathbf{n}), \quad (19.4)$$

with

$$\operatorname{div}^{\mathcal{A}}\mathbf{I}^{\mathcal{A}} = \kappa \mathbf{n}. \quad (19.5)$$

The surface divergence theorem is an analogue of the general divergence theorem for a two-dimensional hyperspace \mathcal{A} , embedded in three-dimensional space, and limited by the curve \mathcal{C} . It is written as

$$\int_{\mathcal{A}} \operatorname{div}^{\mathcal{A}}(\bullet) \, da = \int_{\mathcal{C}} (\bullet) \cdot \mathbf{n}^{\mathcal{C}} \, dc - \int_{\mathcal{A}} \kappa(\bullet) \cdot \mathbf{n} \, da, \quad (19.6)$$

where \mathbf{n} denotes the normal vector field of surface \mathcal{A} and $\mathbf{n}^{\mathcal{C}}$ denotes the normal vector field of the surface's boundary \mathcal{C} , pointing outwards of the surface and tangential to it.

An infinitesimal change of an initial surface area \mathcal{A} under displacement \mathbf{u} can be written as²¹, cf. [83],

$$\delta\mathcal{A} = \int_{\mathcal{A}} \operatorname{div}^{\mathcal{A}}\mathbf{u} \, da. \quad (19.7)$$

The above expressions relate to the initial geometry \mathcal{A} , i.e. before variational deformation.

The description of a curve can be carried out by its Frenet frame, i.e. the orthogonal tangent, normal, and binormal unit vectors, \mathbf{e}_t , \mathbf{e}_n , and $\mathbf{e}_m = \mathbf{e}_t \times \mathbf{e}_n$. The curve unity tensor can be then introduced as

$$\mathbf{I}^{\mathcal{C}} = \mathbf{I} - \mathbf{e}_n \otimes \mathbf{e}_n - \mathbf{e}_m \otimes \mathbf{e}_m = \mathbf{e}_t \otimes \mathbf{e}_t \quad (19.8)$$

while the curve gradient and curve divergence follow as

$$\operatorname{grad}^{\mathcal{C}}(\bullet) = \operatorname{grad}(\bullet) \cdot \mathbf{I}^{\mathcal{C}}, \quad (19.9)$$

$$\operatorname{div}^{\mathcal{C}}(\bullet) = \operatorname{grad}^{\mathcal{C}}(\bullet) : \mathbf{I} = \operatorname{grad}^{\mathcal{C}}(\bullet) : \mathbf{I}^{\mathcal{C}}. \quad (19.10)$$

The line curvature is then defined as

$$\kappa_c := -\operatorname{div}^{\mathcal{C}}(\mathbf{e}_n), \quad (19.11)$$

where $\operatorname{div}^{\mathcal{C}}\mathbf{I}^{\mathcal{C}} = \kappa_c \mathbf{e}_n$. If the line curvature κ_c vanishes, vectors \mathbf{e}_n and \mathbf{e}_m are not uniquely defined with respect to rotations around the \mathbf{e}_t -axis.

For a curve lying in a surface with normal vector \mathbf{n} , the tangential space of the surface is spanned by \mathbf{e}_t and $\mathbf{t}_g := \mathbf{e}_t \times \mathbf{n}$. In this special case, the line curvature can be split into a geodesic and a normal curvature of the line, κ_g and κ_n , as

$$\kappa_c \mathbf{e}_n = \kappa_n \mathbf{n} + \kappa_g \mathbf{t}_g. \quad (19.12)$$

The normal curvature represents the part that is already caused by the curved surface. The geodesic curvature represents the curvature with respect to the surface.

²¹Note the similar mathematical structure for volumes. An infinitesimal change of volume can be related to $\operatorname{div} \mathbf{u}$ instead of $\operatorname{div}^{\mathcal{A}} \mathbf{u}$, cf. Eq. (5.9) for the case of incompressibility.

19.3 Structure of the set of equations

To characterize the dynamic behavior of an oscillating fluid cluster, its movement in time t has to be known. This knowledge requires experimental data or an accurate description by physical laws that can be solved for certain systems. A framework for the latter will be developed in this section.

The current position \mathbf{x}_ζ of any bulk phase, surface, or curve $\zeta \in \{\alpha, \alpha\beta, \alpha\beta\gamma\}$ can be determined from the balance of momentum. This implies a determination of the further unknowns, density $\rho^{\zeta R}$ (1 scalar) and symmetric Cauchy stress tensor $\mathbf{T}^{\zeta R}$ (6 unknowns, symmetry is assumed due to balance of angular momentum). Moreover, the Cauchy stress tensor $\mathbf{T}^{\zeta R}$ can be split into a pressure related part, $-p^\zeta \mathbf{I}$, and extra stresses, $\mathbf{T}_E^{\zeta R}$.

As a first assumption, temperature changes are assumed to be insignificant (in particular, their influence on material properties) although the system is dissipative by nature. The only information required is that about the initial temperature $\vartheta_0 = \vartheta(t_0)$. Therefore, conservation of energy is not required for modeling. The ten unknowns of \mathbf{x}_ζ , $\rho^{\zeta R}$, and $\mathbf{T}^{\zeta R}$ are then determined by: balance of momentum (3), balance of mass (1), and constitutive relationships for the Cauchy stress tensor $\mathbf{T}^{\zeta R}$ (6) including an equation of state for the pressure and a relationship between extra stresses and deformation or velocity gradient respectively.

The following sections will present the leading equations, their physical origins, justified assumptions, and the final mathematical framework. Note that the used structure slightly differs from classical continuum mechanics, because it is geared towards the physical complexity and focuses on the driving physical processes.

19.4 Mass balance

No mass exchange is assumed to appear between the constituents due of evaporation or other sources. Hence, mass conservation holds for each single bulk phase α separately and local conservation of mass is written as

$$\frac{\partial}{\partial t} \rho^{\alpha R} + \operatorname{div} (\rho^{\alpha R} \mathbf{v}_\alpha) = 0. \quad (19.13a)$$

In case of incompressibility, i.e. $\rho^{\alpha R} = \text{const.}$, it reduces to the local volume balance

$$\operatorname{div} (\mathbf{v}_\alpha) = 0. \quad (19.13b)$$

At a later stage, it will be considered that liquids can usually be assumed to be incompressible more likely than gases.

Interfaces and contact curves should have no own mass or density in the presented model, because their mass distribution becomes important at smaller scales only, for example, for molecular dynamics. In the present case, the mass is approximately distributed among the bulk phases only, cf. [79, 144, 148].

19.5 Relationships between stress and deformation

This section is put in front of the momentum balances, because later assumptions and simplifications are principally based on the stress formulations and understanding of the interfaces and contact curves.

19.5.1 Fluids

For a barotropic fluid $\mathfrak{f} \in \{\mathfrak{l}, \mathfrak{g}\}$, pressure, density, and temperature are related by the equation of state. For neglected temperature changes, density and pressure are related in the linearized case by the fluids' bulk modulus $K^{\mathfrak{f}}$ of the initial state as

$$\frac{\rho^{\mathfrak{f}R} - \rho_0^{\mathfrak{f}R}}{\rho_0^{\mathfrak{f}R}} = \frac{p^{\mathfrak{f}R} - p_0^{\mathfrak{f}R}}{K^{\mathfrak{f}}}. \quad (19.14)$$

The fluids \mathfrak{f} are further assumed to be Newtonian fluids. Hence, their extra stress tensor relates to the velocity gradient $\text{grad } \mathbf{v}_{\mathfrak{f}}$ and dynamic viscosity $\eta^{\mathfrak{f}R}$ (for vanishing volume viscosity) as

$$\mathbf{T}_E^{\mathfrak{f}R} = \eta^{\mathfrak{f}R} \left(\left(\text{grad } \mathbf{v}_{\mathfrak{f}} + \text{grad}^T \mathbf{v}_{\mathfrak{f}} \right) - \frac{2}{3} \text{div}(\mathbf{v}_{\mathfrak{f}}) \mathbf{I} \right). \quad (19.15)$$

The (total) Cauchy stress tensor of a fluid phase then becomes

$$\mathbf{T}^{\mathfrak{f}R} = \mathbf{T}_E^{\mathfrak{f}R} - p^{\mathfrak{f}R} \mathbf{I} = \eta^{\mathfrak{f}R} \left(\left(\text{grad } \mathbf{v}_{\mathfrak{f}} + \text{grad}^T \mathbf{v}_{\mathfrak{f}} \right) - \frac{2}{3} \text{div}(\mathbf{v}_{\mathfrak{f}}) \mathbf{I} \right) - p^{\mathfrak{f}R} \mathbf{I} \quad (19.16a)$$

and simplifies for an incompressible fluid to, cf. Eq. (19.13b),

$$\mathbf{T}^{\mathfrak{f}R} = \eta^{\mathfrak{f}R} \left(\text{grad } \mathbf{v}_{\mathfrak{f}} + \text{grad}^T \mathbf{v}_{\mathfrak{f}} \right) - p^{\mathfrak{f}R} \mathbf{I}. \quad (19.16b)$$

Pressure $p^{\mathfrak{f}R}$ generally depends on deformation via density and mass balance and has a negative sign, following the conventions of classical continuum mechanics with positive tensile stresses. In the case of incompressibility, $p^{\mathfrak{f}R}$ is not related to density via a constitutive law, cf. Eq. (19.14). Instead, it plays the role of a Lagrange parameter and is determined by the boundary conditions. Moreover, linear oscillations are assumed, causing arbitrarily small velocities and Reynolds numbers. Thus, turbulent flow effects are neglected.

19.5.2 Solid

The stress tensor $\mathbf{T}^{\mathfrak{s}R}$ of a Hookean material is related to the linearized strain tensor $\boldsymbol{\varepsilon}_{\mathfrak{s}} = \frac{1}{2}(\text{grad } \mathbf{u}_{\mathfrak{s}} + \text{grad}^T \mathbf{u}_{\mathfrak{s}})$ with solid displacement $\mathbf{u}_{\mathfrak{s}} = (\mathbf{x}_{\mathfrak{s}} - \mathbf{x}_{\mathfrak{s},0})$ via the material Lamé parameters μ^{grains} and λ^{grains} as

$$\mathbf{T}^{\mathfrak{s}R} = 2\mu^{\text{grains}} \boldsymbol{\varepsilon}_{\mathfrak{s}} + \lambda^{\text{grains}} \text{tr}(\boldsymbol{\varepsilon}_{\mathfrak{s}}) \mathbf{I}. \quad (19.17)$$

This approach can be further split into a volumetric part ($p^{\mathfrak{s}R} = -1/3 \text{trace}(\mathbf{T}^{\mathfrak{s}R})$) and a deviatoric part ($\mathbf{T}_{\text{dev}}^{\mathfrak{s}R} = \mathbf{T}^{\mathfrak{s}R} + p^{\mathfrak{s}R} \mathbf{I}$) and it can also be extended to a more sophisticated rheology. Nevertheless, its current form is sufficient for the further investigation.

19.5.3 Interfaces - surface energy/tension

A molecule inside a bulk material is equally attracted in all directions by the surrounding molecules. However, this situation changes at the interface with a second material. The attraction forces can differ at both sides of the interface. For example, a water molecule at the surface of a water drop is differently attracted by water molecules inside the drop compared to air molecules outside. Hence, energy is required or released whenever a molecule moves from the interior bulk to the interface and vice versa. This energy - necessary to create the interfacial area between two phases α and β - is called surface energy $\sigma^{\alpha\beta}$. It is an energy per interfacial area with units of N m^{-1} .

A fluid cluster that tries to minimize its energy, therefore, tries to minimize its surface area. Thus, fluid drops shape like perfect spheres in the absence of further influences. Because the interfacial area only changes due to tangential strain, a resistance against tangential stretch of the surface is the result of surface energy. Hence, it is also called surface tension, a force per length acting tangential to the interface. This interpretation is often used for modeling on a length scale, where the material is assumed to be continuous and which is connected to the thermodynamic definition of pressure.

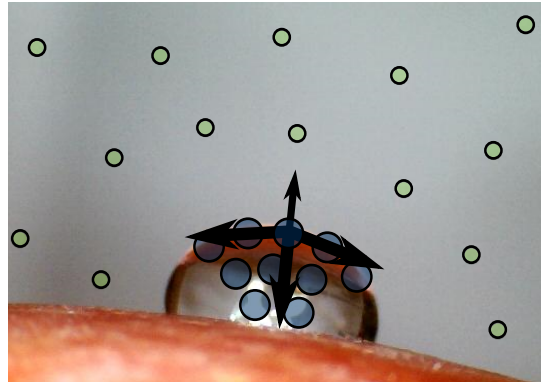


Figure 19.2: Idealized sketch of surface tension as molecular attraction for a water drop on an apple skin.

Generally, surface energy can depend on the two kinds of bulk materials α and β , temperature, density, and geometry. An influence of the geometry can be neglected if the local radii are much bigger than the Tolman-length $\delta_{\text{Tolman}} \leq 10^{-9}$ m [208]. This is assumed for the present investigations. It implies that the surface does not differ significantly from a plane on the molecular scale and the surface molecules are approximately half attracted by each of both materials (the tangential forces sketched in Fig. 19.2 would be parallel and cancel each other out).

A dependence of surface energy on temperature and density changes is also assumed to be of small influence for a linear theory. In conclusion, $\sigma^{\alpha\beta}$ is a constant material parameter in the following investigations. The corresponding interface stress $\mathbf{T}^{\alpha\beta R}$ acts tangentially to the interface and is

$$\mathbf{T}^{\alpha\beta R} = \sigma^{\alpha\beta} \mathbf{I}^A. \quad (19.18)$$

Interpretation as variational work

For better physical understanding, the change of energy, due to surface area variation $\delta\mathcal{A}$ and via displacement \mathbf{u} , can be rewritten as, cf. Eq. (19.5), Eq. (19.6), and Eq. (19.7),

$$\begin{aligned}\sigma^{\alpha\beta} \delta\mathcal{A} &= \sigma^{\alpha\beta} \int_{\mathcal{A}} \operatorname{div}^{\mathcal{A}} \mathbf{u} \, da \\ &= \sigma^{\alpha\beta} \int_{\mathcal{C}} \mathbf{u} \cdot \mathbf{n}^{\mathcal{C}} \, dc - \sigma^{\alpha\beta} \int_{\mathcal{A}} \kappa \mathbf{u} \cdot \mathbf{n} \, da \\ &= \sigma^{\alpha\beta} \int_{\mathcal{C}} \mathbf{u} \cdot \mathbf{n}^{\mathcal{C}} \, dc - \int_{\mathcal{A}} \operatorname{div}^{\mathcal{A}}(\sigma^{\alpha\beta} \mathbf{I}^{\mathcal{A}}) \cdot \mathbf{u} \, da.\end{aligned}$$

The first equation underlines that only the tangential part of strain affects the energy variation. Proceeding with a further split, the second line consists of two parts. The first term shows the influence of the moving boundary \mathcal{C} . For flat surfaces with $\kappa = 0$, for example, a first variation of area only occurs if the boundaries of the flat surface move. It can be compared to elongation of an elastic, plain tissue at its ends.

The second term of the second line accounts for displacements inside the interface. It shows that only normal displacements of the interface influence the area and that it is directly proportional to curvature κ . This effect can be compared to inflation of a soap bubble with fixed borders. In the third line, the second term is replaced by a stress divergence times displacement as it is known from variational calculus. As can be seen, the stress tensor coincides with the expression in Eq. (19.18).

Comparison with other surface models

Note that further dependencies on strain (elastic behavior) or velocity (viscous behavior) are excluded for $\sigma^{\alpha\beta}$ that accounts for the pure attraction difference of both materials. Moreover, shear effects are not taken into account because pure shearing does not change the area. This exception includes shearing tangential to the interface as well as normal to it. Such behavior is different for other surface models such as solid shell structures.

For an analogue example, consider the energy variation for an ideal gas under compression being $p^{\text{gR}} \delta\mathcal{V}$, p^{gR} determining the pressure and the bulk modulus at the same time. In the same way $\sigma^{\alpha\beta}$ counteracts the change of surface area in the tangential directions of $\mathbf{I}^{\mathcal{A}}$, p^{gR} counteracts the change of volume acting in all spatial directions according to \mathbf{I} .

19.5.4 Curves - curve energy/tension

Similar to volumes and surfaces, a line energy or curve energy (or, less common, curve tension) γ^{lgS} is introduced for the contact curve, acting tangential to the curve as

$$\mathbf{T}^{\text{lgSR}} = \gamma^{\text{lgS}} \mathbf{I}^{\mathcal{C}}. \quad (19.19)$$

This energy is connected to a length change of the curve and has the unit of energy/length, i.e. N. It will be demonstrated below that a classical curve energy is not required for the modeling of oscillating fluid clusters, because the attraction potentials are covered by the interface energies and surface irregularities will be modeled by an external friction-like influence.

19.6 Variational approach and momentum balance of bulk volumes

19.6.1 Comprehensive variational approach

In addition to the mass balances, the momentum balances constitute the second part of the major leading equations. A general variational formulation allows to unify the momentum balances of all components, i.e. volumes, surfaces, and curves. It follows from [200] that

$$\begin{aligned}
\delta W = & \sum_{\alpha \in \{\text{l, g, s}\}} \int_{\mathcal{V}_\alpha} \left[-\rho^{\alpha R} \frac{d^2}{dt^2} \mathbf{x}_\alpha + \operatorname{div} \mathbf{T}^{\alpha R} + \mathbf{f}^\alpha \right] \cdot \delta \hat{\mathbf{v}} \, dv \\
& + \sum_{\alpha\beta \in \{\text{lg, ls, gs}\}} \int_{\mathcal{A}_{\alpha\beta}} \left[-\rho^{\alpha\beta R} \frac{d^2}{dt^2} \mathbf{x}_{\alpha\beta} + \operatorname{div}^{\mathcal{A}} \mathbf{T}^{\alpha\beta R} + \mathbf{f}^{\alpha\beta} - \sum_{\substack{\text{adjacent bulk} \\ \text{volumes } \xi \in \{\alpha, \beta\}}} \mathbf{T}^{\xi R} \cdot \mathbf{n}^{\mathcal{A}_\xi} \right] \cdot \delta \hat{\mathbf{v}} \, da \\
& + \sum_{\alpha \in \{\text{l, g, s}\}} \int_{\mathcal{A}_\alpha^b} \left[-\rho^{b, \alpha R} \frac{d^2}{dt^2} \mathbf{x}_{b, \alpha} + \operatorname{div}^{\mathcal{A}} \mathbf{T}^{b, \alpha R} + \mathbf{f}^{b, \alpha} - \sum_{\text{adjacent regions } \xi} \mathbf{T}^{\xi R} \cdot \mathbf{n}^{\mathcal{A}_\xi} \right] \cdot \delta \hat{\mathbf{v}} \, da \\
& + \int_{\mathcal{C}_{\text{lg s}}} \left[-\rho^{\text{lg s} R} \frac{d^2}{dt^2} \mathbf{x}_{\text{lg s}} + \operatorname{div}^{\mathcal{C}} \mathbf{T}^{\text{lg s} R} + \mathbf{f}^{\text{lg s}} - \sum_{\substack{\text{adjacent interfaces} \\ \xi \in \{\text{lg, ls, gs}\}}} \mathbf{T}^{\xi \chi R} \cdot \mathbf{n}^{\mathcal{C}_{\xi \chi}} \right] \cdot \delta \hat{\mathbf{v}} \, dc \\
& + \sum_{\alpha\beta \in \{\text{lg, ls, gs}\}} \int_{\mathcal{C}_{\alpha\beta}^b} \left[-\rho^{b, \alpha\beta R} \frac{d^2}{dt^2} \mathbf{x}_{b, \alpha\beta} + \operatorname{div}^{\mathcal{C}} \mathbf{T}^{b, \alpha\beta R} + \mathbf{f}^{b, \alpha\beta} - \sum_{\substack{\text{adjacent} \\ \text{surfaces } \xi \chi}} \mathbf{T}^{\xi \chi R} \cdot \mathbf{n}^{\mathcal{C}_{\xi \chi}} \right] \cdot \delta \hat{\mathbf{v}} \, dc
\end{aligned} \tag{19.20}$$

vanishes for all variations $\delta \hat{\mathbf{v}}$. The relationship between total (material) and partial time derivative

$$\frac{d^2}{dt^2} \mathbf{x}_\zeta = \frac{\partial}{\partial t} \mathbf{v}_\zeta + \operatorname{grad}(\mathbf{v}_\zeta) \cdot \mathbf{v}_\zeta. \tag{19.21}$$

will be used in the final equations to express acceleration in terms of velocity becoming a primary variable.

The validity of Eq. (19.20) for arbitrary variations $\delta \hat{\mathbf{v}}$ yields local validity of the individual parts. It results in the required set of equations and boundary conditions, technically. Nevertheless, this section aims at the physical description and the individual equations are therefore investigated in more detail. Special attention is given to two key aspects by separate sections: momentum balance at interfaces, resulting in the Young-Laplace equation, and momentum balance at the contact curve, resulting in the definition of Young's contact angle. These sections are comprehensively discussed because they determine the characteristic behavior of dynamic liquid clusters.

19.6.2 Momentum balance for bulk volumes

For bulk volumes \mathcal{V}_α , the local momentum balance reads

$$\rho^{\alpha R} \frac{d^2}{dt^2} \mathbf{x}_\alpha - \operatorname{div} \mathbf{T}^{\alpha R} = \mathbf{f}^\alpha,$$

where the volume forces are typically gravity forces

$$\mathbf{f}^\alpha = \rho^{\alpha R} \mathbf{g}.$$

Solid

Using the constitutive law of a Hookean material, Eq. (19.17), the local momentum balance for the solid results in the Lamé-Navier equations

$$\rho^{sR} \frac{d^2}{dt^2} \mathbf{u}_s - (\mu^{\text{grains}} \operatorname{div} \operatorname{grad} \mathbf{u}_s + (\mu^{\text{grains}} + \lambda^{\text{grains}}) \operatorname{grad} \operatorname{div} \mathbf{u}_s) = \rho^{sR} \mathbf{g}.$$

Fluids

The constitutive law for a Newtonian fluid, Eq. (19.16a), yields the local momentum balance for compressible fluids $\mathfrak{f} \in \{\mathfrak{l}, \mathfrak{g}\}$

$$\begin{aligned} \rho^{fR} \left(\frac{\partial}{\partial t} \mathbf{v}_f + \operatorname{grad}(\mathbf{v}_f) \cdot \mathbf{v}_f \right) + \operatorname{grad} p^{fR} \\ - \eta^{fR} \operatorname{div} \left(\left(\operatorname{grad} \mathbf{v}_f + \operatorname{grad}^T \mathbf{v}_f \right) - \frac{2}{3} \operatorname{div}(\mathbf{v}_f) \mathbf{I} \right) = \rho^{fR} \mathbf{g} \end{aligned} \quad (19.22a)$$

and for incompressible fluids, cf. Eq. (19.16b),

$$\rho^{fR} \left(\frac{\partial}{\partial t} \mathbf{v}_f + \operatorname{grad}(\mathbf{v}_f) \cdot \mathbf{v}_f \right) + \operatorname{grad} p^{fR} - \eta^{fR} \operatorname{div} \left(\operatorname{grad} \mathbf{v}_f + \operatorname{grad}^T \mathbf{v}_f \right) = \rho^{fR} \mathbf{g}. \quad (19.22b)$$

Together with the mass balance, Eq. (19.13a) and Eq. (19.13b) respectively, the local momentum balance constitutes the well-known Navier-Stokes equations.

Simplifications

Up to now, the set of equations has a high complexity for analytical or numerical solutions. A few important assumptions can be made, in which $\tilde{\bullet}$ indicates a representative, characteristic value of \bullet . In particular, the solid's deformation will be disregarded because of its relatively high inertia and low formability. This assumption is also used in virtually all other research on this topic, although it is not explicitly mentioned. Furthermore, the relatively low inertia and viscosity of the surrounding gas makes its influence negligible. A later comparison with results from literature will support the following assumptions and justifications, cf. Section 20.2.2.

Rigid solid The fluid cluster is connected with the solid and interacts with the neighboring region, transferring momentum and inducing strain. Such an interacting region can consist of adjacent grains of soil or beams of a foam. Let this region have a characteristic length \tilde{l} and volume $\tilde{V}_s \approx \tilde{l}^3$. A grain diameter is an example for \tilde{l} . Very narrow solid structures such as shells or wires should be neglected, so that the characteristic length is not smaller than the characteristic cluster radius, $\tilde{l} \geq \tilde{R}$.

A representative strain component, denoted by $\tilde{\varepsilon}_s$, can then be approximatively expressed by the ratio of length change to initial length $\tilde{\varepsilon}_s \approx (\tilde{l} - \tilde{l}_0)/\tilde{l}_0$. With it, the elastic strain energy of the solid is not less than the order of $\tilde{E}_s \approx \tilde{V}_s \tilde{K}^{\text{grains}} \tilde{\varepsilon}^2 \approx \tilde{l}_0^3 \tilde{K}^{\text{grains}} ((\tilde{l} - \tilde{l}_0)/\tilde{l}_0)^2 \approx \tilde{l}_0 \tilde{K}^{\text{grains}} (\tilde{l} - \tilde{l}_0)^2$. $\tilde{K}^{\text{grains}}$ represents the solid's elastic stiffness with respect to deformation such as a characteristic bulk modulus.

The energy of creating an interfacial area between both fluids, with characteristic radius \tilde{R} and surface tension $\tilde{\sigma}^{\text{lg}}$, is of the order of $\tilde{E}_{\text{lg}} \approx \tilde{\sigma}^{\text{lg}} \tilde{R}^2$. Let this energy be (completely or incompletely) transferred to the surrounding solid, i.e. $\tilde{E}_s \leq \tilde{E}_{\text{lg}}$. This yields, with typical properties of $\tilde{\sigma}^{\text{lg}} \leq 10^{-1} \text{ N m}^{-1}$, $\tilde{K}^{\text{grains}} \approx 10^{10} \text{ N m}^{-2}$, and $\tilde{l} \geq \tilde{R} \geq 10^{-6} \text{ m}$,

$$\frac{\tilde{l} - \tilde{l}_0}{\tilde{R}} \leq \sqrt{\frac{\tilde{\sigma}^{\text{lg}}}{\tilde{K}^{\text{grains}} \tilde{l}_0}} \leq 10^{-2} \ll 1 \quad \text{and} \quad \frac{d\tilde{l}}{d\tilde{R}} \approx \sqrt{\frac{\tilde{\sigma}^{\text{lg}}}{\tilde{K}^{\text{grains}} \tilde{l}_0}} \ll 1. \quad (19.23)$$

As a result, the solid's volumetric and shear deformation are negligible small compared to the fluid under the load of capillary forces. This is in accordance with everyday experience. In contrast to solids, typical fluids have no resistance against shape change and accommodate surface tension. Consequently, the solid is assumed to be rigid for the further considerations.

Inert solid The solid structure enclosing the fluid cluster should have a significantly larger mass (neglecting structures such as shells, wires or fur), i.e. $\tilde{m}_s \gg \tilde{m}_l$. During oscillations, due to capillary forces, the fluid cluster is accelerated and not more energy is passed to acceleration of the solid. Comparing the corresponding inertia terms, $\tilde{m}_s (d^2 \mathbf{x}_s/dt^2) \leq \tilde{m}_l (d^2 \mathbf{x}_l/dt^2)$, shows that the solid acceleration is relatively small with respect to the fluid cluster, $\|d^2 \mathbf{x}_s/dt^2\| / \|d^2 \mathbf{x}_l/dt^2\| \leq \tilde{m}_l/\tilde{m}_s \ll 1$. This shows that the solid cannot only be assumed to be rigid but also to be unmoved. The solid's influence reduces to that of a rigid boundary and saves further calculation.

Negligible gas as second fluid phase Density and viscosity of a gas at atmospheric conditions are much smaller than the ones of a liquid cluster, $\tilde{\rho}^{\text{gR}} \ll \tilde{\rho}^{\text{lR}}$, $\tilde{\eta}^{\text{gR}} \ll \tilde{\eta}^{\text{lR}}$. Furthermore, the movement of the gas phase near the liquid cluster is coupled to the cluster's movement itself because the behavior of both fluids is connected via the interface's deformation.

Hence, accelerations and velocities as well as their spatial derivatives are assumed to be of same order, $d^2 \mathbf{x}_g/dt^2 \approx d^2 \mathbf{x}_l/dt^2$ and $\text{div grad}(\mathbf{v}_g) \approx \text{div grad}(\mathbf{v}_l)$. At greater distances, the surrounding fluid is assumed to be in rest, so that velocity and acceleration terms vanish. As a first result, corresponding inertia terms, viscous terms, and body forces are negligible for the gas phase as $\tilde{\rho}^{\text{gR}} (d^2 \mathbf{x}_g/dt^2) \ll \tilde{\rho}^{\text{lR}} (d^2 \mathbf{x}_l/dt^2)$, $\tilde{\eta}^{\text{gR}} \text{div grad}(\mathbf{v}_g) \ll \tilde{\eta}^{\text{lR}} \text{div grad}(\mathbf{v}_l)$, $\tilde{\rho}^{\text{gR}} \mathbf{g} \ll \tilde{\rho}^{\text{lR}} \mathbf{g}$. Because these terms also determine the pressure gradient via momentum conservation, pressure gradients inside the gas phase are assumed to be of smaller influence than in the liquid cluster as well. In conclusion, local changes of gas stress are neglected with respect to their effect on the liquid cluster's energy and momentum. The exchange of momentum between liquid cluster and the surrounding fluid is therefore neglected if the second fluid is a gas. The surrounding fluid's influence reduces to a constant surrounding pressure p^{ext} .

19.7 Momentum balance at surfaces

The balance of momentum is now evaluated for interfaces and boundary surfaces. The Young-Laplace equation results from the equilibrium momentum balance at the fluid-fluid interface.

19.7.1 Momentum balance at interfaces and the Young-Laplace equation

At each interface $\mathcal{A}_{\alpha\beta}$, the local momentum balance reads

$$\rho^{\alpha\beta R} \frac{d^2}{dt^2} \mathbf{x}_{\alpha\beta} - \operatorname{div}^{\mathcal{A}} \mathbf{T}^{\alpha\beta R} + \sum_{\substack{\text{adjacent bulk} \\ \text{volumes } \xi \in \{\alpha, \beta\}}} \mathbf{T}^{\xi R} \cdot \mathbf{n}^{\mathcal{A}\xi} = \mathbf{f}^{\alpha\beta}. \quad (19.24)$$

Mass is only distributed to the bulk phases in this model, i.e. $\rho^{\alpha\beta R} = 0$ and $\rho^{\alpha\beta R} \mathbf{g} = \mathbf{f} = \mathbf{0}$. Moreover, the solid is assumed to be rigid and undeformed, so that the solid-fluid interfaces are also in rest and do not need to be considered for calculations. Replacing $\operatorname{div}^{\mathcal{A}} \mathbf{T}^{\alpha\beta R}$ with eqs. Eq. (19.18), Eq. (19.1), and Eq. (19.4), using $\mathbf{n}^{\mathcal{A}\alpha\beta} = \mathbf{n}^{\mathcal{A}\alpha} = -\mathbf{n}^{\mathcal{A}\beta}$, and splitting the stress tensor into pressure and extra stresses yields

$$\left(-\mathbf{T}_E^{\alpha R} + \mathbf{T}_E^{\beta R} \right) \cdot \mathbf{n}^{\mathcal{A}\alpha} + (p^{\alpha R} - p^{\beta R} + \sigma^{\alpha\beta} \kappa) \mathbf{n}^{\mathcal{A}\alpha} = \mathbf{0} \quad (19.25)$$

for the fluid-fluid interfaces. The curvature $\kappa = -\operatorname{div}^{\mathcal{A}}(\mathbf{n}^{\mathcal{A}\alpha\beta})$ is related to the normal vector pointing from inner fluid α to outer fluid β . Without viscous shear stresses $\mathbf{T}_E^{\alpha R}$ and $\mathbf{T}_E^{\beta R}$, cf. Eq. (19.15), this expression results in the famous Young-Laplace equation that relates the pressure difference to surface tension times curvature.

$$p^{\beta R} - p^{\alpha R} = \sigma^{\alpha\beta} \kappa \quad (19.26)$$

The influence of the surrounding fluid becomes negligible if it is a gas, as shown in the paragraph above, i.e. $\mathbf{T}_E^g \cdot \mathbf{n}^{\mathcal{A}\alpha} \approx \mathbf{0}$, $p^{gR} \approx p^{\text{ext}} = \text{const.}$

Simplifications

Incompressible liquids The fluid clusters' oscillations are driven by the stiffness that is due to surface tension times curvature, cf. the resulting pressure difference in Eq. (19.26). In the further investigations, the corresponding pressure difference is assumed to be of the order of $\Delta\tilde{p} = \tilde{\sigma}^{\text{lg}}/\tilde{R} \approx (10^{-1} \text{ N m}^{-1})/(10^{-6} \text{ m}) = 10^5 \text{ N m}^{-2}$ or smaller. The fluid's bulk modulus \tilde{K}^{l} relates it to the volume change of the cluster by $\Delta\tilde{p} = -\tilde{K}^{\text{l}}\Delta\tilde{V}/\tilde{V}$. The combination of these relationships yields $|\Delta\tilde{V}/\tilde{V}| \approx \tilde{\sigma}^{\text{lg}}/(\tilde{R}\tilde{K}^{\text{l}})$. For typical liquids, for example, water and air, with $\tilde{\sigma}^{\text{lg}} \approx 10^{-1} \text{ N m}^{-1}$, $\tilde{K}^{\text{l}} \approx 10^9 \text{ N m}^{-2}$, and $\tilde{R} \geq 10^{-6} \text{ m}$, the relative volume change is of the order of

$$\left| \Delta\tilde{V}/\tilde{V} \right| \approx \tilde{\sigma}^{\text{lg}}/(\tilde{R}\tilde{K}^{\text{l}}) \leq 10^{-4}. \quad (19.27)$$

Hence, the liquid volume is assumed to remain constant. Consequently, density changes are negligible because fluid cluster mass is constant and $|\Delta\tilde{\rho}^{\text{LR}}/\tilde{\rho}^{\text{LR}}| \approx |\Delta\tilde{V}/\tilde{V}|$. The assumption of a constant density simplifies the balances of mass and momentum and eliminates the need for an equation of state. The initial pressure can also be set to an arbitrary reference value when using the appropriate initial density value.

Furthermore, this assumption prevents the propagation of local sound waves that have wavelengths much smaller than R and occur at relatively small time spans. As a result, local sound propagation processes are not considered and do not need to be calculated. This is consistent with the long wavelength approximation for macroscopic theories, in which such smaller-scale waves are not stimulated.

19.7.2 Momentum balance at boundary surfaces

Pure boundary surfaces are artificial boundaries of the physical system, which is why they miss mass and surface energy by default. Acceleration terms, volume forces, and surface stresses vanish. The two adjacent regions are the inner bulk volume of solid, liquid, or gas and the surrounding environment with opposite normal vectors. Let $\mathbf{t}^{\text{ext}} := \mathbf{T}^{\text{ext}} \cdot \mathbf{n}^{\text{ext}}$ be the forces due to the external load of the surrounding environment and normal on the system's boundary. The local momentum balance

$$\rho^{\text{b},\alpha R} \frac{d^2}{dt^2} \mathbf{x}_{\text{b},\alpha} - \text{div}^{\mathcal{A}} \mathbf{T}^{\text{b},\alpha R} - \mathbf{f}^{\text{b},\alpha} + \sum_{\text{adjacent regions } \xi} \mathbf{T}^{\xi R} \cdot \mathbf{n}^{\mathcal{A}\xi} = \mathbf{0} \quad (19.28)$$

becomes the typical boundary condition (Cauchy theorem)

$$\mathbf{T}^{\alpha R} \cdot \mathbf{n}^{\mathcal{A}\text{b}} = \mathbf{t}^{\text{ext}}. \quad (19.29)$$

If the boundary surface coincides with an interface between two bulk phases, the surrounding environment corresponds to the surrounding fluid and both conditions become

$$\mathbf{T}_E^{\alpha R} \cdot \mathbf{n}^{\mathcal{A}\alpha} - (p^{\alpha R} - \sigma\kappa) \mathbf{n}^{\mathcal{A}\alpha} = -\mathbf{t}^{\text{ext}} = \mathbf{T}_E^{\beta R} \cdot \mathbf{n}^{\mathcal{A}\alpha} - p^{\beta R} \mathbf{n}^{\mathcal{A}\alpha}. \quad (19.30)$$

19.8 Momentum balance at curves

The balance of momentum is now evaluated for contact curves and boundary curves. Momentum balance at the contact curves leads to the derivation of (equilibrium) Young's contact angle as well as advancing and receding contact angles for static and the dynamic clusters.

19.8.1 Momentum balance at contact curves and contact angles

Local momentum balance at contact the curve $\mathcal{C}_{\text{lg}\text{s}}$ is

$$\rho^{\text{lg}\text{s}R} \frac{d^2}{dt^2} \mathbf{x}_{\text{lg}\text{s}} - \text{div}^{\mathcal{C}} \mathbf{T}^{\text{lg}\text{s}R} + \sum_{\text{adjacent interfaces } \xi_{\chi} \in \{\text{lg}, \text{ls}, \text{gs}\}} \mathbf{T}^{\xi_{\chi} R} \cdot \mathbf{n}^{\mathcal{C}\xi_{\chi}} = \mathbf{f}^{\text{lg}\text{s}}. \quad (19.31)$$

Until now, it is assumed that the contact curve has no mass, curve energy, and volumetric forces, because all energy contributions are captured by the bulk phases and interfaces. The adjacent interfaces $\mathcal{A}_{\xi_{\chi}}$, $\xi_{\chi} \in \{\text{lg}, \text{ls}, \text{gs}\}$, have a stress tensor of the form $\sigma^{\xi_{\chi}} \mathbf{I}^{\mathcal{A}}$ and the normal vectors are tangential to the interfaces, so that $\mathbf{I}^{\mathcal{A}} \cdot \mathbf{n}^{\mathcal{C}\xi_{\chi}} = \mathbf{n}^{\mathcal{C}\xi_{\chi}}$, cf. Fig. 19.1. With it, the local momentum balance at the contact curve simplifies to

$$-(\sigma^{\text{lg}} \mathbf{n}^{\mathcal{C}\text{lg}} + \sigma^{\text{ls}} \mathbf{n}^{\mathcal{C}\text{ls}} + \sigma^{\text{gs}} \mathbf{n}^{\mathcal{C}\text{gs}}) = \mathbf{0}. \quad (19.32)$$

Physically, the contact curve moves until the system minimized energy with respect to the three different interface energies. Another interpretation is that of a balance of surface tensions, which may be more obvious in the upper equation. The outcome consists of three angles between each pair of the tangential vectors summing up to 360° , cf. Fig. 19.3. Nevertheless, the special but justified assumption of a rigid solid in Section 19.6.2 yields the following practical interpretations.

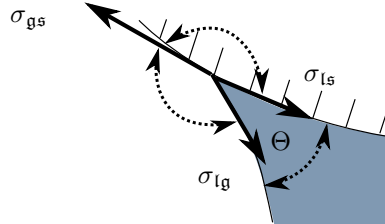


Figure 19.3: Contact curve C_{lg^s} with three enclosed angles (dotted arrows) and balance of surface tensions (solid arrows).

Curve energy at rigid walls

An interesting effect can be achieved if curve energy is considered in combination with a rigid solid, even though classical curve energy will be neglected in the further investigation. The divergence of the stress tensor can be reformulated with Eq. (19.19), Eq. (19.8), and Eq. (19.11) to

$$\operatorname{div}^C \mathbf{T}^{lg^s R} = \kappa_c \gamma^{lg^s} \mathbf{m}. \quad (19.33)$$

For an unmoved, rigid, impermeable solid, the fluid does not move normal to the wall. Thus, any variation of movement or velocity vanishes in this direction, $\delta \mathbf{v} \cdot \mathbf{n} = 0$. Use of Eq. (19.12) then results in

$$\operatorname{div}^C \mathbf{T}^{lg^s R} \cdot \delta \mathbf{v} = \kappa_c \gamma^{lg^s} \mathbf{e}_n \cdot \delta \mathbf{v} = \kappa_g \gamma^{lg^s} \mathbf{t}_g \cdot \delta \mathbf{v}. \quad (19.34)$$

Interestingly, only the geodesic curvature κ_g and the tangential movement of the contact curve $\mathbf{t}_g \cdot \delta \mathbf{v}$ contribute to the variation of energy at the solid wall. The normal curvature of the curve, cf. Eq. (19.12), is due to the geometry of the (rigid) wall surface and has no influence.

Young's contact angle

In addition to the Young-Laplace equation, Eq. (19.26), Young's contact angle is the second basic property of static drops on solid surfaces. For this reason, let us consider a rigid and smooth solid surface. In this special case, only two of the three enclosed angles at the contact curve are variable, Fig. 19.3. The angle between the fluid-solid interfaces \mathcal{A}_{ls} and \mathcal{A}_{gs} is fixed by the solid. The remaining two angles sum up to an angle that is predetermined by the solids geometry, so that only one of them is independent. Furthermore, normal vectors $\mathbf{n}^{c_{ls}} = -\mathbf{n}^{c_{gs}}$ point in opposite directions for the case of a sufficiently smooth, differentiable, solid surface. Θ is now defined to be the angle between $\mathbf{n}^{c_{ls}}$ and $\mathbf{n}^{c_{ls}}$ with $\cos \Theta = \mathbf{n}^{c_{lg}} \cdot \mathbf{n}^{c_{ls}}$. Multiplying Eq. (19.32)

with $-\mathbf{n}^{C_{1s}}$ yields for the equilibrium state, with $\Theta_{\text{Young}} := \Theta_{\text{eq}}$,

$$\sigma^{\text{lg}} \cos \Theta_{\text{Young}} + \sigma^{\text{ls}} - \sigma^{\text{gs}} \stackrel{\text{eq}}{=} 0 \quad \overset{\sigma^{\text{lg}} \neq 0}{\Leftrightarrow} \quad \cos \Theta_{\text{Young}} \stackrel{\text{eq}}{=} \frac{\sigma^{\text{gs}} - \sigma^{\text{ls}}}{\sigma^{\text{lg}}}. \quad (19.35)$$

The left equation can be interpreted as a balance of surface tensions in tangential direction, cf. Fig. 19.3. In equilibrium, Θ is also known as Young's contact angle Θ_{Young} . For $0^\circ \leq \Theta_{\text{Young}} < 90^\circ$, the enclosed fluid is called the wetting phase and the outer one is the non-wetting phase and vice versa for $90^\circ < \Theta_{\text{Young}} \leq 90^\circ$.

Another important situation appears for a rigid solid. The increase of \mathcal{A}_{ls} then equals to the decrease of \mathcal{A}_{gs} meaning $d\mathcal{A}_{\text{ls}} = -d\mathcal{A}_{\text{gs}}$ and $\sigma^{\text{ls}}d\mathcal{A}_{\text{ls}} + \sigma^{\text{gs}}d\mathcal{A}_{\text{gs}} = (\sigma^{\text{ls}} - \sigma^{\text{gs}})d\mathcal{A}_{\text{ls}} = -\sigma^{\text{lg}} \cos \Theta_{\text{Young}} d\mathcal{A}_{\text{ls}}$. In conclusion, the energetic state of the interfaces is completely determined by the two material parameters σ^{lg} and Θ_{Young} . It reduces the number of material parameters from originally three surface energies to two. Accordingly, experimental data is often available for surface tensions between liquids (σ^{lg}) and contact angles for the solid-fluid-fluid combination (Θ_{Young}). Information about surface energies between solids and other materials is more difficult to determine and rarely available.

Static advancing and receding contact angle

Surface tension and Young's contact angle are two important parameters of a fluid cluster but do not suffice for a realistic description. This should be explained by an example. Under ideal conditions, a water drop on a flat surface spreads its contact curve until it reaches a circular shape and Young's contact angle. However, one knows from experiments and daily observations that this is not the case: rain drops on a window are not perfectly round and water on an apple skin can show different contact angles at the same time, Fig. 19.4a). Surface tension or Young's contact angle cannot explain this behavior. The origins are namely "local surface defects (chemical and topographical)" Tadmor [203]. Each surface is practically irregular because of geometrical or chemical changes on smaller scales. This causes energetic potentials the contact curve has to pass.

Detailed knowledge and modeling of this smaller scale imperfections is usually limited to investigations at corresponding length scales, for instance, at a resolution of surface roughness. It comes with too much effort for many applications and modeling including the present case. Therefore, this situation is accounted for by the so-called static advancing and receding contact angles, $\Theta_{\text{re}} \leq \Theta_{\text{Young}} \leq \Theta_{\text{ad}}$. These angles determine in which range, $[\Theta_{\text{re}}, \Theta_{\text{ad}}]$, the contact angle can change without movement of the contact curve. This phenomenon is also known as contact angle hysteresis or angular hysteresis.

The modeling approach follows the idea of Santos & White [182], which was inspired by Adam & Jessop [1], and implements contact angle hysteresis analogously to static, dry friction (in contrast to velocity-related, viscous friction inside the cluster). It is a local property of the solid's surface due to chemical or mechanical treatment. Hence, a friction force per length, $\mathbf{f}^{\text{fgs}}(\Theta)$, is introduced acting perpendicular to the curve and tangential to the solid's surface as

$$\begin{aligned} \mathbf{f}^{\text{fgs}}(\Theta) &:= \mathbf{f}^{\text{fgs}}(\Theta) \mathbf{n}^{C_{1s}} := (\sigma^{\text{lg}} \cos \Theta + \sigma^{\text{ls}} - \sigma^{\text{gs}}) \mathbf{n}^{C_{1s}} \\ &= \sigma^{\text{lg}} (\cos \Theta - \cos \Theta_{\text{Young}}) \mathbf{n}^{C_{1s}}, \quad \text{if } \Theta_{\text{re}} \leq \Theta \leq \Theta_{\text{ad}}. \end{aligned} \quad (19.36)$$

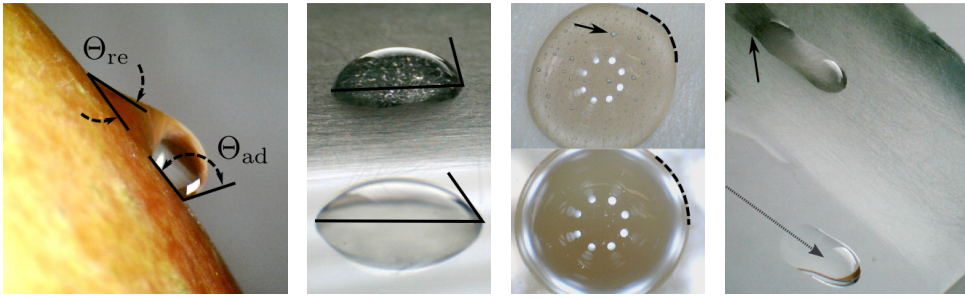
Therewith, the local momentum balance enhances from Eq. (19.32) to

$$-(\sigma^{\text{lg}} \mathbf{n}^{C_{1g}} + \sigma^{\text{ls}} \mathbf{n}^{C_{1s}} + \sigma^{\text{gs}} \mathbf{n}^{C_{g^s}}) + \mathbf{f}^{\text{fgs}} = \mathbf{0} \quad (19.37)$$

and the relationship of Young's contact angle, Eq. (19.35), enhances to

$$-(\sigma^{lg} \cos \Theta + \sigma^{ls} - \sigma^{gs}) + f^{lgs}(\Theta) = -\sigma^{lg} (\cos \Theta - \cos \Theta_{\text{Young}}) + f^{lgs}(\Theta) = 0. \quad (19.38)$$

The character of the additional term is that of a volume force, although other models in literature sometimes use curve energy for this purpose. A description via a classical curve energy should be avoided here, because this physical phenomenon has no origin at the curve itself. Moreover, typical curve energy works tangentially to the curve only. Hence, for zero curvature κ_c or geodesic curvature κ_g , such curve energy has no influence, cf. Eq. (19.33) and Eq. (19.34). In contrast, curvature free defects exist and should be considered, for example, a straight gap that prevents the cluster's contact curve from moving over it. Thus, a friction-based force is preferred, accounting for the smaller scale imperfections of the solid's surface.



a) Receding and advancing contact angle b) Different contact angles c) Trapped air and distorted circular shape on a rough surface d) Rough surface requires a steeper slope for moving and causes a water film

Figure 19.4: Influence of solid imperfections: Picture a) shows the receding and advancing contact angle of a water drop on an apple under gravity. Pictures b) - d) show water drops on a clean surface (from the factory; lower drops) and on a roughen surface (by emery paper; upper drops) of acrylic glass. The situation of trapped gas inclusions at the liquid-solid surface is also called Cassie-Baxter state in contrast to an inclusion-free Wenzel state.

Dynamic advancing and receding contact angle

Similar to for static, dry friction, the threshold values of $[\Theta_{\text{re}}, \Theta_{\text{ad}}]$ may be exceeded causing the contact curve to move. For this case, the definition of f^{lgs} is extended, as suggested by Santos & White [182] and similar to dynamic, dry friction, as

$$f^{lgs}(\Theta) := \begin{cases} \sigma^{lg} (\cos \Theta_{\text{re,dyn}} - \cos \Theta_{\text{Young}}) & , \text{ once } \Theta < \Theta_{\text{re}}, \text{ while } \Theta < \Theta_{\text{re,dyn}} \\ \sigma^{lg} (\cos \Theta - \cos \Theta_{\text{Young}}) & , \text{ if } \Theta_{\text{re}} \leq \Theta \leq \Theta_{\text{ad}}, \\ \sigma^{lg} (\cos \Theta_{\text{ad,dyn}} - \cos \Theta_{\text{Young}}) & , \text{ once } \Theta > \Theta_{\text{ad}}, \text{ while } \Theta > \Theta_{\text{ad,dyn}} \end{cases} \quad (19.39)$$

As dry, static and dynamic friction can differ in classical mechanic systems, the static and dynamic contact angles can differ in the receding or advancing case. With it, the behavior of the contact curve is determined by the material properties σ^{lg} , Θ_{Young} , Θ_{ad} , Θ_{re} , $\Theta_{\text{ad,dyn}}$, and $\Theta_{\text{re,dyn}}$. In general, these material properties need to be determined for each fluid-fluid-solid combination and also depend on the treatment of

the solid (cleaned chemically, polished, etc.). In the special case of pinned clusters (i.e. no slip occurs at the solid wall), f^{fgs} can be modeled as an arbitrarily high threshold value to resist each excitation. In the other special case of sliding clusters (i.e. slip occurs at the solid wall) and negligible resistance of the contact curve (for example, for an almost perfectly regular solid surface), $f^{\text{fgs}} \rightarrow 0$.

Slip and no-slip condition near the moving contact curve

The no-slip boundary condition is a well-established assumption for many situations of fluid flow between solid walls. However, this assumption does not only fail if a continuum theory is not applicable, for example, at the molecular length scale, but obviously also contradicts the present description of a moving contact curve. Thus, another boundary condition is necessary if a dynamic contact curve should be included.

Modeling fluids's slip near the contact curve can become difficult, as a lower-scale phenomenon, and is still not fully discovered by current research investigations [169]. Typical approaches make use of molecular dynamics or continuous composition fields, modeling the interfaces as compositions of both fluids with a finite depth [169, 176]. A rough approximation of the necessary boundary condition can be based on the so-called generalized Navier boundary condition as described by Qian et al. [169] and reading

$$\int_{l_{\mathcal{A}_{\text{tg}}}} \beta^{\text{slip}} \mathbf{v}_{\text{slip}} dx = \int_{l_{\mathcal{A}_{\text{tg}}}} -\eta^{\text{LR}} \left(\text{grad} \mathbf{v}_{\text{f}} + \text{grad}^T \mathbf{v}_{\text{f}} \right) \cdot \mathbf{n}^{\mathcal{C}_{\text{ts}}} dx - \left[\sigma^{\text{tg}} (\cos \Theta - \cos \Theta_{\text{Young}}) - f^{\text{fgs}}(\Theta) \right] \mathbf{n}^{\mathcal{C}_{\text{ts}}}.$$

This implementation requires an appropriate resolution and/or approximation of the contact curve region with thickness $l_{\mathcal{A}_{\text{tg}}}$. The slip velocity \mathbf{v}_{slip} coincides with the fluid velocity \mathbf{v}_{f} for the case of a rigid solid. The left hand side and the first term of the right hand side constitute the Navier boundary equation. The slip coefficient β^{slip} is usually high enough to assume no-slip conditions, $\mathbf{v}_{\text{slip}} \approx \mathbf{0}$, for single phase flows on scales much larger than the molecule scale. The second term of the right hand side adds the so-called uncompensated Young stress due to the contact curve. This term is able to mobilize the contact curve and the fluid near it. In this case, β^{slip} becomes an important local parameter determining the behavior of the contact curve and the entire cluster.

Summary of contact curve conditions

In conclusion, three typical boundary conditions can be classified with respect to the contact curve behavior, Fig. 19.5. First, the classical no-slip boundary condition, $\mathbf{u}_{\text{f}} - \mathbf{u}_{\text{s}} = \mathbf{0}$, holds for pinned clusters and the contact angle remains between the static receding and advancing limit. This is practically valid for most cases if the acting forces are small enough, due to the imperfections of solids. Second, the use of the generalized Navier boundary conditions becomes necessary if the acting forces reach a threshold value and the contact curve starts to move. For such a dynamic contact curve, the boundary condition is of Neumann type and more precisely momentum transfer is proportional to $\beta^{\text{slip}} \mathbf{v}_{\text{slip}}$.

Moreover, a special case occurs for total wetting. No contact curve exists, if the cluster's fluid covers the entire solid wall. The contact area between surrounding fluid and solid is missing. Still, for modeling purposes, the cluster can be described separately from the fluid film. It interacts with the covering fluid film via viscous stresses (that depend on the velocity gradient as shown in Eq. (19.16a)) and is not coupled to the solid by a velocity boundary condition. Assuming an underground of a continuous fluid film with constant thickness, the contact angle Θ becomes 180° and resistance against contact curve movement vanishes, $f^{\text{lg}s} \rightarrow 0$.

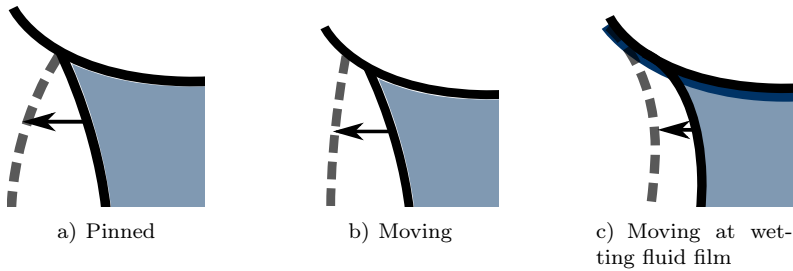


Figure 19.5: Movement for typical contact curve conditions.

19.8.2 Momentum balance at boundary curves

Boundary curves have no energy or mass as a part of an artificial boundary of the system. Surface energy is constant in the present investigation and, therefore, surface stress is constant on both sides of an artificial boundary curve within an interface. Additionally, the surface is assumed to be smooth and the tangential vectors of the surface are assumed to be continuously differentiable. Thus, normal vectors on the boundary curve are opposite to each other for both adjacent surfaces and the stresses cancel each other out. With it, local momentum conservation

$$\rho^{b,\alpha\beta R} \frac{d^2}{dt^2} \mathbf{x}_{b,\alpha\beta} - \operatorname{div}^C \mathbf{T}^{b,\alpha\beta R} + \sum_{\substack{\text{adjacent} \\ \text{surfaces } \xi\chi}} \mathbf{T}^{\xi\chi R} \cdot \mathbf{n}^{C\xi\chi} = \mathbf{f}^{b,\alpha\beta} \quad (19.40)$$

becomes trivial, namely $\mathbf{0} = \mathbf{0}$. In other applications, such as solid shell structures, this equation becomes a boundary condition for the surface stress. Furthermore, the momentum balances of the boundary curve and contact curve superpose to that of the contact curve, if both curves coincide.

Closing remarks The physical phenomena mentioned above can be explained in more detail on smaller scales. The measurable contact angle can differ from the one measured on the mm-scale on scales of a few Å. In addition, a precursor-film can be found on this scale for moving contact curves [234]. Furthermore, the pressure difference inside the cluster becomes unlimited, theoretically, for decreasing radii and continuum descriptions (including the classical pressure definition) thus become invalid. Properties of the solid, such as surface tension or contact angle hysteresis, can be related to smaller scale geometric structures like those used by the lotus plant. Moreover, relationships between equilibrium contact angle, contact angle hysteresis, and curve energy can be found [203].

19.9 Final equations for an incompressible, Newtonian liquid cluster surrounded by gas in a rigid matrix

Until now, the physical processes were explained and described mathematically. The very general case considers deformation of the solid, movement of the surrounding fluid, etc. It is included in the basic approach Eq. (19.13a) and Eq. (19.20), where the corresponding constitutive relationships (such as the equation of state and the stress-strain/strain rate relationship) need to be inserted. The final equations are then constituted by the balance of momentum and balance of mass.

Nevertheless, certain simplifications were explained and justified for the typical liquid cluster that is surrounded by a gas in a stiff solid matrix. This special situation is of particular interest for the macroscopic wave theory at residual saturation, as presented in Part III. Hence, the assumptions are summarized below and followed by a final overview of leading equations for an incompressible, Newtonian liquid cluster surrounded by gas of constant pressure in a rigid matrix. Moreover, the equations are specified for different kind of oscillations in a variational form.

19.9.1 Summary of assumptions

The following assumptions and simplifications have been discussed in the former part and are used for the final set of equations:

- characteristic magnitudes: cluster radii $\tilde{R} \geq 10^{-6}$ m, surface energy $\tilde{\sigma}^{\text{lg}} \leq 10^{-1} \text{ N m}^{-1}$, liquid's bulk modulus $\tilde{K}^{\text{l}} \geq 10^9 \text{ N m}^{-2}$, characteristic solid length $\tilde{l} \geq \tilde{R}$, solid's Lamé parameters $\tilde{\mu}^{\text{grains}}, \tilde{\lambda}^{\text{grains}} \geq 10^{10} \text{ N m}^{-2}$
- temperature changes are negligible
- surface energy σ^{lg} is constant
- the solid is rigid, immobile, and impermeable
- the cluster liquid is incompressible
- the influence of a surrounding gas on the oscillating liquid cluster reduces to that of constant pressure
- the boundaries of the cluster and the system coincide

Note that the characteristic magnitudes do not constitute fixed conditions and may vary one magnitude or more without canceling the validity of the simplifications.

19.9.2 Governing equations

An incompressible, oscillating Newtonian liquid cluster inside an inflexible, impermeable solid matrix, surrounded by a gas of constant pressure can be described by the following equations. All properties belong to the cluster fluid.

- local mass balance inside the cluster

$$\operatorname{div} \mathbf{v}_l = 0. \quad (19.41a)$$

- local momentum balance inside the cluster

$$-\rho^{lR} \left(\frac{\partial}{\partial t} \mathbf{v}_l + \operatorname{grad} \mathbf{v}_l \cdot \mathbf{v}_l \right) - \operatorname{grad} p^{lR} + \eta^{lR} \operatorname{div} \left(\operatorname{grad} \mathbf{v}_l + \operatorname{grad}^T \mathbf{v}_l \right) + \rho^{lR} \mathbf{g} = \mathbf{0}. \quad (19.41b)$$

- local momentum balance/stress boundary condition at the boundary fluid-fluid interface, which reduces to Young-Laplace equation in equilibrium

$$-\eta^{lR} \left(\operatorname{grad} \mathbf{v}_l + \operatorname{grad}^T \mathbf{v}_l \right) \cdot \mathbf{n} + (p^{lR} + \sigma^{lg} \kappa) \mathbf{n} = p^{\text{ext}} \mathbf{n}. \quad (19.41c)$$

- boundary conditions at the solid wall (three types)

- no slip condition for pinned clusters

$$\mathbf{v}_l = \mathbf{0} \quad (19.41d)$$

- moving contact curve at an impermeable wall with

$$\begin{aligned} \mathbf{v}_l \cdot \mathbf{n}^{\mathcal{A}_{ls}} &= 0, \\ \mathbf{t}^{\text{ext}} &= - \int_{l_{\mathcal{A}_{lg}}} \beta^{\text{slip}} \mathbf{v}_l \, dx. \end{aligned} \quad (19.41e)$$

acting additionally along the contact curve width $l_{\mathcal{A}_{lg}}$ and including an appropriate velocity distribution; a combination with the far field region $\mathcal{A}_{lg} \setminus l_{\mathcal{A}_{lg}}$ can be achieved via a Robin boundary condition.

- sliding motion on a wetting fluid film of negligible thickness and negligible contact angle resistance; resistance occurs due to viscosity only

$$\begin{aligned} \mathbf{v}_l \cdot \mathbf{n}^{\mathcal{A}_{ls}} &= 0, \\ \mathbf{t}^{\text{ext}} &= -\mathbf{T}^{lR} \cdot \mathbf{n}^{\mathcal{A}_{ls}}, \\ \Theta_{\text{Young}} &\rightarrow 180^\circ \quad (\text{complete wetting}). \end{aligned} \quad (19.41f)$$

- local momentum balance/stress boundary condition at the boundary contact curve, which results in Young's contact angle in equilibrium for perfectly regular surfaces

$$[\sigma^{lg} (\cos \Theta - \cos \Theta_{\text{Young}})] \mathbf{n}^{\mathcal{C}_{ls}} = f^{lgs}(\Theta) \mathbf{n}^{\mathcal{C}_{ls}}, \quad (19.41g)$$

where

$$\begin{aligned} \cos \Theta &= \mathbf{n}^{\mathcal{A}_{lg}} \cdot \mathbf{n}^{\mathcal{A}_{ls}}, \\ f^{lgs}(\Theta) &:= \begin{cases} \sigma^{lg} (\cos \Theta_{\text{re,dyn}} - \cos \Theta_{\text{Young}}) & , \text{ once } \Theta < \Theta_{\text{re}}, \text{ while } \Theta < \Theta_{\text{re,dyn}} \\ \sigma^{lg} (\cos \Theta - \cos \Theta_{\text{Young}}) & , \text{ if } \Theta_{\text{re}} \leq \Theta \leq \Theta_{\text{ad}}, \\ \sigma^{lg} (\cos \Theta_{\text{ad,dyn}} - \cos \Theta_{\text{Young}}) & , \text{ once } \Theta > \Theta_{\text{ad}}, \text{ while } \Theta > \Theta_{\text{ad,dyn}} \end{cases} \end{aligned}$$

These equations are provided as variational formulations of pressure $\delta \hat{p}^{lR}$ and velocity $\delta \hat{\mathbf{v}}_l$ for different types of movement (pinned, sliding, etc.) in Tab. 19.1.

mass balance
$0 = \int_{\mathcal{V}_l} \operatorname{div} \mathbf{v}_l \delta \hat{p}^{IR} dv$
momentum balance
general
Without any specification of boundary conditions or contact curve behavior
$\begin{aligned} & \int_{\mathcal{V}_l} \left(-\rho^{IR} \left(\frac{\partial}{\partial t} \mathbf{v}_l + \operatorname{grad} \mathbf{v}_l \cdot \mathbf{v}_l \right) - \operatorname{grad} p^{IR} + \eta^{IR} \operatorname{div} \left(\operatorname{grad} \mathbf{v}_l + \operatorname{grad}^T \mathbf{v}_l \right) + \rho^{IR} \mathbf{g} \right) \cdot \delta \hat{\mathbf{v}}_l dv \\ & + \int_{\mathcal{A}_{lg}} \left(-\eta^{IR} \left(\operatorname{grad} \mathbf{v}_l + \operatorname{grad}^T \mathbf{v}_l \right) \cdot \mathbf{n}^{\mathcal{A}_{lg}} + \left(p^{IR} - p^{\text{ext}} + \sigma^{lg} \kappa \right) \mathbf{n}^{\mathcal{A}_{lg}} \right) \cdot \delta \hat{\mathbf{v}}_l da \\ & + \int_{\mathcal{A}_{ls}} \left(-\eta^{IR} \left(\operatorname{grad} \mathbf{v}_l + \operatorname{grad}^T \mathbf{v}_l \right) \cdot \mathbf{n}^{\mathcal{A}_{ls}} + p^{IR} \mathbf{n}^{\mathcal{A}_{ls}} + \mathbf{t}^{\text{ext}} \right) \cdot \delta \hat{\mathbf{v}}_l da \\ & + \int_{\mathcal{C}_{lgs}} \left(\sigma^{lg} \left(\cos(\Theta_{\text{Young}}) - \cos(\Theta) \right) + f^{lgs}(\Theta) \right) \mathbf{n}^{\mathcal{C}_{lgs}} \cdot \delta \hat{\mathbf{v}}_l dc = 0 \end{aligned}$
pinned oscillations
f^{lgs} is high enough to resist uncompensated Young stresses \rightarrow no slip occurs at the solid wall yielding $\delta \hat{\mathbf{v}}_l = 0$ on \mathcal{C}_{lgs} and \mathcal{A}_{ls} .
$\begin{aligned} & \int_{\mathcal{V}_l} \left(-\rho^{IR} \left(\frac{\partial}{\partial t} \mathbf{v}_l + \operatorname{grad} \mathbf{v}_l \cdot \mathbf{v}_l \right) - \operatorname{grad} p^{IR} + \eta^{IR} \operatorname{div} \left(\operatorname{grad} \mathbf{v}_l + \operatorname{grad}^T \mathbf{v}_l \right) + \rho^{IR} \mathbf{g} \right) \cdot \delta \hat{\mathbf{v}}_l dv \\ & + \int_{\mathcal{A}_{lg}} \left(-\eta^{IR} \left(\operatorname{grad} \mathbf{v}_l + \operatorname{grad}^T \mathbf{v}_l \right) \cdot \mathbf{n}^{\mathcal{A}_{lg}} + \left(p^{IR} - p^{\text{ext}} + \sigma^{lg} \kappa \right) \mathbf{n}^{\mathcal{A}_{lg}} \right) \cdot \delta \hat{\mathbf{v}}_l da = 0 \end{aligned}$
moving contact curve
Interaction at \mathcal{A}_{ls} is replaced by the near-field region at the contact curve $l_{\mathcal{A}_{ls}}$ (Navier boundary condition). For the remaining far-field region no slip is assumed but can be replaced by slip (cf. lower equation) or a Robin boundary condition.
$\begin{aligned} & \int_{\mathcal{V}_l} \left(-\rho^{IR} \left(\frac{\partial}{\partial t} \mathbf{v}_l + \operatorname{grad} \mathbf{v}_l \cdot \mathbf{v}_l \right) - \operatorname{grad} p^{IR} + \eta^{IR} \operatorname{div} \left(\operatorname{grad} \mathbf{v}_l + \operatorname{grad}^T \mathbf{v}_l \right) + \rho^{IR} \mathbf{g} \right) \cdot \delta \hat{\mathbf{v}}_l dv \\ & + \int_{\mathcal{A}_{lg}} \left(-\eta^{IR} \left(\operatorname{grad} \mathbf{v}_l + \operatorname{grad}^T \mathbf{v}_l \right) \cdot \mathbf{n}^{\mathcal{A}_{lg}} + \left(p^{IR} - p^{\text{ext}} + \sigma^{lg} \kappa \right) \mathbf{n}^{\mathcal{A}_{lg}} \right) \cdot \delta \hat{\mathbf{v}}_l da \\ & + \int_{\mathcal{C}_{lgs}} \left[\int_{l_{\mathcal{A}_{ls}}} -\eta^{IR} \left(\operatorname{grad} \mathbf{v}_l + \operatorname{grad}^T \mathbf{v}_l \right) \cdot \mathbf{n}^{\mathcal{A}_{ls}} - \beta^{\text{slip}} \mathbf{v}_l dx \right] \cdot \delta \hat{\mathbf{v}}_l dc \\ & + \int_{\mathcal{C}_{lgs}} \left(\sigma^{lg} \left(\cos(\Theta_{\text{Young}}) - \cos(\Theta) \right) + f^{lgs}(\Theta) \right) \mathbf{n}^{\mathcal{C}_{lgs}} \cdot \delta \hat{\mathbf{v}}_l dc = 0 \end{aligned}$
sliding motion on a fluid film
No three-phase contact curve appears, $f^{lgs} \rightarrow 0$ and $\Theta_{\text{Young}} \rightarrow 180^\circ$. The boundary stress at former \mathcal{A}_{ls} becomes that of the surrounding liquid.
$\begin{aligned} & \int_{\mathcal{V}_l} \left(-\rho^{IR} \left(\frac{\partial}{\partial t} \mathbf{v}_l + \operatorname{grad} \mathbf{v}_l \cdot \mathbf{v}_l \right) - \operatorname{grad} p^{IR} + \eta^{IR} \operatorname{div} \left(\operatorname{grad} \mathbf{v}_l + \operatorname{grad}^T \mathbf{v}_l \right) + \rho^{IR} \mathbf{g} \right) \cdot \delta \hat{\mathbf{v}}_l dv \\ & + \int_{\mathcal{A}_{lg}} \left(-\eta^{IR} \left(\operatorname{grad} \mathbf{v}_l + \operatorname{grad}^T \mathbf{v}_l \right) \cdot \mathbf{n}^{\mathcal{A}_{lg}} + \left(p^{IR} - p^{\text{ext}} + \sigma^{lg} \kappa \right) \mathbf{n}^{\mathcal{A}_{lg}} \right) \cdot \delta \hat{\mathbf{v}}_l da \\ & + \int_{\mathcal{C}_{lgs}} -\sigma^{lg} \left(1 + \cos(\Theta) \right) \mathbf{n}^{\mathcal{C}_{lgs}} \cdot \delta \hat{\mathbf{v}}_l dc = 0 \end{aligned}$

Table 19.1: Final variations of mass and momentum balance for different conditions.

19.10 The oscillating fluid cluster as a harmonic oscillator

19.10.1 Motivation and concept

A detailed description of oscillating fluid clusters is scientifically interesting but can include geometries of high complexity. Additionally, oscillating fluid clusters are also important as components of major systems, for example, for wave propagation in residually saturated porous media. In such cases, the clusters' complexity often needs to be reduced for efficient modeling of the entire system. Their oscillation behavior requires a classification by a few characteristic parameters.

Therefore, three properties were demonstrated in the previous theoretical investigation: (i) the cluster has inertia due to its mass (or density ρ^{lR} in local form); (ii) it is damped due to viscosity (represented by $\eta^{lR} \text{grad } \mathbf{v}$ in local form); and (iii) it has stiffness due to the attempt of minimizing surface energy ($\sigma^{lq} \kappa$ in local form). These three properties correspond to the properties of a harmonic oscillator, whose motion $q(t)$ is described by the partial differential equation

$$m \ddot{q} + d \dot{q} + c q = F(t), \quad \text{cf. Eq. (3.2).}$$

For that reason and inspired by the ideas in [72, 198], an oscillating fluid cluster is modeled as an uni-dimensional harmonic oscillator, cf. Fig. 19.6. This approach is supported by oscillator-like resonance effects observed in theory, experiment, and numerical simulation [38, 96, 122, 183].

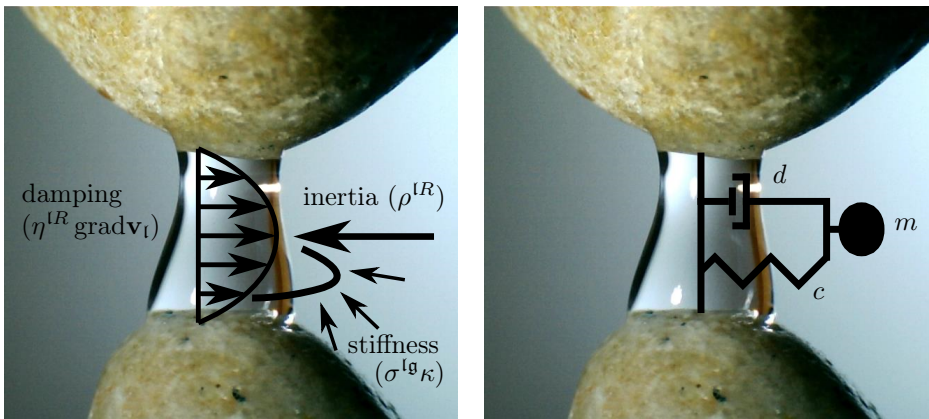


Figure 19.6: Physical behavior of an oscillating fluid cluster as a harmonic oscillator with mass m , stiffness c , and damping d .

As a result, the barycentric motion of an oscillating fluid cluster can be described by the three properties: mass m , stiffness c , and damping d . All properties of a harmonic oscillator can be applied as introduced in Section 3.2. Thus, the oscillating cluster can be alternatively described by the set of mass m , undamped eigenfrequency ω_0 , and damping ratio D . This triple, $\{m, \omega_0, D\}$, turns out to be highly beneficial for the physical description and classification of oscillating fluid clusters, cf. Chapter 16. Hence, special attention will be given to classification of fluid clusters by those three characteristic, dynamic properties. Moreover, further properties such as resonance frequencies or amplification factors can be derived from them.

19.10.2 Typical forms of cluster oscillations

Various forms of cluster oscillations can occur depending on the condition at the contact curve (pinned/moving). Some classical forms of fluid cluster oscillations can be characterized as follows.

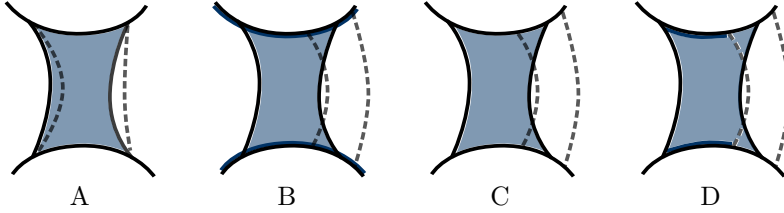


Figure 19.7: Typical forms of cluster oscillations for different conditions.

- A Imperfections of the surface prevent contact curve movement for small deviations. The cluster is pinned. This is the case in many applications without a special treatment of the surface.
- B A fluid film covers the entire solid surface, $\Theta_{\text{Young}} \rightarrow 180^\circ$ and $f^{\text{fgs}} \rightarrow 0$. The cluster slides on the film and is described separately. Only viscous effects and geometric restrictions, resulting in a changing interface area, counteract a movement.
- C The contact curve starts to move if the deviation is large enough to overcome the limits of the static contact angle, Θ_{re} or Θ_{ad} . The moving contact curve damps the oscillations in addition to the viscous flow.
- D Similar to C but at a surface with significant defects, the moving cluster leaves a fluid film behind. This is a mix of cases B and C. The film is increased by every oscillation, due to the new contact area between fluid and solid.

Typical linear oscillations are represented by case A. Linear sliding oscillations are given for two special cases of perfectly regular surfaces: case B and case C with negligible pinning forces ($\Theta_{\text{re}} \approx \Theta_{\text{Young}} \approx \Theta_{\text{ad}}$). Case C and D generally require deviations that are not arbitrarily small and change from one kind of movement to another like a stick slip. Thus, they describe non-linear oscillations.

19.10.3 Limitations and extensions of the harmonic-oscillator model

The reduction of an oscillating continuum to an uni-dimensional oscillator comes with simplifications and three important limitations need to be considered.

Multiple oscillation modes

A fluid cluster is a continuous body and can oscillate via different modes. For example, Sanz & Diez [183] proved theoretically and experimentally different transversal modes of an oil bridge. This effect can be accounted for by various extensions. One approach is the introduction of frequency-dependent stiffness and damping. For each mode, the

corresponding stiffness and damping change near the respective oscillation frequency. This approach is convenient if the different oscillation modes should be distinguished in the frequency regime. Another possible approach is the use of a lumped-mass model, including more than one degree of freedom.

For applications, the lowest modes of oscillation are often the most important because they gather the highest amount of energy. The excitation of a specific oscillation mode depends, amongst others, on the cluster position in relation to external stimulation, which leads over to the next point.

Directional dependence

As a three-dimensional system, a fluid cluster can oscillate in various directions. There are often preferred directions, for instance, lateral and transversal to the symmetry axis of a water bridge. Further oscillation modes consist of superposition or as multiples of the basic modes. The stimulation of a certain direction depends on the position of the fluid cluster with respect to the stimulating boundary condition such as a passing wave front.

In the case of randomly distributed fluid clusters in porous media, the fluid clusters can be assumed to be stimulated evenly distributed from all possible directions. The anisotropy of a single cluster is averaged over the REV to an isotropic and even distribution of different excitation directions. Higher multiples of the same direction can then be included by a frequency dependence of the dynamic parameters or a lumped mass approach as mentioned above.

Frequency-dependent velocity profile

A further local effect of the fluid cluster is simplified because of the uni-dimensional approach: the velocity flow profile. The harmonic-oscillator model does not contain information about the velocity distribution because its motion has only one degree of freedom. Nevertheless, it is known that the velocity profile of an oscillating fluid flow in a pore channel depends on the oscillation frequency [25, 112, 226]; also see Section 10.3. Additionally, the flow profile determines damping via its gradient and stiffness via curvature of the interface shape. In conclusion, stiffness c and damping d (or undamped eigenfrequency ω_0 and damping ratio D respectively) generally depend on oscillation frequency ω with respect to the barycentric motion.

Following the classical approach of Biot [25] and Womersley [226], the frequency dependence can be rewritten as a dependence on the dimensionless number

$$N(\omega) = \frac{\rho^{lR} h^2 \omega}{\eta^{lR}}. \quad (19.42)$$

The characteristic length h is related to the direction of the velocity gradient, i.e. perpendicular to the main flow direction. In the case of an oscillation parallel to the solid walls, h is comparable to the wall distance or pore diameter and N becomes the squared Womersley number, cf. Eq. (10.6). If the cluster oscillations are not parallel to the enclosing pore channel walls, h will account for another characteristic length, for example, for the cluster diameter between the fluid-fluid interfaces.

It follows for free cluster oscillations that eigenfrequency ω_0 is a solution of the implicit problem

$$\omega_0 = \sqrt{\frac{c(N(\omega_0))}{m}}. \quad (19.43)$$

One unique solution exists for $c = \text{const}$. For general $c(N)$ -relationships, however, a solution can become arbitrarily complex; if there is at least one solution. The same situation occurs with respect to damping d or ω_0 and D , respectively. Nevertheless, the study of frequency-dependent flow profiles in [25, 226] and the observed oscillator-like behavior in [94, 122, 183] are reasonable grounds to assume that a frequency dependence of the dynamic properties is limited and an oscillator-like rheology is a good approximation. This is supported by the findings of the following two chapters.

Chapter 20

Systematic, numerical investigation of oscillating, pinned liquid clusters

The previous chapter provided insights into the theoretical description and classification of oscillating fluid clusters. This chapter follows with a comprehensive, quantitative, numerical analysis.

Two basic types of water clusters surrounded by air are investigated with variations of different geometric and material properties. They are pinned to account for a typical form of linear oscillations. The first cluster type is based on a cylinder that is pinned at top and bottom representing a liquid bridge between two grains. The second type is based on a slender cylinder that is pinned along its lateral surface. It represents a water cluster enclosed in a slender pore channel. Moreover, frequency dependence of the characteristic, dynamic properties is determined for different clusters and limited in the case of resonance effects.

20.1 Methodology

20.1.1 Governing equations

A variational formulation of mass and momentum balance was used to determine the transient motion of the cluster. The applied equations can be found in Tab. 19.1 (mass balance and the second version of momentum balance). Due to restrictions of the used Finite Element (FE) solver determining the total curvature of a surface κ , the momentum balance was slightly reformulated. For this reason, the surface divergence theorem Eq. (19.6) was combined with the definition of surface stress and contact angle as

$$\int_{\mathcal{C}_{s^{lg}}} -\sigma^{lg} \cos(\Theta) \mathbf{n}^{C_{ls}} \cdot \delta \mathbf{v} \, dc + \int_{\mathcal{A}_{lg}} \sigma^{lg} \kappa \delta \mathbf{v} \cdot \mathbf{n}^{\mathcal{A}_{lg}} \, da = \int_{\mathcal{A}_{lg}} \sigma^{lg} \operatorname{div}^{\mathcal{A}}(\delta \mathbf{v}) \, da,$$

where the first term vanishes for pinned oscillations. Additionally, the divergence theorem was applied to $\mathbf{T}^{lg} \cdot \delta \mathbf{v}$ with symmetric, liquid stress tensor \mathbf{T}^{lg} in order to

replace

$$\int_{\mathcal{V}_t} \operatorname{div} \mathbf{T}^{IR} \cdot \delta \mathbf{v} \, dv - \int_{\mathcal{A}_{tg} \cup \mathcal{A}_{ts}} (\mathbf{T}^{IR} \cdot \delta \mathbf{v}) \cdot \mathbf{n} \, da = \int_{\mathcal{V}_t} \mathbf{T}^{IR} : \operatorname{grad}(\delta \mathbf{v}) \, dv.$$

20.1.2 Numerical implementation and processing

There have been different numerical approaches for the simulation of static and dynamic fluid clusters, each with its own advantages and shortcomings, cf. Section 18.1. In the present study, mass and momentum balance were solved using the FE package Comsol Multiphysics. Based on the variational approach, the equations were derived in an updated Lagrange formulation. Derivatives are taken with respect to the Eulerian (spatial) coordinates.

This method does not require an adaptation of material parameters for interaction terms, in contrast to particle-based methods, and successfully avoids numerical loss of volume. Furthermore, the flexibility of an FE-solution for not pre-stabilized, general, partial differential equations in a weak formulation was an important advantage for the present work. The Eulerian viewpoint allowed a precise investigation of solid and fluid physics within a general mathematical framework. The isolation from further transformations between material and spatial coordinates proved to be beneficial for the foregoing, theoretical study because a comparison with well-known equations was straightforward. A total Lagrange formulation can be achieved as well but detailed transformation exceeds the scope of this work, cf. the theoretical framework of Belytschko et al. [14] and Steinmann [200] as well as the comprehensive methodic description provided by Saksono & Perić [177, 178].

Mass and momentum balance were implemented as fully-coupled weak formulations. A moving mesh (geometry shape order 2, Winslow smoothing type) accounted for the updated interface geometry. Velocities were discretized by quadratic shape functions of Lagrange type while linear shape functions were used for the pressure²². Furthermore, standard and well-established FE-solvers (Pardiso) were used. Remeshing (due to eddies and distorted elements) turned out to be not necessary for the first periods of oscillations.

The final work flow of the numerical investigation is summarized in Fig. 20.1.

20.1.3 Clusters investigated

Two typical kinds of clusters were investigated and are denoted as model I and model II. The origin of material parameters is water surrounded by air at ambient conditions ($\rho^{IR} = 1000 \text{ kg m}^{-3}$, $\eta^{IR} = 10^{-3} \text{ Pa s}$, $\sigma^{lg} = 70 \times 10^{-3} \text{ N m}^{-1}$, Θ_{Young} initially set to 90°). Appendix E.1 contains a tabular overview.

Model I

Model I is a water cylinder that is pinned at top and bottom between two parallel walls of distance l , cf. Fig. 20.2. It can represent a liquid bridge between two grains. The initial version is of 1 mm length and width. Characteristic geometrical properties

²²The liquid is assumed to be incompressible. This assumption requires lower order shape functions for pressure compared to velocity according to the Babuška-Brezzi condition, cf. Braess [31] and/or the use of Taylor-Hood elements.

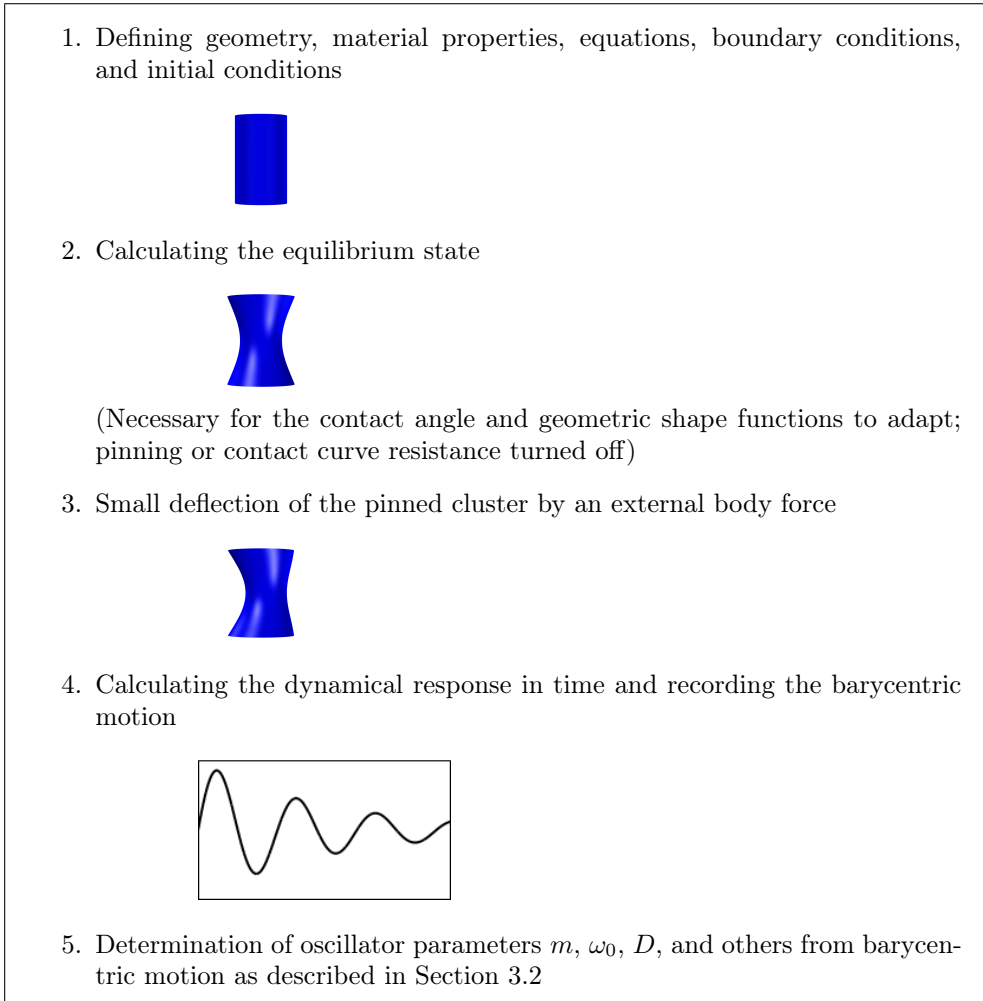


Figure 20.1: Numerical work flow for the study of cluster oscillations.

include volume $V := \mathcal{V}_l$, hydraulic radius $R = \sqrt{V/(\pi l)}$, specific interfacial areas²³ $a^{lg} = \mathcal{A}_{lg}/\mathcal{V}_l$ as well as $a^{ls} = \mathcal{A}_{ls}/\mathcal{V}_l$, and slenderness $\Lambda = l/R$.

The investigation of model I includes general variations of oscillation direction (transversal and parallel to the symmetry axis in equilibrium), volume V , slenderness Λ , Young's contact angle Θ_{Young} , density ρ^{lR} , dynamic viscosity η^{lR} , and surface tension σ^{lg} . The variations are by factors 1/8, 1/4, 1/2, 2, 4, and 8, except for Young's contact angle (which varies between 34° and 117°) and slenderness (which is limited by instability of very slender geometries). These variations cover a wide range of possible combinations.

²³Note that interfacial areas are defined with respect to the cluster volume. They are linked to the macroscopic definition via saturation, cf. [86].

Model II

Model II is a water cylinder pinned along the lateral surface like a water column that is trapped in a pore channel, cf. Fig. 20.2. The basis version is of 10 mm length and 1 mm width. Again, l describes the length parallel to the axis of symmetry but is connected to the dilatation of the solid-liquid surface for model II.

The investigation of model II varies volume V , length l , slenderness Λ , as well as dynamic viscosity η^{lR} . The variations are larger than for model I to cover extreme ranges in geometry and viscosity as they may occur at different depths in soil. Due to physical restrictions (including overdamped oscillators for high viscosities or decomposing and rapture for extreme slenderness) and technical limitations (including meshing of high aspect ratios) the investigated samples are not as many as for model I but cover a broader range. In addition, this model was also winded with different parameters $\tau \in \{0, 1/4, 1/2, 1, 2\}$, cf. Fig. 20.2.

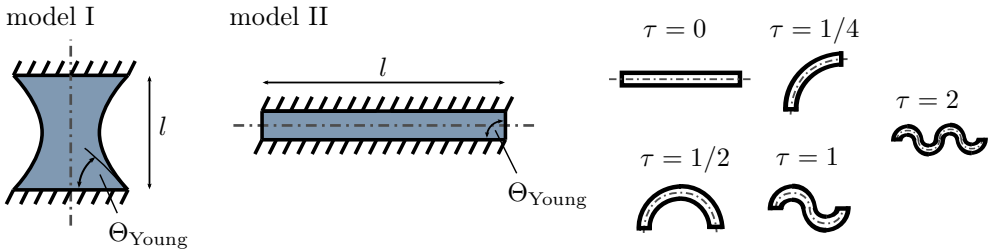


Figure 20.2: Investigated types of fluid clusters.

Frequency-dependent stiffness and damping

A frequency dependence of cluster stiffness and damping can occur, due to frequency-dependent flow profiles as explained in Section 19.10.3. Furthermore, it was motivated and replaced by the dependence on a dimensionless number N .

To quantify the frequency dependence of stiffness and damping, four different clusters were studied for various values of N . These include a small and a big version of model I ($l = 10^{-5}$ m and $l = 10^{-2}$ m, $\Lambda = 2$) as well as a small and a big version of model II ($l = 10^{-4}$ m and $l = 10^{-1}$ m, $\Lambda = 20$). The characteristic length h is chosen to be half of the initial cluster diameter transversal to flow direction, which is the pore radius for typical oscillating flow through channels.

The influence of the frequency-dependent flow profile was studied for different dimensionless numbers N by varying density ρ^{lR} . As a result, $c(N)$ and $d(N)$ were determined. The pair $\{\omega_0, D\}$ cannot be compared for different $N(\rho)$ directly, because it also depends on density, explicitly. Nevertheless, $c(N)$ and $d(N)$ do not depend on ρ , except via $N(\rho)$, and are therefore an appropriate representation of frequency-dependent damping and stiffness. Moreover, N is directly proportional to the oscillation frequency, which is why frequency-dependent stiffness and damping of an oscillating fluid cluster can be deduced from their dependence on N .

20.2 Results and discussion

The multiplicity of simulated clusters entails a large amount of interpretable data. Hence, the results are categorized with respect to individual properties and directly followed by the corresponding discussion. The main focus was determination of ω_0 and D for various cluster types. Raw data can be found in Section E.1.

20.2.1 Accuracy and sensitivity of the numerical solutions

Numerical processing and evaluation has been tested with respect to its accuracy in several points. The cluster excitation has been tested with an external body force, initial displacement, and a sinusoidal body force of different amplitudes for unmodified model I and different viscosities. The results of these excitation methods diverged less than one percent (except for seven percent for D in the case of very small, sensitive values $D < 0.02$), which is in the range of the expected uncertainty of the numerical method. Therefore and because of its simple numerical implementation, a body force has been chosen for stimulation in the other cases.

A fast Fourier transformation (FFT) was applied to the calculated signal of time-dependent barycentric motion numerically. This procedure was based on the Matlab FFT-function and enhanced by a Tukey window and zero-padding to obtain an improved numerical performance. The FFT of the signals showed a major peak at one frequency with a deviation of less than 5% from the measurement via the oscillation's period, cf. Eq. (3.9). Only for the cases of extreme slenderness (factor > 4 or $< 1/4$), further peaks of minor intensity occurred at multiples of the first peak's frequency. Thus, it can be assumed that the first eigenmodes have been stimulated and observed. This will be further supported by comparison with results from literature. Calculated ω_0 values could be assumed to be stable within deviations of a few percent or less with respect to variations of: mesh size, time stepping, deflection/volume force amplitude, and choice of the time interval among multiple oscillation periods. The solution of damping parameter D was sensitive for weakly damped oscillations because of the relatively small changes in amplitude. As a result, the instability for $D \leq 0.01$ is expected in the order of $\leq 15\%$.

Pressure difference in equilibrium deviated less than one percent from the analytic solution of the Young-Laplace equation, which was available in all cases except for the variation of the contact angle. This very good agreement supports the choice of the spatial discretization and geometric shape functions.

In conclusion, the solutions for ω_0 were stable in the lower single-digit percentage area. Damping coefficients deviated stronger for low damping ($\leq 15\%$ for $D \leq 0.01$) but the order of magnitude and the qualitative behavior was still captured in these cases.

20.2.2 Comparison with literature

Sanz & Diez [183] provided experimental data of an oscillating oil column tested during the D-1 Spacelab Mission [135]. The measured angular resonance frequency of the oil cylinder, pinned between two 35 mm-discs, was in the range of 1.068 s^{-1} and 1.194 s^{-1} . This result is supported by Liang & Kawaji [122]. The presented method agrees well with an angular resonance frequency of 1.181 s^{-1} .

In addition, Hilpert et al. [94] derived an analytic solution for the resonance frequency of undamped fluid clusters in a straight tube with radius R and length l of

$$\omega_{\text{Hilpert}} = \sqrt{(\sigma^{\text{lg}} \sin(180^\circ - \Theta_{\text{Young}})(1 + \sin(180^\circ - \Theta_{\text{Young}}))^2 / (\rho^{\text{lg}} R^2 l)}.$$

in the present notation. For model II, ω_{Hilpert} yields an angular frequency of 669.328 s^{-1} while the presented method yields 623.517 s^{-1} (-6.84% deviation) for the variation of lowest viscosity. Moreover, the analytic solution ω_{Hilpert} of [94] predicts that the undamped eigenfrequency depends on cluster mass but not on its slenderness. This

was confirmed in the numerical calculations of varying slenderness. The constant $\omega_0(\Lambda)$ relationship can be specifically seen in Fig. 20.7. Fluctuations of few percent around a constant value occur and can be explained by two reasons: first, by influence of the changing velocity profile for different radii and, second, by other wave modes, which were observed in the FFT for very high values of slenderness. Nevertheless, these fluctuations are very small for the investigated clusters and the prediction of Hilpert's solution is in good agreement.

Liang & Kawaji simulated an oil bridge surrounded by air numerically using a Level Set Function [122]. This cluster type is comparable to the one investigated experimentally by Sanz & Diez [183], but it additionally accounts for a surrounding air phase. The surface oscillation amplitude reached its peak at a stimulating angular frequency of 56.55 s^{-1} . The simulation of the presented method agrees well again predicting an angular resonance frequency of 55.66 s^{-1} (-1.57% deviation).

Eventually, the good agreement with results from literature confirms the used methods. All comparisons, including experiments [183], analytical solutions [94], as well as other numerical methods [122], demonstrated a very good accordance with deviations of a few percent. Additionally, the theoretical assumptions, including a rigid wall and a negligible gas phase, were fully supported.

20.2.3 Systematic classification

The major focus of this quantitative analysis is to provide an overview of the characteristic, dynamic parameters ω_0 and D for various kinds of fluid clusters. Mass m can be easily determined from its geometry and density. The basic simulation results can be found in Section E.1 and are figuratively presented in Fig. 20.4 and Fig. 20.5.

Model I

The first model was studied for oscillations perpendicular and parallel to the symmetry axis. Both directions show the same behavior qualitatively, cf. the overview in Fig. 20.4 and Fig. 20.5. In general, the investigated clusters' angular, undamped eigenfrequencies ω_0 were up to several thousand s^{-1} . Furthermore, damping was low with $D \leq 0.1$.

A limitation of slenderness occurred for very long bridges of model I and can be explained physically. For large wall distances, the clusters started necking in their center because the physical configuration of two single blobs at the walls was more stable. Irregularities, for example, due to numerical effects, caused the system to turn from an unstable cylindrical equilibrium into two single blobs.

Considering ω_0 , surface tension σ^{lg} reflected its role as stiffness while density ρ^{lR} and volume $V = \mathcal{V}_l$ composed the cluster mass. More precisely, each doubling of surface tension or bisection of density or volume increased ω_0 by a factor of $\sqrt{2}$ with high accuracy (deviation from factor $\sqrt{2}$ was less than 1.5% for all investigated cases). This coincides with the behavior of a classical harmonic oscillator.

Furthermore, ω_0 fell with growing slenderness Λ and also decreased slightly for higher values of dynamic viscosity η^{lR} . Interestingly, the undamped eigenfrequency showed a peak for varying equilibrium contact angle Θ_{Young} . In equilibrium, the cluster's curvature can be described by two radii; one for the circumferential and one for the lateral direction. In case of the maximum of $\omega_0(\Theta_{\text{Young}})$, both radii combine to the stiffest combination. On both sides of this peak, two different contact angles can result in the same stiffness.

Damping parameter D was already low ($< 5\%$) for the initial case. It increased exponentially with growing viscosity η^{LR} . On the contrary, D decreased for all other variations in the order of one magnitude. Each case was still within the range of low damping.

Model II

The second model initially showed a higher damping ($\times 3$) and lower eigenfrequency ($\times 1/2$) compared to model I with transversal oscillation direction, cf. Fig. 20.6. The variations were larger and support the former observations of model I with respect to common variations.

Changes of ω_0 occurred also for different winding but were within the uncertainty of the calculations. A dependence could not be confirmed for the investigated variations. Another comparable independence occurred for altering slenderness, which is in agreement with the analytical prediction by Hilpert et al. [94] as mentioned during the comparison with literature above. Very small deviations around the mean value of $\omega_0(\Lambda)$ can be explained by a dependence on the dimensionless number N or limited numerical accuracy. A change of cluster length influenced ω_0 markedly and according to the respective increase of mass.

Damping ratio D increased significantly for higher winding τ . This can be explained by secondary flows caused by the tortuous geometry. Another substantial increase in damping, however, is demonstrably connected to larger slenderness and length. The reason is an increasing influence of viscous forces (inside the bulk cluster) compared to decreasing influence of the capillary forces (at the fluid-fluid interfaces) for larger slenderness.

In addition to the principle relationships mentioned, a curve fitting of ω_0 and D is provided in Tab. E.1 and Tab. E.2, see also the example in Fig. 20.3. These tables serve as an important quantitative classification for further application and indicator for sensitivity of specific variations. For instance, the eigenfrequencies and damping ratios can be calculated explicitly for various volumes, contact angles, or viscosities.

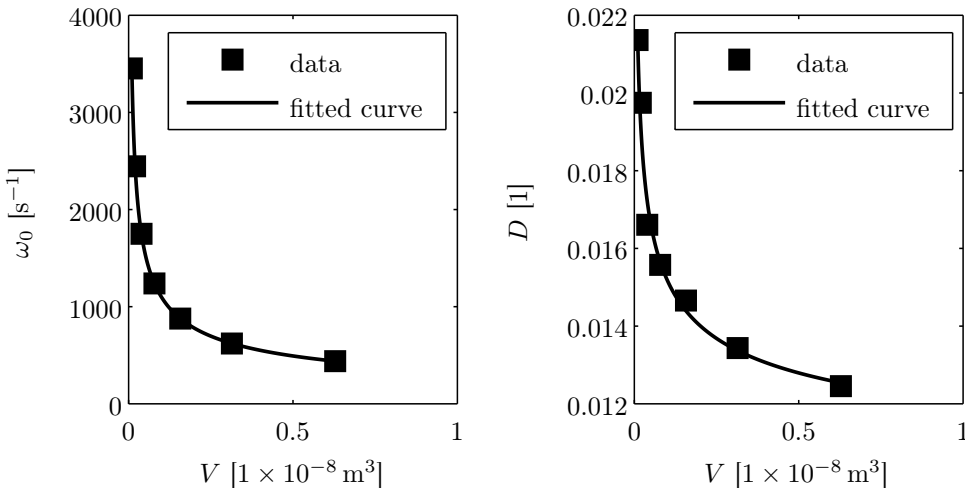


Figure 20.3: Fitted curves for variations of V of model I, transversal oscillation direction according to Tab. E.1 and Tab. E.2.

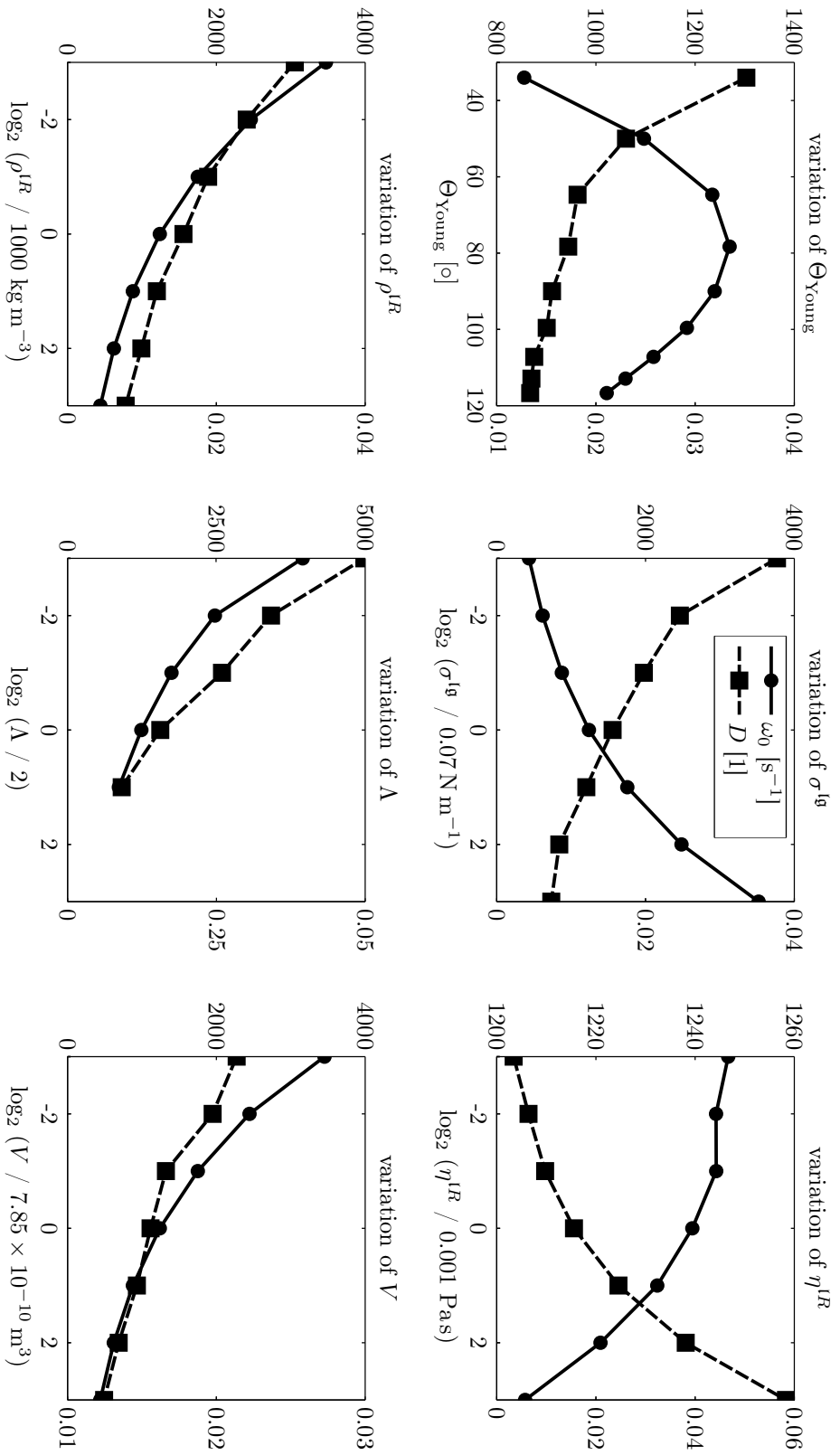


Figure 20.4: Eigenfrequency and damping for model I and its variations with oscillation direction transversal to the symmetry axis. The left (right) axis of the ordinates is related to ω_0 (D).

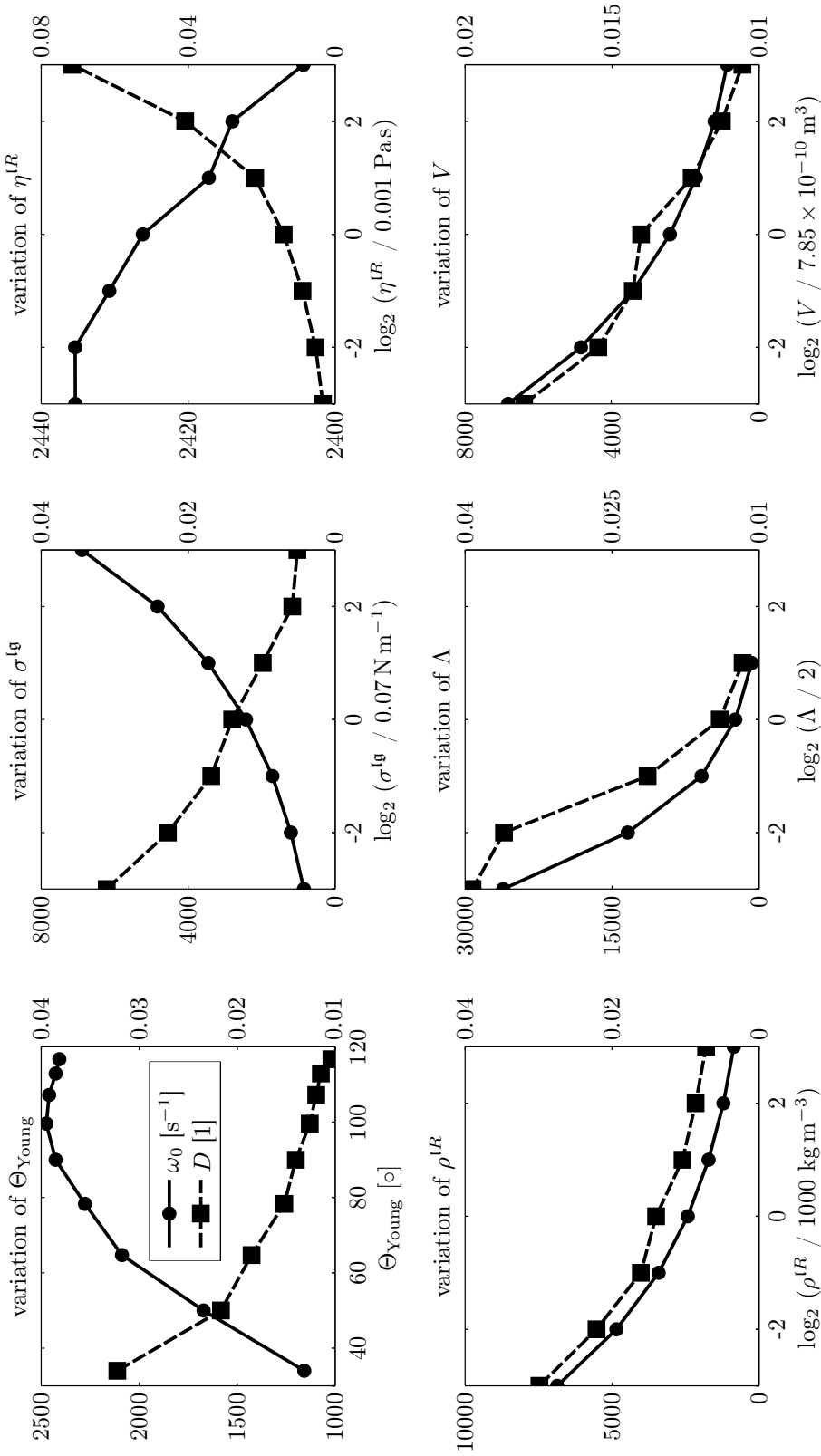


Figure 20.5: Eigenfrequency and damping for model I and its variations with oscillation direction parallel to the symmetry axis. The left (right) axis of the ordinates is related to ω_0 (D).

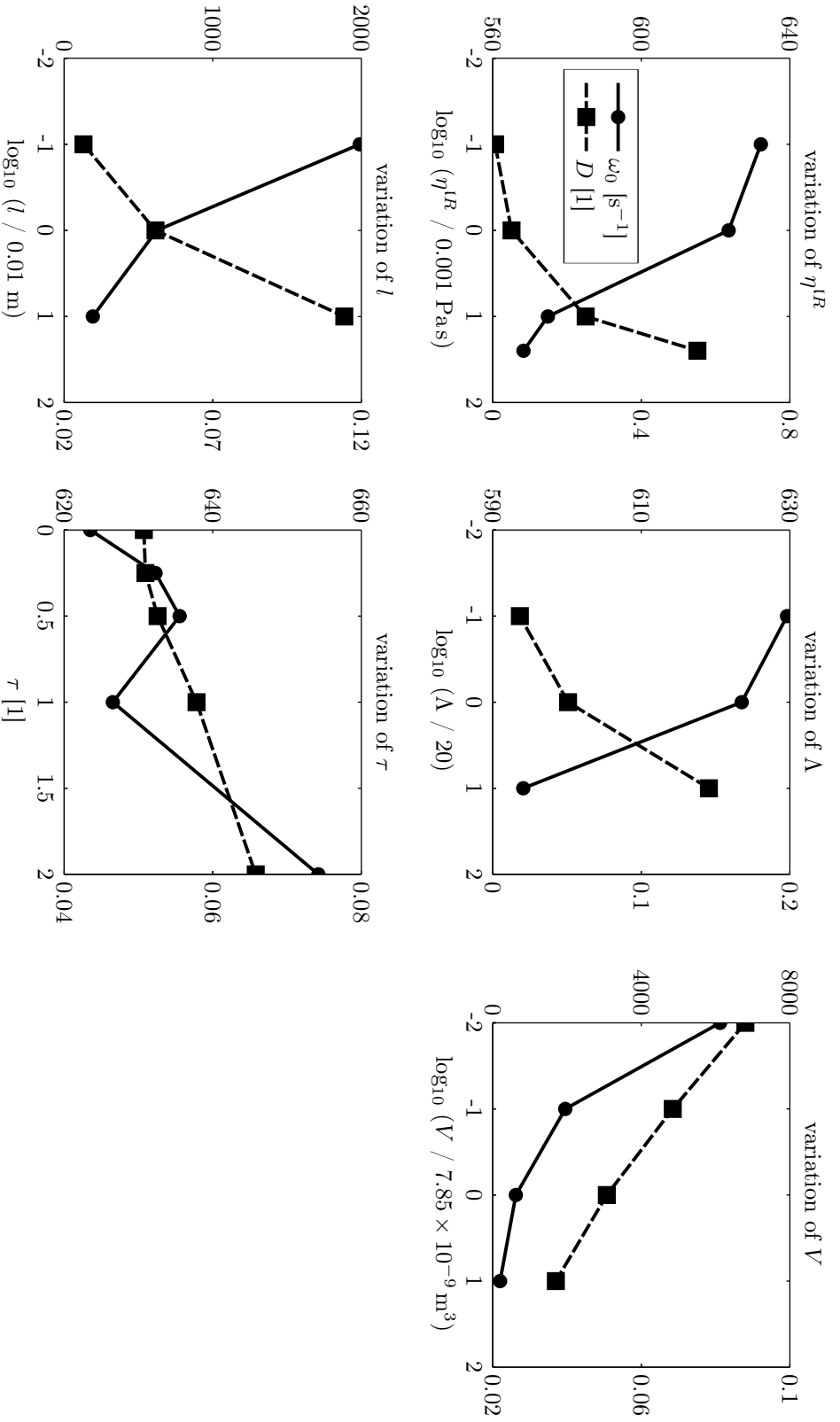


Figure 20.6: Eigenfrequency and damping for model II and its variations with oscillation direction parallel to the symmetry axis. The left (right) axis of the ordinates is related to ω_0 (D).

20.2.4 Interfacial areas

(Specific) interfacial areas ($a^{lg} = \mathcal{A}_{lg}/\mathcal{V}_l$ and $a^{ls} = \mathcal{A}_{ls}/\mathcal{V}_l$) are characteristic geometric parameters of the physical system. They take a special position in macroscopic theories, containing additional micro-structure information next to volume fractions. Thus, interfacial areas are investigated separately because they can be directly connected to macroscopic theories²⁴.

Geometrically, interfacial areas of the cluster liquid and the solid, a^{ls} , can be interpreted as the inverse characteristic diameter of the interface between both liquids, for instance, as a pore space diameter. Interfacial areas between both fluids, a^{lg} , represent an inverse characteristic diameter of the interface between solid and cluster, for example, the cluster length in pore direction. Both kinds of interfacial areas depend on other geometric properties such as volume, length, slenderness, or contact angle. Hence, they cannot be treated as distinct microscopic properties but change with the other variations.

Focusing first on a^{lg} , no consistent relationship occurs between a^{lg} and the dynamic cluster properties ω_0 and D . The observations show an opposed correlation between a^{lg} and ω_0 or D respectively for varying slenderness and volume, cf. Fig. 20.7. For example, a^{lg} decreases and the cluster becomes more inert ($\downarrow \omega_0$) with increasing volume. On the contrary, a^{lg} decreases as well for decreasing slenderness but the cluster becomes more stiff ($\uparrow \omega_0$). Thus, neither an explicit causality nor a correlation can be predicted on the basis of the investigated samples.

For the other type of interfacial areas, ω_0 tended to increase with high a^{ls} values for the geometric variations investigated. Large a^{ls} represent a system with a small wall distance. Hence, the cluster is stiffer. This is also known from the fact that a cluster sags less under gravity load when the surrounding walls (such as two fingertips) approach each other. Damping ratio D also tended to ascend with a^{ls} because the amount of viscous interaction raises compared to the influence of capillary effects.

Equilibrium contact angle Θ_{Young} plays a special role because it influences geometry, but it is a material parameter itself. The observed influence on ω_0 and D via interfacial areas is lower than by the other variations. Interestingly, the hysteresis effect is reproduced. There can be different contact angles with different interfacial areas, which result in the same capillary response.

20.2.5 Frequency dependence

The dynamic parameters of four different water clusters were studied with respect to their dependence on the dimensionless number N and the oscillation frequency ω ($\propto N$). A big and a small variation of model I and II were investigated to enclose a wide range of cluster types. Basic data is given in Section E.1 and visualized in Fig. 20.8.

The results demonstrate a dependence on N for c and d and consequently for ω_0 and D . Stiffness $c(N)$ and the product $\omega_0(N)d(N)$ were comparable for different sizes of the same cluster type. Within the investigated range, d varied about one decade and c within borders of 20%. In particular, a change of N affected damping d (or D respectively) strongly. Thus, a general dependence of the dynamic, characteristic parameters on oscillation frequency can be deduced.

²⁴Note that the macroscopic definition of interfacial areas, as in [89], requires a further multiplication by liquid saturation.

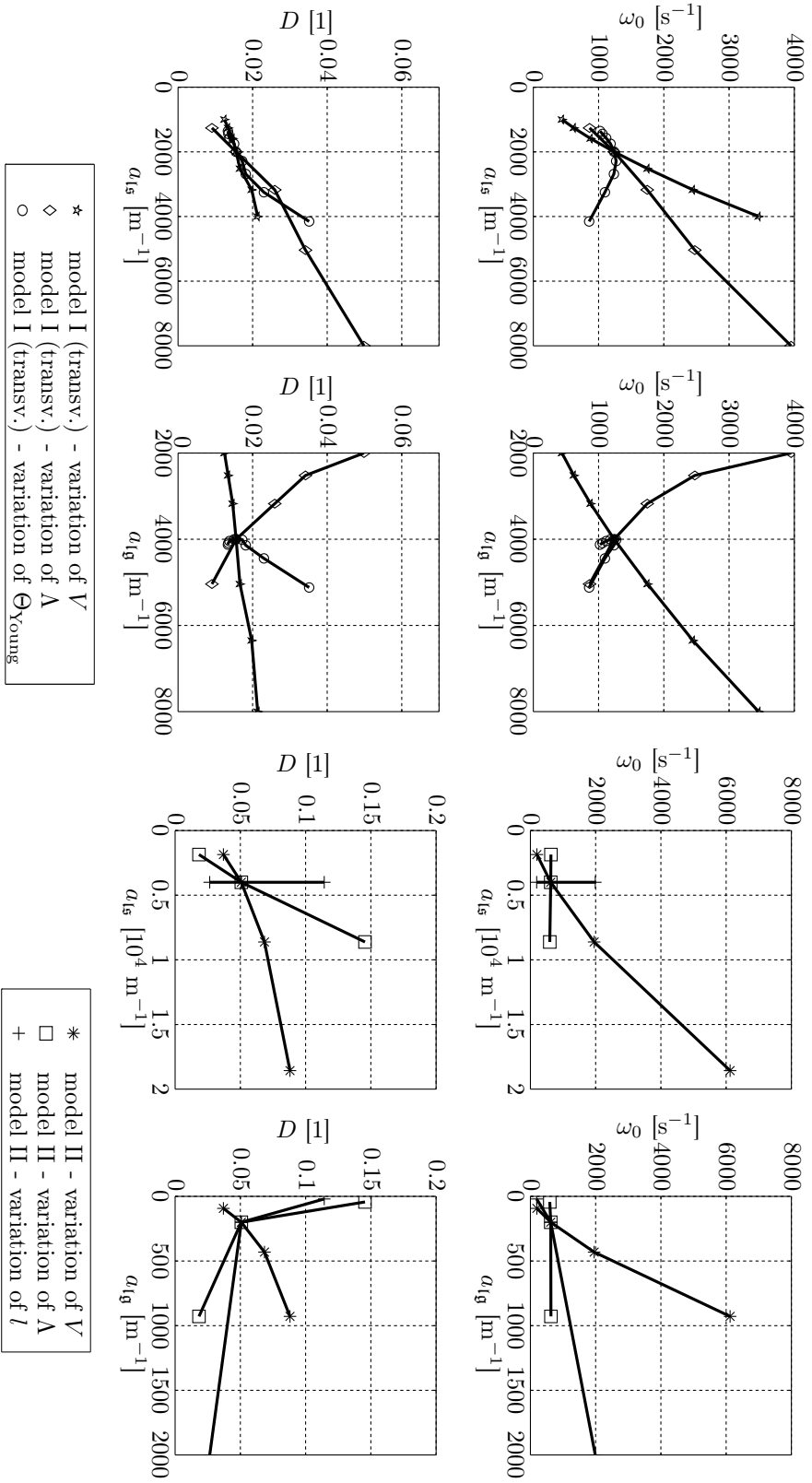


Figure 20.7: Eigenfrequency and damping ratio over interfacial areas of model I (transversal oscillation direction) and II. Note that a_{ls} does not change with length l for model II.

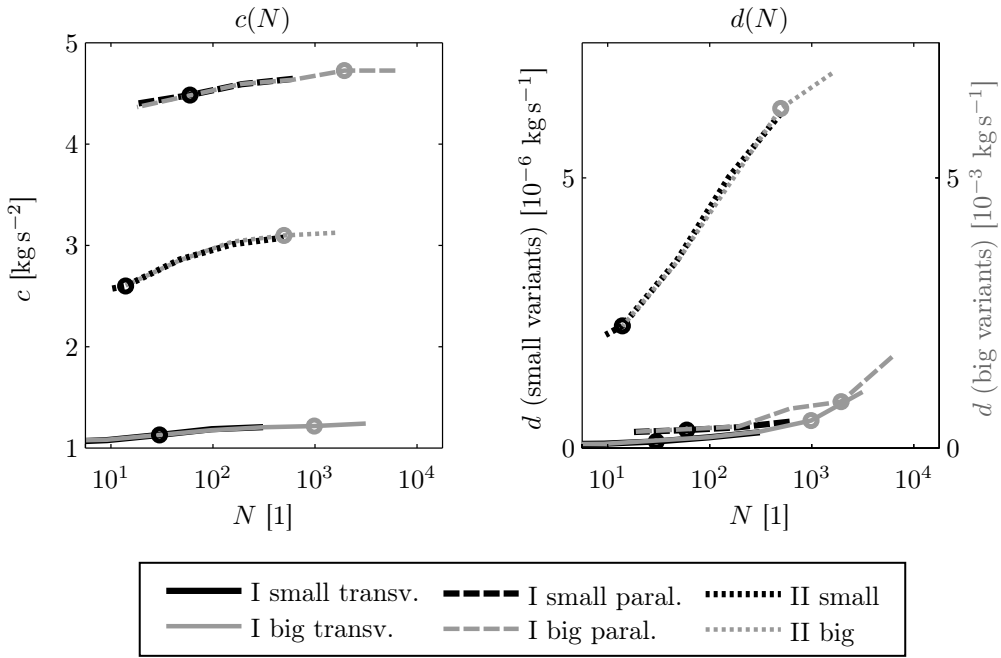


Figure 20.8: Stiffness and damping for different N values and cluster types. Circles indicate the origin values with typical water properties at free oscillations.

The appearance of this dependence is supported by the $\omega_0(\eta^{IR})$ behavior of the basic study, cf. Fig. 20.4. Viscosity does not influence mass or surface tension directly but still showed a perceivable influence on ω_0 that exceeds the limit of numerical uncertainty. In contrast, the undamped eigenfrequency ω_0 of a classical oscillator is expected to depend only on stiffness and mass but not on damping effects. Such divergent behavior is explained by the changing flow profile and mathematically by the influence of η^{IR} on ω_0 via $N(\eta^{IR})$. Consistently, it is depicted by the changing flow profile of clusters with identical geometry, mass, and surface tension but at oscillations with different N values, Fig. 20.9.

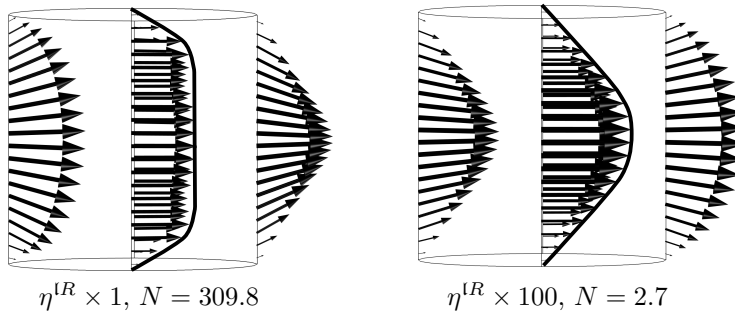


Figure 20.9: Influence of N on the velocity profile at the first zero crossing after excitation of model I via viscosity modification. For small N , viscous effects dominate and the velocity profile inside the cluster is that of Hagen-Poiseuille-flow. For large N , inertia effects dominate and the velocity profile flattens. N and η^{IR} are not completely inversely proportional because the free-oscillation frequency changes slightly for both variations.

With respect to later application, further quantitative conclusions should be drawn. Considering the amplification function of a harmonic oscillator, cf. Fig. 3.3b), the important range of resonance is within $\omega_0 \pm 50\%$. In this range, the interpolated deviations of the four investigated clusters are limited to $\leq 4\%$ for c and $\leq 30\%$ for d . Taking these mentioned uncertainties into account, the uncertainty of the corresponding resonance frequency Ω_{res} is below 5% for initial $D \leq 0.2$ and below 10% for initial $D \leq 0.3$. Additionally, the amplification function of an oscillator at very low and high driving frequencies Ω is independent of the oscillator properties. For low frequencies, i.e. $\Omega \rightarrow 0 \text{ s}^{-1}$, the amplification function is one and vanishes for $\Omega \rightarrow \infty \text{ s}^{-1}$, Fig. 3.3b).

In conclusion, the dynamic properties ω_0 and D generally depend on the stimulation (or oscillation) frequency. Based on the solutions of oscillating flows, for example, see [25] and Chapter 10, the resonance behavior is assumed to be bounded by two typical processes (low and high N). Moreover, various research proved resonance effects of fluid clusters [38, 96, 122, 183]. Thus, a real, oscillating fluid cluster is not expected to coincide exactly with a harmonic oscillator but still shows a similar behavior changing smoothly from one set of dynamic properties to another, cf. Fig. 3.3b) and [122] (Fig. 5 *ibid.*).

The resonance behavior of the low- and high-frequency regime becomes independent of deviations of ω_0 and D . For weakly damped clusters ($D \leq 0.3$), the resonance regime $\omega_0 \pm 50\%$ is well approximated with uncertainties as mentioned above. Hence, applications that are predominantly affected by resonance effects of the clusters may still use constant ω_0 and D (around $\omega = \omega_0$) for modeling the dynamic behavior of oscillating fluid clusters. Such applications can be ganglia mobilization or wave propagation in residually saturated media as presented in Part III.

Comment on an influence of the interface

The comparison of velocity profiles for different N revealed that the velocity profiles do not only change inside the cluster, but also at the interfaces at zero crossing position, cf. Fig. 20.9. One possible reason is the frequency-dependent profile inside the bulk volume, influencing the interface shape. Congruously, also capillary forces at the interface may further influence a frequency dependence of the characteristic, dynamic properties ω_0 and D . Whereas N accounts for the ratio of viscous forces to inertia forces inside the cluster, another dimensionless number is required to describe the interface physics. This can be achieved, for instance, via the capillary number

$$\text{Ca}(\omega) = h\omega \frac{\eta^{LR}}{\sigma^{lg}}. \quad (20.1)$$

Ca can be understood as the ratio of two velocities: the characteristic oscillation velocity $h\omega$ and the relaxation velocity of the near-surface region σ^{lg}/η^{LR} , which is reduced by viscous damping. An alternative interpretation is the ratio of the oscillation period ($\propto 1/\omega$) to the relaxation time of the near-surface region $h\eta^{LR}/\sigma^{lg}$.

Therefore, a frequency dependence of $\{c, d\}$ or $\{\omega_0, D\}$ may be considered more generally via $N(\omega)$ and $\text{Ca}(\omega)$. Moreover, a coupling can be achieved, for example, via a geometric parameter weighting their individual influence. A further statement about its practical influence requires quantitative investigation of the specific cluster and exceeds this investigation.

Independent of a more general or specific description, the encouraging findings remain valid. First, the dynamic properties of the oscillator-like modeling approach

are frequency-dependent in general. Second, the typical oscillator-like behavior of the investigated clusters supports an oscillator-like modeling with constant $\{\omega_0, D\}$ for the resonance regime and respective applications. The oscillator rheology is further supported by the experiments of the following chapter.

Chapter 21

Experimental study of a liquid bridge

The behavior of an oscillating, cylindrical liquid bridge is investigated experimentally in this chapter. The bridge consists of a pigmented test ink with preset surface energy and is pinned between two steel beams. A high-speed camera is used to evaluate the dynamic behavior for free and driven oscillations. As predicted by the numerical and theoretical studies, an oscillator rheology approximated the first oscillation mode well. Further oscillation modes were detected at higher frequencies. A verifiable frequency dependence of the oscillator rheology was of minor influence and below the detection limit.

21.1 Introduction

The current experimental investigation involved the analysis of an oscillating liquid bridge to determine its dynamic properties. First, the eigenfrequency and damping ratio of free oscillations were determined and compared to numerical results. Based on the decaying oscillations, ω_0 and D of a corresponding oscillator rheology were calculated.

Second, the amplification ratio was recorded for driven oscillations at various frequencies. This study of a broad frequency regime aims at detection of frequency-dependent effects that cause a deviation from the classical oscillator rheology.

21.2 Methodology

21.2.1 Experimental setup

A liquid bridge of $1 \times 10^{-8} \text{ m}^3$ test ink ① was placed between two hardened steel beams ② by the use of an Eppendorf Research pipette, cf. Fig. 21.1. The steel beams' diameter was 2 mm and a distance of 3.18 mm was set between them. The ink's surface energy was predefined and its density as well as viscosity were given (Fischer Test Tinte, green; a pigmented mixture based on water and ethanol, cf. Appendix A for material data). The beams were connected to two parallel plates of acrylic glass ③. The plates were mounted on a linear sliding table ④ that allows

adjusting a precise distance between the plates and between the beams via a micrometer caliper. Moreover, the table was mounted on a Brüel & Kjær Vibration Exciter Type 4809 ⑤. The vibration exciter produced a controlled movement of the table and all connected elements according to the electric signal received from the Brüel & Kjær Power Amplifier Type 2706 ⑥. The latter amplified the preset signal of the Trueform Agilent 33500B Series Waveform Generator ⑦. This setup allows a controlled movement of the liquid bridge perpendicular to its symmetry axis.

The liquid bridge was recorded by a Vision Research Phantom v4.3 high-speed camera in combination with a Schneider-Kreuznach APO-Componon HM 4,5/90 object lens ⑧. A Novoflex Macrolight Plus ⑨ was used for cold light illumination. Additionally, white paper was placed behind the cluster to achieve a sufficient contrast. Adhesive tape was placed on the top of the plates between the liquid bridge and the light source to avoid reflections of the liquid and the steel beams.

The recordings were split into single images, which were evaluated by digital image processing in Matlab. The image resolution was 320 pixels (width) times 504 pixels (height) corresponding to approximately 33 pixels/mm. Appropriate care was taken to achieve a sufficient compromise between a high spatial resolution (requiring larger amplitudes) and linearity of the movement (requiring lower amplitudes). Each recording was evaluated individually with respect to this requirement. The maximum recording rate was 3000 pictures per second resulting in 20 or more pictures per oscillation cycle (at least 40 for the range of the first oscillation mode).

21.2.2 Free oscillations

A total of eight recordings was made over a period of 21 hours at a temperature between 20 °C and 23 °C and at ambient (laboratory) pressure conditions. Consecutively, four liquid bridges were placed between the beams and stimulated by a single pulse with and against the direction of gravity, respectively. After recording of each bridge, the latter was removed and the steel beams were dried. The distance between the beam ends was readjusted after the first half of the experiments.

The major property calculated was the displacement of the liquid bridge in time. For this reason, the average of the lower and upper edge at the bridge center (i.e. the maximum movement of the initial line of symmetry) was determined for each time step. The decaying liquid oscillation was evaluated similar to the procedure in Chapter 20, whereas the first (five to ten) oscillations were excluded to support the tuning of the first linear mode.

21.2.3 Driven oscillations

The second part of the experiment contained driven oscillations at various frequencies. The amplitude ratios of the liquid bridge (maximum amplitude of the initial line of symmetry, cf. Fig. 21.1) to the steel beams were recorded determining the amplification function V_{amp} . An FFT of the beam movement was evaluated to verify the stimulation frequency.

The conditions were similar to those of free oscillations except for the prescribed movement that was based on a constant sinusoidal signal. The liquid bridge was replaced nine times and not later than ten minutes after its placement to avoid mass loss due to vaporization. Furthermore, the frequency was modulated in ascending and descending order.

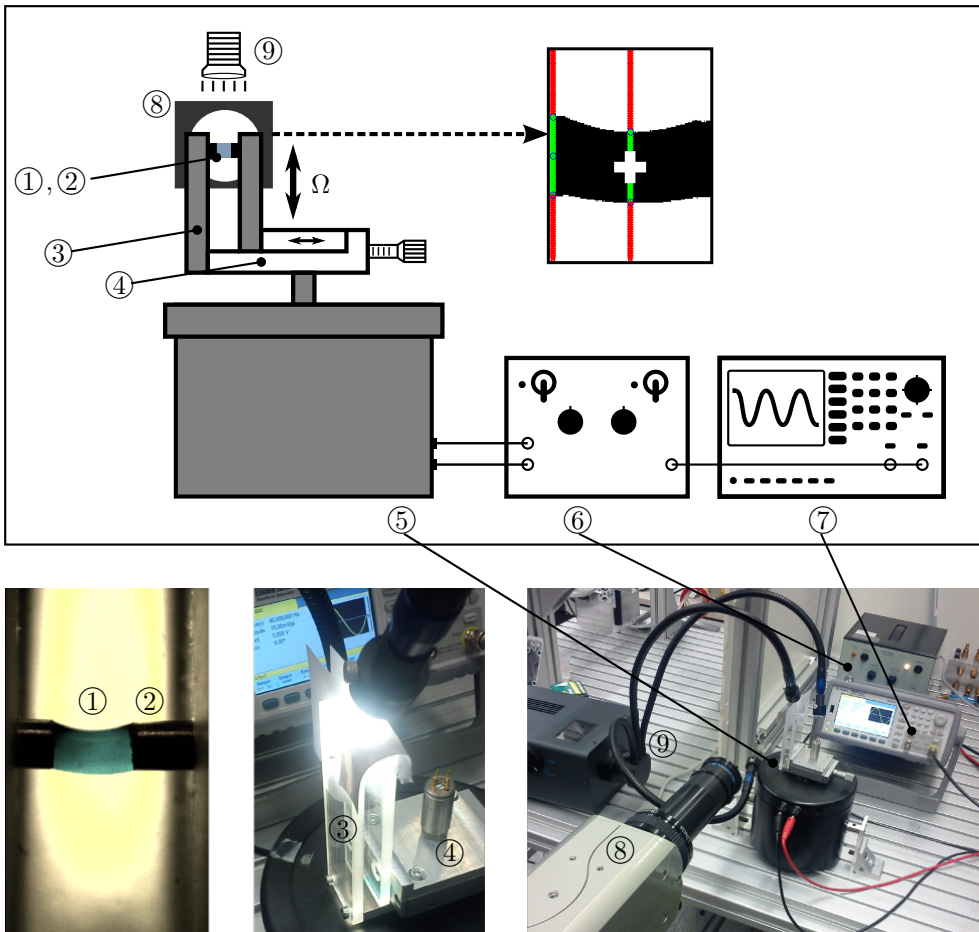


Figure 21.1: Experimental setup of the oscillating liquid bridge. The white cross inside the (upper right) digital image indicates the traced point of the liquid-bridge movement.

21.3 Results and discussion

21.3.1 Free oscillations

The investigation of free oscillations resulted in an eigenfrequency of $\omega_0 = 221.33 \pm 4.33 \text{ s}^{-1}$ and a damping ratio of $D = 0.035 \pm 0.011$ (arithmetic mean \pm standard deviation) for the liquid bridge. Combining these numbers with an oscillator rheology yields a resonance frequency of $\Omega_{\text{res}} = 221.06 \text{ s}^{-1}$ and very weak damping.

The low standard deviation of eigenfrequencies underlines the close match of the individual results. The high reproducibility of ω_0 is caused by a low influence of uncertainties such as the occurring temperature fluctuations. The main reason for the relatively higher standard deviation of D is the spatial resolution of the camera system, which records the total amplitude motion more accurately than the comparably small decay. Nevertheless, the stability of the experimental results prove the exper-

imental setup to be a beneficial possibility for the determination of liquid clusters' dynamic properties and their verification.

Additionally, the liquid bridge under gravity was simulated numerically as described in Chapter 20. The numerical results are $\omega_0 = 297.80 \text{ s}^{-1}$ and $D = 0.011$ (+34.55% deviation for ω_0 and -68.57% for D) and do not coincide with the experimental results as well as with the results from literature in Section 20.2.2.

Because of the low standard deviation of the experimental results, a systematic difference has to be considered. Herein, the most important sources of errors are uncertainties of the material and geometric parameters used. In particular, the distance and parallelism of the steel beam ends were difficult to control accurately. Hence, it may have influenced the radius and the response of capillary pressure that is sensitive to changes of small radii ($\Delta p \propto 1/R$). Additionally, the experimental oscillations required a measurable, thus sufficiently large, displacement, which may have lead to non-linear effects.

Concerning the deviation of D , further viscous flows were induced by wall roughness and differ from the numerical simulation. This was confirmed by the recordings at higher frequencies, at which, for instance, comparably small surface oscillations occurred. Moreover, changes of material data, an interaction with the surrounding air, and a difference between the maximum amplitude and the barycentric motion may have caused a deviation. Eventually, the numerical simulation predicted a correct order of magnitude for the resonance effects and a weakly damped oscillator. A more detailed determination and implementation of the experimental setup, unfortunately, exceeds the scope of this work.

21.3.2 Driven oscillations

The liquid bridge was stimulated at various frequencies. The frequency preset by the waveform generator and the final frequency measured by the FFT of the beam movement diverged by a relatively small value of less than 2.5%. It represents the uncertainty of the frequency domain. The amplitude of the vibration exciter decreased with higher frequencies at constant power and was carefully readjusted to achieve a compromise between spatial resolution and linearity of the movement. A resonance effect of the connected experimental devices occurred at $\omega \approx 2500 \text{ s}^{-1}$ causing an oscillation of the walls. Nevertheless, the corresponding frequency exceeds the frequency range of interest. Oscillations at frequencies higher than 600 s^{-1} exceeded the reliable spatial and temporal resolution in the present case. The measured results can be found in Tab. E.3.

At low frequencies, the liquid bridge moved in phase with the steel beams. This behavior was expected due to viscous coupling and predicted by the oscillator rheology; cf. Fig. 21.2, where the results of driven oscillations are compared to an oscillator rheology that is based on the results of free oscillations from above.

At frequencies around the predicted resonance frequency, $\omega \rightarrow \Omega_{\text{res}}$, resonance effects occurred for the case of driven oscillations with good quantitative agreement. The liquid bridge and the beams moved with opposite phase and the maximum amplification measured was 5.88% smaller than the one predicted by the oscillator model. Furthermore, it occurred at a frequency that was 4.34% lower than predicted.

A peak regime was observable but less pronounced for the case of driven oscillations, cf. Fig. 21.2. The major reason for the occurred fluctuations is the displacement of the beams. The latter was limited to avoid large (non-linear) liquid movements

or even a detachment of the bridge and, therefore, recorded at relatively low spatial resolution. As a result, the amplification function within the resonance regime, i.e. the ratio of cluster displacement to beam displacement, is particularly sensitive to such uncertainties of the denominator. A second reason for the deviations are secondary flows due to imperfections of the geometry or due to non-linearity. They have caused additional viscous damping, which led to an attenuated but expanded resonance regime. Moreover, small changes of the geometry were caused for each placement of a new bridge. Despite the fluctuations, however, the resonance effect could be clearly observed within the predicted frequency range.

The influence of frequency-dependent flow profiles could not be quantified for this exemplary experiment. The frequency range of the first oscillation mode is well approximated by an oscillator rheology with a slight shift of the decreasing part of the amplification function to higher frequencies (frequency deviation $\lesssim 15\%$). However, a frequency-dependent change of stiffness and damping may have influenced the fluctuations but was below the detection limit and cannot be distinguished from other uncertainties (of lower order). Moreover, the oscillator rheology also produced accurate predictions at low frequencies. Thus, frequency-dependent oscillator properties may have occurred but were of lower influence for the investigated case.

At higher frequencies, the amplification function does not vanish completely as predicted by the oscillator rheology. One reason for non-vanishing movement of the bridge is the irregularity of the beams, due to roughness and slight skew. With it, a complete decoupling is prevented. Moreover, surface oscillations occurred and influenced the measurements. The second reason for non-vanishing amplifications are higher wave modes, which require approximations by individual oscillator models. For example, one higher mode could be detected distinctively at 943.40 s^{-1} , cf. Fig. 21.2.

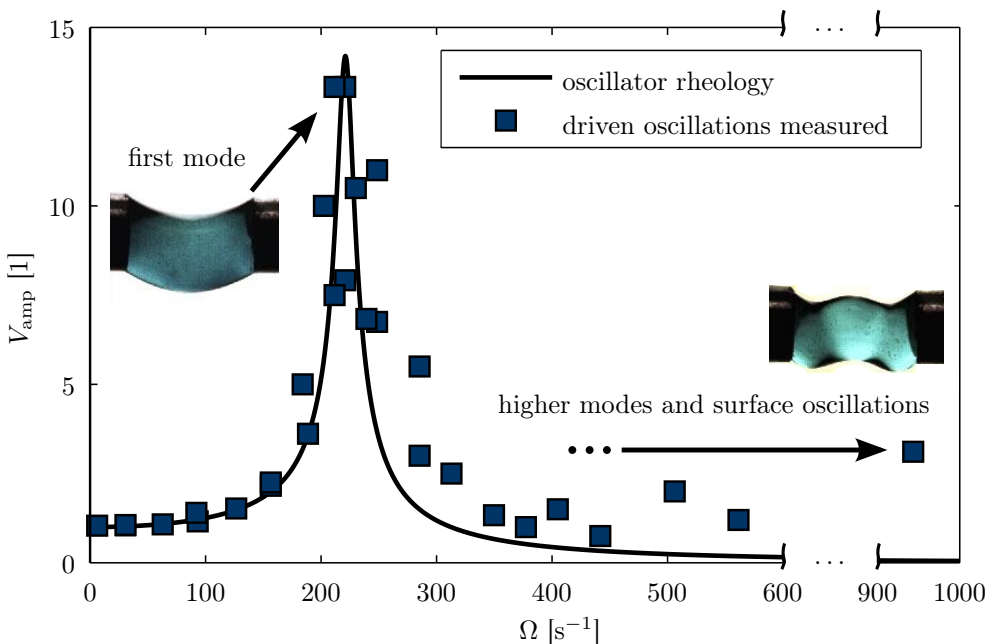


Figure 21.2: Experimental results of the oscillating liquid bridge stimulated at various frequencies. The solid line represents an oscillator rheology that is based on the measurements of free oscillations.

21.4 Conclusion

The investigated liquid bridge demonstrated a classical oscillator behavior with a distinct low-frequency regime, a resonance regime, and a high-frequency range where higher wave modes appeared. The results coincided with the predictions by a harmonic oscillator model for the first wave mode (less than 6% deviation of maximum amplification and resonance frequency). In particular, the measurement of the eigenfrequency via weakly damped, free oscillations benefited from the reproducibility, whereas the numerical implementation was limited by geometrical and material uncertainties.

The experiment agrees with the findings of the previous chapters: an oscillator rheology can predict the behavior of a liquid cluster within a restricted frequency domain. In the present case, the entire first wave mode was well approximated. Eventually, a distinct deviation, due to frequency-dependent flow profiles, could not be observed. The effect of frequency dependence was below the uncertainty of the measurements and, with it, a lower-order effect.

Finally, the concept of oscillator-like modeling is supported by the present experiment. Both, experimental and numerical investigations, will benefit from a focus on free oscillations, due to the corresponding reproducibility and reduced number of samples. Further studies of more intricate geometries will enhance the elementary experiment presented and a comprehensive database may help to focus on the effect of frequency dependence.

Chapter 22

Review

22.1 Summary and main findings

The basic physical phenomena of oscillating fluid clusters were studied first. The most important relationships are momentum balance at the fluid-fluid interface and at the contact curve, resulting in Young-Laplace equation and Young's contact angle. Assumptions have been explained and justified with a special focus on Newtonian liquid clusters surrounded by a gas. Accounting for individual oscillation types such as pinned or sliding clusters, the main results of the theoretical chapter are

- the equations determining the cluster's motion, Tab. 19.1.

A classification of oscillating fluid clusters was then presented. It is based on the rheology of a harmonic oscillator. Each cluster is characterized by its mass m , eigenfrequency ω_0 , and damping ratio D . This characterization also allows a practical implementation into more comprehensive models like that of macroscopic wave propagation in residually saturated porous media.

Theoretical and numerical investigations revealed that the characteristic parameters ω_0 and D generally depend on oscillation frequency. This dependence was expressed by the dimensionless number N , which coincides with the squared Womersley number for the case of oscillations parallel to the solid walls. Moreover, a dependence on the capillary number Ca may also be required to account for the influence of the fluid-fluid interface relaxation time on the flow profile. Finally, frequency-dependent ω_0 and D need to be introduced for two reasons: (i) full accuracy of the cluster motion; and (ii) inclusion of multiple wave modes (different directions and multiples).

Nevertheless, clusters at different length scales (10 μm and 10 mm) showed a behavior very similar to that of a harmonic oscillator in their first eigenmode. Deviations of the predicted resonance frequency were $< 10\%$ for weakly damped clusters. Moreover, excitation by external stimulation becomes independent of the dynamic properties outside the resonance regime. Thus, a classical harmonic-oscillator rheology can be sufficient for modeling resonance effects in applications and scientific investigations. Especially for models of wave propagation in partially saturated porous media, the simple rheology is a good approximation, as long as capillary effects dominate (prediction of Ω_{res} within 5% inaccuracy for $D \leq 0.2$), for instance, for the model presented in Part III. For high cluster damping, a continuous model is preferred (as presented in Part I) and a distinction of the clusters as well as an oscillator model is not required.

One major result is that

- oscillator-like characterization of the residual fluid via the set $\{m, \omega_0, D\}$

is appropriate in its intended field of application. Tab. E.1 and Tab. E.2 include the main results of the numerical chapter for future application via analytical fitting curves. They provide dynamic properties of clusters and their sensitivity for changes of various geometrical and material parameters.

Typical characteristic frequencies were approximately a few thousand s^{-1} and all investigated clusters were weakly damped, with D values of a few percent. Investigated clusters with larger volumes and/or wall distances showed lower resonance frequencies and less damping. Larger pore spaces or larger fluid accumulations with lower solid-fluid connection surface tend to support ganglia excitation. In contrast, smaller or more tortuous versions of the investigated clusters had higher damping and resonance frequencies. For applications, the main finding is

- the provided data of oscillating, liquid clusters, Tab. E.1 and Tab. E.2,

which serves as an important basis for the macroscopic model of wave propagation in residually saturated porous media.

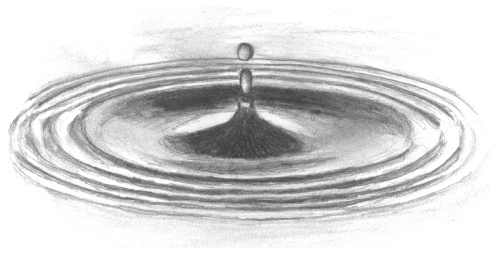
The results of the experimental investigation of a liquid bridge were similar to a classical oscillator rheology for the entire frequency range of the first oscillation mode. The regimes of viscous coupling, decoupling due to resonance effects, and a transition to higher wave modes could be distinguished. The amplification function of the first mode was well predicted by classification via mass, damping, and eigenfrequency.

22.2 Conclusions and outlook

Frequency dependence was investigated qualitatively and quantitatively, using selected examples. The systematic overview of eigenfrequency and damping ratio is important for application to wave propagation in residually saturated porous media, as described in Part III. Furthermore, it is of fundamental interest for modeling theories that account for resonance effects of liquid clusters. Specifically, the investigated types of clusters show resonance frequencies that exceed the seismic range. This behavior can be transferred to non-aqueous liquids with comparable properties. Hence, the superior potential of mobilization techniques via wave stimulation is expected in short-range situations [38, 198], for example, in laboratory samples or groundwater remediation in the vadose zone.

Longer-range situations, as well as consideration of the capillary number, will lead to a deeper understanding of the physical processes involved. Experimental results, for example, in combination with Particle Image Velocimetry (PIV), can support the physical interpretation and improve predictions of the impacts in specific applications. The present theoretical work offers a very general basis for studies of various aspects of oscillating fluid clusters. Several individual enhancements can be made, including turbulent effects or non-Newtonian fluids. In addition to the investigated pinned clusters, sliding clusters will be of particular interest in pre-wetted systems. Because of large deformations and eddies, it will probably be advisable to consider alternative numerical tools for sliding cluster motion, such as Smoothed Particle Hydrodynamics (SPH). Another extension of vital importance is to include another liquid as the second fluid phase, with its own inertia and viscosity. This step can extend the systematic study to general combinations of arbitrary fluids.

Treatise conclusion



Summary

The central objective of this investigation was the propagation of linear, mechanical waves in partially and residually saturated porous media. The general introduction motivated the topic and elucidated the fundamentals of porous media theories and wave propagation.

Part I developed a mathematical model for waves in partially saturated media on the basis of fundamental physical relationships, including balance laws and constitutive equations. The model allowed characterization of three longitudinal waves and one shear wave. Frequency-dependent phase velocities and quality factors have been studied for a variety of systems. Individual influences, including grain compressibility, interfacial fluid-fluid areas, or mesoscopic losses were characterized with respect to the corresponding wave properties.

Part II emphasized the importance of microscopic investigations on macroscopic theories. Frequency-dependent momentum exchange according to Biot was introduced via dimensionless Navier-Stokes equations in a rigid tube. Subsequently, a macroscopic characteristic frequency definition was generalized for weak solid frames, considering the solid's elasticity, inertia, and full-range upscaling. Microscopic, elastic tubes were discussed with the help of specific examples and showed a deviation from the classical rigid-tube assumption on the microscale.

Addressing the special case of residual saturation, Part III completes the macroscopic wave model of Part I. The fluid phase of residual saturation was described in the form of harmonic oscillators. These were distinguished with respect to their mass, eigenfrequency, and damping. An additional attenuation mechanism, due to resonance oscillations, was included. This made it possible to characterize the discontinuous fluid clusters with respect to their individual influence on the dispersion relations.

The microscopic part of the two-scale approach was presented in Part IV. Oscillating fluid clusters were theoretically described and classified via an oscillator-like rheology. The latter proved to be an appropriate model for the frequency range of individual oscillation modes. This was supported by the experimental study of a liquid bridge. The systematic, numerical investigation provided specific data of various liquid clusters for application.

The main findings can be summarized as follows:

Macroscale

- Mathematical model for linear, mechanical wave propagation in partially saturated porous media
 - hybrid model of less complexity if gases are involved
 - flexible implementation to test individual phenomena
- Mathematical model for linear, mechanical wave propagation in residually saturated porous media
 - consideration of the heterogeneous structure of disconnected clusters via their dynamic properties (ω_0 , D , m)
 - additional damping mechanism due to resonance effects

Microscale

- Oscillatory flow properties in rigid and elastic tubes
 - generalized, characteristic, macroscopic frequencies ($\rightarrow \omega^*$)
 - further wave modes due to wall elasticity of deformable tubes
- Characterization of fluid cluster oscillations
 - via an oscillator rheology
 - frequency-dependent, dynamic properties
 - database for different clusters

Conclusions

The model for continuous saturation clarified that specific physical conditions or relationships have a distinct influence on wave properties. Consequently, wave propagation can play a major role in the characterization of many aspects of partially saturated porous media. The final, customizable set of equations provides information about sensitivity and conditions and whether phenomena of interest can be detected via wave propagation or not. On this basis, studies using propagating waves extend other qualitative and quantitative research of properties such as interfacial areas or elastic moduli.

For the case of residual saturation, the heterogeneous structure of disconnected clusters differs significantly from a continuous phase with respect to its impact on wave propagation. This difference is mainly due to resonance effects, which are caused by fluid-fluid interfaces. It was important to distinguish between different kinds of clusters and transfer appropriate properties to the macroscale. The advantage of this two-scale approach relies on a compromise between preserving relevant information on the one hand and availability as well as feasibility on the other.

Two parts about microscopic studies revealed their significance for an accurate description on the larger scale. The corresponding scale transfer proved to be highly beneficial for the current work. In particular, the discussion about characteristic frequencies illustrated the importance of a consistent approach on all considered scales. Moreover, the upscaling process made limitations and loss of information clear, in relation to, for instance, the oscillator rheology used for fluid clusters and stimulation of microscopic wave modes.

In addition to the quantitative results and conceptual frameworks, specific conclusions of the present work are:

- Individual phenomena have a distinct influence on wave properties, especially in the frequency and saturation range.
- Two-scale interaction requires preservation of influential properties, specifically dynamic properties for resonance effects in residually saturated porous media.
- Combination of different scales requires a consistent set of conditions and assumptions.
- Microscopic and macroscopic understanding support each other mutually.

A discussion was provided for each part and its individual sections. It remains to be mentioned that the presented models rely on assumptions and act on specific systems. Generality was preserved as far as possible but had to turn into speciality for specific investigations and quantitative conclusions. Similar to other theoretical and experimental modeling approaches, it is important to have information about the applicability and limitation of the results and the conclusions that are drawn. Furthermore, experimental data that would be required to draw final conclusions about the investigated systems is not currently available. For example, Brooks & Corey parameters, dynamic capillary pressure, or cluster distributions remain to be verified in future experiments. This work can only be one further step towards the combination of propagating waves and partially saturated porous media - interdependent with(in) the fundament of theoretical, numerical, and experimental studies.

Outlook

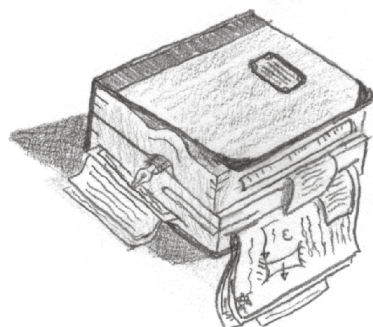
Some questions have been answered and some answers have been questioned.²⁵ Nevertheless, interesting investigations remain. Each discussed part has its own extensions and ongoing research is motivated from many sides. Moreover, the frameworks allow a flexible implementation of a variety of concepts. From the author's point of view and experience, three specific studies should be emphasized because of their scientific significance:

- Waves in residually saturated porous media: relating microscopic, oscillator properties and macroscopic, experimental observations such as attenuation or mobilization.
- Stimulation of microscopic wave modes in highly elastic solid matrices.
- Analysis of frequency-dependent cluster properties: distinguishing between volumetric and interface effects, for instance, numerically via dynamic particle methods or experimentally via particle image velocimetry.

Finally, the author hopes that the present contribution will motivate and support further research especially with the first goal mentioned in the introduction: understanding relevant physical principles.

²⁵Based loosely on Pratchett [161].

Appendix



Appendix A

Material properties

SOLIDS (BULK MATERIALS)			
material parameter		symbol	unit
effective/real density		ρ_0^{sR}	kg m^{-3}
Young's modulus		E^{grains}	Pa
Poisson's ratio		ν^{grains}	1
material	ρ_0^{fR}	E^{grains}	ν^{grains}
silicone	1120	1.47×10^6	0.499 787
steel	7900	200×10^9	0.28

Table A.1: Material properties of bulk solid materials. They are primarily used for the microscopic investigation of oscillations in elastic tubes in Part II. According to a consensus in theories of porous media, the elastic parameters of the bulk solid are indicated by the term *grains*. Properties of silicone were determined by measurement of P-wave velocity and Young's modulus. Note the silicone's behavior close to incompressibility ($\nu^{\text{grains}} = 0.5$).

When comparing elastic parameters of the following porous materials, consider the difference between real and partial extra stresses, Eq. (5.19) and Eq. (5.21), and that the corresponding elastic parameters differ by the factor of n_0^5 . Also note the naturally occurring fluctuations of material properties for natural, organic and non-organic materials such as bones or rocks.

SOLIDS (POROUS MATRIX)						
material parameter			symbol	unit		
effective/real density			ρ_0^{sR}	kg m^{-3}		
porosity			ϕ_0	1		
intrinsic permeability			k^s	m^2		
bulk modulus solid matrix			K^s	Pa		
bulk modulus solid grains			K^{grains}	Pa		
shear modulus solid matrix			μ^s	Pa		
skeleton deformation - grain pressure coupling			Λ^{grains}	Pa		
material	ρ_0^{sR}	ϕ_0	k^s	K^s	K^{grains}	μ^s
aluminum foam	2700	0.937	2.71×10^{-7}	54×10^6	68.6×10^9	21×10^6
Berea sandstone	2650	0.19	1.88×10^{-13}	8×10^9	36×10^9	6×10^9
bone (normal)	1960	0.72	5×10^{-9}	3.9×10^9	20.37×10^9	1.6×10^9
bone (osteop.)	1960	0.95	5×10^{-7}	0.42×10^9	20.37×10^9	0.17×10^9
loose soil	2600	0.3	1×10^{-9}	25×10^6	35×10^9	11.54×10^6
Massilon sandstone	2660	0.23	2.5×10^{-12}	1.02×10^9	35×10^9 ($\Lambda^{\text{grains}} = 10^{10}$)	1.44×10^9
Nivelsteiner sandstone	2640	0.29	1.11×10^{-11}	9.25×10^9	36.6×10^9	6.73×10^9

Table A.2: Material properties of porous solid materials. The bulk modulus of the aluminum foam was calculated from its measured elastic modulus and an estimated Poisson's ratio of 0.33. The permeability of the aluminum foam was estimated via [60] as $(1/150) d_p^2 \phi_0^3 / (1 - \phi_0)^2$ with equivalent particle diameter $d_p = 440.95 \times 10^{-6}$ m. Data for Berea sandstone is taken from [217], except for density of the solid grains that is from [170]. Data of bone is from [196]. Data for (loose surface) soil is estimated on the basis of [27, 201]. Data for Massilon sandstone is based on [151], [219], and [120] (bulk modulus*) with additional parameter Λ^{grains} from [219]. Nivelsteiner properties were taken from the comprehensive experimental results in [105] as averaged quantities of four given samples.

*: The author wishes to express caution with respect to the bulk modulus K^s of (dry) Massilon sandstone. Experimental data of Murphy [151] is often used to fit the material parameters but the conversion between P-, E-, and K-waves requires appropriate care and may lead to confusion (cf. the very similar tables of material data in [219] and [120]). Whereas (dry) sandstones typically show a Poisson's ratio around 0.2, Murphy [151] mentions a value of 0.02 for the total (fluid-saturated) mixture in the investigated low-frequency regime. The latter value is particularly important for the low-frequency behavior (when the entire mixture behaves similar to a single effective material) and it seems to play a major role in the material-parameter determination in [120, 219].

FLUIDS

material parameter		symbol	unit
effective/real density		ρ_0^{fR}	kg m^{-3}
effective dynamic viscosity		η^{fR}	Pa s
bulk modulus		K^f	Pa
surface tension (adjacent to air)		$\sigma^{f,\text{air}}$	N m^{-1}

material	ρ_0^{fR}	η^{fR}	K^f	$\sigma^{f,\text{air}}$
air (ambient conditions)	1.1	17.1×10^{-6}	1.4×10^5	-
air (reservoir depth)	140	-	22×10^6	-
bovine marrow (37 °C)	930	50×10^{-3}	2.0×10^9	-
test ink (20 °C)	808.5	1.2×10^{-3}	-	70×10^{-3}
water	1000	1×10^{-3}	2.2×10^9	70×10^{-3}

Table A.3: Material properties of fluids. Data of bovine marrow is taken from [196]. Information about the test ink, used in Chapter 21, is from the manufacturer's data sheet.

MATERIAL COMBINATIONS

material parameter		symbol	unit
Brooks & Corey parameter		λ_{BC}	1
air entry/bubbly pressure		p^b	Pa
parameter for dyn. extension of cap. pressure		τ_{S}	Pa s
residual liquid saturation		s_{res}^l	1
residual gas saturation		s_{res}^g	1

material	λ_{BC}	p^b	τ_{S}	s_{res}^l	s_{res}^g
Massilon sandstone, water & air	1.5	50×10^3	-1.59×10^8	0.1	0.05
Nivelsteiner sandstone, water & air	0.78	440	-6.74×10^3	0.04	0.04

Table A.4: Properties of material combinations. Data for Massilon sandstone, water & air is from [219] that is based on [151]. Data for the morphology of Nivelsteiner sandstone, water & air is from [195], which is a data-fit based on [179] and on a typical p^c - s^l curve from [185]. Dynamic parameters τ_{S} were determined via Eq. (5.48).

Appendix B

Wave equations for partial saturation

B.1 Exchange of linearization and compositions

The linearization and composition of functions can be exchanged under certain conditions. This is helpful if many and/or complicated functions need to be combined. Let the tensors \mathbf{f} and \mathbf{g} be continuously differentiable functions, which can be linearized and have a composition $\mathbf{g} \circ \mathbf{f}$. The linearization point for \mathbf{f} should be \mathbf{x}_0 and the linearization point for \mathbf{g} should be $\mathbf{f}_0 := \mathbf{f}(\mathbf{x}_0)$. Moreover, $\mathbf{g}_0 := \mathbf{g}(\mathbf{f}(\mathbf{x}_0)) = \mathbf{g}(\mathbf{f}_0)$ and $\Delta \mathbf{x} := \mathbf{x} - \mathbf{x}_0$.

The linearization of the composition around \mathbf{x}_0 is

$$\begin{aligned} (\mathbf{g} \circ \mathbf{f})_{\text{lin}, \mathbf{x}_0}(\mathbf{x}) &= (\mathbf{g} \circ \mathbf{f})(\mathbf{x}_0) + \left. \frac{d}{d\epsilon} \right|_{\epsilon=0} (\mathbf{g} \circ \mathbf{f})(\mathbf{x}_0 + \epsilon \Delta \mathbf{x}) \\ &= \mathbf{g}_0 + \left. \frac{\partial \mathbf{g}}{\partial \mathbf{f}} \right|_{\epsilon=0} \cdot \left. \frac{d}{d\epsilon} \right|_{\epsilon=0} \mathbf{f}(\mathbf{x}_0 + \epsilon \Delta \mathbf{x}). \end{aligned}$$

On the other hand, the composition of the linearized functions is

$$\begin{aligned} (\mathbf{g}_{\text{lin}, \mathbf{f}_0} \circ \mathbf{f}_{\text{lin}, \mathbf{x}_0})(\mathbf{x}) &= \mathbf{g}_0 + \left. \frac{d}{d\epsilon} \right|_{\epsilon=0} \mathbf{g}(\mathbf{f}_0 + \epsilon \Delta \mathbf{f}_{\text{lin}, \mathbf{x}_0}) \\ &= \mathbf{g}_0 + \left. \frac{d}{d\epsilon} \right|_{\epsilon=0} \mathbf{g} \left(\mathbf{f}_0 + \epsilon \left(\mathbf{f}_0 + \left. \frac{d}{d\gamma} \right|_{\gamma=0} (\mathbf{f}(\mathbf{x}_0 + \gamma \Delta \mathbf{x})) - \mathbf{f}_0 \right) \right) \\ &= \mathbf{g}_0 + \left. \frac{d}{d\epsilon} \right|_{\epsilon=0} \mathbf{g} \left(\mathbf{f}_0 + \epsilon \left. \frac{d}{d\gamma} \right|_{\gamma=0} \mathbf{f}(\mathbf{x}_0 + \gamma \Delta \mathbf{x}) \right) \\ &= \mathbf{g}_0 + \left. \frac{\partial \mathbf{g}}{\partial \mathbf{f}} \right|_{\epsilon=0} \cdot \left. \frac{d}{d\epsilon} \right|_{\epsilon=0} \left(\mathbf{f}_0 + \epsilon \left. \frac{d}{d\gamma} \right|_{\gamma=0} \mathbf{f}(\mathbf{x}_0 + \gamma \Delta \mathbf{x}) \right) \\ &= \mathbf{g}_0 + \left. \frac{\partial \mathbf{g}}{\partial \mathbf{f}} \right|_{\epsilon=0} \cdot \left. \frac{d}{d\gamma} \right|_{\gamma=0} \mathbf{f}(\mathbf{x}_0 + \gamma \Delta \mathbf{x}) = (\mathbf{g} \circ \mathbf{f})_{\text{lin}, \mathbf{x}_0}(\mathbf{x}). \end{aligned}$$

Hence, linearization and composition of \mathbf{f} and \mathbf{g} can be exchanged. For complex values, real and imaginary part need to be considered separately according to $\mathbb{C} \cong \mathbb{R}^2$. Furthermore, the so-called Gateaux derivative is used as it is common in classical continuum mechanics. Partial derivatives can be applied likewise via the chain rule.

B.2 Simplification of linearized products

Let scalar f and tensor \mathbf{g} be continuously differentiable, linearizable functions of the same argument \mathbf{x} . The linearization point is \mathbf{x}_0 with $\Delta\mathbf{x} := \mathbf{x} - \mathbf{x}_0$, $f_0 := f(\mathbf{x}_0)$, and $\mathbf{g}_0 := \mathbf{g}(\mathbf{x}_0)$. The linearization of the product becomes

$$\begin{aligned} (f\mathbf{g})_{\text{lin},\mathbf{x}_0}(\mathbf{x}) &= f_0\mathbf{g}_0 + \left. \frac{d}{d\epsilon} \right|_{\epsilon=0} (f\mathbf{g})(\mathbf{x}_0 + \epsilon\Delta\mathbf{x}) \\ &= f_0\mathbf{g}_0 + f_0 \left. \frac{d}{d\epsilon} \right|_{\epsilon=0} \mathbf{g}(\mathbf{x}_0 + \epsilon\Delta\mathbf{x}) + \mathbf{g}_0 \left. \frac{d}{d\epsilon} \right|_{\epsilon=0} f(\mathbf{x}_0 + \epsilon\Delta\mathbf{x}). \end{aligned}$$

It simplifies to

$$\begin{aligned} f_0 \left. \frac{d}{d\epsilon} \right|_{\epsilon=0} \mathbf{g}(\mathbf{x}_0 + \epsilon\Delta\mathbf{x}) &= f_0 \mathbf{g}_{\text{lin},\mathbf{x}_0}(\mathbf{x}), & \text{if } \mathbf{g}_0 = \mathbf{0}, \\ \mathbf{g}_0 \left. \frac{d}{d\epsilon} \right|_{\epsilon=0} f(\mathbf{x}_0 + \epsilon\Delta\mathbf{x}) &= f_{\text{lin},\mathbf{x}_0}(\mathbf{x}) \mathbf{g}_0, & \text{if } f_0 = 0. \end{aligned}$$

Thus, if f or \mathbf{g} vanish at the linearization point, the total expression simplifies and - what is physically more important - information of the other term is only required at the initial state. This state can be the equilibrium state, which is often well characterized for porous media.

A specific example in the present investigations is volume fraction times pressure gradient. This product appears in the momentum balance and depends on the volumetric deformations. The pressure gradient is often assumed to vanish in equilibrium. Thus, the volume fraction is only required to be known at the initial state.

Furthermore, material constants such as skeleton elasticity only need to be determined at initial conditions when multiplied with the divergence of stress tensors vanishing at equilibrium.

B.3 Algebra of the wave decomposition

The following properties have been used to transform the wave equations for a plane wave. Therein, \times indicates the cross product of vectors.

- $\text{div } \mathbf{u}_\alpha^\perp = i \mathbf{k} \cdot \mathbf{u}_\alpha^\perp = 0$
- $\text{rot } \mathbf{u}_\alpha^\parallel = i \mathbf{k} \times \mathbf{u}_\alpha^\parallel = \mathbf{0}$
- $\text{grad div } \mathbf{u}_\alpha = \text{div grad } \mathbf{u}_\alpha + \text{rot rot } \mathbf{u}_\alpha$
- $\text{rot rot } \mathbf{u}_\alpha = \text{rot rot } \mathbf{u}_\alpha^\perp = -\text{div grad } \mathbf{u}_\alpha^\perp + \text{grad div } \mathbf{u}_\alpha^\perp = -\text{div grad } \mathbf{u}_\alpha^\perp$
- $\text{grad div } \mathbf{u}_\alpha = \text{grad div } \mathbf{u}_\alpha^\parallel = \text{div grad } \mathbf{u}_\alpha^\parallel + \text{rot rot } \mathbf{u}_\alpha^\parallel = \text{div grad } \mathbf{u}_\alpha^\parallel$
- $\text{div grad } \mathbf{u} = i^2 k^2 (\mathbf{n}^k \cdot \mathbf{n}^k) \mathbf{u} = -k^2 \mathbf{u}$
- $\partial_t \mathbf{u} = -i \omega \mathbf{u}$
- $\partial_{tt} \mathbf{u} = -\omega^2 \mathbf{u}$
- $\mathbf{u}_\alpha^\parallel \perp \mathbf{u}_\alpha^\perp$, thus, linearly independent

Note that other wave forms such as spherical waves may contain a dependence of wave direction \mathbf{n}^k on location or time, which has to be considered for calculations of the derivatives.

B.4 Coefficients of the stiffness matrices

B.4.1 One solid and two fluid phases

$$\mathbf{C}^P = \begin{pmatrix} \lambda^s + 2\mu^s + \tilde{c}_s^{\parallel} & \tilde{c}_l^{\parallel} & \tilde{c}_g^{\parallel} \\ n_0^l p_{\epsilon_s}^{lR} & n_0^l p_{\epsilon_l}^{lR} & n_0^l p_{\epsilon_g}^{lR} \\ n_0^g p_{\epsilon_s}^{gR} & n_0^g p_{\epsilon_l}^{gR} & n_0^g p_{\epsilon_g}^{gR} \end{pmatrix}$$

$$\mathbf{C}^S = \begin{pmatrix} \mu^s & 0 & 0 \\ 0 & 0 & 0 \\ 0 & 0 & 0 \end{pmatrix}$$

Note that the term

$$M^s := \lambda^s + 2\mu^s = K^s + \frac{4}{3}\mu^s$$

is also called the P-wave modulus accounting for the solid's resistance.

$$\begin{aligned} \tilde{c}_\alpha^{\parallel} &= s_0^l p_{\epsilon_\alpha}^{lR} + (1 - s_0^l) p_{\epsilon_\alpha}^{gR} + (p_0^{lR} - p_0^{gR}) s_{\epsilon_\alpha}^l - n_0^l p_{\epsilon_\alpha}^{lR} - n_0^g p_{\epsilon_\alpha}^{gR} \\ p_{\epsilon_s}^{lR} &= (\Pi_\phi^{lR} + \Pi_{s^l}^{lR} \sigma_\phi) \varphi_{\epsilon_s} \\ p_{\epsilon_l}^{lR} &= \Pi_{\epsilon_l}^{lR} + \Pi_{s^l}^{lR} \sigma_{\epsilon_l} + (\Pi_\phi^{lR} + \Pi_{s^l}^{lR} \sigma_\phi) \varphi_{\epsilon_l} \\ p_{\epsilon_g}^{lR} &= \Pi_{s^l}^{lR} \sigma_{\epsilon_g} + (\Pi_\phi^{lR} + \Pi_{s^l}^{lR} \sigma_\phi) \varphi_{\epsilon_g} \\ p_{\epsilon_s}^{gR} &= (\Pi_\phi^{gR} + \Pi_{s^l}^{gR} \sigma_\phi) \varphi_{\epsilon_s} \\ p_{\epsilon_l}^{gR} &= \Pi_{s^l}^{gR} \sigma_{\epsilon_l} + (\Pi_\phi^{gR} + \Pi_{s^l}^{gR} \sigma_\phi) \varphi_{\epsilon_l} \\ p_{\epsilon_g}^{gR} &= \Pi_{\epsilon_g}^{gR} + \Pi_{s^l}^{gR} \sigma_{\epsilon_g} + (\Pi_\phi^{gR} + \Pi_{s^l}^{gR} \sigma_\phi) \varphi_{\epsilon_g} \\ \varphi_{\epsilon_s} &= \frac{r_{\epsilon_s}^s + \rho_0^{sR}}{\frac{\rho_0^{sR}}{1-\phi_0} - r_\phi^s}, \quad \varphi_{\epsilon_l} = \frac{r_{\epsilon_l}^s}{\frac{\rho_0^{sR}}{1-\phi_0} - r_\phi^s}, \quad \varphi_{\epsilon_g} = \frac{r_{\epsilon_g}^s}{\frac{\rho_0^{sR}}{1-\phi_0} - r_\phi^s} \\ r_{\epsilon_s}^s &= -\Lambda^{\text{grains}} \frac{\rho_0^{sR}}{K^{\text{grains}}} \\ r_{\epsilon_l}^s &= \frac{\rho_0^{sR}}{K^{\text{grains}}} \left[(1 - s_0^l) \Pi_{s^l}^{gR} \sigma_{\epsilon_l} + s_0^l (\Pi_{\epsilon_l}^{lR} + \Pi_{s^l}^{lR} \sigma_{\epsilon_l}) + (p_0^{lR} - p_0^{gR}) \sigma_{\epsilon_l} \right] \\ r_{\epsilon_g}^s &= \frac{\rho_0^{sR}}{K^{\text{grains}}} \left[(1 - s_0^l) (\Pi_{\epsilon_g}^{gR} + \Pi_{s^l}^{gR} \sigma_{\epsilon_g}) + s_0^l \Pi_{s^l}^{lR} \sigma_{\epsilon_g} + (p_0^{lR} - p_0^{gR}) \sigma_{\epsilon_g} \right] \\ r_\phi^s &= \frac{\rho_0^{sR}}{K^{\text{grains}}} \left[(1 - s_0^l) (\Pi_\phi^{gR} + \Pi_{s^l}^{gR} \sigma_\phi) + s_0^l (\Pi_\phi^{lR} + \Pi_{s^l}^{lR} \sigma_\phi) + (p_0^{lR} - p_0^{gR}) \sigma_\phi \right] \\ \sigma_{\epsilon_l} &= \frac{K^l}{\frac{\partial p^{\Delta g|l}}{\partial s^l} \Big|_0 - \left(\frac{K^g}{1-s_0^l} + \frac{K^l}{s_0^l} \right)}, \quad \sigma_{\epsilon_g} = \frac{-K^g}{\frac{\partial p^{\Delta g|l}}{\partial s^l} \Big|_0 - \left(\frac{K^g}{1-s_0^l} + \frac{K^l}{s_0^l} \right)} \\ \sigma_\phi &= \frac{\frac{K^l - K^g}{\phi_0}}{\frac{\partial p^{\Delta g|l}}{\partial s^l} \Big|_0 - \left(\frac{K^g}{1-s_0^l} + \frac{K^l}{s_0^l} \right)} \end{aligned}$$

$$\begin{aligned}\Pi_{\epsilon_l}^{lR} &= -K^l, & \Pi_{\phi}^{lR} &= -K^l/\phi_0, & \Pi_{s_0^l}^{lR} &= -K^l/s_0^l \\ \Pi_{\epsilon_g}^{gR} &= -K^g, & \Pi_{\phi}^{gR} &= -K^g/\phi_0, & \Pi_{s_0^l}^{gR} &= K^g/(1-s_0^l)\end{aligned}$$

Hybrid model If the grains are assumed to be incompressible, i.e. $K^s \rightarrow \infty$, the derivatives of the fluid pressures with respect to the volumetric deformations, $p_{\epsilon_\alpha}^{fR}$, become directly:

$$\begin{aligned}p_{\epsilon_s}^{lR} &= -K^l \left(\frac{1}{\phi_0} + \frac{1}{s_0^l} \frac{\frac{K^l - K^g}{\phi_0}}{\frac{\partial p^{\Delta g|l}}{\partial s^l} \Big|_0 - \left(\frac{K^g}{1-s_0^l} + \frac{K^l}{s_0^l} \right)} \right) (1 - \phi_0) \\ p_{\epsilon_l}^{lR} &= -K^l \left(1 + \frac{1}{s_0^l} \frac{K^l}{\frac{\partial p^{\Delta g|l}}{\partial s^l} \Big|_0 - \left(\frac{K^g}{1-s_0^l} + \frac{K^l}{s_0^l} \right)} \right) \\ p_{\epsilon_g}^{lR} &= \frac{K^l}{s_0^l} \left(\frac{K^g}{\frac{\partial p^{\Delta g|l}}{\partial s^l} \Big|_0 - \left(\frac{K^g}{1-s_0^l} + \frac{K^l}{s_0^l} \right)} \right) \\ p_{\epsilon_s}^{gR} &= -K^g \left(\frac{1}{\phi_0} - \frac{1}{1-s_0^l} \frac{\frac{K^l - K^g}{\phi_0}}{\frac{\partial p^{\Delta g|l}}{\partial s^l} \Big|_0 - \left(\frac{K^g}{1-s_0^l} + \frac{K^l}{s_0^l} \right)} \right) (1 - \phi_0) \\ p_{\epsilon_l}^{gR} &= \frac{K^g}{1-s_0^l} \left(\frac{K^l}{\frac{\partial p^{\Delta g|l}}{\partial s^l} \Big|_0 - \left(\frac{K^g}{1-s_0^l} + \frac{K^l}{s_0^l} \right)} \right) \\ p_{\epsilon_g}^{gR} &= -K^g \left(-1 + \frac{1}{1-s_0^l} \frac{-K^g}{\frac{\partial p^{\Delta g|l}}{\partial s^l} \Big|_0 - \left(\frac{K^g}{1-s_0^l} + \frac{K^l}{s_0^l} \right)} \right)\end{aligned}$$

B.4.2 Biphasic mixture (one solid and one fluid)

For one single fluid phase, the stiffness matrix obtained by Biot, Eq. (11.3c), can be used. In case of the rigid-grain assumption, a version of the P-wave stiffness matrix with less complexity can be derived, for instance, from the case of three phases above as

$$\mathbf{C}_{\text{biphasic, rigid grains}}^P = \begin{pmatrix} -(2\mu^s + \lambda^s) - \frac{(1-\phi_0)^2}{\phi_0} K^f & -(1-\phi_0)K^f \\ -(1-\phi_0)K^f & -\phi_0 K^f \end{pmatrix}. \quad (\text{B.1})$$

This was introduced by Steeb [196] as the so-called hybrid model for a biphasic mixture.

Appendix C

Analytical investigation of the characteristic frequencies

The inverse quality factor of a biphasic medium, $Q_\chi^{-1} = 2 \Im k^\chi / \Re k^\chi$ with $\chi \in \{P1, P2, S\}$, depends on the solutions of the wave number k^χ . The squared wave number can be written in terms of the matrix coefficients, cf. Eq. (11.3c),

$$\begin{aligned} k_S^2 &= \frac{1}{\mu^s} \frac{a_{11}a_{22} - a_{12}^2}{a_{22}}, \\ k_{P1,2}^2 &= \frac{1}{2} \frac{2S_{BW}a_{12} - P_{BW}a_{22} - R_{BW}a_{11}}{P_{BW}R_{BW} - S_{BW}^2} \left(-1 \pm \sqrt{1 - \Delta} \right), \\ \Delta &= 4 \frac{P_{BW}R_{BW} - S_{BW}^2}{2S_{BW}a_{12} - P_{BW}a_{22} - R_{BW}a_{11}} (a_{11}a_{22} - a_{12}^2), \\ \sqrt{1 - \Delta} &\stackrel{\Delta \ll 1}{\approx} 1 - \frac{\Delta}{2} - \frac{\Delta^2}{8} - \dots \end{aligned}$$

with abbreviation

$$\begin{pmatrix} a_{11} & a_{12} \\ a_{12} & a_{22} \end{pmatrix} = \omega^2 \mathbf{A}_{\text{Biot}} + i\omega \mathbf{B}_{\text{Biot}}.$$

It has been used that the square root of a complex-valued number $a + ib$ can be achieved from

$$\begin{aligned} a + ib &= (c + id)^2, \quad a, b, c, d \in \mathbb{R}, \\ d &= \pm \sqrt{\frac{1}{2} \left(-a + \sqrt{a^2 + b^2} \right)}, \\ c &= \frac{b}{2d}. \end{aligned}$$

A distinction of cases with respect to the sign of d is not necessary here, because it appears as d^2 in the required solutions. Furthermore, it is helpful to express the inverse quality factor as $Q_\chi^{-1} = \xi_\chi + \sqrt{\xi_\chi^2 - 1}$, because

$$\xi_\chi = \Re(k^{\chi 2}) / \Im(k^{\chi 2})$$

can be derived more easily from the eigenvalue formulation. For one dominating diagonal element of the stiffness matrix, ξ_χ can be written in the form of

$$\xi_\chi(\omega) = [\dots] \frac{\omega}{\Re(c_{\text{JKD}}(\omega/\omega_{c,f}))} - [\dots] \frac{\Re(c_{\text{JKD}}(\omega/\omega_{c,f})) + \Im^2(c_{\text{JKD}}(\omega/\omega_{c,f}))}{\Re(c_{\text{JKD}}(\omega/\omega_{c,f}))} \frac{1}{\omega} - [\dots] \frac{\Im(c_{\text{JKD}}(\omega/\omega_{c,f}))}{\Re(c_{\text{JKD}}(\omega/\omega_{c,f}))},$$

where [...] represent constants depending on the entries of the density and damping matrices. Moreover, the necessary and sufficient conditions for unique maxima become

$$\begin{aligned} \frac{d}{d\omega} Q_{P1,S}^{-1}(\omega) = 0 &\Leftrightarrow \frac{d}{d\omega} \xi_{P1,S}(\omega) = 0, \\ \frac{d^2}{d\omega^2} Q_{P1,S}^{-1}(\omega) < 0 &\Leftrightarrow \frac{d^2}{d\omega^2} \xi_{P1,S}(\omega) < 0. \end{aligned}$$

Appendix D

Upscaling of discontinuous fluid clusters

Basic and preliminary definitions

Let $\mathcal{M}_{\text{cl,mic}}$ contain all countable (finitely or infinitely many) indices of the microscopic clusters in one REV. Furthermore, \mathcal{M}_{ω_0} and \mathcal{M}_D contain all countable indices of different occurring eigenfrequencies and damping ratios respectively. The volume occupied by the fluid clusters with eigenfrequency $\omega_{0,k}$ and damping ratio D_l is denoted as

$$V_{kl} = \bigcup_{\substack{j \in \mathcal{M}_{\text{cl,mic}} \\ \omega_{j,0} = \omega_{k,0} \\ D_j = D_l}} V_{\text{mic},j}. \quad (\text{D.1})$$

The volume occupied by all clusters in one REV, i.e. by the entire discontinuous phase, is

$$V_{\mathfrak{d}} = \bigcup_{[k,l] \in \mathcal{M}_{\omega_0} \times \mathcal{M}_D} V_{kl}. \quad (\text{D.2})$$

The following volume ratios can be derived from it:

$$n^{kl} = \frac{V_{kl}}{V_{\text{REV}}}, \quad (\text{D.3})$$

$$n^{\mathfrak{d}} = \frac{V_{\mathfrak{d}}}{V_{\text{REV}}}, \quad (\text{D.4})$$

$$\alpha^{kl} = \frac{V_{kl}}{V_{\mathfrak{d}}} = \frac{n^{kl}}{n^{\mathfrak{d}}}. \quad (\text{D.5})$$

Mass and density of a cluster with undamped eigenfrequency $\omega_{k,0}$ and damping ratio D_l becomes

$$m_{kl} = \sum_{\substack{j \in \mathcal{M}_{\text{cl,mic}} \\ \omega_{j,0} = \omega_{k,0} \\ D_j = D_l}} m_{\text{mic},j}, \quad (\text{D.6})$$

$$\rho^{kl} = \frac{m_{kl}}{V_{\text{REV}}}, \quad (\text{D.7})$$

$$\rho^{klR} = \frac{m_{kl}}{V_{kl}} = \rho^{kl} n^{\text{d}} \alpha^{kl}. \quad (\text{D.8})$$

Mass-weighted averaging of the microscopic cluster displacement yields the definition of a macroscopic cluster displacement

$$\mathbf{u}_{kl} := \frac{1}{m_{kl}} \sum_{\substack{j \in \mathcal{M}_{\text{cl,mic}} \\ \omega_{j,0} = \omega_{k,0} \\ D_j = D_l}} m_{\text{mic},j} \mathbf{u}_{\text{mic},j}. \quad (\text{D.9})$$

Within the framework of a linear theory, the microscopic term $m_{\text{mic},j} \mathbf{u}_{\text{mic},j}$ becomes $m_{\text{mic},j,0} \mathbf{u}_{\text{mic},j}$ after linearization around equilibrium. It follows that

$$\mathbf{u}_{kl} = \frac{1}{m_{kl,0}} \sum_{\substack{j \in \mathcal{M}_{\text{cl,mic}} \\ \omega_{j,0} = \omega_{k,0} \\ D_j = D_l}} m_{\text{mic},j,0} \mathbf{u}_{\text{mic},j},$$

$$\dot{\mathbf{u}}_{kl} = \frac{1}{m_{kl,0}} \sum_{\substack{j \in \mathcal{M}_{\text{cl,mic}} \\ \omega_{j,0} = \omega_{k,0} \\ D_j = D_l}} m_{\text{mic},j,0} \dot{\mathbf{u}}_{\text{mic},j},$$

$$\ddot{\mathbf{u}}_{kl} = \frac{1}{m_{kl,0}} \sum_{\substack{j \in \mathcal{M}_{\text{cl,mic}} \\ \omega_{j,0} = \omega_{k,0} \\ D_j = D_l}} m_{\text{mic},j,0} \ddot{\mathbf{u}}_{\text{mic},j}$$

after linearization. Moreover, it is assumed that the adjacent solid walls (asw) move like the solid phase in average

$$\mathbf{u}_{\text{s}} \approx \frac{1}{m_{kl}} \sum_{\substack{j \in \mathcal{M}_{\text{cl,mic}} \\ \omega_{j,0} = \omega_{k,0} \\ D_j = D_l}} m_{\text{mic},j} \mathbf{u}_{\text{asw},j}. \quad (\text{D.10})$$

Upscaling

Finally, the upscaling process can be accomplished with the parameters introduced above. Averaging a microscopic variable $(\bullet)_{\text{mic},j}$ over one REV is executed systematically by

$$\frac{1}{V_{\text{REV}}} \sum_{\substack{j \in \mathcal{M}_{\text{cl,mic}} \\ \omega_{j,0} = \omega_{k,0} \\ D_j = D_l}} (\bullet)_{\text{mic},j} = n^{\text{d}} \alpha^{kl} \frac{1}{V_{kl}} \sum_{\substack{j \in \mathcal{M}_{\text{cl,mic}} \\ \omega_{j,0} = \omega_{k,0} \\ D_j = D_l}} (\bullet)_{\text{mic},j}. \quad (\text{D.11})$$

In contrast to classical homogenization theories such as [86–88], integration over an REV is replaced by summation over the clusters. This difference occurs because the

microscopic discontinuous fluid phase is already modeled by a countable set of harmonic oscillators. Additionally, the present upscaling procedure utilizes the linearized version of the equations. This prevents the need for further terms (of higher order) such as time-dependent mass change inside the REV.

Each part of the microscopic momentum balance, Eq. (15.3), is now averaged. It will be used that the initial effective density of the clusters is assumed to be constant, $\rho_0^{klR} =: \rho_0^{\delta R} \approx \text{const}$. Moreover, the equation is upscaled in its linearized form around equilibrium. It follows

$$\begin{aligned} \frac{1}{V_{\text{REV}}} \sum_{\substack{j \in \mathcal{M}_{\text{cl,mic}} \\ \omega_{j,0} = \omega_{k,0} \\ D_j = D_l}} m_{\text{mic},j,0} \ddot{\mathbf{u}}_{\text{mic},j} &= n_0^{\delta} \alpha_0^{kl} m_0^{kl} \ddot{\mathbf{u}}_{kl} = \alpha_0^{kl} \rho_0^{\delta} \ddot{\mathbf{u}}_{kl}, \\ \frac{1}{V_{\text{REV}}} \sum_{\substack{j \in \mathcal{M}_{\text{cl,mic}} \\ \omega_{j,0} = \omega_{k,0} \\ D_j = D_l}} [m_{\text{mic},j,0} \omega_{0,j}^2 (\ddot{\mathbf{u}}_{\text{mic},j} - \ddot{\mathbf{u}}_{\text{mic,solid walls}}) \\ &+ 2 m_{\text{mic},j,0} \omega_{0,j} D_j (\dot{\mathbf{u}}_{\text{mic},j} - \dot{\mathbf{u}}_{\text{mic,solid walls}})] \\ &= \alpha_0^{kl} \rho_0^{\delta} [\omega_{0,k}^2 (\mathbf{u}_{kl} - \mathbf{u}_s) + 2 \omega_{0,k} D_l (\dot{\mathbf{u}}_{kl} - \dot{\mathbf{u}}_s)], \\ \frac{1}{V_{\text{REV}}} \sum_{\substack{j \in \mathcal{M}_{\text{cl,mic}} \\ \omega_{j,0} = \omega_{k,0} \\ D_j = D_l}} - \hat{\mathbf{p}}_{\text{mic}}^j &=: -\hat{\mathbf{p}}^{kl}. \end{aligned}$$

Expansion by m^{kl}/m^{kl} has been used in the derivation process. Applying the harmonic approach²⁶, Eq. (5.52), to the displacements and combining the single terms yields

$$\alpha_0^{kl} \rho_0^{\delta} \omega^2 \mathbf{u}_{kl} = \alpha_0^{kl} \rho_0^{\delta} [\omega_{0,k}^2 (\mathbf{u}_{kl} - \mathbf{u}_s) - 2 \omega_{0,k} D_l \omega i (\mathbf{u}_{kl} - \mathbf{u}_s)] = -\hat{\mathbf{p}}^{kl}. \quad (\text{D.12})$$

The left equation in Eq. (D.12) can be used to express \mathbf{u}_{kl} by \mathbf{u}_s as

$$\mathbf{u}_{kl} = \frac{\omega_{0,k}^2 - 2 \omega_{0,k} \omega D_l i}{(\omega_{0,k}^2 - \omega^2) - 2 \omega_{0,k} \omega D_l i} \mathbf{u}_s. \quad (\text{D.13})$$

This step eases the set of equations because the oscillator displacements do not need to be solved. If the oscillator displacements are of particular interest, Eq. (D.13) is suggested for their determination rather than solving an eigenvalue formulation similar to Eq. (5.56) with a matrix size that increases with the number of oscillators. Furthermore, momentum interaction with the solid can be written as

$$\hat{\mathbf{p}}^{kl} = -\alpha_0^{kl} \rho_0^{\delta} (\omega_{0,k}^2 - 2 \omega_{0,k} \omega D_l i) \left(\frac{\omega_{0,k}^2 - 2 \omega_{0,k} \omega D_l i}{(\omega_{0,k}^2 - \omega^2) - 2 \omega_{0,k} \omega D_l i} - 1 \right) \mathbf{u}_s. \quad (\text{D.14})$$

²⁶Note that Steeb et al. [198] used a harmonic approach of $e^{+i\omega t}$ instead $e^{-i\omega t}$ for the single oscillator. The different sign does not contradict the results of the current framework.

Distinction with respect to the eigenfrequencies only

An approach of less complexity is achieved by exclusive differentiation of the eigenfrequencies. Following the averaging process above, the damping ratio becomes an averaged value for all clusters of same eigenfrequency $\omega_{0,k}$ as

$$D_k^* = \frac{\sum_{\substack{j \in \mathcal{M}_{\text{cl,mic}} \\ \omega_{j,0} = \omega_{k,0}}} m_{\text{mic},j,0} (\dot{\mathbf{u}}_{\text{mic},j} - \dot{\mathbf{u}}_{\text{mic,solid walls}}) D_j}{\sum_{\substack{j \in \mathcal{M}_{\text{cl,mic}} \\ \omega_{j,0} = \omega_{k,0}}} m_{\text{mic},j,0} (\dot{\mathbf{u}}_{\text{mic},j} - \dot{\mathbf{u}}_{\text{mic,solid walls}})}. \quad (\text{D.15})$$

Appendix E

Investigation of oscillating fluid clusters

E.1 Numerical data

Specific data is of interest for comparison with other investigations and is, therefore, presented in a compact form. The results of the systematic, numerical investigation of oscillating fluid clusters are given in the following.

E.1.1 Numerical results

Model I

Initial values:

ρ_0^{LR} [kg m ⁻³]	η_0^{LR} [Pa s]	σ_0^{lg} [N m ⁻¹]	$\theta_{\text{Young},0}$ [°]	V_0 [m ³]	Λ_0 [1]	l_0 [m]	R_0 [m]
1000	0.001	0.07	90	7.85×10^{-10}	2	0.001	5×10^{-4}

Variations:

$\Theta_{\text{Young},0}$ [°]	transversal oscillations		parallel oscillations			
	ω_0 [s ⁻¹]	D [1]	ω_0 [s ⁻¹]	D [1]	$\mathcal{A}_{\text{lg}}^*$ [10 ⁻⁶ m ²]	$\mathcal{A}_{\text{ls}}^*$ [10 ⁻⁶ m ²]
34	855.3842	0.035165	1157.7258	0.032229	4.021	3.262
50	1096.8329	0.023033	1671.452	0.021658	3.491	2.550
64.7	1234.6209	0.018149	2087.7955	0.018533	3.250	2.110
78.3	1269.5184	0.017209	2276.7791	0.01519	3.152	1.800
90	1239.4374	0.015576	2426.1786	0.014015	3.142	1.571
99.6	1183.4079	0.015039	2473.8911	0.012591	3.143	1.375
107.2	1116.1247	0.013781	2459.3475	0.011935	3.180	1.240
112.9	1059.6556	0.013498	2426.0997	0.011464	3.210	1.130
116.7	1021.7475	0.013374	2407.4805	0.010385	3.240	1.065

*: equilibrium interface areas for different contact angles are provided from numerical results because they cannot be derived easily.

Model II**Initial values:**

ρ_0^{IR} [kg m ⁻³]	η_0^{IR} [Pa.s]	σ_0^{Ig} [N m ⁻¹]	$\theta_{Young,0}$ [°]	V_0 [m ³]	Λ_0 [1]	l_0 [m]	R_0 [m]	τ_0 [1]
1000	0.001	0.07	90	7.85×10^{-9}	20	0.01	5×10^{-4}	0

Variations:

ratio	V/V_0		Λ/Λ_0		l/l_0	
	ω_0 [s ⁻¹]	D	ω_0 [s ⁻¹]	D	ω_0 [s ⁻¹]	D
1/100	6121.3796	0.088025				
1/10	1954.0498	0.068479	629.6177	0.018289	1989.049	0.026513
1	623.5168	0.050726	623.5168	0.050726	623.5168	0.050726
10	198.9052	0.037008	594.1154	0.14551	192.8236	0.11427
25						

ratio	η^{IR}/η_0^{IR}		τ [1]	$(R, V = \text{const.})$	
	ω_0 [s ⁻¹]	D		ω_0 [s ⁻¹]	D
1/100			0	623.5168	0.050726
1/10	632.1859	0.0065448	1/4	632.2969	0.050943
1	623.5168	0.050726	1/2	635.5441	0.052574
10	574.8614	0.25032	1	626.5519	0.057818
25	568.2999	0.55112	2	654.2157	0.065786

Frequency dependence**Initial values:**

initial values	V_0 [m ³]	λ_0 [1]	l_0 [m]	R_0 [m]	τ_0 [1]
model I, small	7.85E-16	2	1.00E-5	5.00E-6	-
model I, big	7.85E-7	2	1.00E-2	5.00E-3	-
model II, small	7.85E-15	20	1.00E-4	5.00E-6	0
model II, big	7.85E-6	20	1.00E-1	5.00E-3	0

Material parameters are initial values as defined above.

Variations:

model I, small, transversal oscillations:

ρ^{IR}/ρ_0^{IR}	ω_0 [s ⁻¹]	D [1]	N [1]	c [kg s ⁻²]	d [10 ⁻⁹ kg s ⁻¹]
100	123942.6984	0.0150	309.822	1.207	292.559
10	388654.1452	0.0325	97.112	1.186	198.234
1	1199312.0032	0.0647	29.919	1.129	121.934
0.1	3705759.2590	0.1399	9.173	1.079	81.471
0.01	11598215.7563	0.3888	2.671	1.057	70.833

model I, big, transversal oscillations:

ρ^{IR}/ρ_0^{IR}	ω_0 [s ⁻¹]	D [1]	N [1]	c [kg s ⁻²]	d [10 ⁻⁶ kg s ⁻¹]
10	12.5756	0.0053	3143.857	1.242	1038.235
1	39.3697	0.0082	984.209	1.217	509.119
0.1	123.8879	0.0157	309.682	1.205	304.845
0.01	387.1066	0.0331	96.724	1.177	200.698
0.0001	3712.5430	0.1348	9.197	1.083	78.587
0.00001	11671.3996	0.3891	2.688	1.070	71.332

model I, small, parallel oscillations:

ρ^{IR}/ρ_0^{IR}	ω_0 [s ⁻¹]	D [1]	N [1]	c [kg s ⁻²]	d [10 ⁻⁹ kg s ⁻¹]
100	243177.1711	0.0128	607.8933	4.6445	487.982
10	764591.4105	0.0320	191.0498	4.5914	384.686
1	2389432.2355	0.0888	59.4999	4.4841	333.264
0.1	7484650.7963	0.2531	18.1024	4.3998	297.566

model I, big, parallel oscillations:

ρ^{IR}/ρ_0^{IR}	ω_0 [s ⁻¹]	D [1]	N [1]	c [kg s ⁻²]	d [10 ⁻⁶ kg s ⁻¹]
10	24.5301	0.0044	6132.466	4.726	1689.079
1	77.5717	0.0070	1939.244	4.726	858.989
0.1	242.9437	0.0191	607.249	4.636	728.007
0.01	764.7981	0.0332	191.094	4.594	398.245
0.0001	7455.3265	0.2567	18.014	4.365	300.628

model II, small:

ρ^{IR}/ρ_0^{IR}	ω_0 [s ⁻¹]	D [1]	N [1]	c [kg s ⁻²]	d [10 ⁻⁹ kg s ⁻¹]
1000	19793.9393	0.0199	494.750	3.077	6189.845
100	61924.7694	0.0516	154.606	3.012	5016.179
10	190869.7971	0.1156	47.398	2.861	3464.392
1	575327.1543	0.2503	13.925	2.600	2261.654
0.5	808642.5622	0.3299	9.542	2.568	2094.962

model II, big:

ρ^{IR}/ρ_0^{IR}	ω_0 [s ⁻¹]	D [1]	N [1]	c [kg s ⁻²]	d [10 ⁻⁶ kg s ⁻¹]
10	6.3078	0.0070	1576.911	3.125	6934.599
1	19.8624	0.0201	496.459	3.099	6284.573
0.1	62.1882	0.0499	155.276	3.037	4878.584
0.01	190.6260	0.1148	47.342	2.854	3436.312
0.001	575.8403	0.2493	13.941	2.604	2255.350

E.1.2 Fitted ω_0 - and D -relationships

model	δ	a_0	a_1	a_2
I, trans.		$\omega_0(\delta) [\text{s}^{-1}] \approx a_0 \delta^{a_1} + a_2$		
	$\rho^{IR} [\text{kg m}^{-3}]$	3.7785×10^4	-0.4941	-5.5282
	$\eta^{IR} [\text{Pa.s}]$	-1.2061×10^3	0.6850	1.2495×10^3
	$\sigma^{Iq} [\text{N m}^{-1}]$	4.7106×10^3	0.5013	-3.1055
	$V [\text{m}^3]$	0.0436	-0.4896	-12.7107
	$\Lambda [1]$	1.2454×10^3	-0.7407	455.5227
		$\omega_0(\delta) [\text{s}^{-1}] \approx a_0 + a_1 \delta + a_2 \delta^2$		
	$\Theta_{\text{Young}} [^\circ]$	40.6290	30.6553	-0.1916
I, paral.		$\omega_0(\delta) [\text{s}^{-1}] \approx a_0 \delta^{a_1} + a_2$		
	$\rho^{IR} [\text{kg m}^{-3}]$	7.7624×10^4	-0.5028	14.7913
	$\eta^{IR} [\text{Pa.s}]$	-194.8149	0.3010	2.4498×10^3
	$\sigma^{Iq} [\text{N m}^{-1}]$	9.2066×10^3	0.5018	-1.3399
	$V [\text{m}^3]$	0.0739	-0.4963	-8.0223
	$\Lambda [1]$	7.7757×10^3	-0.9185	-1.5940×10^3
		$\omega_0(\delta) [\text{s}^{-1}] \approx a_0 + a_1 \delta + a_2 \delta^2$		
	$\Theta_{\text{Young}} [^\circ]$	-475.9924	57.3362	-0.2795
II		$\omega_0(\delta) [\text{s}^{-1}] \approx a_0 \delta^{a_1} + a_2$		
	$V [\text{m}^3]$	0.0597	-0.4959	-0.3258
	$\Lambda [1]$	-0.9950	0.6830	631.2151
	$l [\text{m}]$	62.5843	-0.5011	-5.6027
	$\eta^{IR} [\text{Pa.s}]$	-237.6737	0.2470	659.5487
		$\omega_0(\delta) [\text{s}^{-1}] \approx a_0 + a_1 \delta + a_2 \delta^2$		
	$\tau [1]$	628.5854	-2.9795	7.5994

Table E.1: Fitting of ω_0 for variations δ . Most variations cover a range of factors 1/8 to 8, except for slenderness and the special cases of Young's contact angle and winding. Further note that ω_0 increases very accurately by the factor $\sqrt{2}$ for each doubling of σ^{Iq} or bisection of ρ^{IR} , V , or l in the investigated range of low damping, which is indicated by exponents a_1 close to ± 0.5 .

model	δ	b_0	b_1	b_2
I, trans.		$D(\delta) [1] \approx b_0 \delta^{b_1} + b_2$		
	$\rho^{IR} [\text{kg m}^{-3}]$	0.1614	-0.3531	0.0011
	$\eta^{IR} [\text{Pa s}]$	1.0984	0.6033	-0.0013
	$\sigma^{lg} [\text{N m}^{-1}]$	0.0022	-0.5645	0.0045
	$V [\text{m}^3]$	1.1219×10^{-5}	-0.3045	0.0090
	$\Lambda [1]$	0.0395	-0.3532	-0.0150
	$\Theta_{\text{Young}} [^\circ]$	8.5945	-1.6607	0.0104
I, paral.		$D(\delta) [1] \approx b_0 \delta^{b_1} + b_2$		
	$\rho^{IR} [\text{kg m}^{-3}]$	0.2951	-0.5072	0.0042
	$\eta^{IR} [\text{Pa s}]$	4.4395	0.8601	0.0018
	$\sigma^{lg} [\text{N m}^{-1}]$	0.0054	-0.3812	-0.0019
	$V [\text{m}^3]$	4.7021×10^{-4}	-0.1507	0.0024
	$\Lambda [1]$	0.0534	-0.2063	-0.0300
	$\Theta_{\text{Young}} [^\circ]$	1.0522	-1.0149	0.0027
II		$D(\delta) [1] \approx b_0 \delta^{b_1} + b_2$		
	$V [\text{m}^3]$	0.0235	-0.0732	-0.0411
	$\Lambda [1]$	0.0122	0.4654	0.0014
	$l [\text{m}]$	0.2694	0.4190	0.0116
	$\eta^{IR} [\text{Pa s}]$	13.1007	0.8636	0.0083
		$D(\delta) [1] \approx b_0 + b_1 \delta + b_2 \delta^2$		
	$\tau [1]$	0.0500	0.0060	9.7862×10^{-4}

Table E.2: Fitting of D for variations δ . Most variations cover a range of factors 1/8 to 8, except for slenderness and the special cases of Young's contact angle and winding.

E.2 Experimental data

The following table summarizes the experimental results of the driven oscillations described in Chapter 21.

stimulation frequency Ω [s^{-1}]	amplification function V_{amp} [1]
6.14	1.04
30.68	1.04
30.68	1.06
62.89	1.08
92.04	1.40
93.18	1.16
126.55	1.52
156.47	2.16
156.47	2.25
184.08	5.00
188.68	3.62
202.49	10.00
211.69	13.33
211.69	7.50
220.89	13.33
220.89	7.92
230.10	10.50
239.30	6.83
248.51	11.00
248.51	6.75
285.32	5.50
285.32	3.00
312.93	2.50
349.75	1.33
377.36	1.00
404.97	1.50
441.79	0.75
506.21	2.00
561.44	1.20
943.40	4.17

Table E.3: Experimental results of a stimulated, oscillating liquid bridge. The stimulation frequency was determined via an FFT of the beam oscillations while the measured amplification function relates the movement of the liquid-bridge center to the movement of the beams. The last value is mentioned as a representative, distinctively captured, higher oscillation mode.

Appendix F

About objectivity and the initial configuration in engineering literature

F.1 Introduction

Objectivity or material frame indifference is a term that is widely used in physics and theoretical engineering science. The following considerations focus on the use of objectivity in the framework of continuum mechanics as it is used in engineering. Other definitions of objectivity - although connected by the same basic concept - are out of the current scope, including the enhancement of classical Newton's mechanics to the theory of relativity.

Even in continuum mechanics, there does not seem to be a common unique definition of objectivity [6, 12, 90, 126]. Rather, there seem to be a rough, tacit consent of its meaning or use. In theoretical continuum mechanics, an objective quantity is often defined as a quantity that is independent of the observer. For example, a velocity is not objective but subjective, because its value can appear differently to two observers moving with their own, possibly different velocities. On the contrary, a velocity difference is objective because the observer velocities cancel out in its determination.

Consequently, a physical system that independent of any observer is assumed to depend solely on objective quantities. This fact is used to limit and reformulate possible dependencies or relationships determining the system's behavior. However, confusion can occur - consciously or unconsciously - due to a misleading definition in engineering science including textbooks and lecture notes. The mistake is not wrong by default but subject to misunderstanding and misinterpretation within a missing strict consensus. This should be investigated and highlighted here as it remains a possible source of wrong conclusions.

The mentioned misunderstanding has been pointed out, for example, in the contribution of Liu [126] but, to the authors best knowledge, often remains disregarded in actual works on continuum mechanics. A scientific dispute between Liu and Murdoch developed about further implementation and application to constitutive equations [127, 150], but it does not affect the point of interest addressed in this chapter.

F.2 Recapitulation

The theory of continuum mechanics models, amongst others, the physical behavior of fluids and solids. The conservation of momentum for solids includes the description of stresses depending on strain. Furthermore, the definition of strain depends on a deformation between two configurations. Therefore, a so-called initial/reference configuration at initial time t_0 is often introduced. This can be a configuration where all quantities are known, for example, the equilibrium state.

From that reference time t_0 , the physical system develops in time t . Moreover, a length $d\mathbf{X} := d\mathbf{x}(t_0)$ between two points changes to $d\mathbf{x}(t)$. $d\mathbf{X}$ belongs to the initial/reference configuration, whereas $d\mathbf{x}$ belongs to the current configuration.

An arbitrary point \mathcal{P} should be described by one observer as $\mathcal{P} = \sum_i p_i \mathbf{b}_i$; \mathbf{b}_i taken as the basis of the observer and p_i as the corresponding coordinates. Another observer should have the basis $\hat{\mathbf{b}}_i$ with description $\mathcal{P} = \sum_i \hat{p}_i \hat{\mathbf{b}}_i$. For the sake of convenience, the bases $\{\mathbf{b}_1, \mathbf{b}_2, \mathbf{b}_3\}$ and $\{\hat{\mathbf{b}}_1, \hat{\mathbf{b}}_2, \hat{\mathbf{b}}_3\}$ should be orthonormal bases of a three-dimensional space. This simplification is not necessary, but can be chosen without limitation of validity of the following findings. It includes the assumption that both observers measure with the same units (for example, no transformation between angles and lengths or meters and feet).

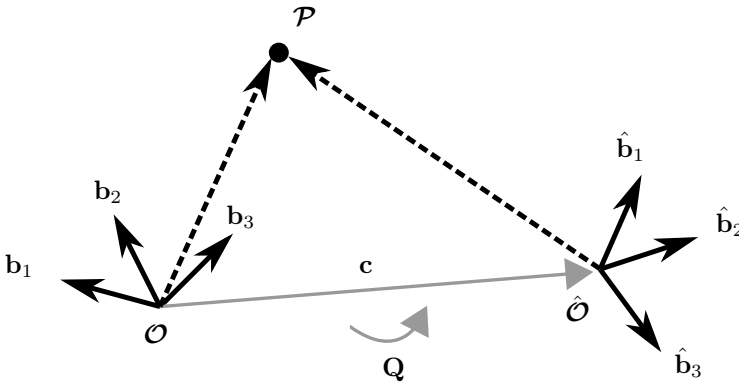


Figure F.1: One point for two observers. The length between the point and the origin of measurement is obviously different.

A possible difference between the coordinates determined by the two observers can be described by an Euclidean transformation²⁷ as

$$\hat{p}_i = \sum_j Q_{ij} p_j + c_i. \quad (\text{F.1})$$

Herein, Q_{ij} describes a rotation between both observers with $|\det Q_{ij}| = 1$ and $Q_{ij}^T = Q_{ij}^{-1}$, whereas c_i describes a translation between the origins. They depend on the relationship of the two observer systems, $\{\mathbf{b}_1, \mathbf{b}_2, \mathbf{b}_3\}$ with origin \mathcal{O} and $\{\hat{\mathbf{b}}_1, \hat{\mathbf{b}}_2, \hat{\mathbf{b}}_3\}$ with origin $\hat{\mathcal{O}}$.

²⁷Note that a distinction of an active and a passive interpretation appears in some literature. It is often linked to moving from one observer to the other for the same point vs. moving one point to another position for the same observer, so that both interpretations describe the same transformation. Also note that some textbooks reduce the Euclidean transformation to Galilean transformation implying a constant Q .

Considering geometric properties and focusing on strain measurements, a vector \mathbf{a} is now called to be objective, if both observers measure the same length for it. This can be expressed by the fact that

$$\hat{a}_i = \sum_j Q_{ij} a_j. \tag{F.2}$$

Because Q_{ij} is orthogonal, the length of objective vectors does not change between both observers, i.e. $\|a_i\| = \|\hat{a}_i\|$. It is observer-invariant. In an analogous manner, one can define a tensor $\mathbf{T} = \sum_{i,j} T_{ij} \mathbf{b}_i \otimes \mathbf{b}_j = \sum_{i,j} \hat{T}_{ij} \hat{\mathbf{b}}_i \otimes \hat{\mathbf{b}}_j$ to be objective if it does not change the length of a vector or if the transformation between two observers is

$$\hat{T}_{ij} = \sum_{k,l} Q_{ik} T_{kl} Q_{lj}^T. \tag{F.3}$$

These definitions of objectivity were taken from literature, cf. [6, 12, 90, 126], and are limited as we will see now.

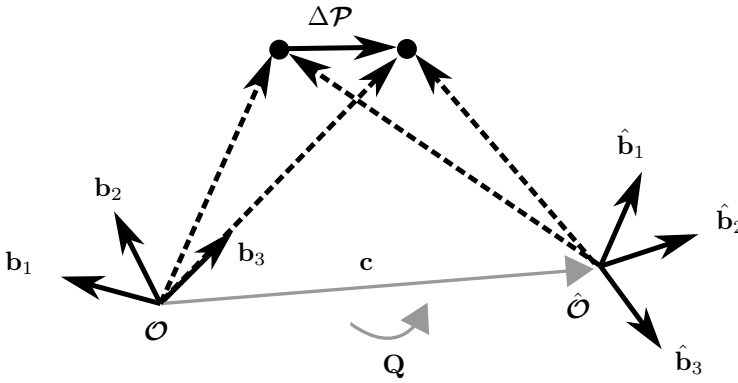


Figure F.2: A vector between two points for two observers. The distance between both points is identical for both observers.

F.3 Source of misunderstanding

Up to now, two important terms have been introduced: initial/reference configuration and objectivity. Many textbooks state that a vector difference is objective. It follows for $d\mathbf{x}$ that

$$d\hat{x}_i = \sum_j Q_{ij} dx_j. \tag{F.4}$$

On the contrary, many authors state for $d\mathbf{X} = d\mathbf{x}(t_0)$ of the initial/reference configuration that

$$d\hat{X}_i = dX_j \tag{F.5}$$

and $d\mathbf{X}$ would not be objective. Furthermore, they conclude that the deformation tensor $\mathbf{F} = d\mathbf{x}/d\mathbf{X}$ is also not objective, because their deduction

$$\frac{d\hat{x}_i}{d\hat{X}_j} = \sum_k Q_{ik} \frac{dx_k}{dX_j}. \tag{F.6}$$

contradicts the objectivity requirement for tensors Eq. (F.3), cf. [6, 12].

This is not appropriate in general. The source of misunderstanding is Eq. (F.5). The fact that is stated in Eq. (F.5) is an assumption without justification, because:

- **Contradiction:** A so-called reference/initial configuration is a subjective identification of a special time t_0 . This identification is independent of arbitrary observers and the definition of objectivity. Every time could be chosen to be the reference time. Thus, at every time, vector differences would not be objective. This is a contradiction within the theoretical framework itself.
- **Example:** Let two arbitrary observers measure the length of a beam at a time t_1 . Subsequently, the beam is stretched and the observers measure the new length at time t_2 . The times t_1 and t_2 should be arbitrary times. An initial/reference configuration should not be accounted for and is not required for the definition of objectivity. The ratio of both lengths will be the same for both observers and therefore objective, even if the orientation or velocity of the beam is different with respect to their system.
- **Missing proof:** A direct proof of Eq. (F.5) does not exist, but is introduced as a simple statement. It remains an assumption.

There can be many reasons for stating Eq. (F.5). For example, analytical and numerical calculations in solid continuum mechanics practically always use the reference configuration to address coordinates of material points. For $t > t_0$, material points move, each with its own coordinate system and origin. Thus, it suggests itself to say that all material points share the same frame at $t = t_0$. However, the system of a material point and that of a measuring observer should not be mixed.

Sometimes, the description via tensorial notation and index notation is also mixed. Note that, first of all, a point \mathcal{P} remains the same point \mathcal{P} in tensorial notation for two observers. The difference for both observers consists of what they (can) measure, i.e. the coefficients. No rotation or translation exists or can be determined if the bases of two observers are not specifically taken into account. Thus, a tensorial (just basis-free) notation should be used with appropriate care.

F.4 Explanation

In order to clarify the situation finally, one has to consider the meaning of Eq. (F.5). It assumes that the two observers share the same origin and basis at t_0 . This implies that $Q_{ij} = \delta_{ij}$ and $c_i = 0$ at $t = t_0$. Thus, one can write

$$\frac{d\hat{x}_i}{d\hat{X}_j} = \sum_k Q_{ik} \frac{dx_k}{dX_j} = \sum_k Q_{ik} \frac{dx_k}{dX_l} \delta_{lj}^T = \sum_{k,l} Q_{ik}(t) \frac{dx_k}{dX_l} Q_{lj}^T(t_0). \quad (\text{F.7})$$

This formulation adds an important, missing term: $Q_{lj}^T(t_0)$. Simply, the assumption of $Q_{lj}(t_0) = \delta_{lj}$ is too strict. In contrast, $Q_{lj}(t_0)$ should be an arbitrary rotation.

At least, it is obvious that different transformations can appear for different times. As a matter of course, the comparison of measurements between two observers requires consideration of the time when the measurements were taken. $Q(t)$ belongs to $d\mathbf{x}$ of the current configuration and $Q(t_0)$ belongs to $d\mathbf{X}$ of the initial/reference configuration. Just, the assumption of identical observers at t_0 is a, by default, unproven condition or assumption. Generally, $Q(t_0)$ can be an arbitrary transformation

between the observers. It was also revealed by Liu [126] and Haupt [90] with notation $Q(t_0) = K$. In conclusion,

$$d\hat{X}_i = Q_{ij}(t_0) dX_j. \tag{F.8}$$

should be preferred to Eq. (F.5). With this extension of arbitrary $Q(t_0)$, also $d\mathbf{X}$ and the deformation tensor become objective quantities (even within the restrictive assumption of identical observers at t_0). It coincides with the three counter-arguments from above and the initial misunderstanding is solved.

A more general objectivity condition for a quantity Ξ that depends on vectors $\mathbf{a}(t_a)$, $\mathbf{b}(t_b)$, $\mathbf{c}(t_c)$, \dots , could be

$$\Xi(\hat{a}_i, \hat{b}_j, \hat{c}_k, \dots) = \Xi \left(\sum_l Q_{il}(t_a) a_i, \sum_l Q_{jl}(t_b) b_j, \sum_l Q_{kl}(t_c) c_k, \dots \right). \tag{F.9}$$

Such definition of objectivity considers that measurements are compared at the time they were taken. Nevertheless, further discussion exceeds the scope of this comment. It should be summarized that many works using objectivity in continuum mechanics assume identical observers at the initial/reference state. This is an assumption and no conclusion. With it, the definition of objectivity is limited and appropriate care has to be taken for use and comparison. In general continuum mechanics, there is no unique definition of objectivity and specific definitions are not wrong by default but different.

In any case, it is important to know the appropriate, physical interpretation of the definition used. Equation Eq. (F.9) should give a first idea of a possible objectivity condition in a sense of observer-invariant measurements. A more comprehensive theory with alternative and further objectivity definitions can be found, for example, in Liu's contribution [126].

Bibliography

- [1] N. K. Adam and G. Jessop. CCL.-Angles of contact and polarity of solid surfaces. *Journal of the Chemical Society, Transactions*, 127:1863–1868, 1925.
- [2] M. Adelinet, J. Fortin, and Y. Guéguen. Dispersion of elastic moduli in a porous-cracked rock: Theoretical predictions for squirt-flow. *Tectonophysics*, 503(1-2):173–181, 2011. doi:10.1016/j.tecto.2010.10.012.
- [3] B. Albers. Analysis of the propagation of sound waves in partially saturated soils by means of a macroscopic linear poroelastic model. *Transport in Porous Media*, 80(1):173–192, 2009. doi:10.1007/s11242-009-9360-y.
- [4] B. Albers and K. Wilmanski. Acoustics of two-component porous materials with anisotropic tortuosity. *Continuum Mechanics and Thermodynamics*, 24(4-6):403–416, 2012. doi:10.1007/s00161-011-0218-5.
- [5] J. F. Allard. *Propagation of sound in porous media*. Elsevier Applied Science, London and New York, 1993.
- [6] H. Altenbach and J. Altenbach. *Einführung in die Kontinuums-Mechanik*. Teubner Verlag, 1994.
- [7] R. J. Atkin and R. E. Craine. Continuum theories of mixtures: Applications. *J. Inst. Math. Appl.*, 17(2):153–207, 1976. doi:10.1093/imamat/17.2.153.
- [8] M. Ayub and R. G. Bentsen. Interfacial viscous coupling: a myth or reality? *Journal of Petroleum Science and Engineering*, 23(1):13–26, 1999. doi:10.1016/S0920-4105(99)00003-0.
- [9] J. Ba, J. M. Carcione, and J. X. Nie. Biot-Rayleigh theory of wave propagation in double-porosity media. *Journal of Geophysical Research: Solid Earth*, 116(B6), 2011. doi:10.1029/2010JB008185.
- [10] R. Bansevicius and V. Kargaudas. Wave propagation in rigid cylindrical tubes with viscous and heat-conducting fluid. *Ultragarsas*, 56:7–10, 2005.
- [11] R. Bansevicius and V. Kargaudas. Wave propagation in elastic cylindrical tubes with viscous and heat-conducting fluid. *Ultragarsas*, 56:11–16, 2005.
- [12] Y. Basar and D. Weichert. *Nonlinear Continuum Mechanics of Solids: Fundamental Mathematical and Physical Concepts*. Springer, 2000.
- [13] J. Bear. *Dynamics of Fluids in Porous Media*. Dover Publications, Inc., New York, 1988.

- [14] T. Belytschko, W. Liu, and B. Moran. *Nonlinear Finite Elements for Continua and Structures*. Wiley, 2000.
- [15] A. Ben-Menahem and S. J. Singh. *Seismic waves and sources*. Dover Publications, 2nd edition, 2012.
- [16] I. Beresnev. Theory of vibratory mobilization on nonwetting fluids entrapped in pore constrictions. *Geophysics*, 71(6):N47–N56, 2006. doi:10.1190/1.2353803.
- [17] I. A. Beresnev and P. A. Johnson. Elastic-wave stimulation of oil production; a review of methods and results. *Geophysics*, 59(6):1000–1017, 1994. doi:10.1190/1.1443645.
- [18] Y. Bernabé. Oscillating flow of a compressible fluid through deformable pipes and pipe networks: Wave propagation phenomena. In S. Vinciguerra and Y. Bernabé, editors, *Rock Physics and Natural Hazards*, Pageoph Topical Volumes, pages 969–994. Birkhäuser Basel, 2009. doi:10.1007/978-3-0346-0122-1_11.
- [19] J. G. Berryman. Elastic wave propagation in fluid-saturated porous media. *Journal of the Acoustical Society of America*, 69:416–424, 1981.
- [20] J. G. Berryman and H. F. Wang. Double-porosity modeling in elastic wave propagation for reservoir characterization. In S. Hassanizadeh, editor, *Society of Photo-Optical Instrumentation Engineers (SPIE) Conference Series*, volume 3453 of *Society of Photo-Optical Instrumentation Engineers (SPIE) Conference Series*, pages 58–69, October 1998.
- [21] J. G. Berryman. Elastic waves in fluid-saturated porous media. In R. Burridge, S. Childress, and G. Papanicolaou, editors, *Macroscopic Properties of Disordered Media*, volume 154 of *Lecture Notes in Physics*, pages 38–50. Springer Berlin Heidelberg, 1982. doi:10.1007/3-540-11202-2_3.
- [22] J. G. Berryman, L. Thigpen, and R. C. Y. Chin. Bulk elastic wave propagation in partially saturated porous solids. *Journal of the Acoustical Society of America*, 84(1):360–373, 1988. doi:10.1121/1.396938.
- [23] M. A. Biot. General theory of three-dimensional consolidation. *Journal of Applied Physics*, 12:155–164, 1941. doi:10.1063/1.1712886.
- [24] M. A. Biot. Theory of propagation of elastic waves in a fluid-saturated porous solid. I. Low-frequency range. *Journal of the Acoustical Society of America*, 28:168–178, 1956. doi:10.1121/1.1908239.
- [25] M. A. Biot. Theory of propagation of elastic waves in a fluid-saturated porous solid. II. Higher-frequency range. *Journal of the Acoustical Society of America*, 28:179–191, 1956. doi:10.1121/1.1908241.
- [26] J. Bluhm. A consistent model for saturated and empty porous media, 1997. Habilitationsschrift, Universität-GH Essen, Fachbereich Bauwesen 74.
- [27] C. Boley, editor. *Handbuch Geotechnik*. Vieweg + Teubner Verlag, 2012.
- [28] T. Bourbié, O. Coussy, and B. Zinszner. *Acoustics of porous media*. Editions Technip, Paris, 1987.

- [29] R. M. Bowen. Theory of mixtures. In A. C. Eringen, editor, *Continuum Physics*, volume 3, part I. Academic Press, New York, 1976.
- [30] R. M. Bowen. Porous media model formulations by the theory of mixtures. In J. Bear and M. Y. Corapcioglu, editors, *Fundamentals of Transport Phenomena in Porous Media*, volume 82 of *NATO ASI Series*, pages 63–119. Springer Netherlands, 1984. doi:10.1007/978-94-009-6175-3_2.
- [31] D. Braess. *Finite Elements: Theory, Fast Solvers, and Applications in Solid Mechanics*. Cambridge University Press, 2007.
- [32] R. H. Brooks and A. T. Corey. *Hydraulic properties of porous media*. Colorado State University, 1964. Hydrology Paper No. 3.
- [33] O. Bruhns. *Aufgabensammlung Technische Mechanik 3*. Friedr. Vieweg & Sohn Verlagsgesellschaft mbH, Braunschweig/Wiesbaden, 1999.
- [34] W. Brutsaert and J. N. Luthin. The velocity of sound in soils near the surface as a function of the moisture content. *Journal of Geophysical Research*, 69(4): 643–652, 1964. doi:10.1029/JZ069i004p00643.
- [35] J. M. Carcione, editor. *Wave Fields in Real Media Wave Propagation in Anisotropic, Anelastic, Porous and Electromagnetic Media*, volume 38 of *Handbook of Geophysical Exploration: Seismic Exploration*. Pergamon, 2007.
- [36] L. Cardoso, A. Meunier, and C. Oddou. In vitro acoustic wave propagation in human and bovine cancellous bone as predicted by Biot’s theory. *Journal of Mechanics in Medicine and Biology*, 08(02):183–201, 2008. doi:10.1142/S0219519408002565.
- [37] M. Chapman, S. V. Zatsepin, and S. Crampin. Derivation of a microstructural poroelastic model. *Geophysical Journal International*, 151(2):427–451, 2002. doi:10.1046/j.1365-246X.2002.01769.x.
- [38] C. V. Chrysikopoulos and E. T. Vogler. Acoustically enhanced ganglia dissolution and mobilization in a monolayer of glass beads. *Transport in Porous Media*, 64:103–121, 2006. doi:10.1007/s11242-005-1525-8.
- [39] R. Ciz, E. H. Saenger, and B. Gurevich. Pore scale numerical modeling of elastic wave dispersion and attenuation in periodic systems of alternating solid and viscous fluid layers. *Journal of the Acoustical Society of America*, 120(2): 642–648, 2006. doi:10.1121/1.2216687.
- [40] E. Cosserat and F. Cosserat. *Théorie des corps déformables*. A. Hermann et Fils, Paris, 1909.
- [41] O. Coussy. *Poromechanics*. John Wiley & Sons., 2004.
- [42] S. C. Cowin and L. Cardoso. Difficulties arising from different definitions of tortuosity for wave propagation in saturated poroelastic media models. *ZAMM - Journal of Applied Mathematics and Mechanics / Zeitschrift fuer Angewandte Mathematik und Mechanik*, pages 1–1, 2013. doi:10.1002/zamm.201200086.
- [43] H. Darcy. *Les fontaines publiques de la ville de Dijon*. Victor Dalmont, 1856. Paris.

- [44] E. C. David and R. W. Zimmerman. Pore structure model for elastic wave velocities in fluid-saturated sandstones. *Journal of Geophysical Research: Solid Earth*, 117(B7), 2012. doi:10.1029/2012JB009195.
- [45] J. L. Davis. *Wave Propagation in Solids and Fluids*. Springer-Verlag New York, 1988.
- [46] C. Davison. V. Observations and Experiments on the Fluctuations in the Level and Rate of Movement of Ground-water on the Wisconsin Agricultural Experiment Station Farm, and at Whitewater, Wisconsin. By Prof Franklin H. King, United States Department Of Agriculture, Weather Bureau, Bulletin No. 5 (1892). 75 pp., Six Plates. *Geological Magazine (Decade III)*, 10:568–570, 12 1893. doi:10.1017/S0016756800191708.
- [47] R. de Boer. *Theory of Porous Media: Highlights in Historical Development and Current State*. Springer, 1999.
- [48] P.-G. de Gennes, F. Brochard-Wyart, and D. Quéré. *Capillarity and wetting phenomena*. Springer, 2003.
- [49] P. S. de Laplace. Oeuvres complètes de Laplace, t IV, Supplément au livre X du traité de la mécanique cèleste, (complete Works of Laplace, tome 4, Supplement to book 10 of the Treatise on Celestial Mechanics), p. 394. also 2ème supplément au livre X (2nd Supplement to Book 10), p. 419, ch. 1, 1805.
- [50] V. Demin. Problem of the free oscillations of a capillary bridge. *Fluid Dyn.*, 43 (4):524–532, 2008. doi:10.1134/S0015462808040042.
- [51] H. Deresiewicz. The effect of boundaries on wave propagation in a liquid-filled porous solid: IX. Love waves in a porous internal stratum. *Bulletin of the Seismological Society of America*, 55(5):919–923, 1965.
- [52] S. Diebels. Mikropolare Zweiphasenmodelle: Formulierung auf der Basis der Theorie poröser Medien, 2000. Habilitationsschrift, Universität Stuttgart, Fakultät Bauingenieur- und Vermessungswesen.
- [53] Y. Ding, Z. Liu, C. Qiu, and J. Shi. Metamaterial with simultaneously negative bulk modulus and mass density. *Phys. Rev. Lett.*, 99:093904–1 – 093904–4, Aug 2007. doi:10.1103/PhysRevLett.99.093904.
- [54] N. C. Dutta and H. Odé. Attenuation and dispersion of compressional waves in fluid-filled porous rocks with partial gas saturation (White model). Part I: Biot theory. *Geophysics*, 44:1777–1788, 1979. doi:10.1190/1.1440938.
- [55] N. C. Dutta and H. Odé. Attenuation and dispersion of compressional waves in fluid-filled porous rocks with partial gas saturation (White model). Part II: Results. *Geophysics*, 44:1789–1805, 1979. doi:10.1190/1.1440939.
- [56] J. Dvorkin and A. Nur. Dynamic poroelasticity: A unified model with the squirt and the Biot mechanisms. *Geophysics*, 58(4):524–533, 1993. doi:10.1190/1.1443435.
- [57] J. Dvorkin, G. Mavko, and A. Nur. Squirt flow in fully saturated rocks. *Geophysics*, 60(1):97–107, 1995. doi:10.1190/1.1443767.

- [58] J. Dvorkin, R. Nolen-Hoeksema, and A. Nur. The squirt-flow mechanism: Macroscopic description. *Geophysics*, 59:428–438, 1994. doi:10.1190/1.1443605.
- [59] W. Ehlers and J. Bluhm. *Porous Media: Theory, Experiments and Numerical Applications*. Springer, 2002.
- [60] S. Ergun. Flow through packed columns. *Chemical Engineering Progress*, 48: 89–94, 1952. doi:10.1021/ie50474a011.
- [61] A. C. Eringen. *Microcontinuum Field Theories, Vol. I: Foundations and Solids*. Springer-Verlag, Berlin, 1999.
- [62] A. C. Eringen. Micropolar mixture theory of porous media. *Journal of Applied Physics*, 94(6):4184–4190, 2003. doi:10.1063/1.1598640.
- [63] A. C. Eringen and J. D. Ingram. A Continuum theory of chemically reacting media-I. *International Journal of Engineering Science*, 3(2):197–212, 1965. doi:10.1016/0020-7225(65)90044-3.
- [64] H. Fan and D. M. J. Smeulders. Shock-induced borehole waves and fracture effects. *Transport in Porous Media*, 91(1):295–302, 2012. doi:10.1007/s11242-011-9845-3.
- [65] N. Fang, D. Xi, J. Xu, M. Ambati, W. Srituravanich, C. Sun, and X. Zhang. Ultrasonic metamaterials with negative modulus. *Nature Materials*, 5:452–456, 2006. doi:10.1038/nmat1644.
- [66] V. Ferrazzini and K. Aki. Slow waves trapped in a fluid-filled infinite crack: Implication for volcanic tremor. *Journal of Geophysical Research: Solid Earth*, 92(B9):9215–9223, 1987. doi:10.1029/JB092iB09p09215.
- [67] F. Feyel and J.-L. Chaboche. FE² multiscale approach for modelling the elastoviscoplastic behaviour of long fibre SiC/Ti composite materials. *Computer Methods in Applied Mechanics and Engineering*, 183(3-4):309–330, 2000. doi:10.1016/S0045-7825(99)00224-8.
- [68] P. Fillunger. *Erdbaumechanik?* self-published by the author, Wien, 1936.
- [69] T. Fließbach. *Mechanik: Lehrbuch zur Theoretischen Physik I*. Spektrum Akademischer Verlag Heidelberg, 6 edition, 2009.
- [70] R. J. Fogelin. *Routledge philosophy guidebook to Berkeley and the Principles of human knowledge*. Routledge, 2001.
- [71] M. Frehner. *Krauklis Wave Initiation in Fluid-Filled Fractures by a Passing Body Wave*, chapter 11, pages 92–100. American Society of Civil Engineers, 2013. doi:10.1061/9780784412992.011.
- [72] M. Frehner, S. M. Schmalholz, and Y. Podladchikov. Spectral modification of seismic waves propagating through solids exhibiting a resonance frequency: a 1-d coupled wave propagation-oscillation model. *Geophys. J. Int.*, 176(2):589–600, 2009. doi:10.1111/j.1365-246X.2008.04001.x.

- [73] M. Frehner, H. Steeb, and S. M. Schmalholz. Wave velocity dispersion and attenuation in media exhibiting internal oscillations. In A. Petrin, editor, *Wave Propagation in Materials for Modern Applications*, pages 455–476. In-Tech Education and Publishing, Vukovar, Croatia, 2010. doi:10.5772/6866.
- [74] J. Frenkel. On the theory of seismic and electroseismic phenomena in a moist soil. *J. Phys.*, 8(4):230–241, 1944.
- [75] S. K. Garg and A. H. Nayfeh. Compressional wave propagation in liquid and/or gas saturated elastic porous media. *Journal of Applied Physics*, 60(9):3045–3055, 1986. doi:10.1063/1.337760.
- [76] F. Gassmann. Über die Elastizität Poröser Medien. *Viertel. Naturforsch. Ges. Zuerich*, 96:1–23, 1951.
- [77] M. T. v. Genuchten. A closed-form equation for predicting the hydraulic conductivity of unsaturated soils. *Soil Science Society of America Journal*, 44: 892–898, 1980.
- [78] J. Germán Rubino, L. Guarracino, T. M. Mueller, and K. Holliger. Do seismic waves sense fracture connectivity? *Geophysical Research Letters*, 40(4):692–696, 2013. doi:10.1002/grl.50127.
- [79] W. G. Gray and S. M. Hassanizadeh. Macroscale continuum mechanics for multiphase porous-media flow including phases, interfaces, common lines and common points. *Advances in Water Resources*, 21:261–281, 1998. doi:10.1016/s0309-1708(96)00063-2.
- [80] W. G. Gray, A. Leijnse, R. L. Kolar, and C. A. Blain. *Mathematical Tools for Changing Scale in the Analysis of Physical Systems*. CRC Press, 1993.
- [81] I. Gueven, P. Kurzeja, S. Luding, and H. Steeb. Experimental evaluation of phase velocities and tortuosity in fluid saturated highly porous media. *Proceedings in Applied Mathematics and Mechanics*, 12(1):401–402, 2012. doi:10.1002/pamm.201210189.
- [82] I. Gueven, S. Luding, and H. Steeb. Hydraulic and acoustic investigation of sintered glass beads. *AIP Conference Proceedings*, 1542(1):581–584, 2013. doi:10.1063/1.4811998.
- [83] M. E. Gurtin and A. I. Murdoch. A continuum theory of elastic material surfaces. *Archive for Rational Mechanics and Analysis*, 57:291–323, 1975. doi:10.1007/BF00261375.
- [84] Z. Hashin. Analysis of composite materials—a survey. *Journal of Applied Mechanics*, 50:481–505, 1983. doi:10.1115/1.3167081.
- [85] M. Hassanizadeh and W. Gray. High velocity flow in porous media. *Transport in Porous Media*, 2:521–531, 1987.
- [86] M. Hassanizadeh and W. G. Gray. General conservation equations for multiphase systems: 1. averaging procedure. *Advances in Water Resources*, 2:131–144, 1979. doi:10.1016/0309-1708(79)90025-3.

- [87] M. Hassanizadeh and W. G. Gray. General conservation equations for multi-phase systems: 2. mass, momenta, energy, and entropy equations. *Advances in Water Resources*, 2:191–203, 1979. doi:10.1016/0309-1708(79)90035-6.
- [88] M. Hassanizadeh and W. G. Gray. General conservation equations for multi-phase systems: 3. constitutive theory for porous media flow. *Advances in Water Resources*, 3:25–40, 1980. doi:10.1016/0309-1708(80)90016-0.
- [89] S. M. Hassanizadeh. Mechanics and thermodynamics of multiphase flow in porous media including interphase boundaries. *Advances in Water Resources*, 13(4):169–186, 1990. doi:10.1016/0309-1708(90)90040-B.
- [90] P. Haupt. *Continuum mechanics and theory of materials*. Springer, 2002.
- [91] M. Higuera and J. A. Nicolás. Linear nonaxisymmetric oscillations of nearly inviscid liquid bridges. *Physics of Fluids*, 9(2):276–285, 1997. doi:10.1063/1.869148.
- [92] M. Hilpert. Capillarity-induced resonance of blobs in porous media: analytical solutions, lattice-boltzmann modeling, and blob mobilization. *Journal of Colloid and Interface Science*, 309:493–504, 2007. doi:10.1016/j.jcis.2006.11.052.
- [93] M. Hilpert. Velocity-dependent capillary pressure in theory for variably-saturated liquid infiltration into porous media. *Geophysical Research Letters*, 39(6), 2012. doi:10.1029/2012GL051114.
- [94] M. Hilpert, G. H. Jirka, and E. J. Plate. Capillarity-induced resonance of oil blobs in capillary tubes and porous media. *Geophysics*, 65(3):874–883, 2000. doi:10.1190/1.1444784.
- [95] R. Holzner, P. Eschle, S. Dangel, M. Frehner, C. Narayanan, and D. Lakehal. Hydrocarbon microtremors interpreted as nonlinear oscillations driven by oceanic background waves. *Communications in Nonlinear Science and Numerical Simulation*, 14(1):160–173, 2009. doi:10.1016/j.cnsns.2007.06.013.
- [96] S.-Y. Hsu, J. Katz, and M. Hilpert. Theoretical and experimental study of resonance of blobs in porous media. *Journal of Colloid and Interface Science*, 77(5):EN61–EN71, 2012. doi:10.1190/geo2012-0043.1.
- [97] H. H. Huang, C. T. Sun, and G. L. Huang. On the negative effective mass density in acoustic metamaterials. *International Journal of Engineering Science*, 47(4): 610–617, 2009. doi:10.1016/j.ijengsci.2008.12.007.
- [98] P. M. G. J. E. Santos, C. L. Ravazzoli and J. M. Carcione. Numerical simulation of ultrasonic waves in reservoir rocks with patchy saturation and fractal petrophysical properties. *Computational Geosciences*, 9(1):1–27, 2005. doi:10.1007/s10596-005-2848-9.
- [99] C. E. Jacob. On the flow of water in an elastic artesian aquifer. *Transactions, American Geophysical Union*, 21:574–586, 1940. doi:10.1029/TR021i002p00574.
- [100] R. Jänicke. *Micromorphic media: Interpretation by homogenisation*. PhD thesis, Naturwissenschaftlich-Technische Fakultät III, Chemie, Pharmazie, Bio- und Werkstoffwissenschaften der Universität des Saarlandes, Saarbrücken, Germany, 2007.

- [101] X. Jia. Codalike multiple scattering of elastic waves in dense granular media. *Physical Review Letters*, 93(15):154303–1–154303–4, 2004. doi:10.1103/PhysRevLett.93.154303.
- [102] V. Joekar-Niasar, S. Hassanizadeh, and A. Leijnse. Insights into the relationships among capillary pressure, saturation, interfacial area and relative permeability using pore-network modeling. *Transport in Porous Media*, 74:201–219, 2008. doi:10.1007/s11242-007-9191-7.
- [103] D. L. Johnson, J. Koplik, and R. Dashen. Theory of dynamic permeability and tortuosity in fluid-saturated porous media. *J. Fluid Mech.*, 176:379–402, 1987. doi:10.1017/S0022112087000727.
- [104] J. P. Jones. Rayleigh waves in a porous, elastic, saturated solid. *Journal of the Acoustical Society of America*, 33(7):959–962, 1961. doi:10.1121/1.1908865.
- [105] O. Kelder. *Frequency-dependent wave propagation in water-saturated porous media*. PhD thesis, Delft University of Technology, The Netherlands, 1997.
- [106] O. Kelder and D. Smeulders. Observation of the Biot slow wave in water-saturated Nivelsteiner sandstone. *Geophysics*, 62(6):1794–1796, 1997. doi:10.1190/1.1444279.
- [107] R. Knight and R. Nolen-Hoeksema. A laboratory study of the dependence of elastic wave velocities on pore scale fluid distribution. *Geophysical Research Letters*, 17(10):1529–1532, 1990. doi:10.1029/GL017i010p01529.
- [108] L. Knopoff and G. J. F. MacDonald. Attenuation of small amplitude stress waves in solids. *Rev. Mod. Phys.*, 30:1178–1192, Oct 1958. doi:10.1103/RevModPhys.30.1178.
- [109] V. Korneev. Slow waves in fractures filled with viscous fluid. *Geophysics*, 73(1): N1–N7, 2008. doi:10.1190/1.2802174.
- [110] V. Korneev. Krauklis wave in a stack of alternating fluid-elastic layers. *Geophysics*, 76(6):N47–N53, 2011. doi:10.1190/GEO2011-0086.1.
- [111] T. Kowalewski and D. Bruhn. Nonlinear oscillations of viscous droplets, 1994. Japan-Central Europe Joint Workshop on Adv. Comp. in Eng., Pultusk, Poland, 26-28 Sept. 1994.
- [112] P. Kurzeja, H. Steeb, and J. Renner. *The Critical Frequency in Biphasic Media: Beyond Biot's Approach*, chapter 276, pages 2361–2370. American Society of Civil Engineers, 2013. doi:10.1061/9780784412992.276.
- [113] P. Kurzeja and H. Steeb. Residual saturated porous media - from oscillating water blobs to waves in ground earth. *Proceedings in Applied Mathematics and Mechanics*, 2013. in press.
- [114] P. S. Kurzeja and H. Steeb. About the transition frequency in Biot's theory. *Journal of the Acoustical Society of America (Express Letters)*, 131(6):EL454–EL460, 2012. doi:10.1121/1.4710834.

- [115] P. S. Kurzeja and H. Steeb. Microscopical investigation of wave propagation phenomena in residual saturated porous media. *Proceedings in Applied Mathematics and Mechanics*, 12(1):445–446, 2012. doi:10.1002/pamm.201210211.
- [116] P. S. Kurzeja and H. Steeb. Variational Formulation of Oscillating Fluid Clusters and Oscillator-like Classification: Part I - Theory. *Physics of Fluids*, 2013. submitted.
- [117] P. S. Kurzeja and H. Steeb. Variational Formulation of Oscillating Fluid Clusters and Oscillator-like Classification: Part II - Numerical study of pinned liquid clusters. *Physics of Fluids*, 2013. submitted.
- [118] P. Lambossy. Oscillations forcées d'un liquide incompressible et visqueux dans un tube rigide et horizontal. calcul de la force de frottement. *Helv. physica acta*, 25:371–386, 1952. doi:10.1063/1.1786511.
- [119] L. Lambrecht and W. Friedrich. Simulation of Seismic Wave Propagation for Reconnaissance in Mechanized Tunneling using the Spectral Element and Nodal Discontinuous Galerkin Method. In G. Meschke, J. Eberhardsteiner, T. Schanz, K. Soga, and M. Thewes, editors, *EURO:TUN 2013, Computational Methods in Tunneling and Subsurface Engineering*, pages 769–777. Aedificatio Publishers, Freiburg, 2003. Proceedings of the Third International Conference on Computational Methods in Tunneling and Subsurface Engineering, Ruhr University Bochum, April 17-19, 2013.
- [120] P. Li and M. Schanz. Wave propagation in a 1-d partially saturated poroelastic column. *Geophysical Journal International*, 184(3):1341–1353, 2011. doi:10.1111/j.1365-246X.2010.04913.x.
- [121] X. Li, L. Zhong, and L. J. Pyrak-Nolte. Physics of partially saturated porous media: Residual saturation and seismic-wave propagation. *Annual Review of Earth and Planetary Sciences*, 29(1):419–460, 2001. doi:10.1146/annurev.earth.29.1.419.
- [122] R. Liang and M. Kawaji. Surface oscillation of a liquid bridge induced by single and multiple vibrations. *Microgravity Sci. Tec.*, 21(Suppl 1):S31–S37, 2009. doi:10.1007/s12217-009-9116-x.
- [123] L. Lin, J. Cheng, W. Lin, and Y.-X. Qin. Prediction of trabecular bone principal structural orientation using quantitative ultrasound scanning. *Journal of Biomechanics*, 45(10):1790–1795, 2012. doi:http://dx.doi.org/10.1016/j.jbiomech.2012.04.022.
- [124] T. C. Lin and G. W. Morgan. Wave propagation through fluid contained in a cylindrical, elastic shell. *Journal of the Acoustical Society of America*, 28(6):1165–1176, 1956. doi:10.1121/1.1908583.
- [125] Y. Lins and T. Schanz. Determination of hydro-mechanical properties of sand. In T. Schanz, editor, *Unsaturated Soils: Experimental Studies*, volume 93 of *Springer Proceedings in Physics*, pages 15–32. Springer Berlin Heidelberg, 2005. doi:10.1007/3-540-26736-0_2.

- [126] I.-S. Liu. On the transformation property of the deformation gradient under a change of frame. *J. Elasticity*, 71:73–80, 2003. doi:10.1023/B:ELAS.0000005548.36767.e7.
- [127] I.-S. Liu. On euclidean objectivity and the principle of material frame-indifference. *Continuum Mech. Therm.*, 16:177–183, 2004. doi:10.1007/s00161-003-0149-x.
- [128] W.-C. Lo, G. Sposito, and E. Majer. Wave propagation through elastic porous media containing two immiscible fluids. *Water Resources Research*, 41(2), 2005. doi:10.1029/2004WR003162.
- [129] W.-C. Lo, G. Sposito, and E. Majer. Low-frequency dilatational wave propagation through unsaturated porous media containing two immiscible fluids. *Transport in Porous Media*, 68(1):91–105, 2007. doi:10.1007/s11242-006-9059-2.
- [130] W.-C. Lo, C.-L. Yeh, and C.-T. Tsai. Effect of soil texture on the propagation and attenuation of acoustic wave at unsaturated conditions. *Journal of Hydrology*, 338(3-4):273–284, 2007. doi:10.1016/j.jhydrol.2007.02.034.
- [131] A. E. H. Love. *A treatise on the mathematical theory of elasticity*. Dover, New York, 4th edition, 1944.
- [132] J.-F. Lu and A. Hanyga. Linear dynamic model for porous media saturated by two immiscible fluids. *International Journal of Solids and Structures*, 42(9-10): 2689–2709, 2005. doi:10.1016/j.ijsolstr.2004.09.032.
- [133] J.-F. Lu, A. Hanyga, and D.-S. Jeng. A mixture-theory-based dynamic model for a porous medium saturated by two immiscible fluids. *Journal of Applied Geophysics*, 62(2):89–106, 2007. doi:10.1016/j.jappgeo.2006.08.002.
- [134] S. Manthey, S. M. Hassanizadeh, R. Helmig, and R. Hilfer. Dimensional analysis of two-phase flow including a rate-dependent capillary pressure-saturation relationship. *Advances in Water Resources*, 31(9):1137–1150, 2008. doi:10.1016/j.advwatres.2008.01.021.
- [135] I. Martínez. Stability of liquid bridges. Results of SL-D1 experiment. *Acta Astronautica*, 8:449–453, 1987. doi:10.1016/0094-5765(87)90181-0.
- [136] K. S. Matthys, J. Alastruey, J. Peiró, A. W. Khir, P. Segers, P. R. Verdonck, K. H. Parker, and S. J. Sherwin. Pulse wave propagation in a model human arterial network: Assessment of 1-d numerical simulations against in vitro measurements. *Journal of Biomechanics*, 40(15):3476–3486, 2007. doi:10.1016/j.jbiomech.2007.05.027.
- [137] G. Mavko and D. Jizba. Estimating grain-scale fluid effects on velocity dispersion in rocks. *Geophysics*, 56(12):1940–1949, 1991. doi:10.1190/1.1443005.
- [138] G. Mavko and R. Nolen-Hoeksema. Estimating seismic velocities at ultrasonic frequencies in partially saturated rocks. *Geophysics*, 59(2):252–258, 1994. doi:10.1190/1.1443587.

- [139] G. Mavko, T. Mukerji, and J. Dvorkin. *The Rock Physics Handbook: Tools for Seismic Analysis of Porous Media*. Cambridge University Press, 2nd edition, 2009.
- [140] G. Mavko and A. Nur. Melt squirt in the asthenosphere. *Journal of Geophysical Research*, 80(11):1444–1448, 1975. doi:10.1029/JB080i011p01444.
- [141] O. E. Meinzer. Compressibility and elasticity of artesian aquifers. *Geology*, 23:263–291, 1928. doi:10.2113/gsecongeo.23.3.263.
- [142] A. V. Metrikine and H. Askes. One-dimensional dynamically consistent gradient elasticity models derived from a discrete microstructure: Part 1: Generic formulation. *European Journal of Mechanics - A/Solids*, 21(4):555–572, 2002. doi:10.1016/S0997-7538(02)01218-4.
- [143] C. Miehe and A. Koch. Computational micro-to-macro transitions of discretized microstructures undergoing small strains. *Archive of Applied Mechanics*, 72:300–317, 2002. doi:10.1007/s00419-002-0212-2.
- [144] C. A. Miller and P. Neogi. *Interfacial phenomena*, volume 139 of *surfactant science series*. CRC Press, Taylor & Francis Group, LLC, second edition, 2008.
- [145] G. W. Milton and J. R. Willis. On modifications of newton’s second law and linear continuum elastodynamics. *Proceedings of the Royal Society A*, 463(2079):855–880, 2007. doi:10.1098/rspa.2006.1795.
- [146] R. D. Mindlin. Micro-structure in linear elasticity. *Archive for Rational Mechanics and Analysis*, 16:51–78, 1964. doi:10.1007/BF00248490.
- [147] M. Minnaert. XVI. On musical air-bubbles and the sounds of running water. *Philosophical Magazine Series 7*, 16(104):235–248, 1933. doi:10.1080/14786443309462277.
- [148] G. P. Moeckel. Thermodynamics of an interface. *Archive for Rational Mechanics and Analysis*, 57(3):255–280, 1975. doi:10.1007/BF00280158.
- [149] K. K. Muraleetharan and C. Wei. Dynamic behaviour of unsaturated porous media: governing equations using the theory of mixtures with interfaces (tmi). *International Journal for Numerical and Analytical Methods in Geomechanics*, 23(13):1579–1608, 1999. doi:10.1002/(SICI)1096-9853(199911)23:13<1579::AID-NAG58>3.0.CO;2-L.
- [150] A. I. Murdoch. Objectivity in classical continuum physics: a rationale for discarding the ‘principle of invariance under superposed rigid body motions’ in favour of purely objective considerations. *Continuum Mech. Therm.*, 15:309–320, 2003. doi:10.1007/s00161-003-0121-9.
- [151] W. F. I. Murphy. Effects of partial water saturation on attenuation in massilon sandstone and vycor porous glass. *Journal of the Acoustical Society of America*, 71(6):1458–1468, 1982. doi:10.1121/1.387843.
- [152] M. Muskat. Distribution of non-reacting fluids in the gravitational field. *Physical Review*, 35:1384–1393, 1930. doi:10.1103/PhysRev.35.1384.

- [153] S. Nemat-Nasser and M. Hori. *micromechanics: overall properties of heterogeneous materials*. Elsevier Ltd, 1998.
- [154] J. Niessner and S. M. Hassanizadeh. A model for two-phase flow in porous media including fluid-fluid interfacial area. *Water Resources Research*, 44(8), 2008. doi:10.1029/2007WR006721. W08439.
- [155] E. Nikoee, G. Habibagahi, S. M. Hassanizadeh, and A. Ghahramani. The effective stress in unsaturated soils: Insights from thermodynamics. In C. Mancuso, C. Jommi, and F. D’Onza, editors, *Unsaturated Soils: Research and Applications*, pages 5–11. Springer Berlin Heidelberg, 2012. doi:10.1007/978-3-642-31343-1_1.
- [156] R. J. O’Connell and B. Budiansky. Measures of dissipation in viscoelastic media. *Geophysical Research Letters*, 5(1):5–8, 1978. doi:10.1029/GL005i001p00005.
- [157] R. J. O’Connell and B. Budiansky. Viscoelastic properties of fluid-saturated cracked solids. *Journal of Geophysical Research*, 82(36):5719–5735, 1977. doi:10.1029/JB082i036p05719.
- [158] M. Perez, Y. Brechet, L. Salvo, M. Papoular, and M. Suery. Oscillation of liquid drops under gravity: Influence of shape on the resonance frequency. *Europhys. Lett.*, 47(2):189–195, 1999. doi:10.1209/epl/i1999-00371-6.
- [159] J. Pfister, editor. *Klassische Texte der Philosophie*. Reclam, 2011.
- [160] T. J. Plona. Observation of a second bulk compressional wave in a porous medium at ultrasonic frequencies. *Applied Physics Letters*, 36(4):259–261, 1980. doi:10.1063/1.91445.
- [161] T. Pratchett. *Snuff*. Doubleday, 2011.
- [162] W. E. Pratt and D. W. Johnson. Local subsidence of the goose creek oil field. *Journal of Geology*, 34(7):577–590, 1926. doi:10.1086/623352.
- [163] S. Pride and F. Morgan. Electrokinetic dissipation induced by seismic waves. *Geophysics*, 56(7):914–925, 1991. doi:10.1190/1.1443125.
- [164] S. Pride, E. Flekkøy, and O. Aursjø. Seismic stimulation for enhanced oil recovery. *Geophysics*, 73(5):O23–O35, 2008. doi:10.1190/1.2968090.
- [165] S. R. Pride, J. M. Harris, D. L. Johnson, A. Mateeva, K. T. Nihel, R. L. Nowack, J. W. Rector, H. Spetzler, R. Wu, T. Yamamoto, J. G. Berryman, and M. Fehler. Permeability dependence of seismic amplitudes. *The Leading Edge*, 22(6):518–525, 2003. doi:10.1190/1.1587671.
- [166] S. R. Pride and J. G. Berryman. Linear dynamics of double-porosity dual-permeability materials. i. governing equations and acoustic attenuation. *Physical Review E*, 68, 2003. doi:10.1103/PhysRevE.68.036603.
- [167] S. R. Pride and J. G. Berryman. Linear dynamics of double-porosity dual-permeability materials. II. fluid transport equations. *Physical Review E*, 68, 2003. doi:10.1103/PhysRevE.68.036604.

- [168] Q. Qi, T. M. Mueller, P. N. Sahay, and C. D. Piane. *Slow Shear Waves in Poroelasticity and the Concept of Dynamic Permeability*, chapter 37, pages 316–325. American Society of Civil Engineers, 2013. doi:10.1061/9780784412992.037.
- [169] T. Qian, X.-P. Wang, and P. Sheng. Molecular hydrodynamics of the moving contact line in two-phase immiscible flows. *Communications in Computational Physics*, 1:1–52, 2006. arXiv:cond-mat/0510403.
- [170] B. Quintal, M. Frehner, C. Madonna, N. Tisato, M. Kuteynikova, and E. H. Saenger. Integrated numerical and laboratory rock physics applied to seismic characterization of reservoir rocks. *The Leading Edge*, 30(12):1360–1367, 2011. doi:10.1190/1.3672480.
- [171] B. Quintal, H. Steeb, M. Frehner, and S. M. Schmalholz. Quasi-static finite element modeling of seismic attenuation and dispersion due to wave-induced fluid flow in poroelastic media. *Journal of Geophysical Research: Solid Earth*, 116(B1), 2011. doi:10.1029/2010JB007475.
- [172] J. W. S. Rayleigh. *Theory of sound II*. Macmillan, London, 2nd edition, 1896.
- [173] L. Reddi and S. Challa. Vibratory mobilization of immiscible liquid ganglia in sands. *Journal of Environmental Engineering*, 120(5):1170–1190, 1994. doi:10.1061/(ASCE)0733-9372(1994)120:5(1170).
- [174] L. Reddi and H. Wu. Mechanisms involved in vibratory destabilization of NAPL ganglia in sands. *Journal of Environmental Engineering*, 122(12):1115–1119, 1996. doi:10.1061/(ASCE)0733-9372(1996)122:12(1115).
- [175] P. M. Roberts, A. Sharma, V. Uddameri, M. Monagle, D. E. Dale, and L. K. Steck. Enhanced DNAPL transport in a sand core during dynamic stress stimulation. *Environmental Engineering Science*, 18(2):67–79, 2001. doi:10.1089/10928750151132230.
- [176] J. P. Rothstein. Slip on superhydrophobic surfaces. *Annual Review of Fluid Mechanics*, 42(1):89–109, 2010. doi:10.1146/annurev-fluid-121108-145558.
- [177] P. H. Saksono and D. Perić. On finite element modelling of surface tension. Variational formulation and applications - Part I: Quasistatic problems. *Computational Mechanics*, 38:265–281, 2006. doi:10.1007/s00466-005-0747-5.
- [178] P. H. Saksono and D. Perić. On finite element modelling of surface tension. Variational formulation and applications - Part II: Dynamic problems. *Computational Mechanics*, 38:251–263, 2006. doi:10.1007/s00466-005-0745-7.
- [179] J. E. Santos, J. M. Corbero, and J. Jim Douglas. Static and dynamic behavior of a porous solid saturated by a two-phase fluid. *Journal of the Acoustical Society of America*, 87(4):1428–1438, 1990. doi:10.1121/1.399439.
- [180] J. E. Santos, J. Jim Douglas, J. Corbero, and O. M. Lovera. A model for wave propagation in a porous medium saturated by a two-phase fluid. *Journal of the Acoustical Society of America*, 87(4):1439–1448, 1990. doi:10.1121/1.399440.

- [181] J. E. Santos, C. L. Ravazzoli, P. M. Gauzellino, J. M. Carcione, and F. Cavallini. Simulation of waves in poro-viscoelastic rocks saturated by immiscible fluids: Numerical evidence of a second slow wave. *Journal of Computational Acoustics*, 12(01):1–21, 2004. doi:10.1142/S0218396X04002195.
- [182] M. J. Santos and J. A. White. Theory and simulation of angular hysteresis on planar surfaces. *Langmuir*, 27(24):14868–14875, 2011. doi:10.1021/la202771u.
- [183] A. Sanz and J. L. Diez. Non-axisymmetric oscillations of liquid bridges. *J. Fluid Mech.*, 205:503–521, 1989.
- [184] M. D. Schakel, D. M. J. Smeulders, E. C. Slob, and H. K. J. Heller. Seismoelectric fluid/porous-medium interface response model and measurements. *Transport in Porous Media*, 93(2):271–282, 2012. doi:10.1007/s11242-011-9869-8.
- [185] A. E. Scheidegger. *The physics of flow through porous media*. MacMillan, New York, 1957.
- [186] A. E. Scheidegger. *The physics of flow through porous media*. University of Toronto Press, 3rd edition, 1974.
- [187] P. Scott and W. Rose. An explanation of the yuster effect. *T. Am. I. Min. Met. Eng.*, 198:323–324, 1953. doi:10.2118/953323-G.
- [188] S. A. Shapiro. *The Pressure Dependence of Permeability as a Function of Stiff and Compliant Porosities*, chapter 291, pages 2500–2509. American Society of Civil Engineers, 2013. doi:10.1061/9780784412992.291.
- [189] D. Singh and S. K. Tomar. Wave propagation in micropolar mixture of porous media. *International Journal of Engineering Science*, 44(18-19):1304–1323, 2006. doi:10.1016/j.ijengsci.2006.07.006.
- [190] J. C. Slattery. Flow of viscoelastic fluids through porous media. *AIChE Journal*, 13(6):1066–1071, 1967. doi:10.1002/aic.690130606.
- [191] D. Smeulders. Experimental evidence for slow compressional waves. *Journal of Engineering Mechanics*, 131(9):908–917, 2005. doi:10.1061/(ASCE)0733-9399(2005)131:9(908).
- [192] D. M. J. Smeulders and M. E. H. van Dongen. Wave propagation in porous media containing a dilute gas-liquid mixture: Theory and experiments. *Journal of Fluid Mechanics*, 343:351–373, 1997.
- [193] B. d. Spinoza. *Ethica. English*. Public domain (e-)book, 2011. translated by R. H. M. Elwes, first published in 1677.
- [194] F. Stauffer. Time dependence of the relations between capillary pressure, water content and conductivity during drainage of porous media, 1978. Symp. IAHR, Thessaloniki, Greece.
- [195] H. Steeb. Non-equilibrium processes in porous media, 2009. Habilitationsschrift, Universität des Saarlandes, F8 Naturwissenschaftlich-Technische Fakultät III.

- [196] H. Steeb. Ultrasound propagation in cancellous bone. *Archive of Applied Mechanics*, 80(5):489–502, 2010. doi:10.1007/s00419-009-0385-z.
- [197] H. Steeb, M. Frehner, and S. Schmalholz. Waves in residual-saturated porous media. In G. A. Maugin and A. V. Metrikine, editors, *Mechanics of Generalized Continua*, volume 21 of *Advances in Mechanics and Mathematics*, pages 179–187. Springer New York, 2010. doi:10.1007/978-1-4419-5695-8_19.
- [198] H. Steeb, P. S. Kurzeja, M. Frehner, and S. M. Schmalholz. Phase velocity dispersion and attenuation of seismic waves due to trapped fluids in residual saturated porous media. *Vadose Zone Journal*, 11, 2012. doi:10.2136/vzj2011.0121.
- [199] H. Steeb, P. Kurzeja, and S. M. Schmalholz. Wave propagation in unsaturated porous media. *Acta Mechanica*, 2013. submitted.
- [200] P. Steinmann. On boundary potential energies in deformational and configurational mechanics. *Journal of the Mechanics and Physics of Solids*, 56:772–800, 2008. doi:10.1016/j.jmps.2007.07.001.
- [201] H. P. R. Strauß. *Ingenieurgeologie*. Spektrum Akademischer Verlag Heidelberg, 2011.
- [202] M. A. Strutz. Untersuchung der Ausbreitung periodischer Druckpulse in kompressiblen Flüssigkeiten innerhalb von verformbaren Rohren. Master thesis, Ruhr-Universität Bochum, Germany, 2009.
- [203] R. Tadmor. Line energy and the relation between advancing, receding, and young contact angles. *Langmuir*, 20(18):7659–7664, 2004. doi:10.1021/la049410h.
- [204] K. Terzaghi and O. K. Fröhlich. *Theorie der Setzung von Tonschichten*. Deuticke Leipzig/Wien, 1936.
- [205] K. Terzaghi. *Theoretical soil mechanics*. Chapman London, 1944.
- [206] C. V. Theis. The relation between the lowering of the piezometric surface and the rate and duration of discharge of a well using groundwater storage. *Transactions of the American Geophysical Union*, 16:519–524, 1935. doi:10.1029/TR016i002p00519.
- [207] H. Tijdeman. On the propagation of sound waves in cylindrical tubes. *Journal of Sound and Vibration*, 39(1):1–33, 1975. doi:http://dx.doi.org/10.1016/S0022-460X(75)80206-9.
- [208] R. C. Tolman. The effect of droplet size on surface tension. *Journal of Chemical Physics*, 17(3):333–337, 1949. doi:10.1063/1.1747247.
- [209] C. Truesdell. Sulle basi della thermomeccanica. *Rendiconti Lincei*, 22:33–38 and 158–166, 1957. Translated in [210].
- [210] C. Truesdell. *Continuum mechanics II: The rational mechanics of materials*. Gordon and Breach, New York, 1965.
- [211] K. Tuncay and M. Yavuz Corapcioglu. Body waves in poroelastic media saturated by two immiscible fluids. *Journal of Geophysical Research: Solid Earth*, 101(B11):25149–25159, 1996. doi:10.1029/96JB02297.

- [212] D. Uribe, E. Saenger, R. Jaenicke, H. Steeb, and O. Ruiz. Microscale investigations of highfrequency wave propagation through highly porous media. *Proceedings in Applied Mathematics and Mechanics*, 12(1):555–556, 2012. doi:10.1002/pamm.201210266.
- [213] J. Verne. *Journey to the Centre of the Earth*. Oxford University Press, 1992. Translation, introduction, and notes by William Butcher.
- [214] C. Vinci, J. Renner, and H. Steeb. Analysis and modeling of the hydro-mechanics of deformable fractures. *Proceedings in Applied Mathematics and Mechanics*, 12(1):387–388, 2012. doi:10.1002/pamm.201210182.
- [215] M. A. Walkley, P. H. Gaskell, P. K. Jimack, M. A. Kelmanson, and J. L. Summers. Finite element simulation of three-dimensional free-surface flow problems. *Journal of Scientific Computing*, 24(2):147–162, 2005. doi:10.1007/s10915-004-4611-0.
- [216] M. A. Walkley, P. H. Gaskell, P. K. Jimack, M. A. Kelmanson, and J. L. Summers. Finite element simulation of three-dimensional free-surface flow problems with dynamic contact lines. *International Journal for Numerical Methods in Fluids*, 47:1353–1359, 2005. doi:10.1002/fld.839.
- [217] H. F. Wang. *Theory of linear poroelasticity with applications to geomechanics and hydrogeology*. Princeton Series in Geophysics. Princeton University Press, 2000.
- [218] A. Warning, A. Dhall, D. Mitrea, and A. K. Datta. Porous media based model for deep-fat vacuum frying potato chips. *J. Food Eng.*, 110(3):428–440, 2012. doi:10.1016/j.jfoodeng.2011.12.024.
- [219] C. Wei and K. K. Muraleetharan. A continuum theory of porous media saturated by multiple immiscible fluids: I. linear poroelasticity. *International Journal of Engineering Science*, 40(16):1807–1833, 2002. doi:10.1016/S0020-7225(02)00068-X.
- [220] C. Wei and K. K. Muraleetharan. Acoustical characterization of fluid-saturated porous media with local heterogeneities: Theory and application. *International Journal of Solids and Structures*, 43(5):982–1008, 2006. doi:http://dx.doi.org/10.1016/j.ijsolstr.2005.06.008.
- [221] C. Wei and K. K. Muraleetharan. Linear viscoelastic behavior of porous media with non-uniform saturation. *International Journal of Engineering Science*, 45(2-8):698–715, 2007. doi:10.1016/j.ijengsci.2007.03.013.
- [222] S. Whitaker. The transport equations for multi-phase systems. *Chemical Engineering Science*, 28(1):139–147, 1973. doi:10.1016/0009-2509(73)85094-8.
- [223] J. E. White, N. Mihailova, and F. Lyakhovitsky. Low-frequency seismic waves in fluid-saturated layered rocks. *Journal of the Acoustical Society of America*, 57(S1):S30–S30, 1975. doi:10.1121/1.1995164.
- [224] K. Wilmański. A few remarks on Biot’s model and linear acoustics of poroelastic saturated materials. *Soil Dynamics and Earthquake Engineering*, 26:509–536, 2006. doi:10.1016/j.soildyn.2006.01.006.

- [225] L. Wittgenstein. *Philosophische Untersuchungen*. Suhrkamp Verlag, 2003.
- [226] J. R. Womersley. Method for the calculation of velocity, rate of flow and viscous drag in arteries when the pressure gradient is known. *The Journal of Physiology*, 127:553–563, 1955.
- [227] J. R. Womersley. XXIV. Oscillatory motion of a viscous liquid in a thin-walled elastic tube-I: The linear approximation for long waves. *Philosophical Magazine Series 7*, 46:199–221, 1955. doi:10.1080/14786440208520564.
- [228] J. R. Womersley. Oscillatory Flow in Arteries: the Constrained Elastic Tube as a Model of Arterial Flow and Pulse Transmission. *Physics in Medicine and Biology*, 2:178–187, 1957. doi:10.1088/0031-9155/2/2/305.
- [229] J. R. Womersley. Oscillatory Flow in Arteries. II: The Reflection of the Pulse Wave at Junctions and Rigid Inserts in the Arterial System. *Physics in Medicine and Biology*, 2:313–323, 1958. doi:10.1088/0031-9155/2/4/301.
- [230] J. R. Womersley. Oscillatory Flow in Arteries. III: Flow and Pulse-Velocity Formulae for a Liquid whose Viscosity varies with Frequency. *Physics in Medicine and Biology*, 2:374–382, 1958. doi:10.1088/0031-9155/2/4/307.
- [231] B. Würsig, C. G. Jr., and T. Jefferson. Development of an air bubble curtain to reduce underwater noise of percussive piling. *Marine Environmental Research*, 49(1):79–93, 2000. doi:10.1016/S0141-1136(99)00050-1.
- [232] Q. Xu and M. Solaimanian. Modelling linear viscoelastic properties of asphalt concrete by the huet-sayegh model. *International Journal of Pavement Engineering*, 10(6):401–422, 2009. doi:10.1080/10298430802524784.
- [233] T. Young. *A course of lectures on natural philosophy and the mechanical arts*, volume 2. London: Printed for J. Johnson, 1807.
- [234] P. C. Zielke. *Experimentelle Untersuchung der Bewegung von Tropfen auf Festkörperoberflächen mit einem Gradienten der Benetzbarkeit*. PhD thesis, Technische Fakultät, Universität Erlangen-Nürnberg, 2008.
- [235] C. Zwikker and C. W. Kosten. *Sound absorbing materials*. New York: Elsevier Publishing Company, Inc., 1949.

CURRICULUM VITAE - Patrick Sebastian KURZEJA

PLACE AND DATE OF BIRTH: Gliwice, Poland | 16 June 1985

School Education

AUGUST 1991 - Elementary School
JULY 1995 Hermann-Gmeiner-Schule, Hamm, Germany
AUGUST 1995 - Abitur (A-levels)
JUNE 2004 Märkisches Gymnasium, Hamm, Germany

University Education

OCTOBER 2005 - Dipl.-Ing. | Mechanical Engineering
FEBRUARY 2010 Ruhr-Universität Bochum, Germany
Concentration in Applied Mechanics
Graduated with distinction and the Price of the Faculty
of Mechanical Engineering
DECEMBER 2006 - Student assistant
MARCH 2009 Chair of Technical Mechanics, Ruhr-Universität
Bochum, Germany
since OCTOBER 2008 Study of Mathematics, B. Sc.
Ruhr-Universität Bochum, Germany (with interruption)
since MARCH 2010 PhD student and research assistant
Chair of Mechanics - Continuum Mechanics, Ruhr-
Universität Bochum, Germany
since JULY 2010 Member of RUB Research School
APRIL 2011 - PhD Studentship
SEPTEMBER 2013 Studienstiftung des deutschen Volkes
(German National Academic Foundation)
JUNE - JULY 2011 Research visit | Princeton University, New Jersey, USA
Department of Civil and Environmental Engineering

Non-university Education and Experience

SEPTEMBER 2004 - Alternative civilian service
MAY 2005 Alfred-Delp-Schule, Hamm, Germany, School for men-
tally and physically handicapped children
JUNE - AUGUST 2005 Internship | Hydraulics
Montanhydraulik GmbH, Hamm, Germany
APRIL 2008 - Bronnbacher Studentship
MARCH 2009 Program of the Association of Arts and Culture of the
German Economy at the Federation of German Industries
APRIL - JUNE 2009 Internship | Turbomachinery
Siemens AG, Mülheim an der Ruhr, Germany

*“I’m a scientist, so I must be scientific about this.
I cautioned you about disrupting the continuum for your own personal benefit.”*

Dr. Emmett “Doc” Brown (1990, Back to the Future III)

**Mitteilungen aus dem Institut für Mechanik
RUHR-UNIVERSITÄT BOCHUM
Nr. 159**

ISBN 978-3-935892-37-7